Cost-effective and Reliable Copperplated Metallisation for Silicon Solar Cells: A Development Path

Author:
Wang, Xi

Publication Date:
2017

DOI:
https://doi.org/10.26190/unsworks/19844

Cost-effective and Reliable Copper-plated Metallisation for Silicon Solar Cells: A Development Path

By

Xi Wang

School of Photovoltaic and Renewable Energy Engineering

University of New South Wales

Sydney, Australia

A thesis submitted in fulfilment of the requirements for the degree of Doctor of Philosophy

March 2017

THE UNIVERSITY OF NEW SOUTH WALES
Thesis/Dissertation Sheet

Surname or Family name: **Wang**

First name: **Xi** Other name/s:

Abbreviation for degree as given in the University calendar: **PhD**

School: **School of Photovoltaic and Renewable Energy Engineering** Faculty: **Engineering**

Title: **Cost-effective and Reliable Copper-plated Metallisation for Silicon Solar Cells: A Development Path**

Copper (Cu) plating can reduce the consumption of silver for silicon (Si) photovoltaic manufacturing, whilst also offering the potential to increase cell efficiency by way of reduced shading due to very narrow fingers and contacting Si surfaces without requiring high dopant concentrations. A cost-effective and reliable plating method for both n-type and p-type Si surfaces can make possible low-cost Cu metallisation for a range of different cell structures. A single side plating method called field-induced plating (FIP), also known as forward-bias plating, was developed to plate metal contacts to p-type Si surfaces. This process was used in combination with light-induced plating (LIP) to fabricate Cu-plated bifacial laser-doped Si solar cells with efficiencies of up to 19.2%. However two key performance limiting factors were identified: (i) increased recombination due to p-type laser-doping (which limited the fill factor of cells to 75%; and (ii) poor adhesion of the plated metal.

The introduced recombination was analysed using injection-dependent lifetime analyses of quasi-steady-state photoluminescence and photoconductance (QSSPL and QSSPC) measurements. Although boron laser doping resulted in the local ideality factor increasing to ~1.5, the introduced recombination could not be analysed assuming a single Shockley-Reed Hall defect. Since some activation of the deep-level boron-oxygen (B-O) defect was suspected during cell processing, the recombination properties of this defect were analysed. The electron/hole capture cross-section ratio of the B-O defect was estimated to be 9.7±1.7 and 9.7±1.9 using QSSPL and QSSPC measurements, respectively, performed after belt furnace annealing, light soaking and regeneration of wafers that were symmetrically-passivated with SiNx and rapidly annealed after deposition.

Surface roughness was identified to be a key factor for contact adhesion. It was shown that use of a UV ps laser to ablate the SiNx antireflection coating to form openings for a plated metal grid can result in average 180º pull test forces of 2.1 N/mm, substantially exceeding the industry benchmark of 1 N/mm. Pull forces were too low to be measured for laser-doped and ns UV laser ablated openings. However, due to different plating rates occurring across a cell in LIP, busbar pull forces were shown to not always be a good indicator for plated finger adhesion. Stylus-based finger adhesion measurements were therefore used to demonstrate how contact formation, plating rate and chemistry, grid geometry and annealing can all affect finger adhesion. This thesis presents a compelling case for metallisation metrology if reliable plated metallisation is to be achieved in an industrial environment.

FOR OFFICE USE ONLY Date of completion of requirements for Award:

ORIGINALITY STATEMENT

'I hereby declare that this submission is my own work and to the best of my knowledge it contains no materials previously published or written by another person, or substantial proportions of material which have been accepted for the award of any other degree or diploma at UNSW or any other educational institution, except where due acknowledgement is made in the thesis. Any contribution made to the research by others, with whom I have worked at UNSW or elsewhere, is explicitly acknowledged in the thesis. I also declare that the intellectual content of this thesis is the product of my own work, except to the extent that assistance from others in the project's design and conception or in style, presentation and linguistic expression is acknowledged.'

Signed ……..

Date ……..

ABSTRACT

Copper (Cu) plating can reduce the consumption of silver for silicon (Si) photovoltaic manufacturing, whilst also offering the potential to increase cell efficiency by way of reduced shading due to very narrow fingers and contacting Si surfaces without requiring high dopant concentrations. A cost-effective and reliable plating method for both n-type and p-type Si surfaces can make possible low-cost Cu metallisation for a range of different cell structures. A single side plating method called field-induced plating (FIP), also known as forward-bias plating, was developed to plate metal contacts to p-type Si surfaces. This process was used in combination with light-induced plating (LIP) to fabricate Cu-plated bifacial laser-doped Si solar cells with efficiencies of up to 19.2%. However two key performance limiting factors were identified: (i) increased recombination due to p-type laser-doping (which limited the fill factor of cells to 75%; and (ii) poor adhesion of the plated metal.

The introduced recombination was analysed using injection-dependent lifetime analyses of quasi-steady-state photoluminescence and photoconductance (QSSPL and QSSPC) measurements. Although boron laser doping resulted in the local ideality factor increasing to ~1.5, the introduced recombination could not be analysed assuming a single Shockley-Reed Hall defect. Since some activation of the deep-level boron-oxygen (B-O) defect was suspected during cell processing, the recombination properties of this defect were analysed. The electron/hole capture cross-section ratio of the B-O defect was estimated to be 9.7±1.7 and 9.7±1.9 using QSSPL and QSSPC measurements, respectively, performed after belt furnace annealing, light soaking and regeneration of wafers that were symmetrically-passivated with SiN_x and rapidly annealed after deposition.

Surface roughness was identified to be a key factor for contact adhesion. It was shown that use of a UV ps laser to ablate the SiN_x antireflection coating to form openings for a plated metal grid can result in average 180º pull test forces of 2.1 N/mm, substantially exceeding the industry benchmark of 1 N/mm. Pull forces were too low to be measured for laser-doped and ns UV laser ablated openings. However, due to different plating rates occurring across a cell in LIP, busbar pull forces were shown to not always be a good indicator for plated finger adhesion. Stylus-based finger adhesion measurements were therefore used to demonstrate how contact formation, plating rate and chemistry, grid geometry and annealing can all affect

finger adhesion. This thesis presents a compelling case for metallisation metrology if reliable plated metallisation is to be achieved in an industrial environment.

ACKNOWLEDGMENT

I wasn't expected to achieve a PhD degree when I arrive Sydney eight years ago, I was only hope to finish my undergraduate course without fail any course. The only bigger wish I was having at that time was to get a chance to do a master by research degree in SPREE so that I can work in the lab. But now, I can't even imagine I am writing this acknowledgement and finishing this PhD thesis. So, I want to say thank you to so many people around me and help me achieve all of this.

First and the most important person is my supervisor Dr. Alison Lennon, without your patience and tolerance on all mistakes I made, I will not have any chance to even start a PhD which totally changed my life. With your warm guide and wonderful advice, I would be able to process, continue and enjoy all the hard works. You taught me how to work, the way of 'Propose hypothesis，prove the hypothesis by practical experiment' is extremely valuable and will be remembered for my future career. You also taught me how to behave, your kindness, honesty, adhere to the principle and sincere will influence the rest of my life. Especially at end of this PhD, your tolerance and huge amount of the help supported me going through one of the hardest time in these years. There is not enough word to explain how much I appreciate your help, and it is very lucky that I have got such a great supervisor! I would also like to thank Dr. Matthew Edwards being my co-supervisor, your suggestions and advisers during annual reviews were very helpful.

There are many people in SPREE I would like to thank. Paget, who is helping me all the way through my PhD, it always been so wonderful and fun to work on all kinds of 'homemade hi-tech' experiment setups, your calm personality is something I should learn. I also would like to thank Valantis who introduced me in the LIP/FIP work at beginning, your guides at begin help me to developed the fundamental lab skills, and all these LIP/FIP work later expanded to this PhD projects. I would like to thank Xi Wang who I worked with in second and third year of my PhD, your passion and perfection helps me further improved my working skill, and I have learnt large amount of knowledge from you and the time we work on adhesion tester and time spend on fishing will be remembered for the rest of my life. I also want to thank

Mattias Juhl in help me with QSSPL, your patience and attitude towards the work helps me went through the hardest chapter of my PhD work. I also would like to thank Yu Yao, Ou Yang, Jie Cui, Licheng Liu, Alex Han who help me in leaning lab works and research skills at beginning of my PhD, you advise and encourage will not be forget. I also want to thank Zhong Lu, Doris, John, Jack, Nino, Kai Wang, Li Yang, Zhongtian and Arman, it has been wonderful to work with you in SPREE. I would like to thank LDOT, Kian, Alan, Nick, Bernhard, Nancy, Jill and Lawrence, your helps are extremely appreciated. I also want to thank Ben and Alex from MQU, who help me with all the laser works, it is wonderful to meet you guys. At end, because there are too many people helped me in these years, I would like to thank everyone in SPREE who had helped me.

I would like to thank my friend outside SPREE, WenFang, WuAng, Sunqing, Zibo, Heke and Patrick. Thank you for your accompany these years, there are so many great moment left in my memory and will never be forget!

Finally, I want to thank my wife Liya, it has been long and hard way to come here. With your selfless and strong support, I went through this hardest time in my life. Your kindness, brave and tolerance can never achieved by anyone else. Thank you for your sacrifice and understanding all these years, thank you! And I love you!

Last but not least, my father and mother. You are my model of life, your firm support, encourage and love is so selfless, there is no way I can achieve this without you. There is no word that can or enough to explain how much appreciation and love I have for you. You taught me how to be strong, brave and responsible. I love you!

TABLE OF CONTENTS

CHAPTER 1
INTRODUCTION

1.1 Background and Motivation

Extraction of current from silicon (Si) solar cells requires that metal electrodes, or contacts, are formed to each of the n and p polarities of the Si absorber. In the dominant industrial Si photovoltaic (PV) technology, metal contacts to the cell are formed using screen-printed silver (Ag) and aluminium (Al). In 2016 the typical manufactured Si solar cell used 100 mg of Ag [1]. For mass production where in excess of 3000 wafers are produced in every hour [2], this amounts to ~ 50 kg of Ag being required per week. The monetary value of these large amounts of Ag and the capacity of the world's resources to supply the necessary metal needs to be considered if production of Si photovoltaics is to expand to levels of 80 GW year by 2022 [1].

Silver was one of the earliest forms of casted money and used for possibly the earliest mass-produced coins that were traded. Silver usage in coins dates back to Ancient Greece (see Figure 1-1), however it was quickly adopted worldwide as the preferred metal for coinage. Consequently, the first thing that people often think of when Ag is mentioned is "monetary value".

Figure 1-1. Silver coin from CALABRIA, Tarentum, Circa 302 BC (from [3]).

Besides being used for coins and more generally for financial currency, Ag has evolved to have many applications due to its unique chemical properties (see Figure 1-2). Its shiny appearance makes it attractive for use in jewellery, with the metal's monetary worth contributing value to items. Silver's ability to disrupt the growth of bacteria has resulted in its use as an antibacterial agent [4]. Wound dressings containing Ag have been used for more than a century with soldiers in World War I, in the absence of antibiotics, relying heavily upon such dressings [5]. In more recent times, Ag has been used in many medical antibacterials [6], added to drinking water in airlines, food packaging and used for swimming pool purification [7-9]. Finally Ag's high resistance to corrosion and electrical conductivity has made it an ideal electrical conductor for not only solar cells, but a wide range of electrical and electronic devices. This presents a picture of a highly versatile and useful metal, being increasingly in demand for a range of applications. However, due to Ag's investment value its price is highly volatile.

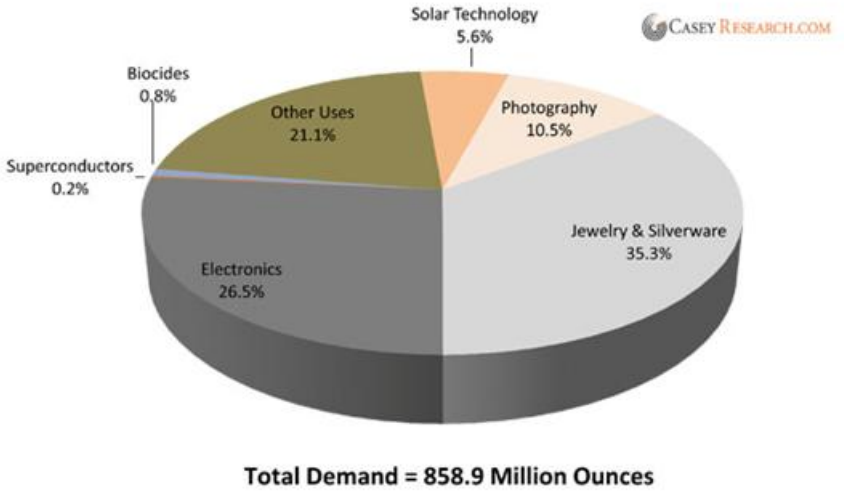

Figure 1-2. Silver usage in different industries (from [10]).

'Forget gold, silver is on fire and could hit $25 an ounce by the end of 2016', a recent media article by Saefong [11] reported. This view is shared by many investors [12-14]. As Figure 1-3 shows, the spot price of Ag fluctuated like a roller coaster between the years 2003 to 2016, climbing to a peak of ~US$1400/kg in 2011, and then rapidly dropping to values of ~ US$500/kg recently [15]. Although the prices of Ag pastes for PV manufacturing do not necessarily numerically reflect the base metal price because the paste manufacturers typically buy metal at contract prices which can effectively smooth some of the variations, ultimately

the base metal price is reflected in the prices that PV manufacturers pay for their pastes. The 2013 Edition of the International Technology Roadmap for Photovoltaics (ITRPV) report quoted Ag paste prices in the order of UD$1000/kg in 2012 [16].

Although the price of Ag tends to track with that of the other investment metal gold (Au), Ag is known as "the poor man's gold". It is relatively cheaper, however in recent years, due to the instability of the Chinese stock market, large amounts of (Chinese) money has been invested in Ag and, due to the large population of China [11, 17-20], it was predicted that the Ag price would begin increasing again towards the end of 2016 [11, 12]. Figure 1-3 seems to suggest that indeed the Ag price is trending upward.

Whilst Ag is subject to this price instability, the price of copper (Cu) has remained relatively stable and significantly lower than that of Ag between 2003 and 2016 (see Figure 1-3). This stability is in part due to the large available resources of Cu on Earth. It is estimated that there are 10^{14} tons of Cu located within 1 km from the Earth's surface [21]. It is predicted that with the current Cu production rate, the Earth's Cu resources will last 5 million years assuming that all new Cu is mined. The fact that most of the Cu is relatively near to the surface means that mining can be relatively lower cost. Copper can also be effectively recycled [22, 23], thereby extending the Earth's resources further. Consequently, historically the Cu price has remained low, and in the last 20 years it has not exceeded $8.27/kg. Moreover, due to Cu's excellent electrical conductivity of 5.96×10^7 S/m, which is only slightly lower than that of Ag's 6.30×10^7 S/m, and its durability, Cu has been widely used for electrical conduction wires. The above-mentioned properties of Cu make it extremely attractive for large-scale manufacturing.

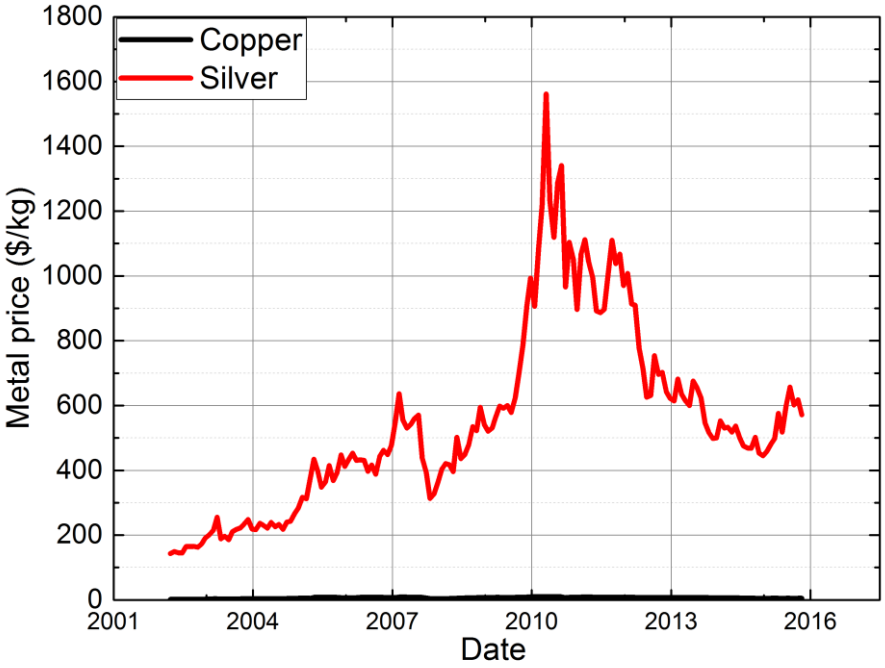

Figure 1-3. Comparative Ag and Cu prices in US$/kg between 2003 and 2016 (from [15, 24]).

Returning now to the use of Ag in Si PV metallisation, although the screen printing of Ag pastes is a well understood process with a mature equipment market, if the peak Ag paste prices of 2012 were to return (i.e., in the order of UD$1000/kg [16]), then Ag metallisation costs at a production rate of 3000 cells/hr would increase by almost a factor of two to ~ US$50,000 per week. More importantly, if the Ag metallisation was replaced by Cu metallisation on an equal weight basis, metallisation costs could be reduced to less than US$500 per week for production of 3000 cells/hr. This sobering scenario provides the motivation to develop Cu-based alternatives to screen-printed Ag metallisation for Si PV and is reflected in a predicted trend to Cu metallisation at the expense of screen-printed Ag in all of the ITRPV reports published since 2010. The 2016 ITRPV report predicts that by 2026, ~30% of the Si solar cell market will have adopted Cu plating (see Figure 1-4).

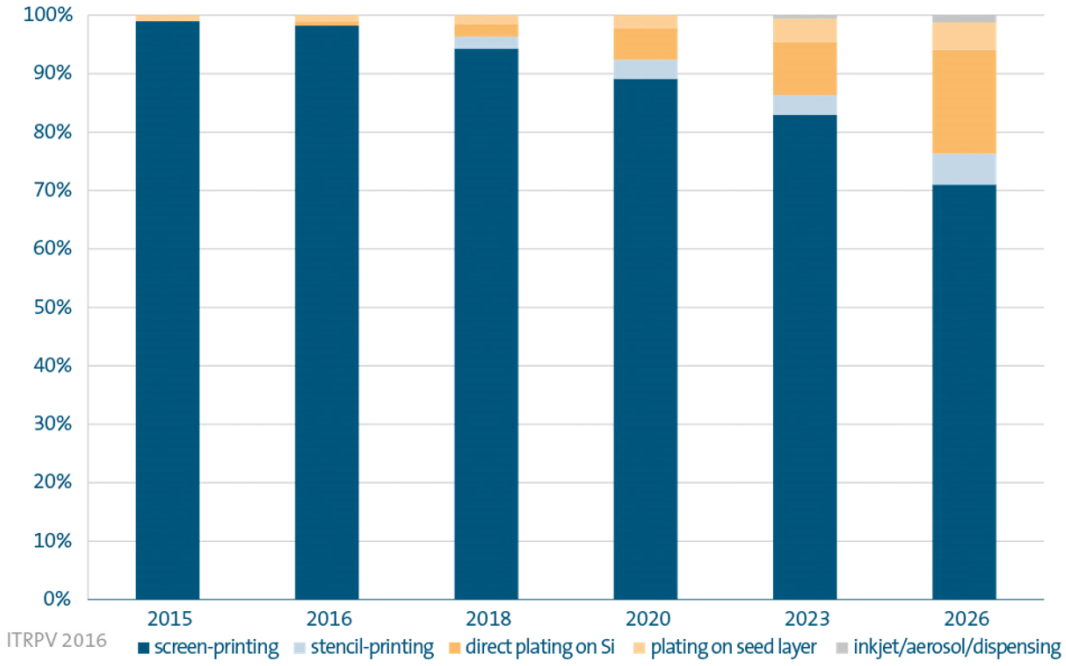

Figure 1-4. Predicted market share trend for different front side metallization methods (from [1]).

The most effective way of forming highly conductive metal grids using Cu is to use metal plating. Several companies and research institutes have demonstrated the possibility of Cu-plated metallisation. Solarex used electroless nickel (Ni) deposition followed by solder build-up to form the metal contacts for the interconnection of their terrestrial cells [25, 26] in the 1970s. Then, in the early 1990's, the buried contact Si solar cell was introduced by Wenham and Green [27, 28]. This cell design used electroless plating, with a Ni seed layer and Cu being plated in selectively-doped laser grooves [29, 30]. Due to the reduced shading (as a result of the narrower plated fingers) and the use of a selective emitter, higher cell efficiencies were achieved using the buried contact cell design than were possible with cells metallised using screen printing at that time. BP Solar commercialised the buried contact cell design as its Laser Buried Grid (LBG) Saturn technology and continued to produce modules using this technology until 2009. Saturn modules have now been operating in the field in a Toledo (Spain) power plant with a performance ratio that exceeds that of comparatively-aged screen-printed modules [31]. This result suggests that the Ni/Cu/Ag plating process used by BP Solar was sufficiently reliable for field operation, and indeed may provide some advantages over the screen-printed metallisation used at the time in terms of module longevity in the field.

Nickel/Cu plated metallisation was again introduced into production by Suntech in their laser-doped selective-emitter (Pluto) technology [32, 33]. Suntech replaced the electroless plating process with light-induced plating (LIP) [34] making possible lower-cost bath maintenance and a faster, higher throughput process [26]. However unlike BP Solar's Saturn cells, Pluto cells with plated busbars could not be interconnected by soldering [35, 36]. This necessitated a more complicated fabrication process in which busbars were screen-printed and fingers laser-doped and plated. Furthermore, Pluto production was plagued by reports of plated finger peeling [37], a problem which was not experienced by BP Solar, presumably due to the 'buried' nature of the metal grid where the sidewalls of the grooves could increase the adhesive contact area.

The added process complexity and quality control requirements of Suntech's plated metallisation process eroded any efficiency advantage that the Pluto selective emitter may have initially promised. This led to Suntech abandoning its Pluto production in favour for a more standard screen-printed Si PV production process. Since then, although the solderability of plated busbars has since been demonstrated to be possible through the use of ps laser ablation [38-41], plated metallisation has failed to find traction in Si PV production due largely to the relatively low prices of Ag pastes and the continuing efficiency improvements of screen-printed cells made possible by innovations in both emitter engineering, pastes and equipment. However with the price of Ag pastes expected to increase in the near future, it will be important to address some of the problems that have been experienced in the past with plated metallisation so that reliable, low-cost Cu-plated modules can be produced in large scale manufacturing.

1.2 Thesis Aim and Scope

With the motivation of reducing the metallisation cost of Si PV cells by using Cu as the main conductor instead of Ag without the reduction of cell efficiency, the aim of this thesis was to investigate industrially-feasible processes for contact formation and metal plating for p-type Si solar cells, and in particular, to further the understanding of the role of contact formation in fabricating reliable and adhesive plated metal contacts.

The research that was conducted as part of this thesis firstly focused on developing a robust and high-yield plating method that could be used to deposit metal on both the n-type and p-type surfaces of bifacial Si solar cells. This initial study highlighted a number of issues to

address which included: (i) the generation of surface and deeper defects during laser doping processes; and (ii) the poor interfacial adhesion of the plated metal fingers.

Experiments were then conducted with a view to understanding the cause and nature of the laser-introduced defects by monitoring the injection-dependent effective minority carrier lifetime using quasi-steady state photoluminescence (QSSPL) and quasi-steady state photoconductance (QSSPC) as the cell was progressively fabricated and then degraded due to exposure to light.

Finally, a new stylus based adhesion tool was used to assess the adhesion of the plated metal fingers thus enabling process improvements in the plating processes that were being used. Used in conjunction with conventional busbar pull tests, experiments were performed to determine the relationship(s) between the plating process and finger and busbar adhesion.

1.3 Thesis Outline

Chapter 2 reviews existing contact formation methods used for Si solar cells providing a historical context. Methods developed to improve the cell efficiency and reduce cell metallisation cost (e.g., by reducing finger thickness) are also discussed. A review is then presented of the use of plating for Si solar cell contact formation, with examples of electroplating and electroless plating being discussed. Finally, plating tools that have been developed for lab scale research use and large-scale production are critically reviewed.

The development of a new method which enables the plating of Ni and Cu to p-type Si, called field-induced plating (FIP) is reported in Chapter 3. The FIP process, which evolved from an earlier contactless electroplating (CLEP) process, enabled metal contacts to be plated to p-Si surfaces. Used in conjunction with LIP, FIP makes possible the plated metallisation of bifacial cells. The chapter reports on the optimisation of the p-type and n-type laser doping processes and refinements in FIP which enabled bifacial Cu-plated laser-doped cells with an efficiency of 19% to be fabricated. The performance of the fabricated cells was limited by a low pseudo fill factor (*pFF*) attributed largely to the laser doping on the p-type surface. A further limitation of the process was the relatively poor adhesion of the plated grid. Not only did this poor adhesion prohibit the soldered interconnection of cells, periodic finger peeling was also observed.

The experiments reported in Chapter 4 aimed to gain an enhanced understanding of the underlying reasons for the low *pFF* observed in the bifacial cells fabricated and reported in Chapter 3. Thermal treatments and light-induced degradation resulted in reductions in *pFF* and increased local ideality factors. With the aid of QSSPL and QSSPC, the effective minority carrier lifetime degradation, due to defect formation, was carefully monitored to understand how these defects changed with processing and how they potentially impacted the final cell efficiency. The injection dependent effective minority carrier, measured through a combination of QSSPL and QSSPC, was also used to estimate the capture cross section ratio for the boron-oxygen (B-O) defect in symmetrically-diffused boron-doped wafers, with the use of the QSSPL providing the low injection data.

Chapter 5 examines the critical issue of plated contact adhesion and reports on the development of a new stylus adhesion tester tool to evaluate the plated finger adhesion. The importance of surface roughness of the laser-processed regions in determining whether the plated grid is solderable is discussed and the basic principles of how plating process parameters (e.g., plating speed and plating electrolyte) can cause stress differences in the busbars and fingers which can result in finger peeling, even in cases where the busbars were able to be soldered, are explained. The chapter concludes with a discussion of how the laser-doping process could be adapted so that improved plated contact adhesion can be achieved.

Chapter 6 concludes with a summary of the key results of this project, the original contributions from the author and suggestions for further research.

CHAPTER 2
LITERATURE REVIEW

2.1 Contact Formation

Contact formation, or solar cell metallisation, impacts both the optical and electrical performance of solar cells. A metal grid formed on the illuminated surface of the cell shades the cell preventing carriers from being generated in the underlying Si. Clearly the less the shaded fraction the larger the potential J_{SC} is for the cell. The geometrical properties of the metal contacts can also influence the amount of light, initially reflected from the metal grid, that is internally reflected by the glass of the module when the cell is encapsulated in a module [42]. Rounded metal contact surfaces are therefore preferable to flat surfaces as the reflected light will encounter the glass at a sufficiently large angle to the normal to ensure total internal reflection [43-45] .

Metal contacts can also affect the electrical performance of solar cells through power loss due to series resistance, R_S, and contact recombination. Ideally, electrical contact results in low contact resistance whilst not requiring heavy doping at the Si surface. However, if the minority carrier concentration is too high at the interface of the Si and metal, then the open circuit voltage (V_{OC}) of the cell can be reduced by contact recombination. Finally, the contacts need to be formed with sufficient conductivity so the R_S due to conduction of the collected current in the metal grid (and to adjacent cells in the module) are minimised. This factor is arguably the easiest to achieve as it does not involve a compromise.

This section reviews the development of metallisation methods for Si solar cells, considering the trends from the first Si cells to current day manufacturing of p-type Si solar cells which uses the dominant screen printing technology. The review focuses on the contact formation for p-type Si cells, where the metal is in direct contact with the Si absorber.

2.1.1 Historical Perspective

The metal contacts for the first Si solar cells produced in the 1950's at Bell Labs were plated [26, 46, 47], with plating being used because it was not possible to solder leads directly to the cell [48, 49]. Plating continued to be used into the 1970's with companies such as Solarex

and Motorola developing, through iterative improvements, an electroless plating process involving a Ni seed layer, which could be sintered to form a Ni silicide layer for reduced contact resistance, and then Cu was used to provide conductivity for the electrode contacts [26, 50]. However, in the 1970s Spectrolab introduced the use of screen-printing to the metallisation of solar cells [51, 52]. At the time screen-printing was a relatively simple process that had been used successfully for other applications. It offered the simplicity of a single processing step which could replace the many individual steps required for the formation of a plated metal grid and therefore appeared to be well-suited to manufacturing and quickly became the dominant metallisation technology for Si solar cells [53].

2.1.2 Screen Printing

Screen-printing involves a squeegee being moved across a screen, pushing a metal paste through the screen and onto a substrate such as a solar cell (see Figure 2-1)[54]. After high temperature firing, the metal paste solidifies and forms an electrical contact to the Si becoming the fingers and busbars of a front surface metal grid on the solar cell.

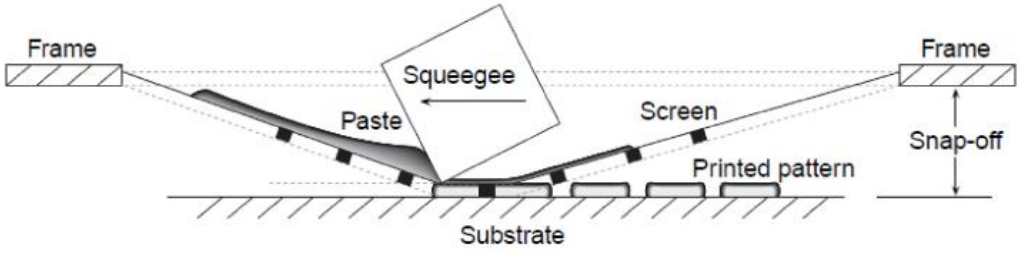

Figure 2-1. Screen-printing process of Si solar cell contact formation.

Figure 2-2 shows the typical flow chart of the screen-printed p-type Czochralski (Cz) Si solar cell fabrication process. After silicon nitride (SiN_x) passivation layer deposition, the cell is placed upside down, screen-printed with an Al paste on the rear and then transferred to an oven which can dry the paste so that the wafer can be placed on the second screen print stage for front Ag finger screen-printing. After the front side paste is dried, the wafer is co-fired in a belt furnace to solidify and form the positive and negative contacts on the solar cell.

Figure 2-2. Process flow diagram for fabrication of a typical p-type Cz screen-printed Si solar cell.

Significant research has been directed into the improvement of p-type Si solar cell efficiency to reduce the energy generation cost. Notable advances have occurred in the development of more lightly-doped emitters for screen-printed contacting [55-57], fabrication processes for rear surface passivation and patterning required for passivated emitter and rear contact cell (PERC) cells [58-60] and processes to permanently deactivate boron-oxygen complexes which become recombination-active on carrier injection (e.g., exposure to light) [61-70]. Although there have also been numerous studies investigating alternative emitter contacting methods [38, 40, 41, 67, 71-79], these alternatives have failed to find traction in the manufacturing industry due to the improved developments and understanding in screen-printed paste contacting [80-85] and emitter engineering. The improvements in screen-printed contact formation have been centred on: (i) fabricating a lightly-doped emitter that can still be effectively contacted by screen-printed Ag pastes; (ii) narrowing the finger width to reduce cell shading; and (iii) reducing the amount of Ag required per cell.

Due to the screen-printing pastes' properties, forming metal contacts to lightly-doped surfaces with low contact resistivity is challenging, consequently surface concentrations exceeding 6.8×10^{19} cm^{-3} are still required for screen-printed contacts [57, 86]. Reducing shading requires narrower fingers which can be achieved through improvements in pastes and screen-printing technology (e.g., screens). Conduction of the current away from the cell requires that the aspect ratio is also increased as fingers are made narrower [87]. After screen-printing of pastes, due to surface tension and gravity, the printed paste spreads laterally on the SiN_x surface. Historically, the resulting fingers were flat (i.e., low aspect ratio) and wide (up to 150 μm in width) and caused significant amounts of shading, consequently leading to a reduction in J_{sc} [88-90]. Over the years, pastes have been systematically improved to achieve narrower and higher-aspect ratio fingers and, in 2016, the width of typical screen-printed fingers was 50 μm [16]. Aligned print-on-print screen-printing, stencil printing [91-95], and dual print [95-97] are approaches which have been used to increase the aspect ratio of fingers.

Aligned print-on-print screen-printing [97], which involves making a second printing pass over a finger-busbar grid, can be used to increase the aspect ratio of a screen-printed grid. Fingers with a height of 20 μm can be achieved, however there can be a considerable variation in printed finger height [98]. The use of print-on-print has necessitated the addition of vision systems to screen printers to enable alignment of the second printing pass.

Dual printing (i.e., printing the busbars separately to the fingers) can be used to both achieve high aspect ratio fingers and perhaps more importantly reduce the amount of Ag required per cell [95, 97]. A reduced paste thickness can be tolerated for the busbar regions as the conductivity of the busbars are enhanced through the interconnection wire. Furthermore, non-contacting busbars can be used to reduce the contacting area of the cell, and thereby increase the cell voltage. The busbars can also be printed with a low-Ag paste further reducing the amount of Ag required per cell.

In early 1996, Moor, et al. reported fine line stencil-printing with a high aspect ratio on Si solar cells [91]. In screen-printing, the wire mesh in the finger aperture of a mesh screen reduces the open area to a value of ~ 60% [95] which places a limit on the obtainable finger height and homogeneity along the finger length. However, in stencil printing 100% of the open finger area is available for the paste (see Figure 2-3). Typically stencil printing requires the use of dual printing (i.e., printing the busbar and fingers in separate printing passes) as it is not easy to form the H-pattern of grids in stencils without reducing the open area of apertures [95]. Using a dual print approach, front metal grids have been printed on 156 mm cells with as little as 68 mg of Ag [97], which is significantly lower than a typical Ag consumption of 100 mg per cell [99]. More recently Hannebauer et al. have reported the use of a single print dual layer stencil that enables the printing of busbars and fingers in a single process step that still features 100% open finger area, however it was demonstrated that the dual print (stencil) process results in a V_{OC} advantage of 1-2 mV over single pass stencil printing due to the ability to use non-fired-through busbars [95].

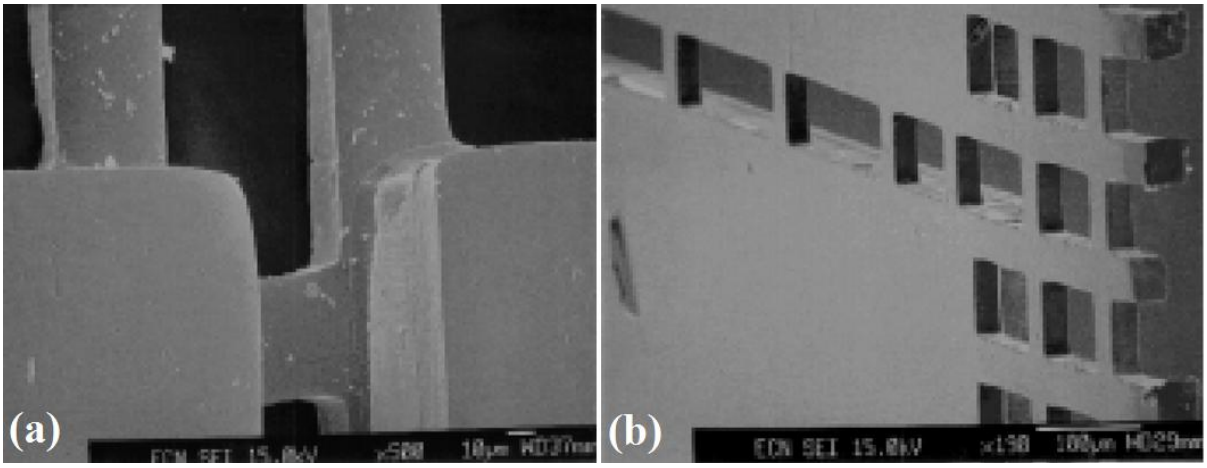

Figure 2-3. (a) Close-up view of a double layer stencil from the substrate side (back side); and (b) a view of the stencil from the squeegee side (front side) showing a finger and part of a busbar on the right (from [92, 94]).

A number of other innovative techniques have been used in the past to increase the aspect ratio of screen-printed grids. One example is the hotmelt technology introduced by Ferro in the early 2000's [100]. Figure 2-4 shows the difference between hotmelt and conventional screen-printing technology at the time. The height of the hotmelt-printed fingers was twice that of fingers formed by screen-printing of conventional pastes. The hotmelt pastes contained a higher concentration of Ag and only became liquid during a heated screen-printing process. The pastes solidified immediately after printing, the rapid solidification preventing excessive spreading and enabling a high aspect ratio printed grid. Although this technology was promising, the ability to achieve higher aspect ratio printed contact grids using a more standard screen-printing process and pastes without the need for equipment changes limited this technology's uptake.

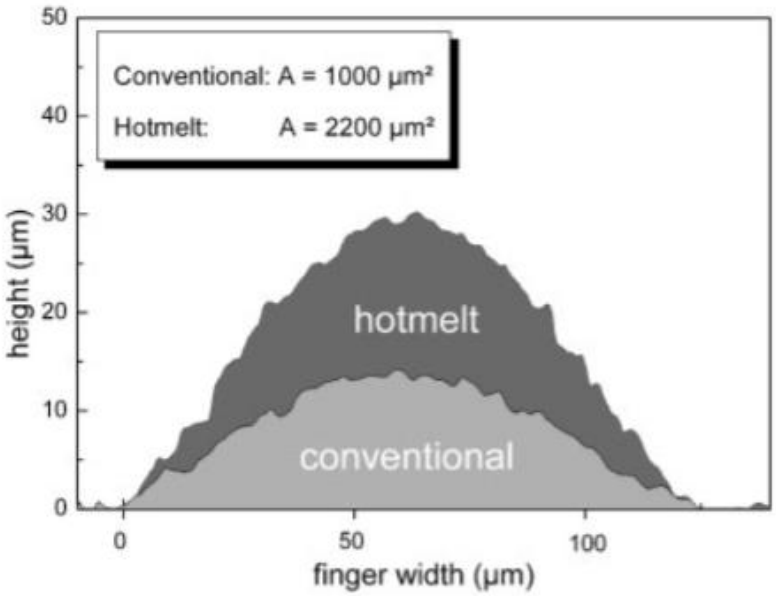

Figure 2-4. Cross section of fingers produced by Hotmelt printing and conventional screen-printing technology(from [100]).

Another technique which used a change in substrate (cell) temperature to achieve narrow, high aspect ratio grid fingers was reported by Erath et al. [101] (see Figure 2-5). By heating the wafer during screen-printing, solvent evaporation was accelerated and this prevented lateral spreading of the paste on the cell. Another advantage of substrate heating is that less paste remains in the mesh than at room temperature printing. Unlike the hotmelt paste printing process, this method could use existing pastes. However, the physical properties of the printed fingers differed from those printed using a more standard process (e.g., hardness) and so changes of this nature require that extensive environmental testing must be performed for modules printed produced with the new or alternative technology.

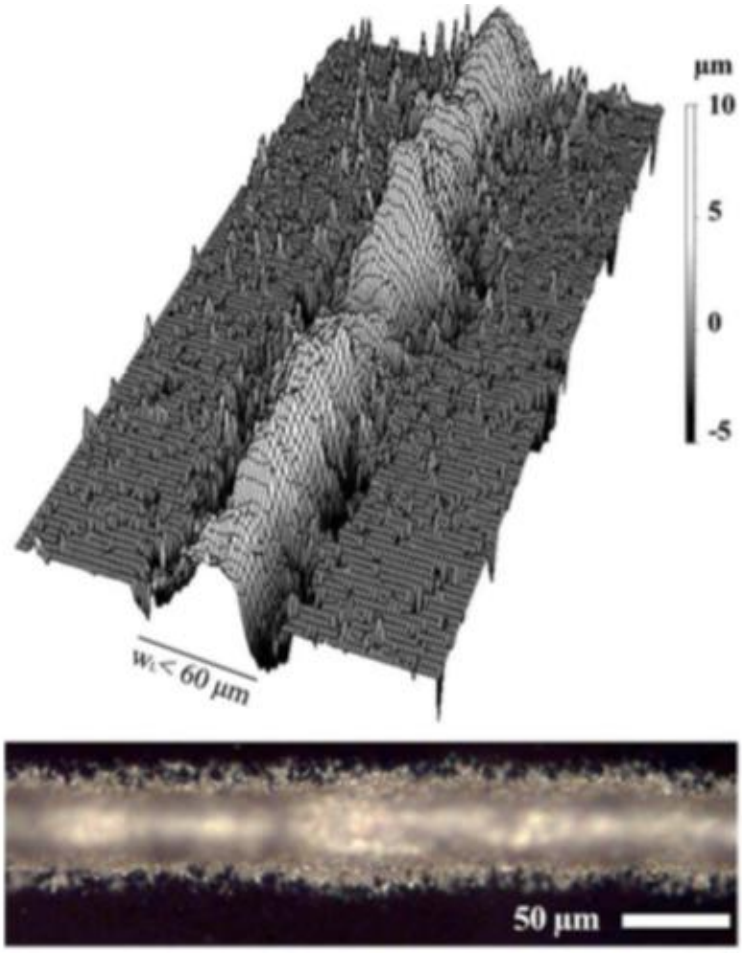

Figure 2-5. Confocal microscope image showing a 60 µm finger achieved by screen-printing on a heated substrate (from [101]).

2.1.3 Other Printing Approaches

In the past 20-30 years there have been numerous attempts to develop alternative printing approaches with the specific objective of decreasing shading (i.e., narrower fingers). In 1987 Teng and Vest reported the inkjet printing of metal-organic inks which decompose after printing to form metal as an alternative to screen-printing [102]. A key advantage of this process over screen printing was the direct writing via digital patterns and non-contact Si wafer processing. However, with the small volumes typically deposited by inkjet printing, many passes are required to form sufficiently thick conductors for the cell. Furthermore, inkjet printing requires fluids to be much less viscous than the pastes used by screen-printing. This therefore limits the solid content of the deposited fluid, making it very challenging to print the entire metal contact without using many printing passes.

Due to these challenges the next use of an alternative non-contact printing approach for front-surface metallisation involved micro-dispensing. Scrypt Inc. and DuPont reported the use of a micro-dispensing nozzle which was moved in the X and Y directions to eject paste on the cell according to a grid pattern [103-105] (see Figure 2-6). With this method, fingers 100 μm wide and 17 μm high were reported, which at the time (in 1988), were much thinner than comparable screen-printed fingers. However, micro-dispensing shares with inkjet printing the problems of nozzle (jet) blockage and poor nozzle (jet) durability. Also use of a single nozzle places a limit on how many wafers can be processed per hour due to the need to scan the entire wafer surface.

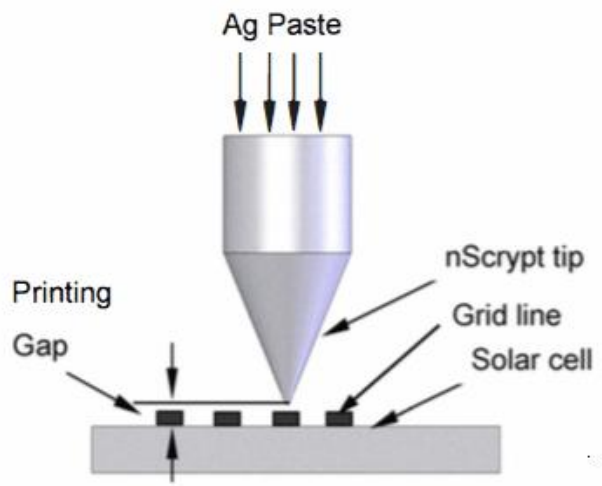

Figure 2-6. Front view of non-contact micro-dispensing nozzle printing paste on a Si solar cell (from [105]).

Mette et al. introduced the use of metal aerosol jet for solar cell metallization [104, 106-108]. Unlike inkjet printing, aerosol printing is a continuous deposition process (see Figure 2-7) method and can deposit fluids with a higher metal loading. A fluid is first atomised into an aerosol or mist and then the generated aerosol is guided to the substrate using a sheath gas to constrain the fluid. However as for the earlier inkjet printing process, it is tedious and slow to build up the entire conductor, and so Mette et al. described a process in which a thin seed layer was printed, and then fired substantially as for screen-printed paste. The conductive seed layer was then thickened using LIP of Ag to complete the metal grid. Although comparable cell efficiencies were achieved with this aerosol printing / plating process, difficulties were incurred in the scaling up of the process for manufacturing. In an attempt to improve throughput, Optomec developed a 40 nozzle aerosol printer that was capable of

printing a Ag seed layer 40 μm wide and 1.5 μm high on a 156 mm cell in 2.5 to 3 s [109] however to the candidate's knowledge this alternative metallisation process was never demonstrated in manufacturing. A key issue at the time that the process was being developed at Fraunhofer, was that it did not provide any advantage in terms of reduced Ag consumption. This was an important consideration in the period from 2010 to 2012 because Ag prices were high at that time.

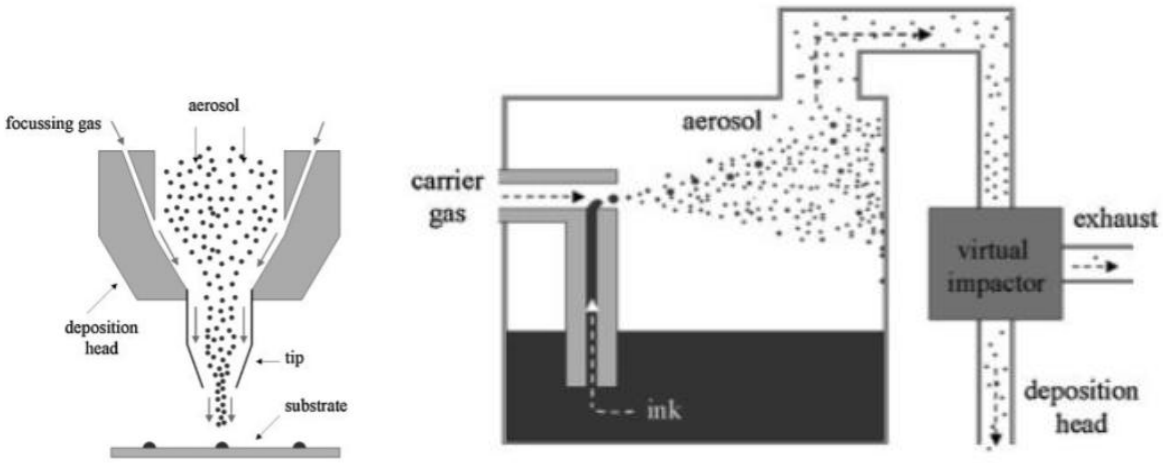

Figure 2-7. A schematic depicting the aerosol jet metal deposition process (from [104]).

The strategy of printing a seed layer and then plating up was also demonstrated using inkjet printing of the seed layer. Ebong et al. and XJet partnered in a development of a process in which an XJet printer was used to rapidly print a seed Ag layer [110-112]. The Xjet printer could process 2400 industrial wafers per hour and was equipped with redundancy features that enabled the detection of blocked nozzles and subsequent correction around the detected printing faults. Figure 2-8 shows a printed seed layer and an example finger after plating using Ag LIP for 10 min.

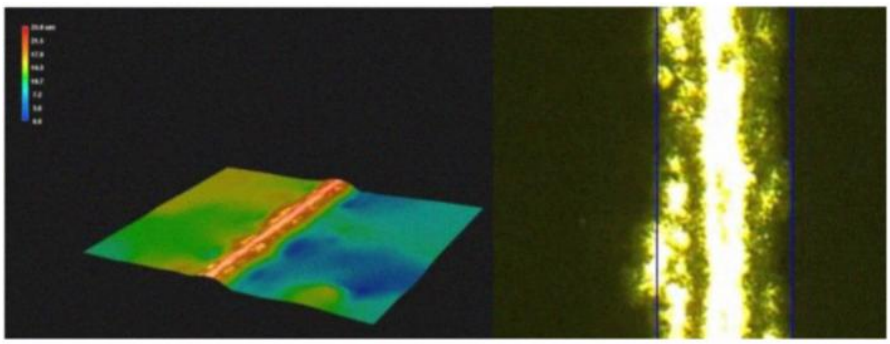

Figure 2-8. (Left) Contour image showing a Ag seed layer (printed using an XJet inkjet printer); (right) an example finger after Ag LIP for 10 min (from [110]).

In order to eliminate complications introduced by the plating step, Ebong et al. later demonstrated fully inkjet-printed Ag grids [45]. In this process all the metal of the conductive grid was printed and then the printed cells were co-fired with the standard Al screen-printed rear surface. Figure 2-9 shows cross-sections of example Ag fingers printed with different numbers of printed layers after co-firing. Using this process a cell efficiency that was comparable to routinely screen-printed cells was achieved. Although Ebong et al. estimated that inkjet printing the entire front metal grid could reduce the amount of Ag required per cell because less ink (i.e., Ag) could be printed at the busbars where sufficient conductivity can be achieved through the subsequently soldered interconnection tabs, this can also be achieved using dual print screen-printing (described in Section 2.1.2). Consequently, like the apparently-successful aerosol-printed/plated cell metallisation process pioneered by Mette et al., this inkjet printing process was never demonstrated in manufacturing.

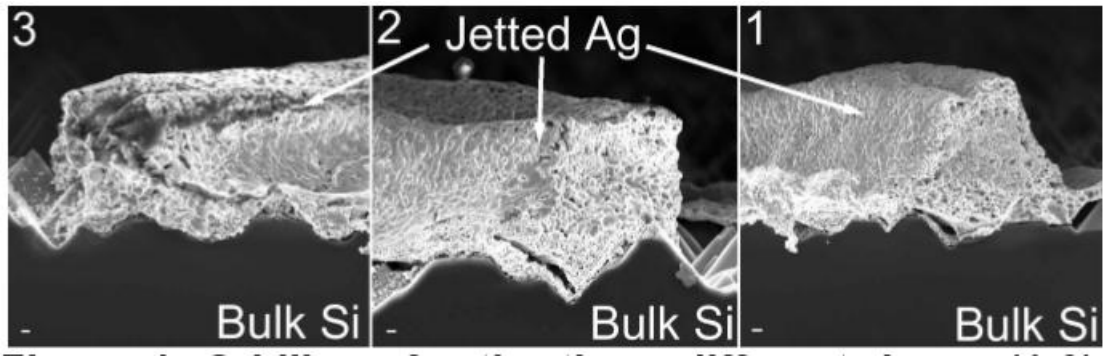

Figure 2-9. Fully inkjet-printed Ag fingers shown for three different doses (i.e., number of printed layers) after co-firing (from [111]).

2.2 Metal Plating

Forming high quality electrical contacts for Si solar cells can also be achieved by wet chemical methods such as metal plating. Metal plating requires that openings are first formed in a dielectric layer which then acts as a mask for plating. Provided that these openings can be formed with a high resolution, plating has the potential to form very narrow and high aspect-ratio conductors. Unlike screen-printing, the conductive material does not spread excessively in a lateral direction and the conductors can be composed of pure and solid metal rather than the mixture of metal and glass particles that comprises screen-printed contacts. As such, the bulk conductivity of the plated metals can be significantly higher than that of screen-printed Ag pastes, necessitating a lower cross-sectional area of conductor. However, perhaps one of most significant potential advantages of metal plating over Ag screen printing is the ability to replace the investment metal Ag by the commodity metal Cu (see Chapter 1). The following sections review the different metal plating methods and associated dielectric structuring processes used in the metallisation of front-surface grids of Si solar cells.

2.2.1 Electroless Plating

Electroless plating refers to the deposition of metal layers chemically without an external supply of electrons [113-115]. It involves aqueous metal salt solutions undergoing both oxidation and reduction reactions between chemical species. The deposition of metal (electrochemical reduction) is the result of gaining electrons from an oxidation reaction, the latter reaction involving either the cell surface or reactant provided in the electroless plating electrolyte.

As mentioned earlier in this chapter, the electrical contacts of the first Si solar cells were formed using electroless plating. However, after an intense period of development for plating processes in the 1970's, the simplicity of screen printing was found preferable to the complicated chemistry and know-how required for plating. Wenham and Green resurrected the earlier-developed electroless Ni/Cu plating processes [26] in their development of the buried contact cell [27-30, 116, 117] (see Figure 2-10), a cell design that was highly innovative at the time in that it demonstrated the use of a selective emitter, laser scribing for selective doping and contact formation and plated metallisation. The 20-30% increment in efficiency (at the time) enabled by these higher efficiency attributes resulted in BP Solar

commercialising the cell design in 1991 as their Laser Buried Grid (LBG) Saturn cells [118-120].

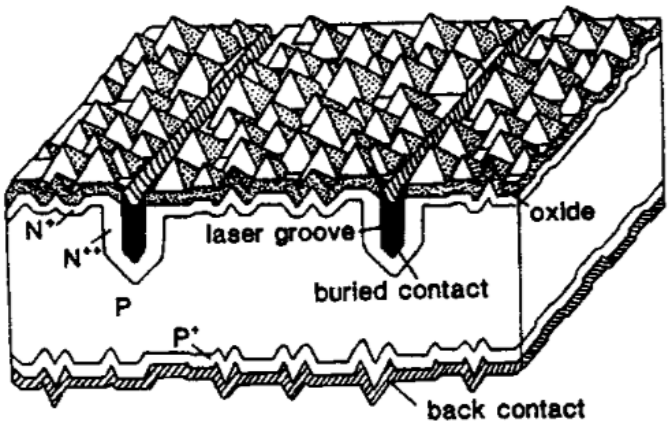

Figure 2-10. Schematic depicting a laser-grooved buried contact solar cell (from [30]).

Alkaline electroless Ni deposition occurs via a two-step mechanism in which Ni nucleation is followed by autocatalytic deposition involving the oxidation of a reductant (e.g., hypophosphite ion) provided in the electrolyte [113, 115]. In the initial nucleation step, Ni is deposited on the surface in 'islands' via a charge transfer reaction in which the surface Si is oxidised [121]:

Step 1: Nucleation

Oxidation:	$\mathrm{Si} + 4\mathrm{OH}^- \rightarrow \mathrm{SiO_2} + 2\mathrm{H_2O} + 4\mathrm{e}^-$	$\mathrm{Eq.}\,2-1$
Reduction:	$\mathrm{Ni}^{2+} + 2\mathrm{e}^- \rightarrow \mathrm{Ni(s)}$	$\mathrm{Eq.}\,2-2$

Once the surface is covered with Ni, Si can no longer react and the source of electrons is provided by the reductant. In general, a number of reactions occur in these electrolytes, with the reductant first being dehydrogenated and then oxidised. The reactions that occur with the use of a hypophosphite reductant are [121]:

Step 2: Autocatalytic Deposition through Hypophosphite Oxidation

Oxidation:	(1) $\mathrm{H_2PO_2^-} + \mathrm{H_2O} \rightarrow \mathrm{H_2PO_3^-} + 2\mathrm{H}^+ + 2\mathrm{e}^-$	$\mathrm{Eq.}\,2-3$
Reduction:	(1) $\mathrm{Ni}^{2+} + 2\mathrm{e}^- \rightarrow \mathrm{Ni(s)}$	$\mathrm{Eq.}\,2-4$
	(2) $2\mathrm{H}^+ + 2\mathrm{e}^- \rightarrow \mathrm{H_2(g)}$	$\mathrm{Eq.}\,2-5$
	(3) $\mathrm{H_2PO_2^-} + 2\mathrm{H}^+ + \mathrm{e}^- \rightarrow \mathrm{P} + 2\mathrm{H_2}$	$\mathrm{Eq.}\,2-6$

Once the electrolessly-plated Ni layer was formed, BP Solar sintered the cells to form a Ni silicide which acted to reduce contact resistance [26, 122]. This Ni silicide contacting process had been developed in the 1970's by early proponents of plated metallisation, Solarex and Motorola [26].

As with electroless Ni deposition, Cu can be deposited using a range of different reductants in the electrolyte and numerous patents have been granted that describe different proprietary formulations that have been developed for printed IC applications. Most electroless Cu plating processes use formaldehyde as the reducing agent [115, 123], and like the electroless Ni process described above, evolve H_2 (g). Cyanide is often used as a complexing agent in the electroless Cu formulations to improve the ductility of the deposits [123]. It acts by competing with adsorbed H and reducing the amount of H that becomes trapped in the growing Cu deposit [113].

Typical plating rates for electroless Cu are of the order of 5 μm per hour (specified for a Transene EL Cu used for IC applications). While this rate may not impose challenges for IC applications, solar cells must conduct significant current to the solar cell's busbars and so the need to plate metal lines that are at least 10 μm thick (for a three busbar cell) can be time consuming. BP Solar used a cyanide-based electroless Cu process and it was challenging to fill the entire groove, which could be up to 40 μm deep, with plated Cu even after plating for several hours. In an effort to move to a faster and more environmentally friendly process, Eager et al. reported the trialling of an cyanide-free electroplating process [120, 124], however it appears that electroplating was not put into production. At the time of commencing production of the LBG technology, the published manufacturing cost from BP Solar also showed a 20-30% economic advantage compared with standard (screen-printed) solar cell manufacturing [27, 125]. However ultimately, the efficiency premium of the Saturn modules was eroded by technology improvements and cost reductions in screen-printing technology and production of the Ni/Cu plated Saturn modules ceased in 2009.

Figure 2-11. Photo of the electroplating arrangement trialled by BP Solar for their plating of LBG solar cells (from [124]).

More recently the electroless Ni plating process substantially as used by BP Solar has resurfaced as a way in which a seed Ni layer can be formed on both the n-type and p-type surfaces of bifacial cells, enabling subsequent plating of both grids by contacted electroplating [121, 126]. This represents an alternative metallisation strategy to the bifacial cell plating process that was developed as part of this thesis and is described in Chapter 3. Bifaciality is of growing interest due to the ability of bifacial modules to absorb significantly more light because the rear surface can capture diffuse light and reflected light from the surrounding environment [127, 128].

Electroless plating can also be achieved through galvanic deposition in the absence of a reductant in the electrolyte [129]. A commonly-used method of 'capping' Ni/Cu plated fingers so that they are resistant to corrosion and able to be soldered is to galvanically displace a surface layer of Cu with Ag [130-132]. This electroless process is self-limiting by the availability of Cu and can provide a dense barrier layer to prevent further oxidation of the grid metal. The reaction can be written as:

$$2Ag^{+} + Cu(s) \longrightarrow Cu^{2+} + 2Ag\,(s) \qquad \text{Eq. } 2-7$$

and occurs galvanically due to the standard reduction potentials of Ag ions being greater than that of Cu ions. Typically the Ag ions are provided through $AgNO_3$ with additives such as Na thiosulphate being used to stabilise the electrolyte [132].

Galvanic displacement of Si has been used to form seed Ni layers. In this process, Si oxidation provides the only source of electrons and so the process is self-limiting allowing the controlled formation of very thin Ni layers. Yao et al. reported the formation of uniform 250 to 400 nm thick Ni layers directly on chemically-etched and laser-doped Si surfaces [26, 133] (see Figure 2-12).

The chemical reactions involved in galvanic deposition of Ni on Si in alkaline $NH_4F/NiSO_4$ solutions are presumably as presented by [134]. Si can be oxidised by both the hydroxide and fluoride ions, resulting in Ni ion reduction.

Oxidation:	$Si + 4OH^- \rightarrow SiO_2 + 2H_2O + 4e^-$	$, E_o = -0.84\ V$	$Eq. 2-8$
	$Si + 6F^-(aq) \rightarrow SiF_6^{2-} + 4e^-$	$, E_0 = -1.20\ V$	$Eq. 2-9$
Reduction:	$Ni^{2+} + 2e^- \rightarrow Ni(s)$	$, E_0 = -0.257\ V$	$Eq. 2-10$

Yao et al. demonstrated the use of this Ni seed layer in the fabrication of p-type Si cells with Al BSFs. They achieved average cell efficiencies of 18.6% and 19.2% using chemical etching and laser doping for the front surface patterning of the SiN_x ARC, respectively. However, maintaining the cells at open circuit during plating was challenging to achieve practically as it was difficult to prevent the electrolyte from contacting the cell edges and rear surface, and any wetting of these surfaces could permit a light-induced current to also flow in the cell (with, for example, Al oxidation sustaining the reaction as described for non-contact LIP in [133]).

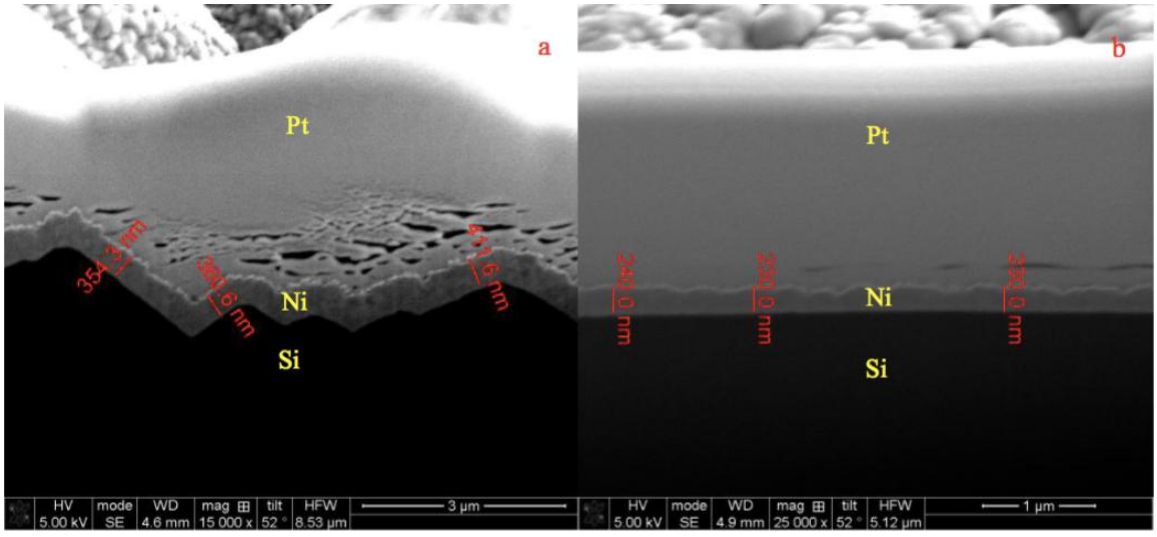

Figure 2-12. Deposition of Ni by galvanic displacement on: (a) a chemically-etched cell; and (b) a laser doped-cell (from [133]).

Rodriguez et al. [135], further investigated the use of the galvanic Ni deposition process reported by Yao et al. to ascertain whether the Si etching that occurs during the galvanic process could provide any advantages in terms of the adhesion. By quantifying the adhesion of plated fingers using the stylus-based scratch measurements (described in Chapter 5 of this thesis), they were able to demonstrate that plated grids which employed a seed galvanically-plated Ni layer, which was sintered before bias-assisted LIP Ni/Cu plating of chemically-etched SiN_x openings, could achieve significantly greater adhesion than grids plated with just bias-assisted LIP Ni/Cu. The sintering process was required however to eliminate voids and an O-rich Si interface layer that formed with the galvanic Ni plating step. The average finger dislodgement force that was achieved for the cells with the adhesion promoting seed layer after sintering at 350 ºC for 10 min was 114 N/mm, which is similar to values of 148 N/mm obtained as part of this project for laser-ablated cells and reported in Section 5.6.3 and in Ref [136]. This suggests that for chemically-etched openings where surface roughness is difficult to achieve, the galvanic Ni deposition process may indeed provide a means by which interfacial adhesion can be improved, presumably through the increased roughness caused by the Si oxidation (etching).

The formation of interfacial oxides with the alkaline electroless plating was also observed by Tous et al. [137]. They attributed the higher temperature required to reduce contact resistance through silicide formation for the electroless Ni compared to sputtered Ni to the oxide residues. Indeed, for any Ni plating process to Si, the propensity for the Si surface to oxidise will always make it challenging to eliminate all interfacial oxides. Consequently, annealing/sintering processes may be a necessary component of all adhesion promoting processes.

In summary, electroless plating of Ni, Cu and Ag have all been demonstrated in industrial manufacturing of p-type Si solar cells, with BP Solar having demonstrated the greatest contribution in regard to volume manufacturing. Whilst the process may be an effective way of forming adhesion-promoting seed layers for chemically-etched solar cells and Ag or Sn capping layers for Ni/Cu plated grids, the plating of the bulk of the conductive grid using electroless plating is slow and process reliability is challenging due to evaporation of solvent from the plating electrolyte due to heating, drifts in pH and the concentrations of chemical components of the electrolyte, and the need to ‘dump’ chemical baths when reaction product

concentrations become too large. Waste treatment of used plating chemicals can be expensive and must be factored into manufacturing costs [138].

2.2.2 Light-Induced Plating

Compared with electro-less plating, LIP for solar cells offers the significant advantage of a higher metal plating rate and controllability, making it more suitable for large-scale production. The earliest report of LIP dates back to 1973, when Siemens AG filed a patent in Germany [139] describing a process which is substantially the process that is now referred to as bias-assisted LIP. Figure 2-13 shows their proposed plating arrangement showing a p-type semiconducting region contacting by an electrode, with metal being plated to exposed n-type semiconducting regions on the other surface of the device. Although an applied bias current/voltage is not shown in Figure 2-13, the patent text mentions that such a bias can be applied.

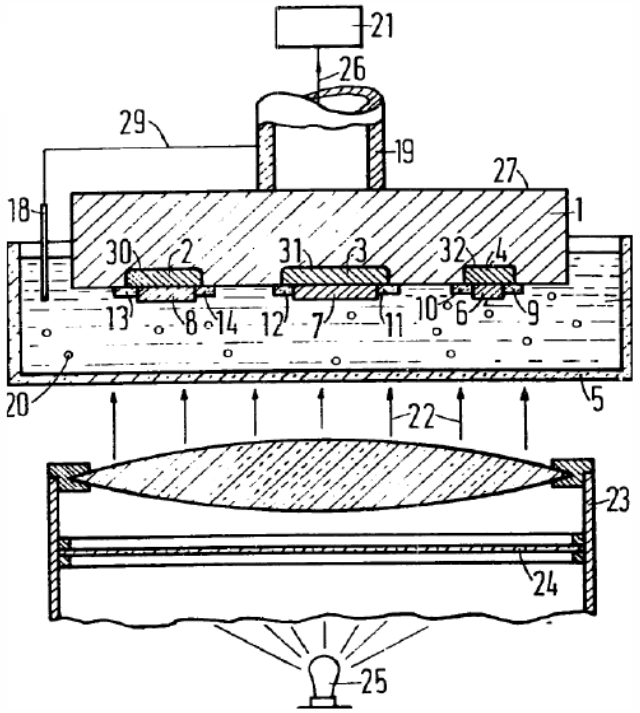

1: cross section of p-doped semiconductor
2-4: n-doped area
5: light permeable container
6-8: metal layer
9-14: SiO_2 area
18: anode
19: metallic suction system
20: metal cations
21: vacuum pump
22: irradiation of light
23: optical device
24: optical filter
25: light source
26: suck direction
27: not covered surface
28: plating bath
29: electrical connector
30-32: p-n junction

Figure 2-13. Light-induced plating apparatus from the patent DE2348182 by Späth (reproduced from [101]).

In 1979, a US patent was granted for bias-free light-induced plating to Durkee and assigned to Solarex [140] (see Figure 2-14). The diagram shows that electrical contacts can be plated

on one or more surfaces of a solar cell by immersing the cell into the plating electrolyte under illumination.

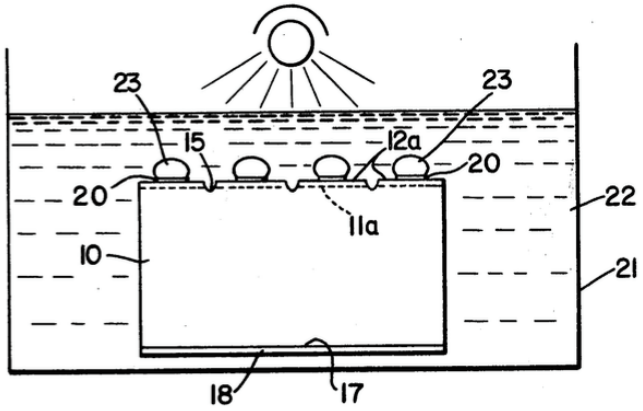

Figure 2-14. Bias-free LIP arrangement from US 4,144,139 by Durkee (reproduced from [140]).

In this LIP method, which has been subsequently referred to as non-contact LIP [133], the plating on the exposed n-type Si surface relies on the oxidation of the p-type surface (also in contact with the electrolyte). When this method is applied to a typical screen-printed p-type Si solar cell, the rear screen-printed Al becomes a scarification anode being oxidized to sustain the light-induced current through the solar cell [133]. Under illumination, the n-type surface becomes a cathode and metal ions in the electrolyte accept electrons from the surface and are reduced to metal. Light-generated holes, transported to the rear Al surface, result in oxidation of the Al. There are two critical factors that affect the success of this non-contact LIP. The first factor is the continuous corrosion of the Al rear surface. During plating, as the Al oxidises, a non-conductive oxide forms to block the further oxidation of Al, and eventually this will stop the plating process. Therefore, corrosive agents (typically Cl or Br ions) are added to the plating electrolytes [141, 142] so that pitting corrosion can sustain the corrosion. The second factor that affects the performance of non-contact LIP is the control of the plating current, since the plating is dependent on the electrical properties of the solar cell.

2.2.3 Bias-Assisted Light-Induced Plating and Electroplating

To avoid corrosion of the rear Al electrode and to achieve a more controllable plating current, bias-assisted LIP is typically used [74, 87, 133, 143, 144]. This method is substantially as described by Späth in 1973 (see Figure 2-13) and involves the application of a bias potential to the p-type surface of the solar cell during LIP (see Figure 2-15). This requires that only the

n-type surface is wetted by the electrolyte and so a more sophisticated plating arrangement is needed. With application of a bias current to offset the resistances in the electrochemical circuit, the cell can operate close to its short circuit state. Furthermore, rear surface Al corrosion can be prevented through keeping that cell surface dry during plating. The application of the bias current during plating can ensure that cells with different electrical properties are all plated using the same plating current and that the plating rate is controlled within the recommended plating rate range for the chemical formation used.

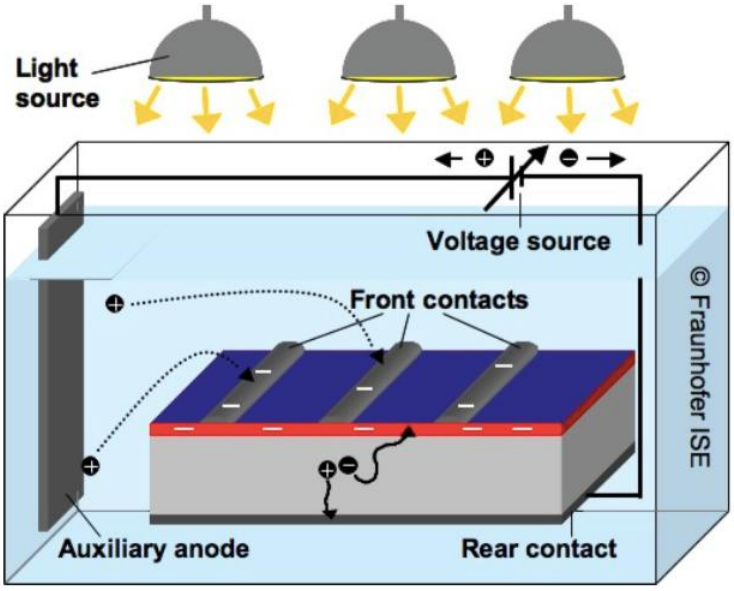

Figure 2-15. Schematic depicting the bias-assisted LIP process (from [145]).

Bias-assisted LIP is effectively electroplating, just with the solar cell providing the majority of the current. The light needs to be sufficiently intense to ensure that the cell is forward-biased as the applied bias current is applied in a reverse-bias direction. This means that the same electrolyte formulations used for electroplating (e.g., acidic $CuSO_4$) can be used for solar cell plating, with corroding anodes being used to maintain the metal ion concentration in the plating bath. This minimises bath maintenance requirements, and so with appropriate filtering and additive maintenance, plating baths can be operated for months without needing to replace the entire bath contents.

Yao et al. [146] demonstrated that a bias-assisted LIP process could be modelled using equivalent circuit analyses in order to determine the most suitable control mode (current control or voltage control) when applying a negative bias potential to the p-type surface of Si. In the circuit she proposed, the solar cell was modelled as two diodes in parallel (Jo1 and Jo2

in Figure 2-16), and the electrochemical reactions occurring at the anode and cathode were represented by two separate Randles circuit elements (Rct-a in parallel with CH-a representing the anode/electrolyte interface and Rct-c and CH-c representing the cathode/electrolyte interface).

As noted earlier, when using a bias during LIP, it is important to ensure that the cell remains forward-biased. Using the equivalent circuit simulations, Yao demonstrated that use of voltage-control could reduce the risk of reverse-bias junction breakdown. Although use of a current controlled mode may be desirable from the perspective of controlling plating rate within the allowed range for a chemical system, there is a risk that if the light intensity is insufficient (or the cell voltage is lower than expected), the cell can be plated at the reverse bias breakdown knee voltage which can electrically damage the cell (e.g., through localised hot spots), leading to a reduction in the final cell efficiency. Yao presented implied V_{oc} and PL imaging results to demonstrate damage that occurred to an example cell that was Ni plated when the light-induced current was significantly less than the applied bias current. Hsiao et al. have also shown that non-uniform Ni plating can result if a cell is allowed to operate under reverse bias during plating [147].

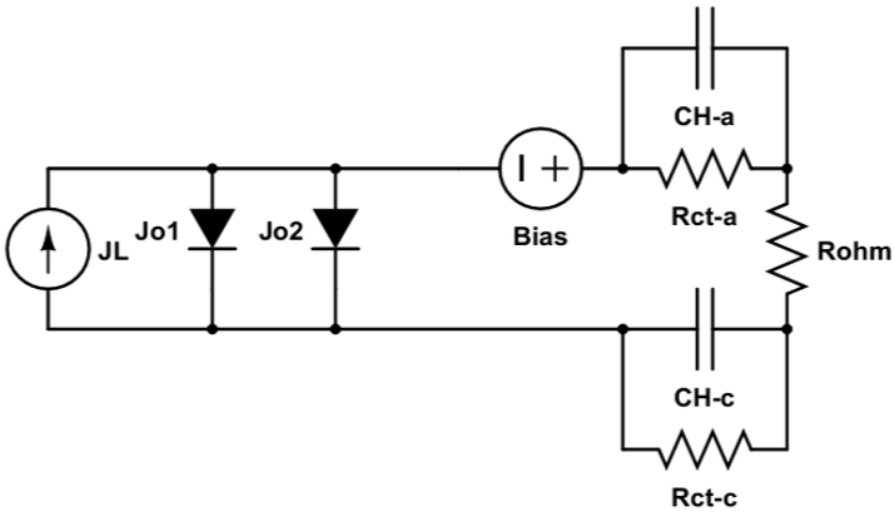

Figure 2-16. Equivalent circuit of a Si solar cell operating under bias-assisted LIP (from [146]).

There are two main challenges incurred with implementing bias-assisted LIP. First, each solar cell needs to be contacted individually to supply the bias current to the rear surface. Second, to completely prevent the corrosion of the Al electrode, the rear surface must be maintained

completely dry. The equipment solutions to date include both lab tools and in-line large volume manufacturing tools which implement single side plating. NB technologies developed a lab tool product called SunCup [148] (see Figure 2-17.). In this plating setup, the cell was single-side contacted with plating electrolyte, and the rear surface was attached to an external voltage contact by vacuum.

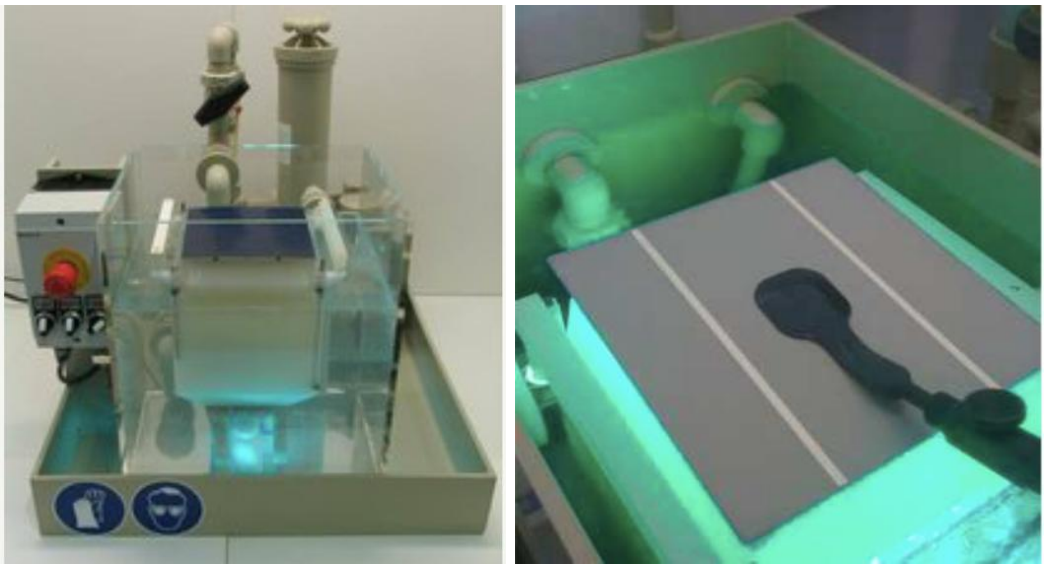

Figure 2-17. SunCup plating tool from NB technologies using a single side plating technique (from [148]).

In large-scale production, the equipment designed by RENA has been used to achieve bias-assisted LIP for high-volume plating (see Figure 2-18) [149]. The SiN_x-coated surfaces of individual cells are in contact with the plating electrolyte and cells move through the plating bath supported by conveyer rollers allowing the plating of 3000 wafers/hr. The bias current is directed into cells as they are conveyed through the bath via a series of fixed contacting elements. This inline tool approach was also used by Kuttler in their design of plating equipment for Suntech [150]. However, it is not straightforward to use this tool design to plate bifacial cells.

Figure 2-18. The Rena bias-assisted LIP tool InCellPlate with a brush contact at the rear and single side plating with wafer transport achieved by conveyer rollers (from [149]).

Meco have developed an immersed clip contact direct plating tool [151] (see Figure 2-19) which can be used to perform LIP and electro-plating with clips contacting the wafers at one edge. The tool's development was inspired by electro-plating processes used in the semiconductor industry, where metal electrodes to be plated are directly contacted. Unlike the through-wafer in-line plating tool shown in Figure 2-18, wafers move through the Meco tool with vertical alignment. Light-induced plating can be used to form the initial layer of the Ni seed, and then this tool can directly plate a denser layer of Ni and Cu by having clips contact the busbars at one edge of the wafer. Meco quote a throughput of 1500-3000 wafers/hr for this tool, which has a proven history in semiconductor plating. Bifacial cell plating can be achieved using this tool, providing that a seed Ni layer can be formed on both surfaces [126].

Figure 2-19. Meco DPL plating tool using a clip and immerse method (from [151]).

2.3 Dielectric Structuring for Plating

Unlike screen-printing and other printing approaches where the printed metal or metal paste is fired through the SiN_x dielectric of cells, metal plating requires that the dielectric ARC is patterned or structured to expose Si regions to which a metal grid can be plated. This dielectric structuring was historically performed by photolithography and chemical etching, however in recent times laser scribing, doping or ablation have been considered as the most industrially-viable dielectric structuring approaches. Laser doping and laser ablation are reviewed below due to their relevance to this thesis study.

2.3.1 Laser Doping

In addition to forming openings in dielectric layers as described for the LBG cell in Section 2.2.1, laser doping can be used to form selective emitter regions [34, 72, 74, 152-158] which can make possible low contact resistance and high operating cell voltages in fabricated cells [159]. There are a number of different laser-doping methods, and these have been comprehensively reviewed by Tjahjono [154], however the process of relevance to this thesis is that involving the application of a liquid dopant source to the surface of a dielectric and the laser doping though that layer. This process serves to use the laser energy to both remove the dielectric (i.e., make an opening) and dope the underlying Si with the source of dopants to form a selective emitter region (see Figure 2-20). Typically the liquid layer is spin-coated on the surface; however spray coating of a dopant source may also be possible.

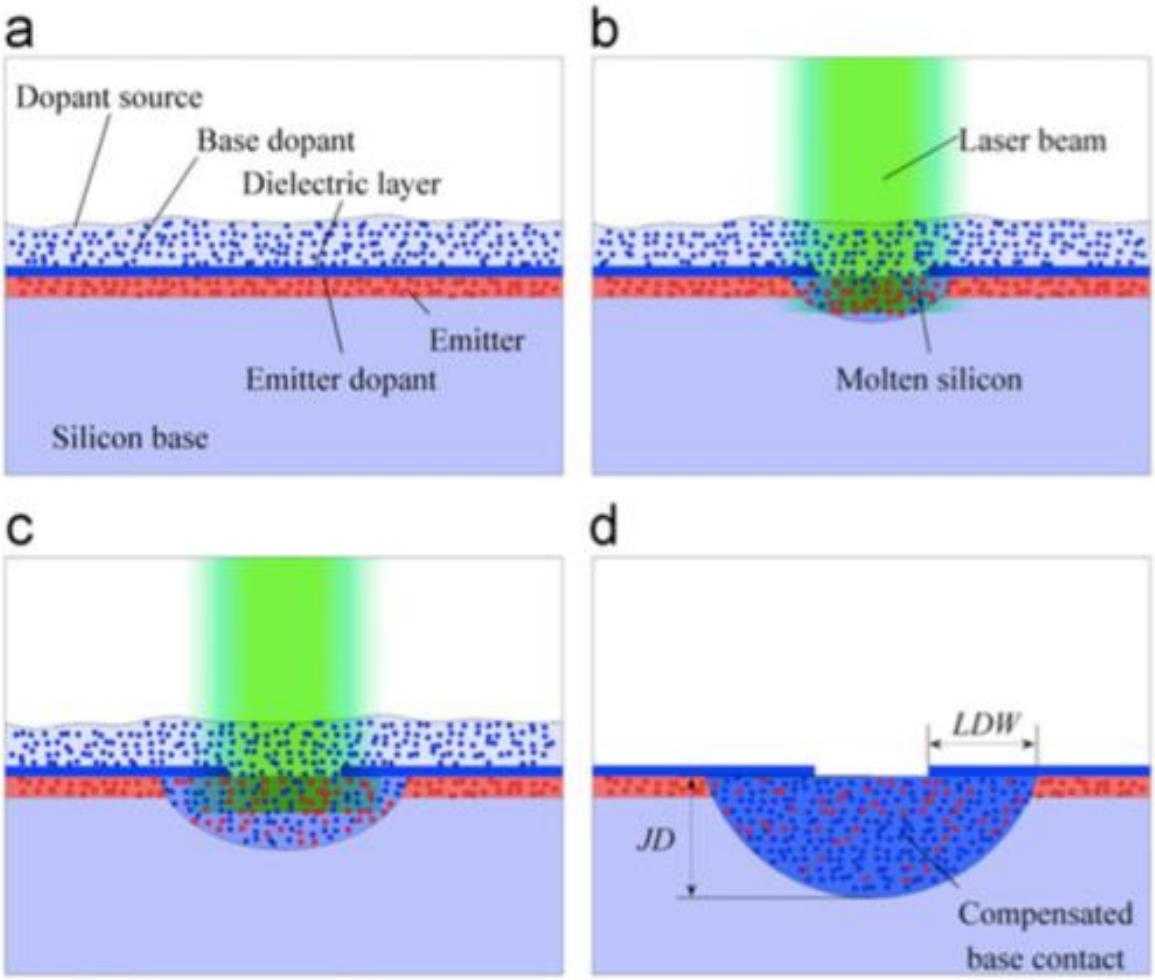

Figure 2-20. The laser doping process for forming selective emitters involving the steps of: (a) spin-coating a dopant source on the Si surface; (b) laser illumination to melt the Si; (c) greater penetration of the melted Si region; and (d) the final cooled doped Si region (from [160]).

By using different laser speeds and dopant source concentrations, it is possible to form laser-doped regions having different resistivity and junction depth. Figure 2-21 shows a combined SEM/EBIC image of a 11 μm deep p-type laser doped region formed in a n-type Si wafer using a 532 nm CW laser, [160]. However, this example is perhaps an extreme case with the depth of P-laser-doped regions into a diffused emitter tending to less than 1 μm [154].

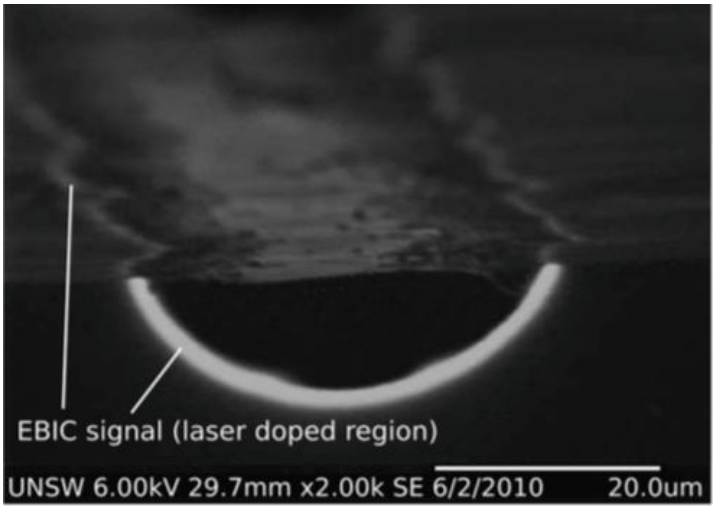

Figure 2-21. Combined SEM/EBIC image showing a p-type laser doped region form though a planar Si n-type surface. The bright curve represents the p-n junction, this region appearing bright because of the high probability of collected carriers at the junction (from [160]).

After laser doping, the SiN_x layer is opened and metal grids can be formed through bias-assisted LIP of Ni and Cu plating [154, 155]. The laser-doped selective emitter (LDSE) process was used in the achievement of a cell efficiency of 19.3% on a Cz 156 mm p-type cell with an Al BSF [74], an efficiency that was reported as a record efficiency at the time.

Suntech Power commercialised the laser-doped selective-emitter cell structure as their Pluto product [32]. Compared to the BP Solar plating process, the plating of the Pluto cells could be achieved in ~ 10 min using the much faster bias-assisted LIP process performed in a multi-lane inline plating tool. However, the Pluto technology highlighted some new challenges for Ni/Cu/Ag plating of front surface grids. The very narrow contact openings that could be achieved (in cases < 20 μm wide) resulted in reduced contact area for adhesion. In the buried contact cells, the laser-scribed grooves were ~20 μm wide [120], and plated metal could adhere to both the base and sidewalls of the grooves. For this reason BP Solar never reported poor adhesion of metal grids for their plated cells and their plated cells were interconnected using soldering of interconnection wire. However, the thin metal fingers of the Pluto technology had limited metal-Si contact area for adhesion. Furthermore, the need to plate as fast as possible for high processing throughput most likely, as demonstrated in Chapter 5 of this thesis, induced stress in the Cu fingers which may have acted to reduce interface adhesion.

The poor interfacial adhesion had the important consequence that the plated cells could not be interconnected by soldering. Consequently, Suntech adopted a hybrid process where the busbars were screen-printed with Ag and the fingers were laser-doped and plated. This strategy enabled the benefits of a selective emitter and reduced shading due to the narrow fingers whilst still being able to use standard soldering and tabbing for interconnection. However, the metallisation process was more complex than simply screen-printing or plating and this would have added to production expense. Another consequence of the poor adhesion was the occurrence of finger peeling, most often at the ends of fingers where there was no pinning by busbars or additional fingers [161].

Suntech's production experience of their Pluto product identified finger adhesion as a critical issue for plated metal grids. Most IC applications of Ni/Cu plating do not require the plating of long thick conductors across a flat substrate and consequently the problem of plated conductors simply "lifting off" from the substrate or peeling had not really been observed previously. The investigations into finger adhesion, reported in Chapter 5, were motivated by the recognition this practical problem for solar cell plating.

Whilst laser doping offers a path to a low-cost selective emitter it does so at a cost. Crystal damage incurred within and adjacent to laser-doped regions due to Si expansion and re-crystallization can limit energy conversion efficiencies [152, 154]. In cases where the crystal damage occurs in or above the heavily-doped regions, the electrical impact can be minimal and in fact the roughness caused by P laser doping may provide anchor points for the plated fingers and increase adhesion. However, when high powers are used (as observed in Chapter 3 of this thesis), high local ideality factors can be observed and are indicative of additional recombination that is introduced into the Si by laser doping. This is discussed further in Chapter 4.

Chapter 3 of this thesis explores the use of laser doping and Ni/Cu plating for the fabrication of bifacial cells, and then in Chapter 4 a QSSPL and QSSPC injection dependent lifetime study is reported that attempts to monitor recombination introduced by different laser-doping processes. Finally in Chapter 5, the thesis returns to the problem of adhesion of plated contacts to both laser-doped and laser-ablated contact regions.

2.3.2 Laser Ablation

Short-pulse laser ablation of dielectrics for Si solar cell applications was first reported by Dube et al. in 1990 [162]. Unlike laser-doping, irradiation by short pulse lasers only removes (ablates) the SiN_x without appreciable heating or melting of the Si. Since Dube et al.'s first report, numerous publications have explored aspects of this process for p-type cell metallisation such as comparisons between pulse length (ns or ps), and wavelength [163-167]. Although laser-ablation does not provide any electrical shielding of minority carriers through localised doping at the Si-metal interface, providing that the contact area can be minimised, contact recombination can be maintained at sufficiently low values to achieve competitive cell efficiencies on both Al BSF and PERC cells [168]. These laser-ablated cells can also benefit from the engineering of emitters that have low surface P concentration ($< 4 \times 10^{19}$ cm^{-3} [78]), enabling lower emitter recombination currents than current screen-printed cells.

However, perhaps one of the benefits of most interest is that short pulse laser ablation results in a rough surface (through non-linear absorption effects which are discussed further below) This can result in strong interface adhesion of plated metal [38, 40, 41, 76, 78]. The pull strength of soldered interconnection wire to Ni/Cu/Ag grids plated to ps-laser ablated contact regions has achieved value of ≥2 N/mm, which meet current module fabrication requirements (see Figure 2-22). The ability to interconnect by soldering using standard industrial equipment is an important consideration for manufacturing.

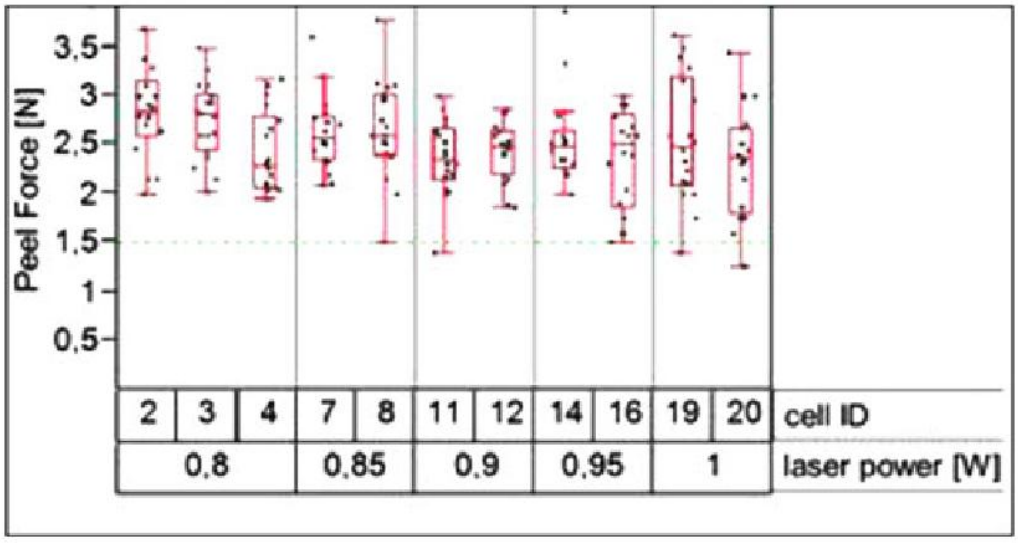

Figure 2-22. Pull test forces under a 90 degree angle for Ni/Cu/Ag plated busbars for different UV ps laser ablation powers (from [78]).

The critical factor that improves the adhesion is believed to be the nanostructured surface morphology. Unlike the laser doping process discussed in Section 2.3.1 where the texturing of the Si is lost through melting, short pulse laser ablation removes only the SiN_x layer without changing the Si pyramid surface texture (see Figure 2-23). In addition, superimposed on the micro-texture is a nanostructure comprising periodic ripples which is absent when the SiN_x is ablated using a ns UV laser [Figure 2-23(b)].

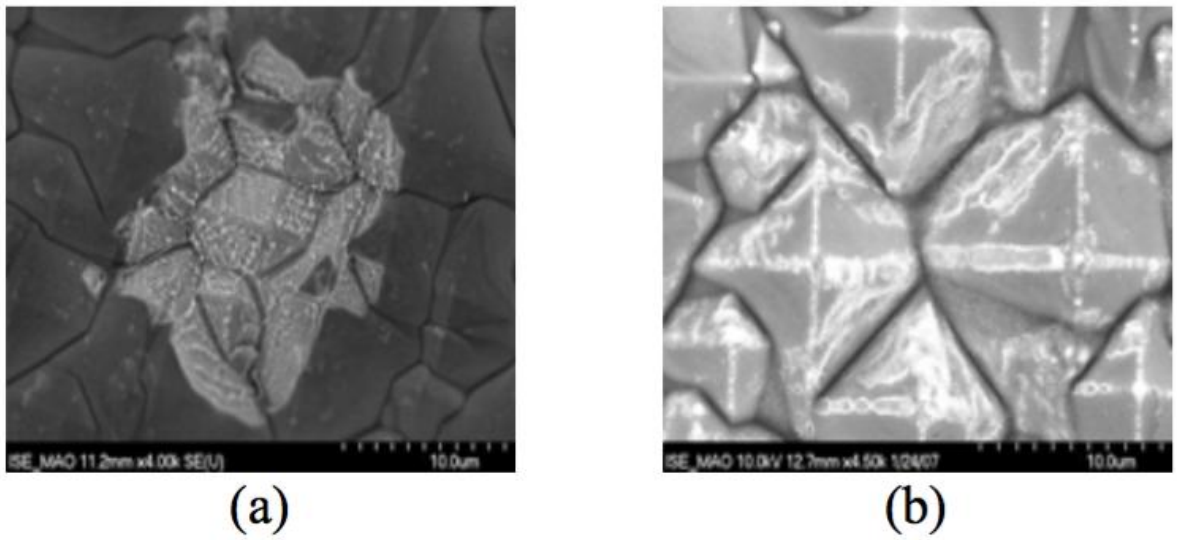

Figure 2-23. Laser-ablated alkaline-textured Si surface by: (a) ps UV laser; and (b) ns UV laser. In both cases the SiN_x layer was removed with no changes in the Si pyramidal texture (from [167]).

The energy that is delivered by short pulse lasers can lead to strong electronic excitation, rapid heating and cooling, and ultrafast mechanical deformation. Laser energy absorbed by free electrons in the target substrate is first thermalised within the electron subsystem and then transferred to the lattice as heat. Many different intertwined processes and phase modifications can be in effect for any application depending on the laser pulse duration and the material being ablated. Shugaev et al. summarised these diagrammatically (see Figure 2-24) [169]. Different groups are identified through the use of different colours, with yellow identifying excitation processes in optically-excited electronic states, green referring to processes where some energy transfers from the electronic exited stated to lattice vibrations (thermalisation through the lattice), and light blue referring to processes where the bulk of the energy is transferred to the lattice resulting in surface modification and lattice heating.

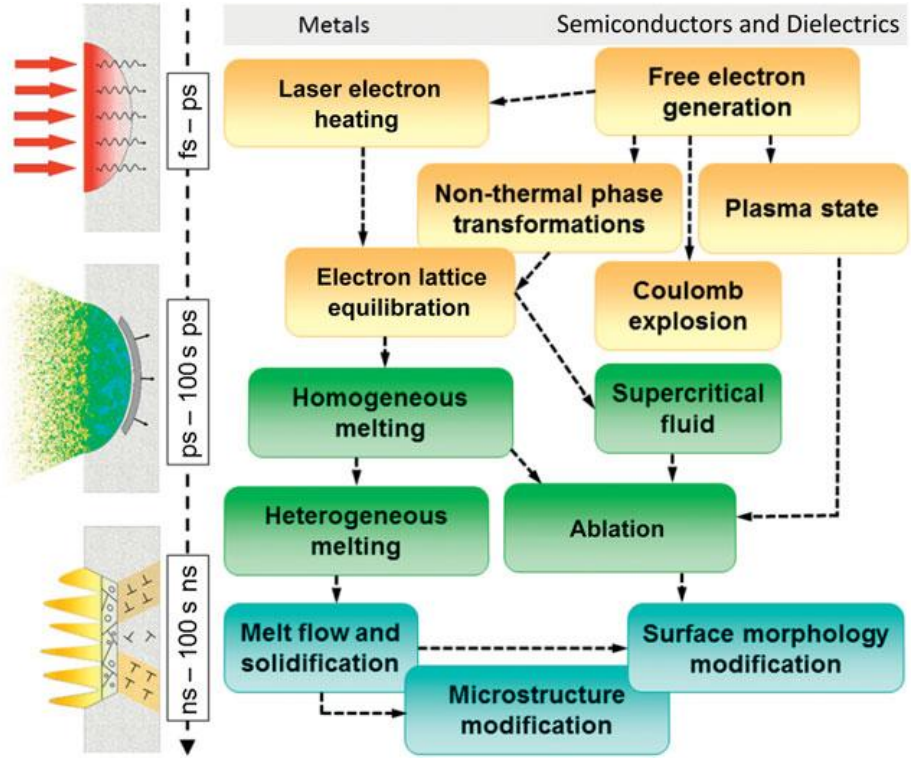

Figure 2-24. Energy dissipation pathways and phase modifications following short pulse irradiation of metals, semiconductors and dielectrics (from [169]).

In metals, the existence of conduction band electrons enables direct absorption of laser energy by electrons undergoing collisions with nuclei (i.e., by inverse Bremsstrahlung [170-174]). However, in semiconductors and dielectrics, electrons have to be excited across the bandgap before they can directly absorb photons. In wide-bandgap dielectrics such as SiN_x the main processes involve multiphoton absorption and avalanche ionization, both of which are highly non-linear. Once the electrons are excited to the conduction band, they absorb laser energy via inverse Bremsstrahlung and can produce a sequence of electron–hole pairs through collisions with valence-band electrons. This process leads to avalanche multiplication of the density of conduction-band electrons [169, 175] and may bring a material to plasma states or even produce a Coulomb explosion due to electron emission and charging of a surface region of a dielectric [169].

If the excited electron concentration increases rapidly due to a large number of laser pulses in a short time, then energy will transfer to the lattice and heat can accumulate and result in an increased substrate temperature, and possible Si melting. This process can be described by the following model [169]:

$$C_e \frac{dT_e}{dt} = -\frac{dQ(z)}{dz} - \gamma(T_e - T_i) + S \qquad \text{Eq. } 2-11$$

$$C_i \frac{dT_i}{dt} = \gamma(T_e - T_i) \qquad \text{Eq. } 2-12$$

$$Q(z) = -\frac{k_e dT_e}{dz}, S = I(t)A\alpha\, exp(\alpha z) \qquad \text{Eq. } 2-13$$

where T_e is electron temperature, T_i is lattice subsystem temperature, z is the perpendicular direction to the substrate surface, $Q(z)$ is the heat flux, S is the laser heating source term, $I(t)$ is the laser intensity, $A = 1 - R$ and i are the surface transmissivity and the material absorption coefficient, C_e and C_i are the heat capacities (per unit volume) of the electron and lattice subsystems, γ is the parameter characterizing the electron-lattice coupling, and k_e is the electron thermal conductivity.

There are many reports which attempt to identify the different processes that occur during laser ablation, however of particular interest to this thesis is the creation of a periodic nanostructured surface on dielectric layer (e.g., SiN_x) ablation on textured Si. Reports suggest that the formation of this 'ripple-like' surface is critical for the strong the adhesion of plated metal [38, 76]. Several reports have provided possible explanations for this nano-scale periodic roughening. Zhu et al. [176] suggested that the periodic 'ripples' evolved to 'spikes' as the number of pulses was increased, with sharper spikes being achieved through the use of fs pulse lengths (see Figure 2-25.). Costache et al [177] reported that the coarse structure of the 'ripple' pattern occurs with a period of $\sim \lambda/3$.

In studies focused on dielectric (ARC) ablation for Si solar cell fabrication, in order to reduce the front surface Si damage, fewer pulses are typically applied during SiN_x ablation, therefore, only 'step-like ripples' are typically observed (see Figure 2-23). These periodic surface structures have been referred to as laser-induced periodic surface structures (LIPSS) [178-182]. The reason underlying their formation has been explained using different theories. Some have postulated that the periodic surface nanostructures arise due to the interference of the incident and a scattered or stimulated wave at the surface [183, 184], whilst other theories suggest the involvement of surface acoustic waves [185], a surface tension gradient [186] or freezing of surface waves [187, 188]. Gurevich et al. [189] reported that the LIPSS can be formed on numbers of different materials including semiconductors, polymers and metals and

that the LIPSS form due not only to optical effects, but also involve temperature-driven hydrodynamic instabilities in the molten layer at the surface.

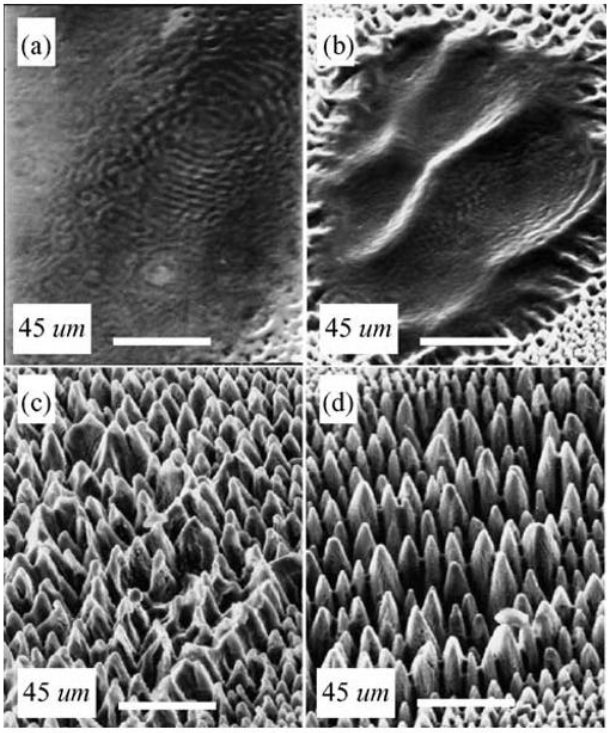

Figure 2-25. SEM images showing the evolution of the surface morphology of Si produced with 35-ps laser pulses in the SF6 ambient upon irradiation with the given number of pulses: (a) 50, (b) 200, (c) 800 and (d) 2400 (from [176]).

Although the results to-date suggest that the adhesion of plated grids to laser-ablated surfaces can enable soldered interconnection (through the equivalence of average busbar pull forces with those of screen-printed cells) and plated modules have passed the IEC 61215 environmental tests [78], the stability of this laser ablation/plating process in mass production has not been demonstrated in large scale manufacturing. Also, since the required laser ablation and plating equipment differs from equipment required for a standard screen-printed production line, the implementation of this alternative metallisation process is also limited by the cost of altering an existing production line. The use of laser ablation to form contact regions for plated metallisation is investigated further in Chapter 5 of this thesis, with respect to the improved adhesion of the plated metal made possible by the laser ablation method.

2.4 Summary

This chapter reviewed different electrical contact formation methods that are applicable to industrially-produced Si solar cells, with a focus on metal plating and the dielectric structuring processes that can be used to form contact regions for plating. It considers the historical trends in contact formation, from the first Si solar cells through to the dominance of Ag screen printing and a number of isolated and limited attempts to introduce plating into mass production.

Although transitioning from Ag to Cu plated metallization can offer significant savings in material cost, history has demonstrated a number of problems associated with this transition. First plating is seen as a more complex process with specific know-how required. It requires a dielectric structuring step, which has been achieved in the past in using lasers, but also a number of different plating steps: (i) Ni for contacting the Si; (ii) Cu for conductivity; and (iii) then a Ag capping layer to prevent corrosion and enable soldering. Secondly, the use of lasers to structure the dielectric can introduce crystal damage. While this damage may not have been critical for lower efficiency Al BSF cells, as the manufacturing industry moves towards increased PERC cell production, elimination of recombination due to laser-induced damage will become more critical. However, perhaps the final and most important problem is that of contact adhesion. Although new interconnection methods such as SWCT [190] and multi-BB [191] are becoming available, the ITRPV Roadmap reports that soldering will remain the dominant interconnection method for some time to come, with 90% of production expected to still use soldered interconnection by 2020 [99].

This thesis investigates the use of plated metallization for Si p-type cells. In Chapter 3, a new bifacial plating method is introduced with bifacially-plated LDSE cells achieving a maximum efficiency of 19%. However, it is shown that use of laser-doping to form contact regions can limit cell efficiency. Chapter 4 then reports on the use of an injection-dependent recombination analysis (through QSSPL and QSSPC measurements) to monitor the introduction of recombination centres through different cell processing steps. Finally, Chapter 5 presents the results of investigations into contact adhesion, considering both finger and busbar adhesion and the role of laser doping and laser ablation in contact adhesion.

CHAPTER 3
LASER-DOPED METAL-PLATED BIFACIAL SILICON SOLAR CELLS

3.1 Introduction

3.1.1 Motivation

A bifacial solar cell is able to increase its power output by capturing albedo radiation from the rear of the solar cell, however to date manufacturing these solar cells is expensive because both P and B diffusions are required and screen-printed Ag grids are used on both surfaces. An alternative metallisation and doping technique could significantly reduce the cost of producing bifacial cells. Light-induced plating has been shown as an effective way of using the light-induced current to provide a source of electrons for metal plating [133] and formation of metal contacts onto n-type Si. It can result in low-cost metallisation due to the use of Cu as the main conductor, relatively simple electrolytes (i.e., no reducing agents required) and minimal bath maintenance where the metal concentration is maintained from the corrosion of anodes comprising the same metal species. However, the method can only be used to metallise the n-type regions of a p-n junction solar cell. Consequently, an alternative method is required to form plated contacts to the p-type regions of Si solar cells.

3.1.2 Objective

The objective of the experiments reported in this chapter was to develop a fabrication method for laser-doped p-type bifacial Si solar cells using self-aligned metal-plated electrical contacts to both cell polarities. A key enabler for the fabrication of these cells was the recognition that p-type Si regions can be made cathodic by forward-biasing the p-n junction of the solar cell. Used in conjunction with LIP for metallisation of the n-type contact regions, this new plating method, which will be referred to as field-induced plating (FIP), was used to form Ni/Cu grids on both semiconductor polarity surfaces of a cell and thereby metallise bifacial solar cells.

It should be noted that this “forward-biased” plating process was independently developed at Roth & Rau AG in Europe and first reported in a patent application to Boehme with a priority date of 25 March 2010 [192]. It has subsequently also been used to plate metal grids to p-type polarity surfaces of heterojunctions cells [193, 194] and B emitters of n-type cells [36, 195], with the work presented as part of this chapter being distinct from the EP 2 369 629 patent to Boehme [192] in that it describes the plating of Ni directly to the Si surface. This work was first reported in a now-granted US patent [196] and at the Silicon PV conference in 2014 [197]. Although the plating technique is now commonly referred to as “forward-bias plating”, the term FIP will be used in this thesis to emphasise the role of the applied electric field in making the p-type surface cathodic.

The simplicity of the FIP process allows it potentially to be performed using the same plating equipment and chemistry as used for LIP. Similar plating rates to those used for LIP (i.e., ~ 1 μm/min for Cu deposition) can be used, however there is also the potential to plate at much faster rates with FIP because the junction is forward-biased and the plating rate is not limited by the light intensity.

3.2 Historical Development of Field-induced Plating

Electrons are minority carriers in the p-type regions of a solar cell, therefore they are not available at sufficient concentration to enable the reduction of metal ions at a p-type Si surface. However, by forward-biasing the p-n junction, electrons can be directed through a p-n junction to make a p-type surface cathodic thereby allowing metal ion reduction to occur at that surface. The following section provides a historical description of the development of FIP (at UNSW) through a series of undergraduate research projects.

3.2.1 Contactless Electroplating

In 2010, a contactless electroplating (CLEP) method was developed by Vais with the objective of plating to p-type surfaces of p-n junction solar cells in a contactless arrangement [198]. The main advantage of CLEP was that no physical contact was required between the contacting electrodes and the solar cell. It was proposed that use of CLEP could potentially increase processing yields for cells using thinner wafers as wafer thickness were predicted to decrease to 140 μm by 2026 [1]

Initially, the experimental process was designed as shown in Figure 3-1 using p-type bifacial cells where both surfaces were passivated by SiN_x layers. The SiN_x, which also acted as a plating mask, was patterned using a continuous wave 532 nm laser and liquid spin-on sources to form laser-doped openings in preparation for metal deposition. The thus-patterned cells were placed inside a container in which an isolation barrier was used to separate a 'negative chamber' in which the n-type surface of the cell was exposed and a 'positive chamber' where the p-type surface of the cell was exposed. The two isolated chambers were filled with plating electrolyte (acid-based $CuSO_4$).

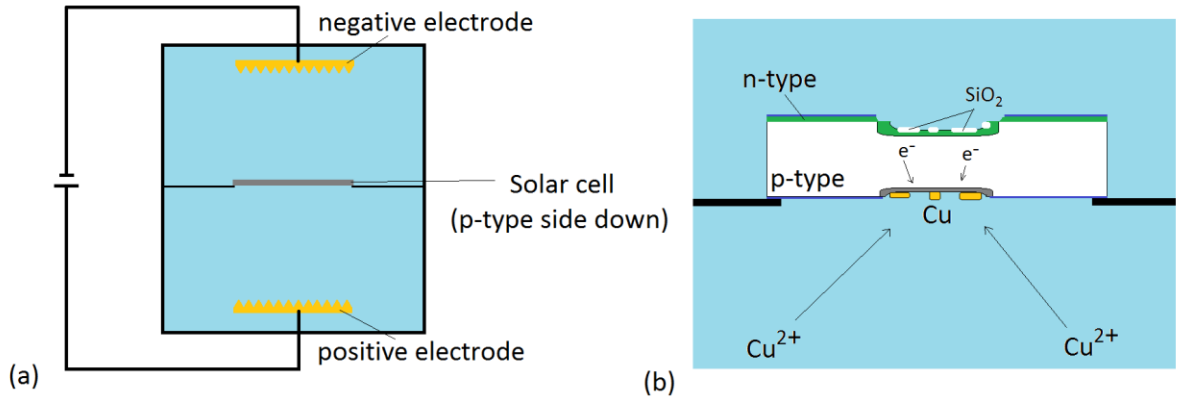

Figure 3-1. (a) The experimental arrangement used in CLEP; and (b) predicted chemical reactions at each surface of the solar cell.

In the plating process, the cell was forward-biased by the application of an external voltage applied between electrodes that were not in contact with the cell [see Figure 3-1 (a)]. In the CLEP concept, provided that there was a high resistance through leakage paths existing in the barrier, it was hypothesised that current would flow through the cell due to the applied electric field with electrons accumulating at the p-type openings where metal ions (e.g., Cu^{2+}) could be reduced. The forward-biased current flow through the cell required that a balancing anodic reaction occurred at the n-type Si openings. Vais proposed that the anodic and cathodic chemical reactions that occurred were:

$$\text{Anodic:} \qquad Si + 2H_2O \rightarrow SiO_2 + 4H^+ + 4e^- \qquad Eq.\,3-1$$

$$\text{Cathodic:} \qquad Cu^{2+} + 2e^- \rightarrow Cu\,(s) \qquad Eq.\,3-2$$

In order to sustain the metal plating process, 1% (w/v) hydrogen fluoride (HF) was added to the $CuSO_4$ electrolyte so that the formed SiO_2 at the n-type openings could be etched (see Eq.

3-3). The experimental arrangement was as shown in Figure 3-2. The patterned cell was placed in the middle plastic container over a square hole which formed an opening in the isolation barrier so that the p-type surface was exposed to the electrolyte in the bottom container.

$$SiO_2 + 6HF \rightarrow H_2SiF_6 + 2H_2O \qquad \text{Eq. } 3-3$$

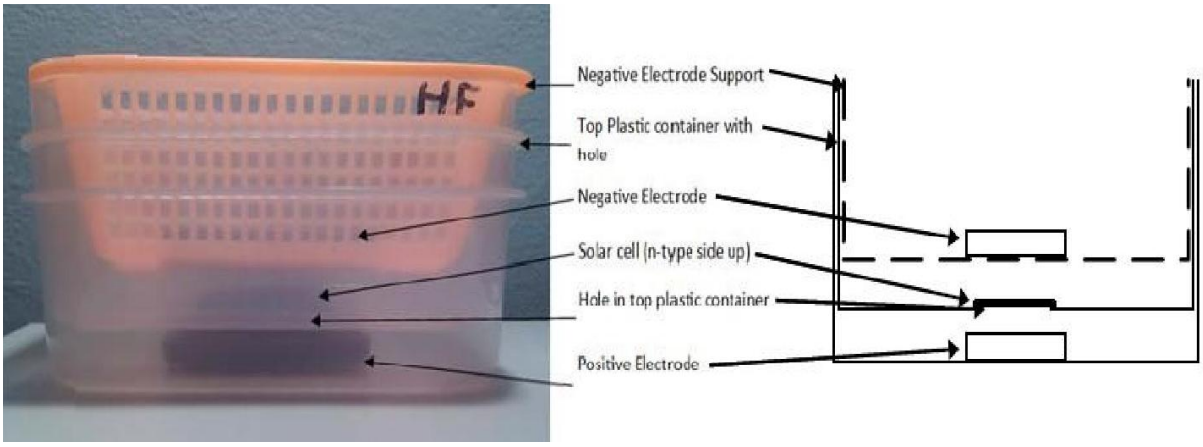

Figure 3-2. The experimental arrangement for CLEP (from [199]).

Vais showed that within 10 min, more than 10 μm of Cu could be deposited on to the laser-doped p-type Si [see Figure 3-3 (b)]. The 'lumpiness' of the deposit suggested that the plating rate had not been well controlled, but this result demonstrated that plating to p-type Si by forward-biasing the junction was potentially feasible. However, the added HF in the electrolyte in the upper container continuously etched the SiN_x layer on n-type surface of the cell during plating. The etching rate of the SiN_x was accelerated over that expected from immersion in 1% HF because the anodic potential at the surface predisposed it to being etched [see Figure 3-3 (a)].

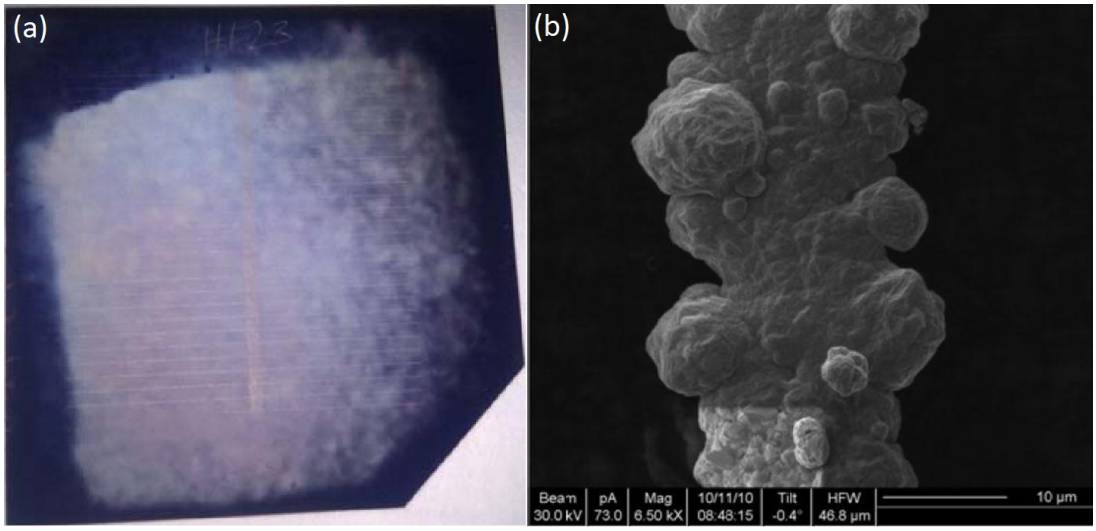

Figure 3-3. (a) Digital photo of an n-type surface showing excessive etching of SiN_x; and (b) SEM image of plated Cu over a p-type laser-doped groove providing evidence of CLEP

3.2.2 Evolution of Field Induced Plating

The CLEP process evolved into FIP through a UNSW Undergraduate Thesis project by Zhao in 2011 [200]. Although the contactless nature of CLEP was very attractive, it was concluded that it was too difficult to control the anodic side reactions (excessive etching of the SiN_x) and effectively seal the upper and lower compartments of the CLEP configuration.[1] In the FIP experimental arrangement, the n-type surface was physically contacted by an electrically-conductive soft material enabling the n-type surface to be maintained dry during the plating process and current to be passed uniformly through the n-type laser-doped openings in the SiN_x, through the wafer and to the p-type openings. In this new arrangement, the solar cell was positioned over a seal foam under pressure with a carbon band soft contact (negative top electrode) contacting the laser openings due to the deformation under the top contact (see Figure 3-4). As with CLEP, a square opening of the same size as the laser-doped cell area was used to expose the p-type openings to the plating electrolyte.

[1] Poor sealing resulted in leakage currents that affected the plating rate making it difficult to control the plating rate at the p-type openings.

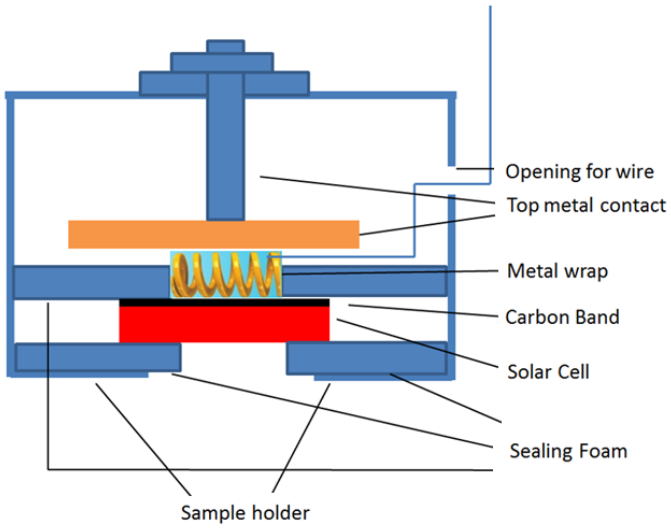

Figure 3-4. Experimental arrangement for the "top contact' used by Zhao to perform FIP in 2011[200].

During the FIP experiments, the dry top contact was placed in a beaker filled with plating electrolyte and a metal anode was placed at the bottom of the beaker (see Figure 3-5). A constant current provided by an external power supply was passed through the n-type laser-doped openings of the solar cell and the exposed p-type Si regions became cathodic and were plated with metal (Cu).

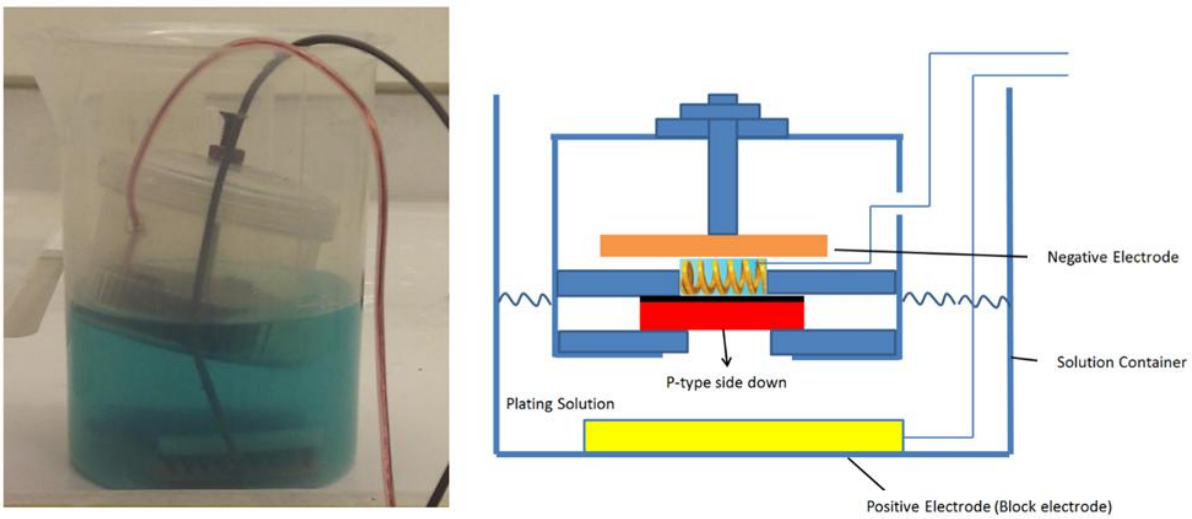

Figure 3-5. Digital photo and schematic of the experimental FIP setup in 2011[200].

In order to achieve bifacial cell plating, the solar cell was simply 'flipped' and placed into the top contact with the n-type surface now exposed to the plating electrolyte. To perform LIP, the anode was shaped into a ring and a light source was placed under the beaker to allow

illumination of the n-type surface (see Figure 3-6) enabling bias-assisted LIP using the same plating apparatus.

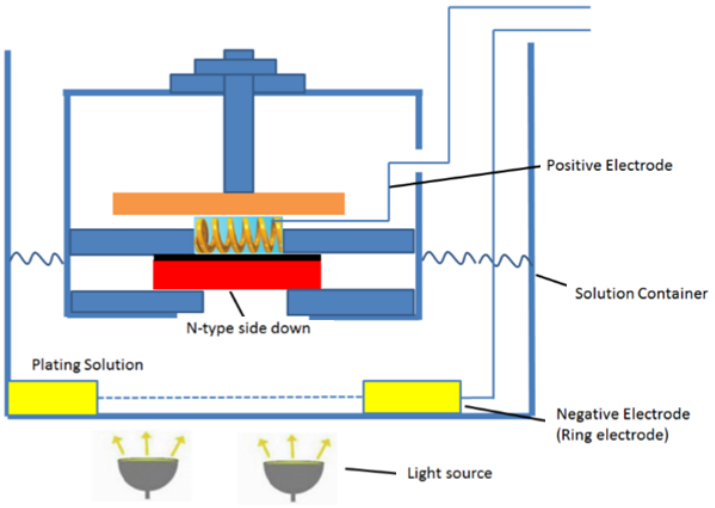

Figure 3-6. Bias-assisted LIP using the FIP setup designed by Zhao in 2011[200].

Zhao's FIP plating setup was used to demonstrate that bifacial plating of a Si solar cell was feasible. The plating arrangement addressed the issue of SiN_x etching during CLEP by physically contacting the n-type laser-doped grooves using a "soft" contact. Zhao achieved more uniform Cu deposition compared to that obtained using CLEP with finger heights of ~ 10 μm being deposited within 10 min of plating at a current density (in the laser-doped openings) of 40 mA/cm^2 (see Figure 3-7). However, the energy conversion efficiency of the thus-plated bifacial laser-doped cells was < 10%.

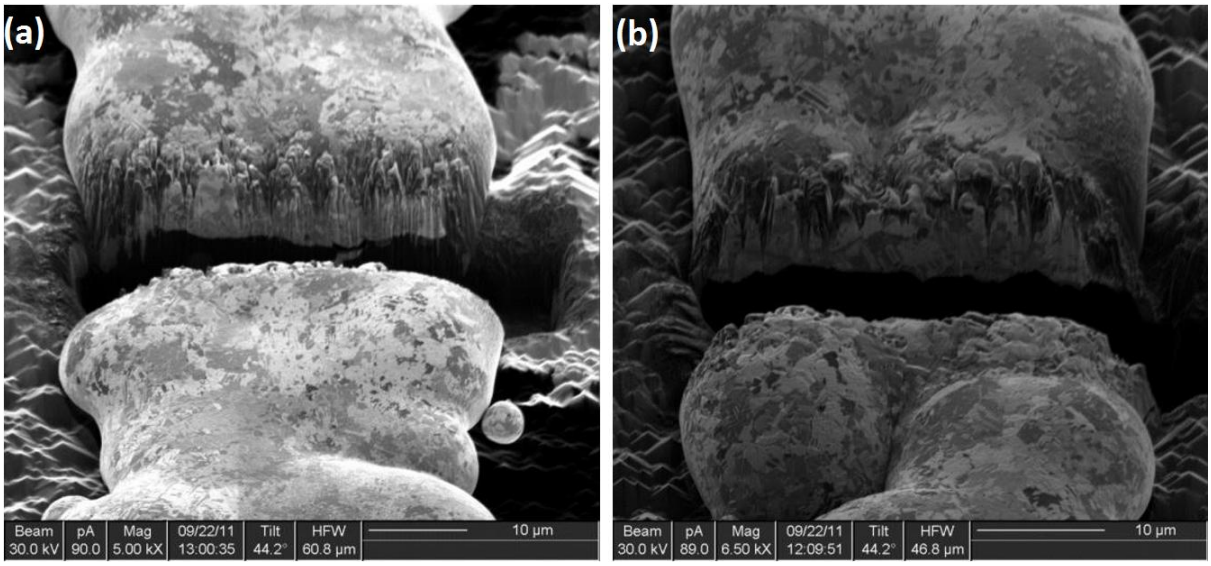

Figure 3-7. Focused ion beam (FIB) images of: (a) a Cu finger plated using FIP of a p-type laser-doped groove; and (b) a Cu finger plated using bias-assisted LIP over an n-type laser-doped groove (from [198]). The two fingers show similar morphology suggesting that the metal plating of FIP can be as well-controlled as that achieved using LIP[200].

3.2.3 Refinement of Bifacial Cell Plating using FIP and Bias-assisted LIP

In 2012, the candidate continued the refinement of the FIP process as part of his Undergraduate thesis research [201] with the objectives of: (i) improving the plating arrangement so as to minimise wafer handling; and (ii) understanding the reason for the low cell efficiency through an analysis of the metal contacting.

3.2.3.1 Improving the Plating Arrangement

In Zhao's arrangement, the pressure holding the carbon band to the wafer surface resulted in significant wafer breakage. Additionally, bubbles (entrapped air or evolved hydrogen) were easily trapped in the exposed area under the cell resulting in non-uniform plating. To address these issues, a new plating arrangement was designed (see Figure 3-8 and Figure 3-9). Soft fibre foam was used as a buffer above the carbon band to absorb some of the applied force when contacting the solar cell. Once the cell was placed on a holder, the level of the plating electrolyte was adjusted to be ~1 mm below the cell surface. Due to the surface tension of the plating electrolyte, gentle agitation of the electrolyte 'wet' the exposed surfaces of the cell whilst keeping the top surface dry and enabling single-side plating.

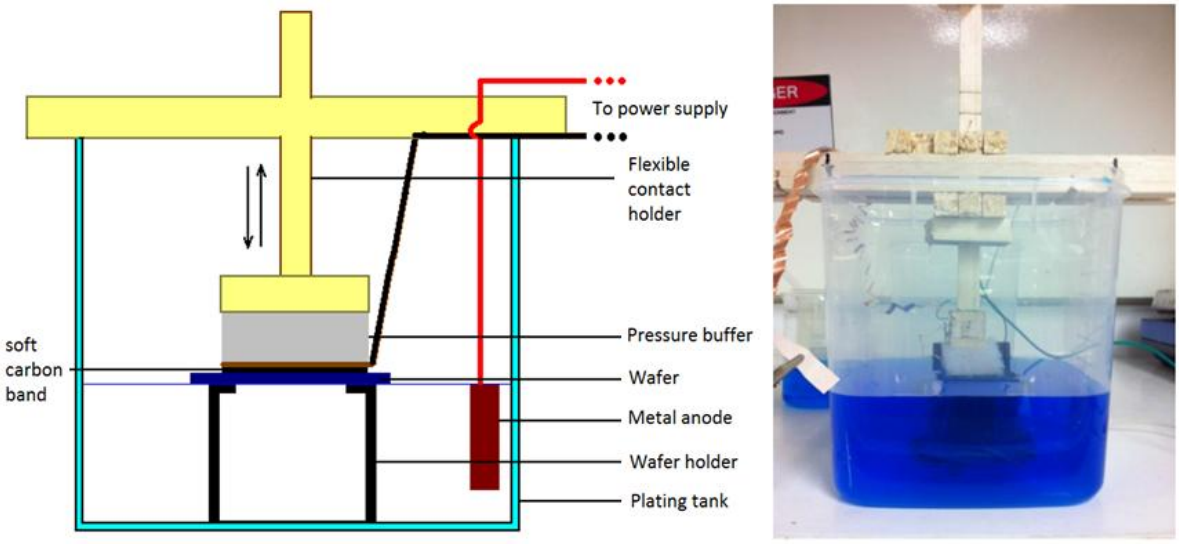

Figure 3-8. Schematic and photo of the plating arrangement used by Wang in 2012 [201].

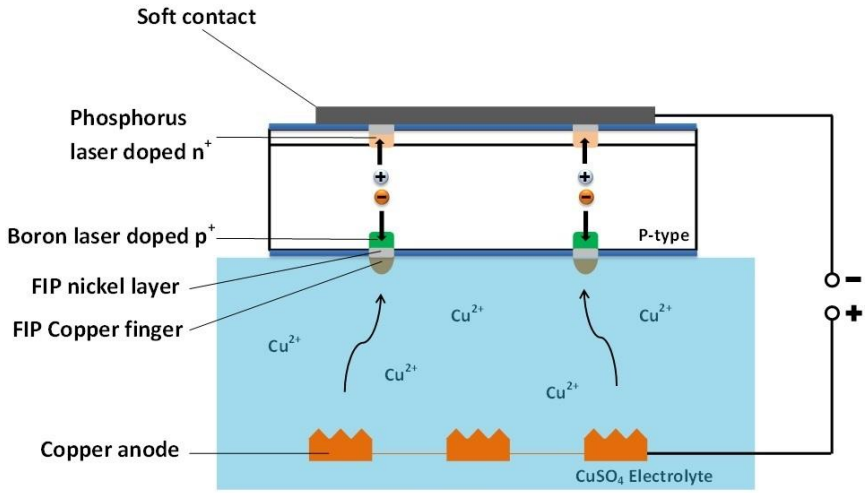

Figure 3-9. Schematic of the FIP process [201].

With the new plating arrangement, the plated fingers and busbars were more uniform than reported by both Vais [198] and Zhao [200] and the plating process was more easily-controlled. Figure 3-10 shows a cross-sectional image of a finger plated using FIP comprising a 1 μm Ni layer under a Cu layer of ~ 10 μm thickness.

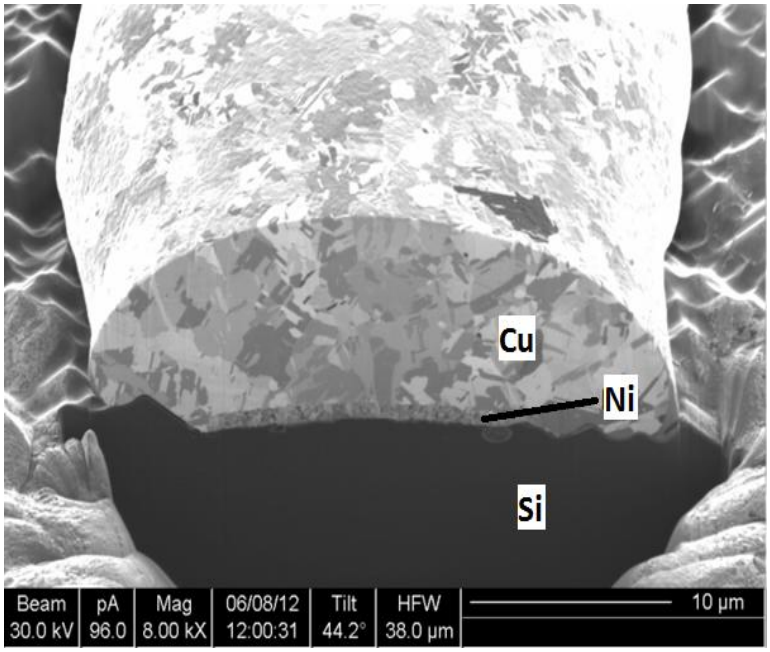

Figure 3-10. Focussed ion beam cross-sectional image of a Cu-plated finger over a p-type laser-doped groove (from [201]). The image shows a 1 um plated Ni layer between the plated Cu and the Si wafer.

3.2.3.2 Addressing the Low Cell Efficiency

The n-type laser-doping process used was identical to that used in the fabrication of LDSE cells [202, 203], consequently it was concluded that the contact problems were most likely arising from the p-type laser-doped regions. Laser speeds of 2.5, 3.0 and 3.5 m s^{-1} were used for B laser-doping, and it was found that, as the laser speed reduced with the same deglazing process (1.5 min in 1% HF) and plating conditions, the plated Ni coverage was reduced (see in Figure 3-11 (b), (d) and (f)). This suggested that with reduced laser speed, the boron silicate glass (BSG) or boron rich layer (BRL) introduced from laser doping through use of the spin-on B source (PBF1 from Filmtronics) may have been significantly increased resulting in low plated Ni coverage (see Figure 3-11). Therefore, a laser speed of 3.5 m s^{-1} was selected for use due to the higher Ni coverage.

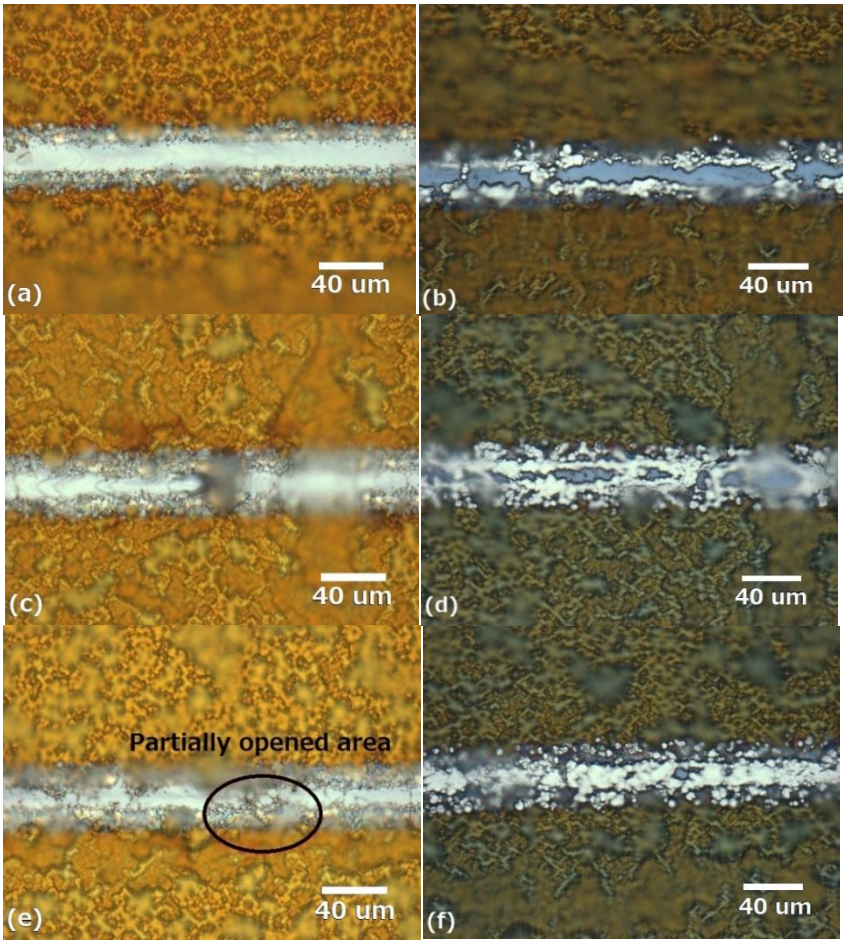

Figure 3-11. Optical microscope images of laser-doped lines formed on the p-type Si surface using the laser scan speeds of: (a) 2.5 m s^{-1}; (c) 3.0 m s^{-1}; and (e) 3.5 m s^{-1}. (b), (d), and (f) show the corresponding laser-doped lines after 1 min of Ni plating (FIP) at a current density of 20 mA/cm^2. As the laser speed increased, the plated Ni coverage improved potentially due to less BSG or BRL layer being introduced during laser doping.

Cells fabricated with the increased Ni coverage were analysed, however although the iV_{OC} was ~ 670 mV after laser doping, the final V_{OC} was < 500 mV in some cases after plating. This large reduction was attributed to the formation of rear Schottky contacts [204, 205] evidenced by the bending back of the Suns-Voc curve as the light intensity increased (see red curve in Figure 3-12). By reducing the laser-doping speed to 0.5 m s^{-1} and thereby increasing the surface concentration of B in the laser-doped grooves (blue curve in Figure 3-12) this behaviour was rectified and the V_{OC} was increased. However, the reduced laser-doping speed increased the difficulty of removing the thicker BRL/BSG layer and increasing the HF deglazing duration was not recommended because it resulted in etching of the SiN_x which caused overplating. Consequently, the problem was addressed by increasing the plating

duration from 1 to 5 min in order to achieve uniform coverage of the Ni on the laser-doped openings (see Figure 3-13).

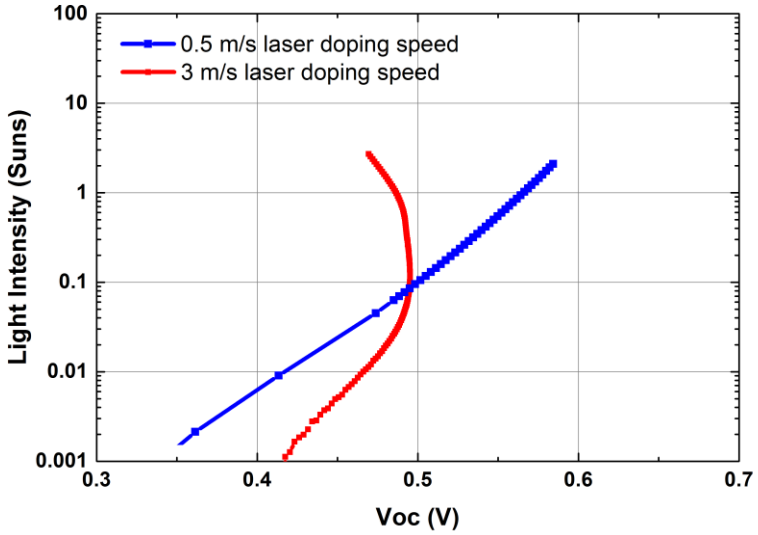

Figure 3-12. Suns-Voc measurements for cells laser-doped using a speed of 3 m s^{-1} showing bending back of the V_{OC} due to Schottky contacts (red) and 0.5 m s^{-1} (blue). The Ni plating (i.e., FIP) durations for the two cells were 1 min and 5 min, respectively (from [201]).

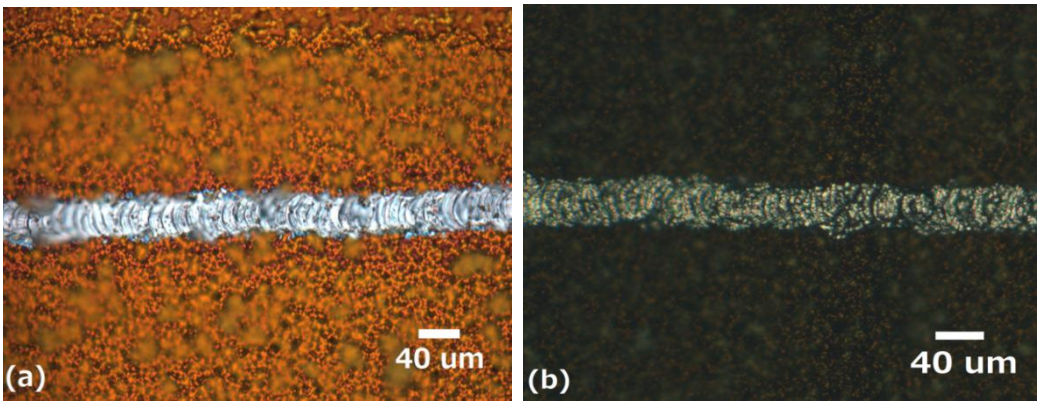

Figure 3-13. Optical microscope images of (a) a B laser-doped finger using a speed of 0.5 m s^{-1} before; and after (b) Ni FIP for 5 min at a current density of 20 mA/cm^2.

Using these modifications, light *I-V* measurements using an example cell resulted in a final V_{OC} of 639 mV and an increased device efficiency of 17.2 % (see Figure 3-14). However, the fill factor (*FF*) remained low (0.68). The measured dark *I-V* curve showed peaks at different operating conditions, especially at the maximum power point where the local ideality factor (*m*) was increased to over 2 [153, 206, 207]. The *FF* was also impacted, at least partly, by a high series resistance of 1.6 Ω cm^2.

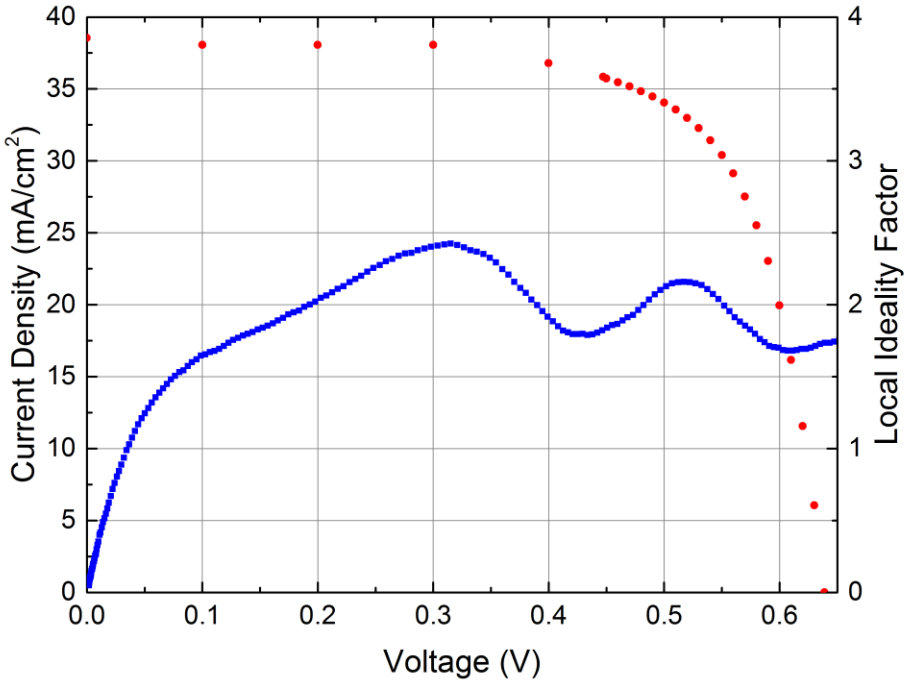

Figure 3-14. Light *IV* curve (red) and bumpy local ideality factor curve (blue) of a 17.5% efficiency cell (from [201]).

Due to the SiO_2/SiN_x passivation layer on the p-type surface of the bifacial cell, it was also suspected that shunting from an inversion layer (formed as a result of the positive charges in the SiN_x [208]) may have contributed to the high *m* and hence low *FF* [209-213]. Spectral response measurements showed that at long wavelengths there was a significant difference in the IQE for the bifacial plated solar cell measured with and without a bias light (see Figure 3-15). This demonstrated that if the carrier injection was insufficient at the rear of the cell then recombination rates at the rear surface were increased resulting in the observed lower IQE and thereby supporting the potential existence of inversion layer shunting at the B laser-doped contacts [212, 213].

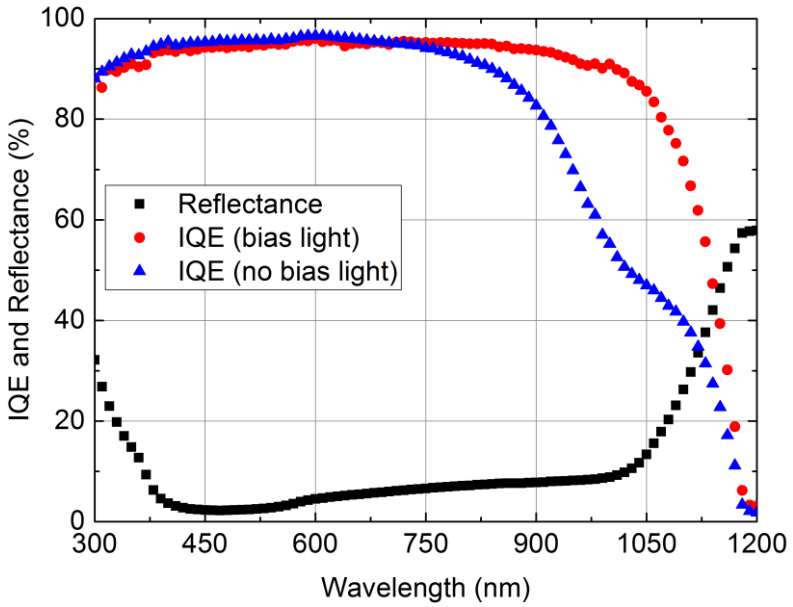

Figure 3-15. Reflectance (black squares) and IQE measured for a bifacially-plated cell with SiO_2/SiN_x rear passivation with (red circles) and reduction of the IQE recorded at long wavelength without a bias light due to insufficient carrier injection to form an inversion layer(blue triangles) (from [201]).

By the end of 2012, it was concluded that FIP could be used as a simple and fast metallization method to deposit Ni and Cu on p-type Si as electrical contacts for solar cells. Combined with bias-assisted LIP, FIP could be used for the fabrication of bifacial cells. The key processes for successful Ni and Cu deposition on p-type laser-doped grooves were identified to be: (i) sufficiently slow p-type laser-doping (i.e., 0.5 m s^{-1}) to prevent the formation of Schottky contacts at the p-type laser-doped grooves; and (ii) sufficiently long Ni plating duration (i.e., 5 min) to achieve the 100% Ni coverage due to increased BSG or BRL layer formation at low laser doping speeds.

A cell efficiency of 17.2% was achieved on a 4.84 cm^2 cell, however the *FF* was only 68% which was due to two main reasons. First, the R_s was high (1.6 Ωcm^2 compared to values of 0.8 Ωcm^2 obtained for LDSE cells with a full-area aluminium alloyed rear electrode [214]). The second reason was the high local ideality factor at the maximum power point which was concluded to be caused by the (slow) laser-doping process possibly resulting in defect formation both at the surface and in the bulk of the Si wafer. These two problems were addressed through the research reported in this chapter.

As mentioned in Section 3.2.2, “forward-bias” plating was developed in Europe independently of the FIP development described in this thesis. It was first applied to the

direct plating of Ni/Cu to Si by Bartsch et al. on B emitters of n-type cells [215] using Rena-manufactured cup plating and inline plating tools. As with cells plated using FIP, uniform plating was achieved and Figure 3-16 shows a Cu finger uniformly-plated on a p-type emitter surface of an n-type cell plated using "forward-bias" plating. Unlike the bifacial cell plating described in this chapter, the electrode contact to the n-type cell surface for Bartsch et al.'s n-type cells could be the same as that used for bias-assisted LIP as the n-type surface was fully conductive (i.e., covered with metal). This contacting approach is not possible if the n-type surface is coated with a dielectric as with the bifacial laser-doped cells described here. A key innovative contribution of the research summarised in the preceding sections was the development of a "soft" electrode material that could contact the Si exposed through patterns of openings in a dielectric layer.

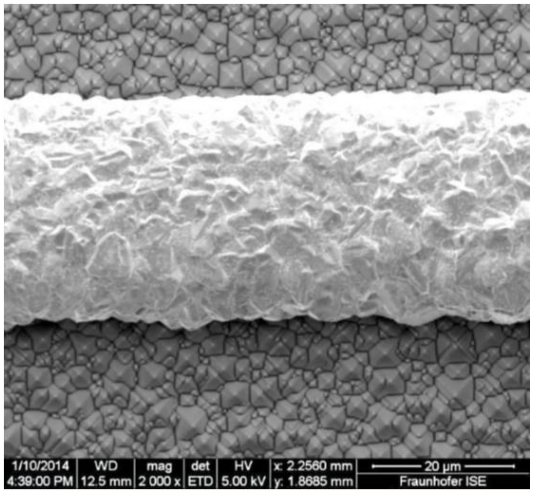

Figure 3-16. Morphology of a forward-biased plated Ni-Cu contact from Bartsch et al. showing continuous Cu fingers (from [215]).

The development of the bifacial plating process is summarised in Figure 3-17. Finally, although it may seem at first more efficient to bifacially-plate cells by contacting both grids simultaneously, it should be noted that the conductivity of the laser-doped grooves is insufficient to enable uniform plating across a 156 mm cell. In order words, Ni would only nucleate close the electrode contact. The described bifacial cell plating process can be applied when:

- There is no seed layer metal at the regions to be metallised; and
- When both surfaces are coated with dielectric layers.

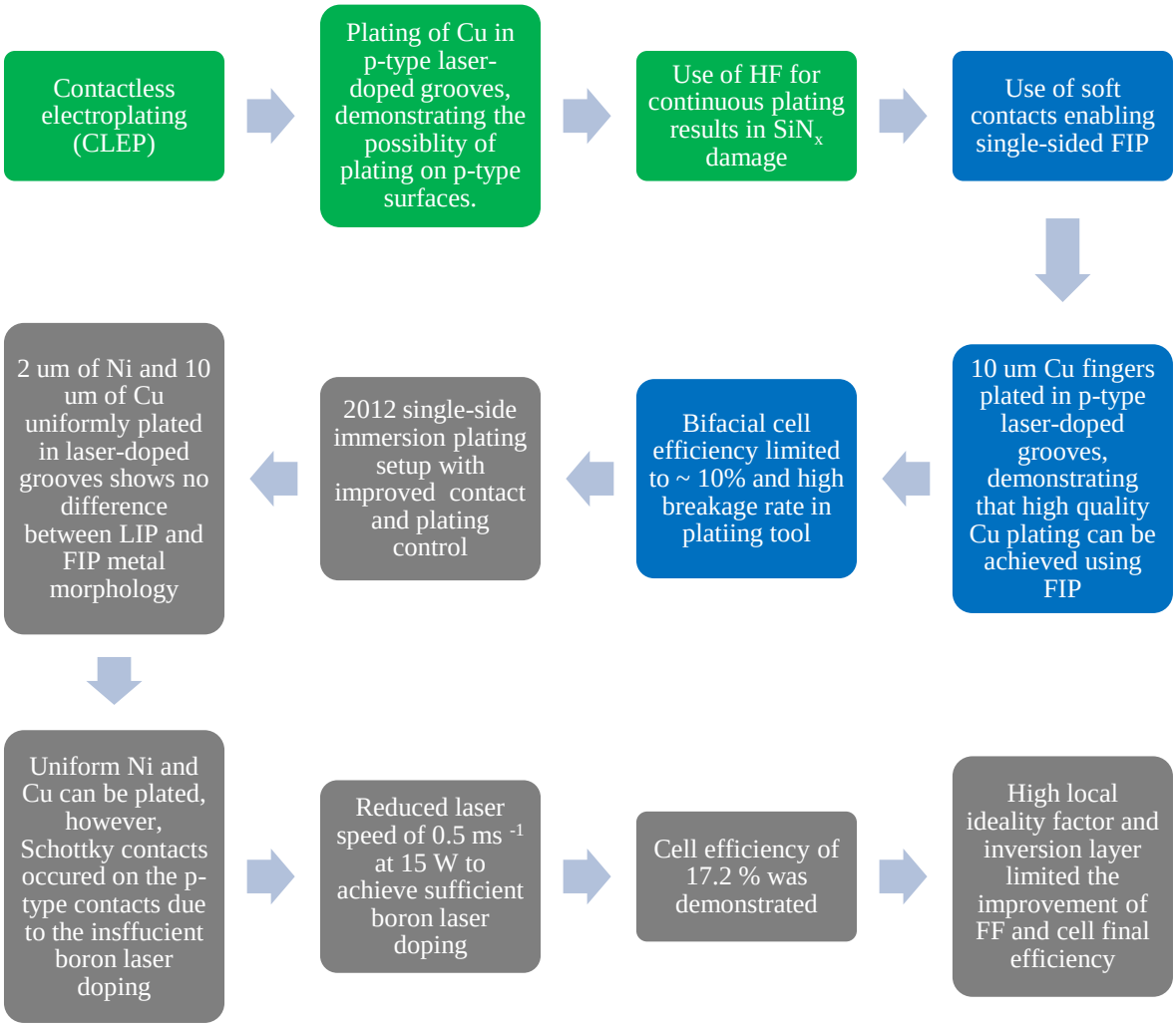

Figure 3-17. Development of FIP at UNSW from 2010 to the end of 2012, where green squares are the development in year 2010, blue are in 2011 and grey are 2012.

3.3 Laser Doping Optimization

3.3.1 Introduction

As discussed in Section 3.2, although FIP showed great potential for the plating of bifacial laser-doped solar cells, two performance-limiting problems remained at the start of this thesis research. These problems were due to the laser doping process. First, the Gaussian distribution of the laser beam [153, 216-218] can cause laser damage at the edges of the laser-doped grooves which can reduce the cell V_{OC} and impact the *pFF*, and second non-uniform doping and residue of BSG or BRL remaining along the laser doped grooves can impact the Ni nucleation. Consequently, it was concluded that further optimization of the laser doping process was required. This section reports on the results of experiments which attempted to

identify the optimal p-type laser doping process parameters for the bifacial cells. The performed experiments demonstrated that the doping profile and extent of damage also depended on the composition and thickness of the dielectric layers, with the reflectance at 532 nm being used to estimate the fraction of the incident laser energy that was available to be absorbed during laser doping.

Although fluence is typically used to quantify the energy delivered to the surface by pulsed lasers, this parameter is only meaningful for CW lasers used in combination with some irradiation time. For this reason, in the following discussion and throughout this chapter, the terms laser power and laser speed are used to characterise the laser doping process.

3.3.2 Experimental

156 mm alkaline-textured B-doped 1-3 Ω cm Cz Si wafers were diffused to an emitter sheet resistance of 100 Ω/□ in a $POCl_3$ furnace. After phosphosilicate glass (PSG) removal, a ~ 10 nm SiO_2 layer was thermally-grown on both wafer surfaces using dry oxidation and 75 nm of SiN_x (refractive index ~ 2.0) was deposited on the n-type surface by plasma-enhanced chemical vapour deposition (PECVD) using a Roth & Rau MAiA tool.

The rear surface of one group of cells was then passivated by deposition of 200 nm SiN_x (Roth & Rau MAiA) over the thin SiO_2 layer (SiO_2/SiN_x rear passivation). The second group of cells was passivated by depositing a 10 nm AlO_x and then 200 nm SiN_x (Roth & Rau MAiA) (AlO_x/SiN_x rear passivation). The third group was passivated by deposition of 10 nm AlO_x and then 100 nm SiN_x (Roth & Rau MAiA) (AlO_x/SiN_x rear passivation). The 156 mm wafers were then laser-cleaved into wafer fragments of ~ 4 cm × 4 cm to complete the processing.

All the laser doping was performed using a Spectraphysics 532 nm CW laser (15-25 W) with a Gaussian beam and a $1/e^2$ beam diameter of 30 μm. The n-type laser doping process was as previously reported [33, 74, 153, 203, 219, 220] and is summarised here for clarity. After spin-coating the n-type surface with the 85 % phosphoric acid (from J.T.Baker), wafers were laser-doped using one pass at a laser speed of 3 m s^{-1}.

A series of experiments were performed to ascertain the optimum p-type laser-doping parameters for different dielectric stacks on the p-type surface of the cells. Initial experiments

relied on the use of a PBF1 B spin-on liquid source (from Filmtronics) to form the p+ laser doped regions on the rear surface of the cell precursors. The spin-on B source was spin-coated at a speed of 3000 rpm for 20 s and then wafers were baked at 130 °C for 10 min to remove organic solvents. However, due to the difficulty in achieving laser-doped grooves without incurring considerable damage, later experiments investigated the ability to use the AlO_x in the dielectric stack as a p+ dopant source. This eliminated the need to first spin-coat the liquid B source on the wafer surface. The final cell area and exposed Si grid area were 6 cm^2 and 0.24 cm^2, respectively, for all experiments reported. The process flow for the experiments is shown in Figure 3-18.

The implied open circuit voltage, iV_{oc}, was calculated from photoconductance measurements of the excess carrier density, Δn, at 1-sun using a Sinton WCT 120 tool from Sinton instruments using:

$$iVoc = \frac{kT}{q} \ln\left(\frac{np}{n_i^2}\right), \qquad \text{Eq.3-4}$$

where $n_i = 9.65 \times 10^9$ cm^{-3} at 25 °C [221].

The value of Δn was estimated using the generalised method [222] (since the wafer's lifetime was ~ 120 μs) and using an optical constant of 0.85 as wafers were alkaline-textured and coated with SiN_x [223, 224]. The reflectance was recorded using a Perkin Elmer Spectrophotometer with a 150 mm integrating sphere.

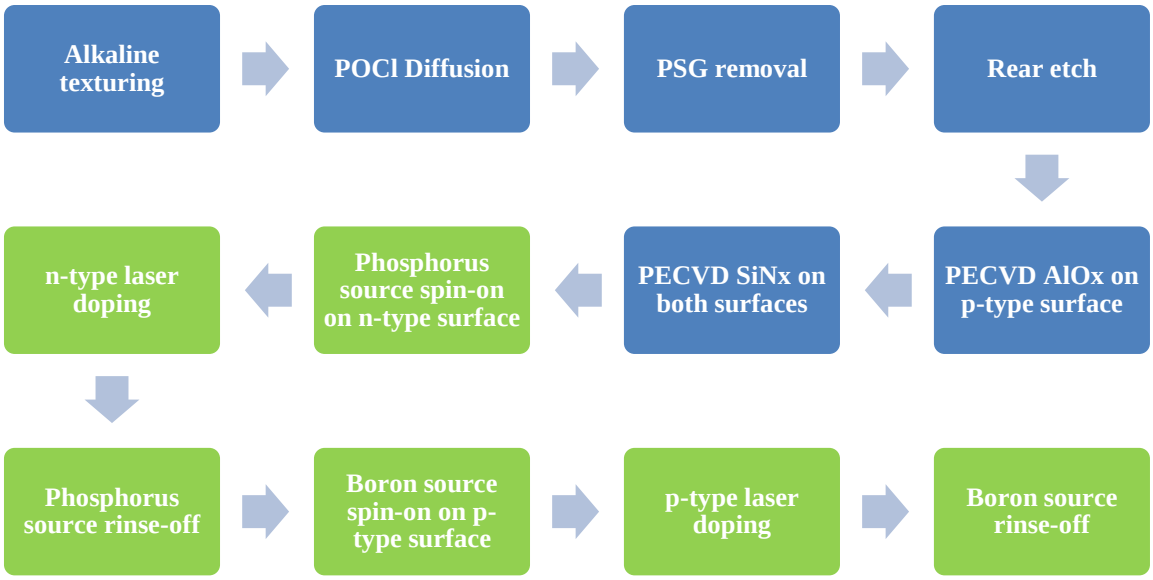

Figure 3-18. Process flow used for the experiments. The processes in blue were performed by an industrial partner on a pilot production line and processes in green were completed at UNSW. In later experiments the B source spin-coating step was omitted as p+ dopants were introduced through the use of the AlO_x in the dielectric layer.

3.3.3 Results

3.3.3.1 P-type Laser-doping with a B spin-on Source

Figure 3-19 shows the influence of laser speed used for both n-type and p-type laser doping (with a B source) on the measured iV_{OC}. All cells experienced a reduction in iV_{OC} of ~ 10 mV after n-type laser doping. This reduction is similar to that reported by Hallam and Hameiri [160, 203, 225]. On the p-type surface, as the laser-doping speed was increased from 0.5 to 3.0 m s^{-1} a larger reduction in iV_{OC} was observed. Although more laser damage is expected for the slower laser-doping speed (see Figure 3-19), this trend in iV_{OC} was also observed by Hallam, et al. [160] and is attributed to the formation of a shallower junction with a lower incorporated B concentration with faster laser doping speeds. Increased recombination occurs due to the increased minority carrier concentration in the laser-doped regions (i.e., less shielding of the minority carriers from the high recombination occurring at the surface). This result confirms the need to use the slower laser speed of 0.5 m s^{-1} for the p-type laser-doping for both contact formation and reduced recombination losses at the laser-doped regions.

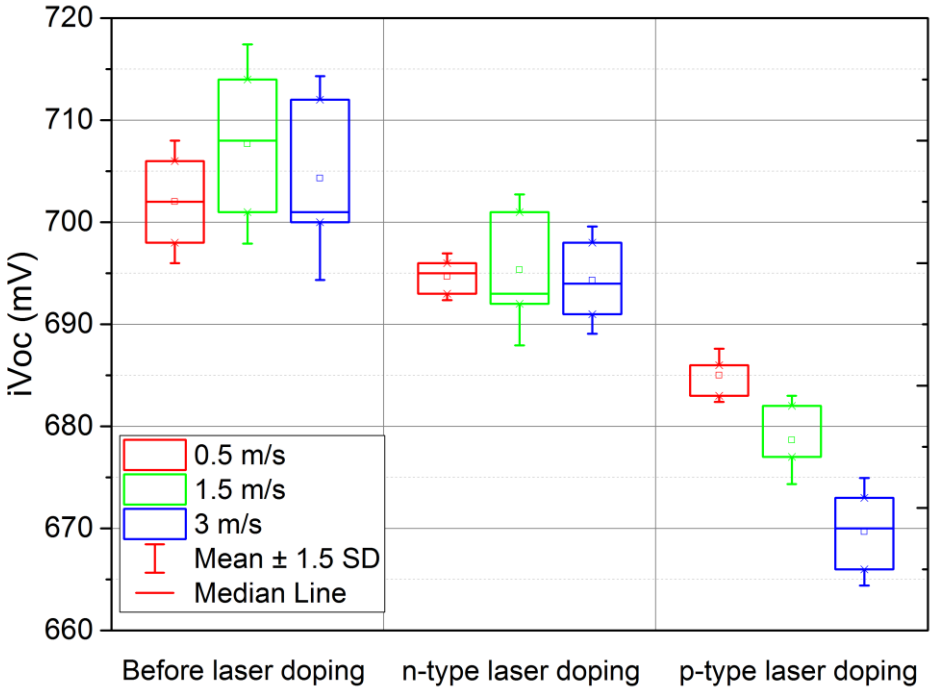

Figure 3-19. Implied V_{OC} changes with different p-type laser doping speeds using a 15 W laser power and PBF1 B source on cells with a 200 nm SiN_x rear passivation layer.

The resulting n-type laser-doped regions were smooth in the middle of the groove [see Figure 3-20 (a)], however at the edges of the laser grooves, the SiN_x layer was only partially removed and the tips of the pyramids had been damaged by the laser [see Figure 3-20 (b)]. Since the laser used had a Gaussian beam energy distribution, the SiN_x regions exposed to the outer extremities of the laser beam experienced a lower power density [153] leading to the SiN_x being only partially removed. Although the damage incurred by the laser appears substantial, it was to a large extent mitigated due to the heavily-diffused Si underneath and the electrical impacts were not significant as discussed by Yao et al. [214].

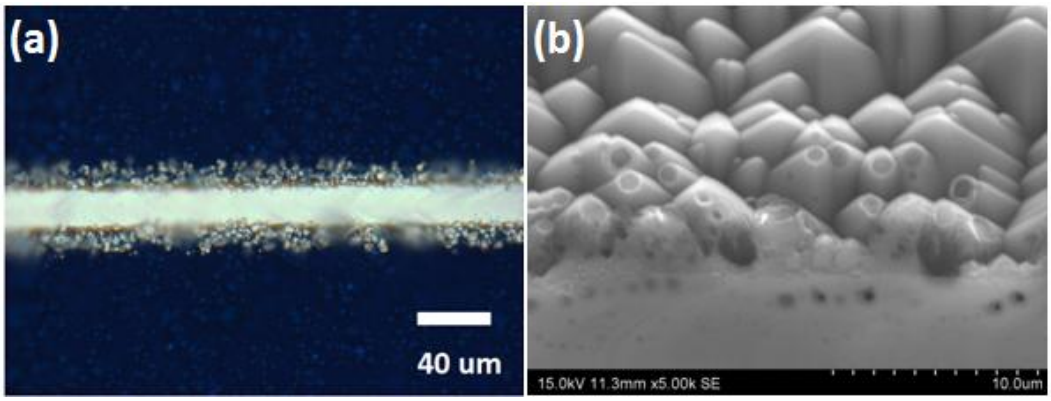

Figure 3-20. (a) Optical image of a P laser-doped groove on the n-type surface of an alkaline-textured Si wafer obtained using a laser speed of 3 m s^{-1}; and (b) a cross-sectional SEM image of a similar laser-doped region showing partial SiN_x ablation and laser damage at the tips of pyramids adjacent to the groove.

The p-type laser-doping with a spin-coated B source was performed using a laser speed of 0.5 m s^{-1} and one pass on wafers with: (i) 200 nm SiN_x; (ii) 10 nm AlO_x/ 200nm SiN_x, and (iii) 10 nm AlO_x / 100 nm SiN_x on the p-type surface. Hallam et al. reported that the junction depth was ~ 5 μm using these parameters [160]. As shown in Figure 3-21 (a) and (b), the resulting laser doping grooves for the dielectric 200 nm SiN_x and 10 nm AlO_x/ 200nm SiN_x were similar in terms of morphology and width for both dielectric layers. Unlike the n-type surface after laser-doping, the damage at the edges of the grooves was considerably reduced. The reduced damage was attributed to: (i) the higher laser energy incident on the surface being able to remove the dielectric layers more uniformly; and (ii) the absence of surface pyramids due to the rear-etching of the Si after the emitter diffusion process. However, the laser grooves for the 10 nm AlO_x / 100 nm SiN_x visually appeared significantly different [Figure 3-21 (c)]. At the edge of the grooves, a dark damaged region was observed where the SiN_x layer was only partially removed.

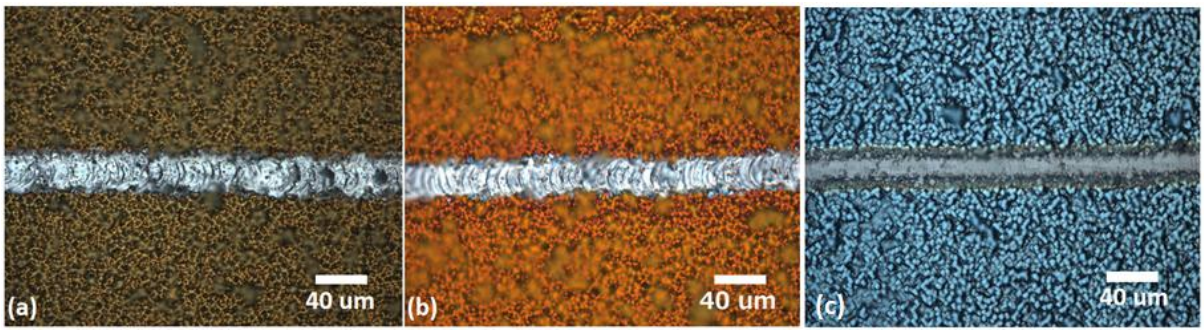

Figure 3-21. Optical microscope images of p-type laser-doped grooves (using B source) obtained from one laser pass at 0.5 m s^{-1} at 15 W on a: (a) 200 nm SiN_x layer; (b) a 10 nm AlO_x / 200 nm SiN_x dielectric stack, on a rear-etched p-type Si surface; and (c) a 10 nm AlO_x /100 nm SiN_x SiN_x dielectric stack, on a rear-etched p-type Si surface

In order to understand the reason(s) for such different laser doping results for the different dielectric stacks using the same laser parameters, the reflectance of the rear surfaces was measured. Figure 3-22. shows that the reflectance at 532 nm (laser wavelength) of the etched surface with the different dielectric stacks differed significantly, especially for the surface passivated with 10 nm AlO_x and 100 nm SiN_x. Due to the high reflectance of this dielectric stack, only 58.5% of the incident laser energy was absorbed. Furthermore, the spin-on B source may have further reduced the fraction of the incident laser energy available for laser-doping, contributing to even greater non-uniformity and increased peripheral damage occurring during laser doping. The measured reflectance values in Figure 3-22. highlight the importance of checking the impact of surface reflectance at the laser wavelength used for laser doping. This is especially important for rear surface laser doping where more variation in the thickness of the dielectric stack is tolerated.

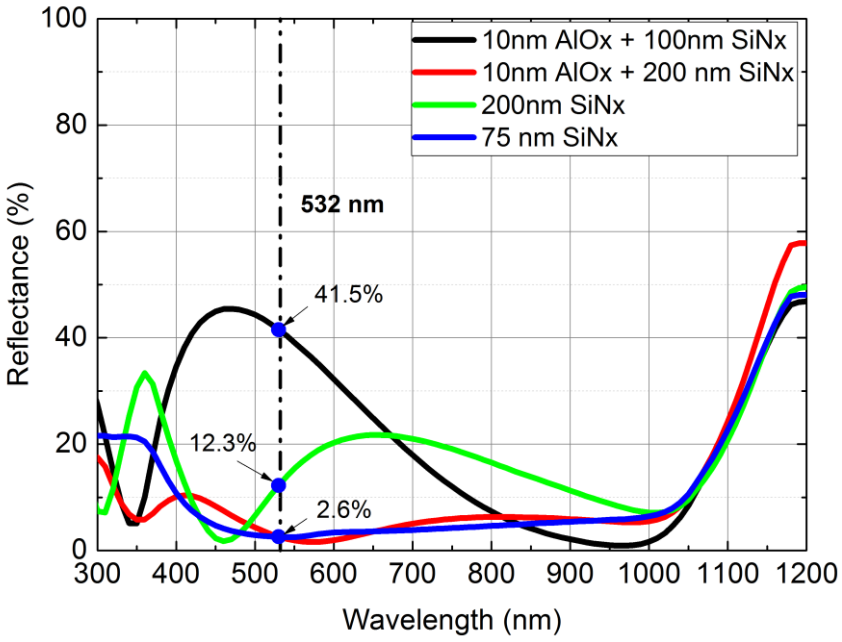

Figure 3-22. Measured reflectance of the different rear passivation layers.

3.3.3.2 P-type Laser-doping without B Spin-on Sources

Laser doping through AlO_x without B spin-on source and using AlO_x layer as the p-type doping source has been previously reported [226, 227], with Hallam and Xiao suggesting that heavily-doped *p*+ layers could be formed with much higher laser speed. One key advantage of laser doping through AlO_x without a B source is that a higher laser speed can be used which can act to reduce the peripheral laser damage. It was found that with B laser doping source, a lower speed is required to achieve sufficient dopant depth and concentration, however, for laser doping through AlO_x without an added B source, use of a higher laser speed can achieve sufficient doping. In addition, the resulting shallower p+ layer appears to cause less laser damage, in particular reducing damage that may penetrate deeper into the wafer from the doped regions (e.g., dislocations and lattice mismatch), making possible higher cell *FFs* and efficiencies [219, 226].

Three laser speeds were tested for laser doping without B source through 10 nm AlO_x/ 100 nm SiN_x dielectric stacks and the results are shown in Figure 3-23. At the laser speed of 0.5 m s^{-1}, the edges of the grooves were dark due to laser damage and cracks were evident [see Figure 3-23 (a)]. Increasing the laser speed avoided the crack formation and reduced the damaged area at the edges of doped grooves [see Figure 3-23 (b),(c) and Figure 3-24 (a)]. With a laser speed of 7 m s^{-1}, there was almost no laser damage evident at the edges of doped

regions [see Figure 3-24 (a)]. In addition, the width of the doped groove decreased with laser speed, from 30 μm at 2 m s^{-1} to only 12 μm when a laser speed of 7 m s^{-1} was used.

It was also observed from the SEM image in Figure 3-24 (b) that use of the faster laser speed resulted in bulged laser-doped regions, instead of grooves. It is believed that the "bulging" is due to the fast laser speed resulting in the melting of a very shallow layer of Si which expands out at the surface due to the fluid surface tension and thermal expansion as described in Refs [228-232].

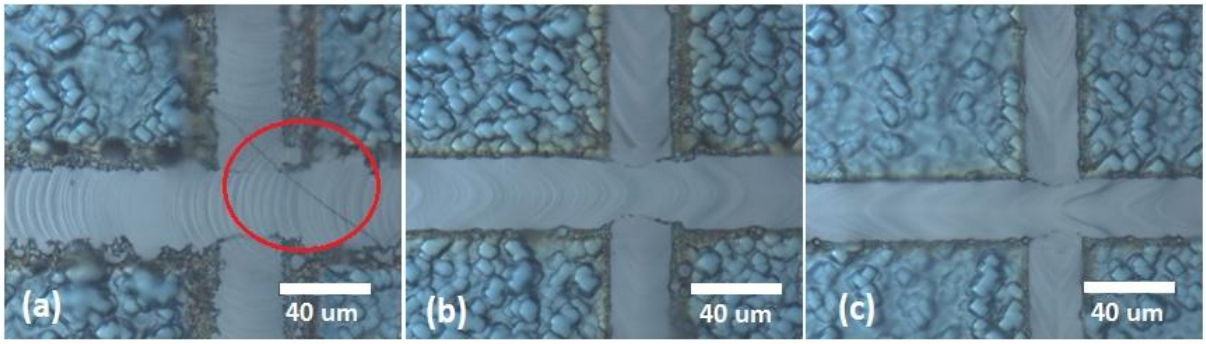

Figure 3-23. Optical microscope images of laser-doped grooves formed without spin-on B source through 10 nm AlO_x and 100 nm SiN_x dielectric stacks at a power of 25 W with laser speeds of: (a) 0.5 m s^{-1}; (b) 2 m s^{-1}; and (c) 4 m s^{-1}.

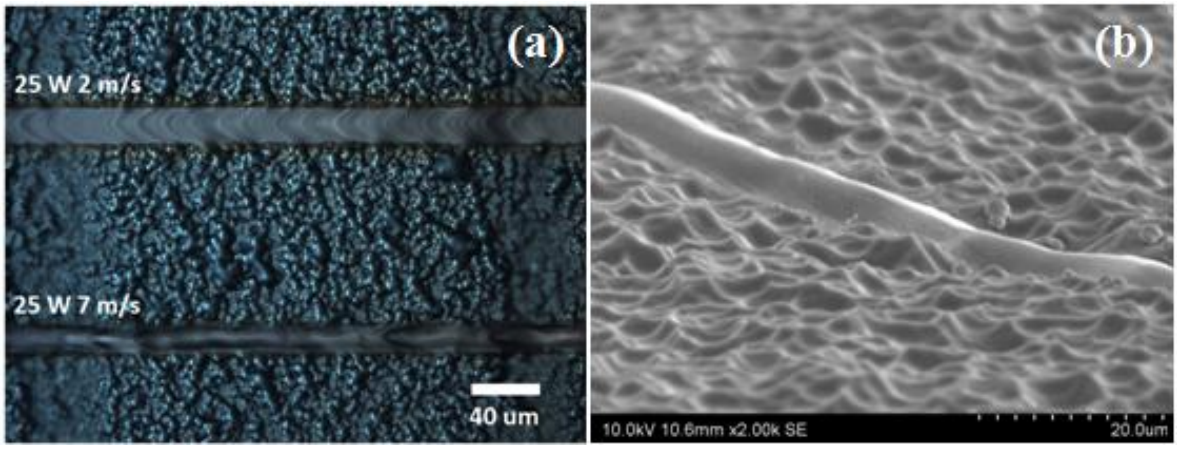

Figure 3-24. (a) Optical microscope images\ showing laser-doped grooves through 10 nm AlO_x and 100 nm SiN_x dielectric layers at a laser power of 25 W with laser speeds of 2 and 7 m s^{-1}; and (b) a SEM image of a laser-doped groove formed using a laser speed of 7 m s^{-1}.

The fast laser speed is advantageous in: (i) ensuring narrower laser openings and reducing the laser damage and non-uniformity at the laser groove edges [160]; and (ii) reducing voids or

cracks forming in the Si bulk (see Figure 3-25.) compared to lower laser doping speeds reported in [226].

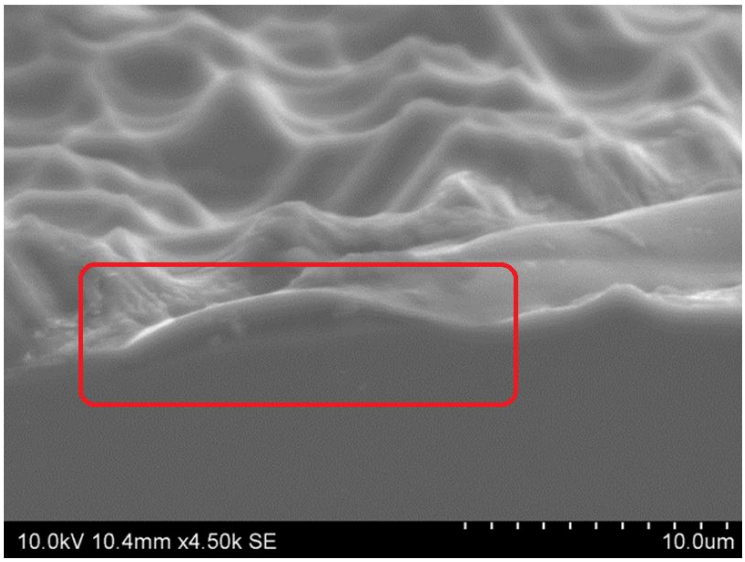

Figure 3-25. Cross–sectional SEM image showing the laser doping without B source on 10 nm AlO_x and 100 nm SiN_x stack using a laser power of 25 W and a laser speed of 7 m s^{-1}.

3.3.4 Conclusions

For the fabrication of plated bifacial laser-doped selective emitter cells, laser doping is a critical process which determines the electrical performance of the metallization process. For n-type surfaces, the most critical issue that is faced is laser damage at the edges of the laser grooves. This damage, which has been investigated previously [133, 153, 225, 226], is attributed to the Gaussian distribution of the laser beam and its interaction with pyramid-textured surfaces, and results in non-uniform P doping and incomplete SiN_x opening occurred at the edges of laser grooves. Consequently, a top-hat laser beam [233] and smaller textured pyramids are preferred for an n-type (front surface) laser doping process since there is less light scattering effects [234-236].

On the p-type (rear) surface, a higher laser power was required to achieve sufficient B laser doping (using a spin-on B source) to avoid the formation of Schottky contacts. However, different rear surface dielectric stacks can result in significant differences in the reflectance at the laser wavelength of 532 nm. Dielectric stacks consisting of 10 nm AlO_x / 100 nm SiN_x and 10 nm AlO_x / 200 nm SiN_x reflected 41.5% and 2.6% of incident 532 nm light, respectively. Consequently, the laser doping conditions needed to be adjusted according to

the surface reflectance to ensure similar laser energy absorption. The laser power was increased from 15 to 25 W for the dielectric stacks having higher reflectance.

Finally, it was demonstrated that laser doping through AlO_x without a B spin-on source can also achieve p+ selective emitter formation. By using the AlO_x layer as the source of p+ doping, faster laser speeds can be used enabling a reduction in both peripheral laser damage, and the elimination of voids and cracks both within the grooves and at the edges of the laser-exposed regions. With the faster laser speeds, the doped regions appeared to be 'bulged' due to the thermal expansion and fluid surface tension. It was therefore concluded that fast laser scribing through AlO_x (i.e., laser doping without a spin-on B source) may be a promising option for increasing the efficiency of the bifacial laser-doped p-type cells.

3.4 Plating Optimization

3.4.1 Introduction

Electroplating has been widely used for many diverse applications, from plated integrated circuit boards to water taps for corrosion prevention in aviation [237-241]. It is commonly known that the key factors for successful electroplating are surface pre-treatment and deposition condition control (e.g., plating current density). However, unlike many applications which involve large parts with high strength and have sacrificial surfaces that can endure etching pre-treatments, Si solar cells are fragile, protected by thin layers of surface SiN_x, and the plating of metal grid electrodes involves the growth of very thin and typically long linear elements adhering to limited areas of Si.

The electrochemistry of the plating is further complicated by the fact that metal is required to plate to a semiconductor [114], rather than the typical case where metals are plated to metal parts. This fact introduces further complexity, as the semiconductor device must be operated or controlled in such a way that electrons are delivered to the surface where metal is required to be plated. For example, as described earlier in this chapter, illumination can be used to provide a source of electrons to exposed n-type Si regions, and a bias potential can be used to provide a source of electrons to a p-type Si surface. This section reports on the results of experiments which aimed to develop a reliable process to plate Ni and Cu to both n-type and p-type laser-doped grooves, and in doing so enable bifacial cell plating.

3.4.2 Plating Rate Considerations and Implications

Bias-assisted LIP and FIP are through-wafer plating processes and so there are a number of ways in which a bias current or voltage can be applied to the cell. The bias current or voltage that is applied depends on the resistances in the circuit and the chemical formulation being used. The following section discusses some considerations and implications of plating rate control during bias-assisted LIP and FIP.

3.4.2.1 Control Mechanisms

Plating to solar cell surfaces can be performed by controlling either the voltage or current of the applied power source. The use of the different control mechanisms for LIP was investigated using equivalent circuit analysis by Yao [146]. She concluded that use of voltage-control was preferable for LIP of laser-doped cells because these cells can have non-uniform distribution of R_s (see for example [242]). Use of voltage-control reduces the probability of the cell operating under reverse bias at localised emitter regions. Performing LIP whilst the solar cell is operating under reverse bias can result in non-uniform Ni plating [147], and in extreme cases can cause electrical damage to the solar cell [146, 147].

Consequently in this study, bias-assisted LIP for both Ni and Cu was performed in potentiostat mode (voltage-controlled), with bias voltages being selected which were sufficient to offset the resistances in the electrochemical circuit whilst maintaining the cell under forward bias. However, FIP was performed in galvanostat mode (current-controlled) to ensure a tight control on the plating rate as small changes in applied voltage can result in significant changes in the plating current which can affect the morphology of the deposits.

3.4.2.2 Plating Rate Limitations Due to Chemistry

From an electroplating perspective, use of current-control is preferable because it allows for tighter control of the plating rate. Proprietary plating chemistries are provided with Technical Data Sheets (TDSs) which specify the plating rate range over which the chemistry will result in metal deposits with desirable and specified properties. In addition to requiring that the metal ion concentration remain within a specified range, most, if not all, proprietary plating formulations contain additives that can enhance the metal properties of the deposited metal [243-246]. For example, chloride ions (through addition of HCl) and polyethylene glycol

($C_{2n}H_{4n+2}O_{n+1}$) are typically used as additives for Cu acid plating electrolytes to control the plating speed and improve the Cu deposition uniformity [247, 248]. Polyethylene glycol can be absorbed to the Cu surface and significantly reduce the Cu deposition rate [247]. Chloride ions can enhance adsorption of Cu and hence improve the Cu plating uniformity [247], However, Shao et al.[248] show that Cl ions can also result in dendritic growth of plated Cu (see Figure 3-26). Addition of Cl ions increases the grain size of the plated Cu and decreases the density of the growing nuclei, due to the reduction of Cu^{2+} first to $CuCl_2$ to then to Cu. The latter reaction becomes the rate-determining step when the Cl ion concentration is high [248].

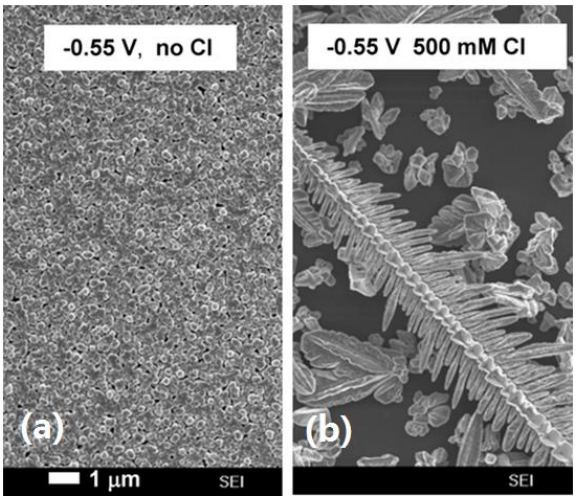

Figure 3-26 SEM images of: (a) uniform Cu deposition in the absence of Cl ions; and (b) plated Cu in the presence of Cl ions resulting in dendritic growth (from [248]).

Other organic additives such as sulfo sulfonate compounds (R_1-$(S)_n$-RSO_3M) and alkylated polyalkylenemine (H_2N-$(CH_2)_n$-NH-R) are also frequently used as additives. These additives can improve the brightness of the plated metal and are known as leveling additives or brighteners [249]. They result in smoother plated Cu and a highly reflective surface with higher plating current densities. These additives also can increase the hardness of the plated Cu.

However, the concentrations of metal ions and additives can change with time if a plating electrolyte is re-used. Although metal ions are replaced by a corroding anode during electroplating (also in LIP and FIP), the metal ion concentration can change due to evaporation of the solvent (e.g., water), especially if elevated temperatures are used for plating. Additives can be consumed through either reacting or through decomposition at

higher temperatures. Consequently it is necessary to periodically check that the plating is being performed at the correct plating rate for a possibly aged electrolyte.

3.4.2.3 Optimizing the Plating Rate

When plating metal grids to cells, the surface area being plated must be estimated, in order to determine the current to apply to the electrode on the other surface of the cell to ensure the required current density at the exposed Si areas. The optimum plating rate, $I_{plating}$, can be estimated using:

$$I_{plating} = J_{DS\text{-}middle\ range} \times (A_{fingers} + A_{Busbars} - A_{Intersections}) \qquad \text{Eq. } 3-5$$

where $J_{DS\text{-}middlerange}$ is the mid in the optimal range specified for the chemistry, $A_{fingers}$, $A_{Busbars}$ and $A_{Intersections}$ represent the area of the fingers, busbars and intersection regions, respectively.

If fresh plating electrolytes are used for each experiment then it can be safely assumed that $I_{plating}$ can be set according to Eq. 3-5. However, typically plating electrolytes are re-used. This means that the metal ion and additive concentrations may vary with time and consequently the optimum plating rate may drift for the electrolyte. One way to ensure that you continue to plate at the optimum rate for a particular chemistry, especially if the electrolyte may have aged, is to periodically perform a Hull cell test [250] (see Figure 3-27).

In this test, a “test plate” cathode is placed at an angle with respect to the anode so the plating current at each point on the test plate increases as the distance to the anode decreases. The morphology of the metal plated on the test plate can then be examined and correlated to a calibrated plating current.

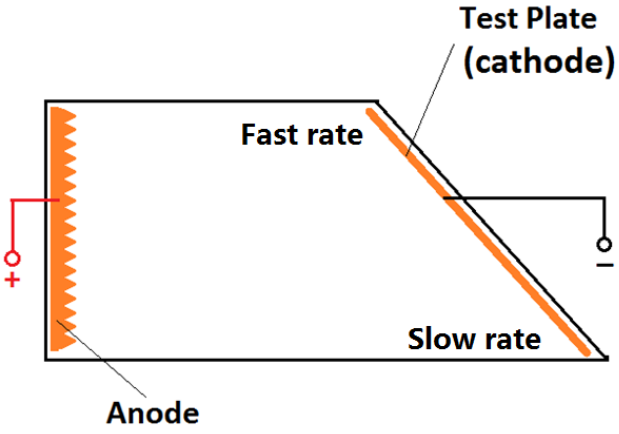

Figure 3-27. Hull Cell test arrangement for determining the optimal plating current for an electrolyte.

Figure 3-28 shows the Hull cell result when new (fresh) Ni and Cu electrolytes are used. Using a provided "ruler" that correlates anode-cathode distance to plating current, the bright and uniform regions of the plated test cathode identify the optimal plating rate ranges. For the Cu and Ni Hull tests, the middle region is at the correct plating current density window where deposited metal is uniform. Due to a high current density at the left corner of the Cu test plate, the deposited metal peeled due to very fast and non-uniform deposition.

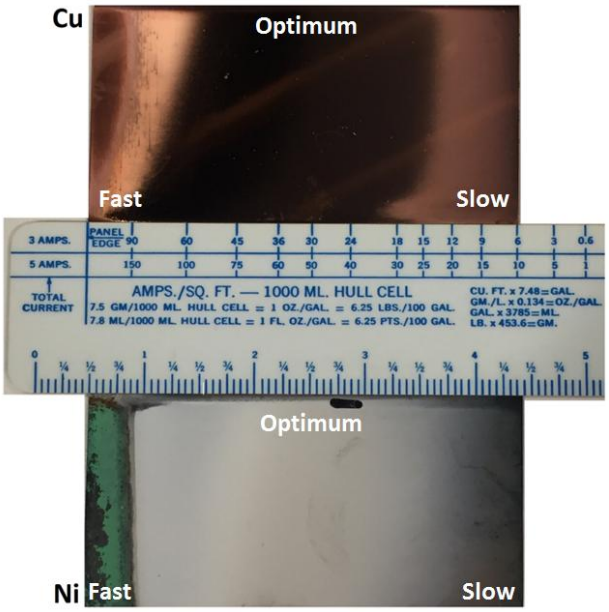

Figure 3-28. Hull cell Ni and Cu plate cathode sheet shows gradients of metal deposition morphology. For Cu plating, the optimum plating occurred in the middle of the sheet where uniform and bright plated Cu is observed. Note, due to the uniformity of the plating in this region, the camera image appeared dark due to the reflection of light. The Ni plating test plate shows evidence of runaway plating at fast plating rate (right hand side) and less Ni plating when plating rate was significantly reduced on the left hand side of the plate.

3.4.3 Bifacial Cell Plating Process Development

This section describes the development of the bifacial cell plating process, with a particular focus on the plating process for p-type laser-doped grooves.

3.4.3.1 Experimental

The plating process adopted by experiments reported in this section is summarised in Figure 3-18 and is described in more detail below with attention being given to the reasons for the different surface treatments and the selection of the bias voltages and currents used for experiments.

In all experiments the p-type and n-type laser-doped grids were aligned to each other so that during FIP current flowed directly through the wafer. This alignment was performed because Vais and Zhao had previously noted that, if the laser-doped grids were perpendicular to each other, then dendritic plating occurred at points where the grid intersected and reduced plating was observed in grooves where there was no overlap [198, 200, 201].

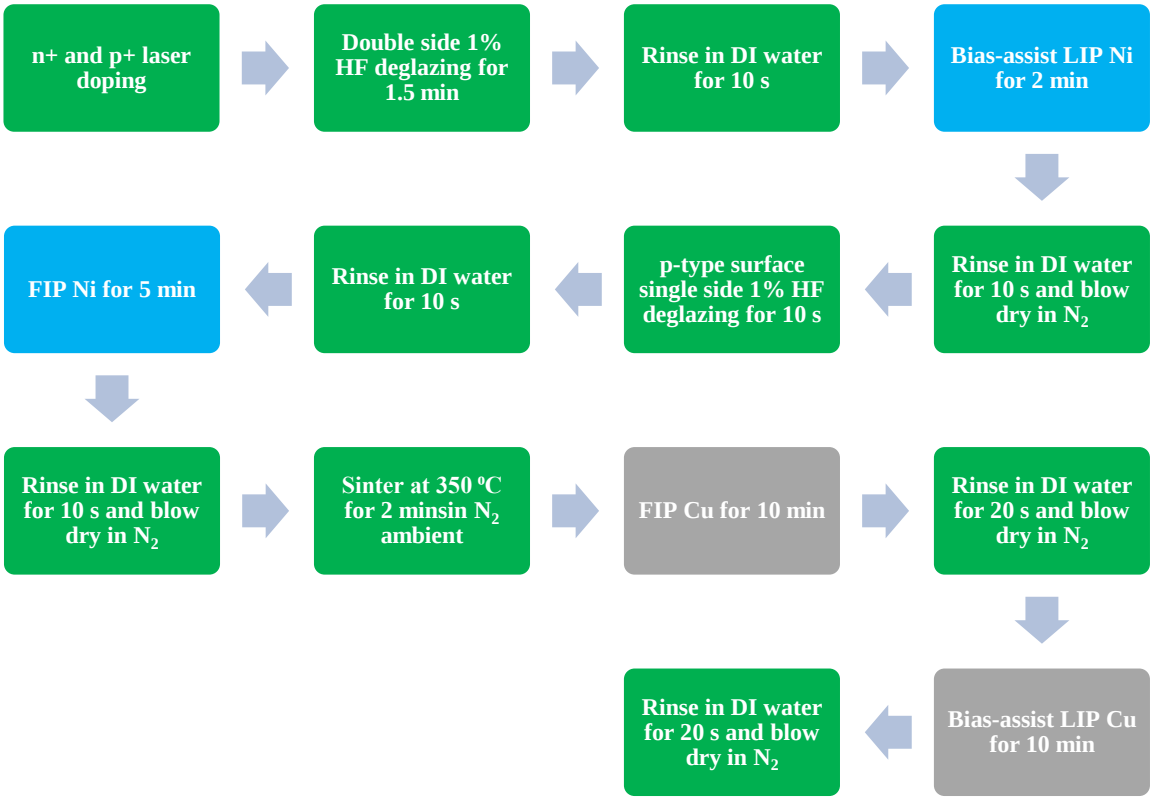

Figure 3-29. Experimental process flow for the plating of the bifacial laser-doped cells. The blue squares represent the first bias-assisted LIP and FIP plating process and grey squares shows the second bias-assisted LIP and FIP plating process after sintering.

After laser doping on both cell surfaces, wafers were immersed in 1% (w/v) HF for 1.5 min to remove the PSG and any remaining BSG (which may have formed during the laser doping process) and therefore ensure that both the n+ and p+ laser-doped surfaces were residue and oxide-free before metal plating. Wafers were then quickly rinsed in running DI water to remove most of the adherent HF and limit drag-out of HF into the Ni plating solution. Presence of HF in the plating chemicals can result in unnecessary etching of SiN_x during Ni plating and subsequent "ghost plating" or overplating as current leaks through thin dielectric regions or pinholes [251].

In the bias-assisted LIP, Barrett SN1 nickel sulphamate (obtained from MacDermid) was used as the plating electrolyte, the light intensity at the wafer surface during plating was 250 W/m^2 and plating was performed using voltage control mode with a 1.2 V reverse bias to maintain the relatively constant plating current density of 15 mA/cm^2. Afterwards, wafers were then rinsed quickly in DI water and then immersed in 1% (w/v) HF for 10 s, to remove

any oxide formation in the p+ grooves that may have occurred during the plating of Ni to the n-type Si surface. Unlike BSG or PSG, native Si oxides are relatively easy to remove by 1% HF, consequently an immersion duration of only 10 s was sufficient. It was also important to keep this second HF immersion step very short to ensure limited further etching of the SiN_x dielectric surfaces of the bifacial cells.

Field-induced plating of Ni to the p-type laser-doped grooves was then performed whilst the n-type surface of the cell was contacted by the plating apparatus. Wafers were then rinsed, dried and sintered in a tube furnace at 350 °C for 2 min in N_2 ambient. This process has been used previously [30, 133, 252] and the assumption was that it results in the formation of a Ni silicide which acts to reduce contact resistance [253-255] and improve contact adhesion [256].

Copper was then directly plated on the sintered Ni layer after immersion in 1 % HF for 5 s to remove the oxide using FIP followed by bias-assisted LIP (bias voltage of 0.1 V), each for 10 min, using a Technisol Cu 2440 solution (obtained from Technic, Inc) to form a Cu grid on both wafer surfaces of height ~ 9 µm.

The optimum cathode current density for the Barrett SN1 and Technisol Cu 2440, as provided in the Technical Data Sheets, were 5 to 216 mA/cm^2 and 40 to 60 mA/cm^2, respectively. The plating (cathode) current densities used for FIP were 35 mA/cm^2 and 50 mA/cm^2 for Ni and Cu, respectively.

3.4.3.2 Results and Discussion

Although $I_{plating}$ can be set as reported in Section 3.4.2.3, if overplating occurs due to pinholes in the SiN_x, edges effects, scratches or other defects, the effective opening area will be different. Furthermore, remaining PSG/BSG or oxides can also contribute errors to the calculated plating rate resulting in non-optimal values of $I_{plating}$ being used. Figure 3-30 (a) shows that very little Ni was deposited and some metallic grey regions were apparent on the surface when Ni FIP was performed for 2 min using a plating current density of 15 mA/cm^2 (calculated from Eq. 3-5). It was concluded that the sparsely-plated regions may have been due to some BSG remaining after deglazing in HF. Consequently, in order to achieve full coverage of Ni, the plating current density was increased to 35 mA/cm^2 for a duration of 2 min. This plating current density was still within the optimum plating range specified for the

Barrett SN1 chemistry. However, due to the now large plating current passing through the partially-opened grooves, the actual plating current density was significantly higher in some groove locations, and consequently, 'run away' plating was observed [see Figure 3-30 (b)] in which oxidized Ni appeared green and 'lumpy' (as on the left side of the Hull test plate sheet in (see Figure 3-28).

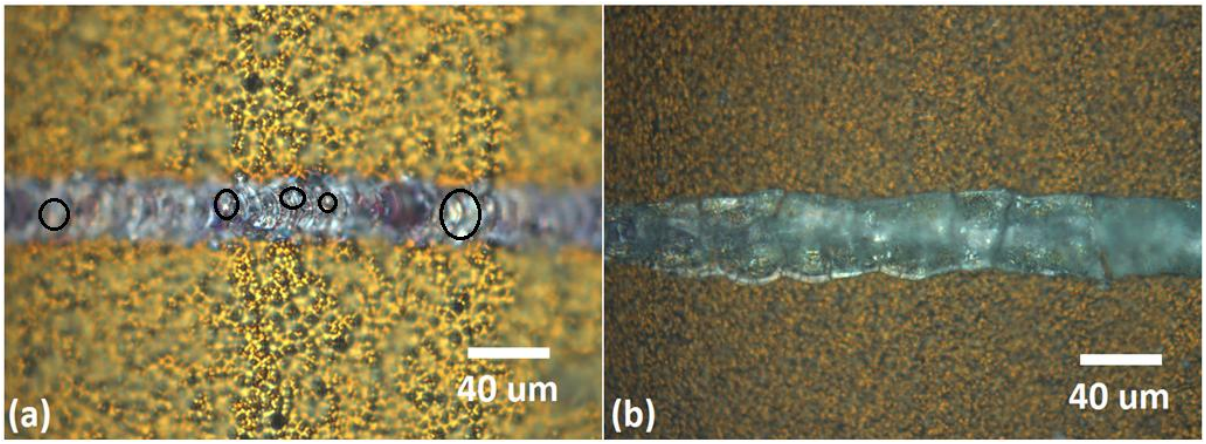

Figure 3-30. Optical microscope images showing different Ni morphology plated by FIP: (a) where the presence of localised BSG residue resulted in limited Ni deposition in 2 min at 15 mA/cm^2; and (b) where use of the increased 35 mA/cm^2 plating current resulted in oxidised Ni after plating for 2 min.

The insufficient removal of surface residue can be rectified by either increasing the HF deglazing time or increasing plating time. However, increasing the HF deglazing time also increased the likelihood of over plating since the SiN_x layer was slowly etched during deglazing. It was determined that the SiN_x stack layers used for the bifacial cells could only be exposed to 1% HF or a maximum of 1.5 min before pin holes formed in the dielectric. Consequently, the approach that was adopted was to increase the plating duration from 2 to 5 min, after which the laser-doped grooves were fully covered with bright Ni. The surface morphology, however, was not smooth since the plating followed the contour of the laser-doped surface in the groove [Figure 3-31(b)]. The PSG was relatively easy to remove on the n-type laser-doped grooves, and after 2 min of Ni plating at 15 mA/cm^2, a uniform, bright and smooth layer of Ni was obtained [Figure 3-31 (a)].

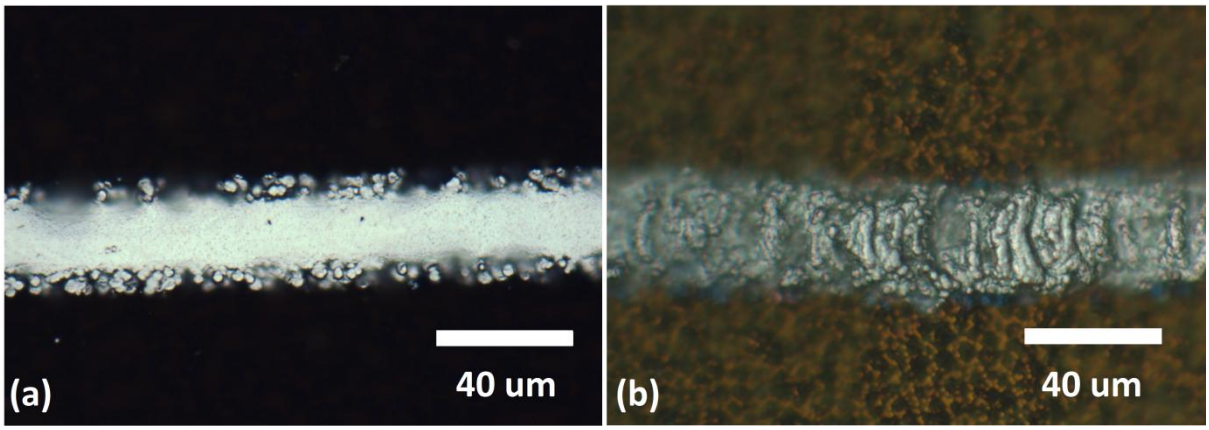

Figure 3-31. Optical microscope images showing uniform and sufficient Ni plating from: (a) bias-assist LIP in 2 min; and (b) FIP Ni for 5 min at 15 mA/cm^2.

Unlike laser doping using a B source (where BSG forms during the laser-doping step), when laser-scribing (i.e., laser doping in the absence of a B source) only 1 min immersion in 1% (w/v) HF was sufficient to remove all the residual oxide after laser doping. Consequently a lower plating current density of 10 mA/cm^2 for a duration of 2 min could be used to achieve grooves fully covered with uniform and bright Ni for the cells with AlO_x/SiN_x (see Figure 3-32).

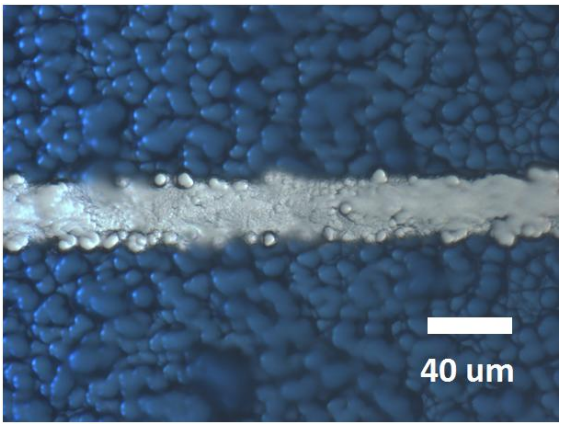

Figure 3-32. Optical microscope image showing uniform and full coverage of Ni plated using FIP for 2 min at 10 mA/cm^2 after laser-doping through AlO_x/SiN_x without B source.

The optimisation process that is required for Cu plating is similar to that described for Ni plating. With an optimised plating current density, a uniform layer of Cu was deposited on the plated Ni to form the fingers and busbars (see Figure 3-33). A too-low plating current density or duration resulted in an insufficient thickness of Cu and high R_s. On the other hand, too high a plating current density resulted in dendritic crystallization of Cu (see Figure 3-34)

which occurs due to the unstable crystal growth when the growth rate is limited by the rate of Cu ion diffusion in the plating electrolyte. Dendritic Cu should be avoided since it is often not continuous and is easy to peel.

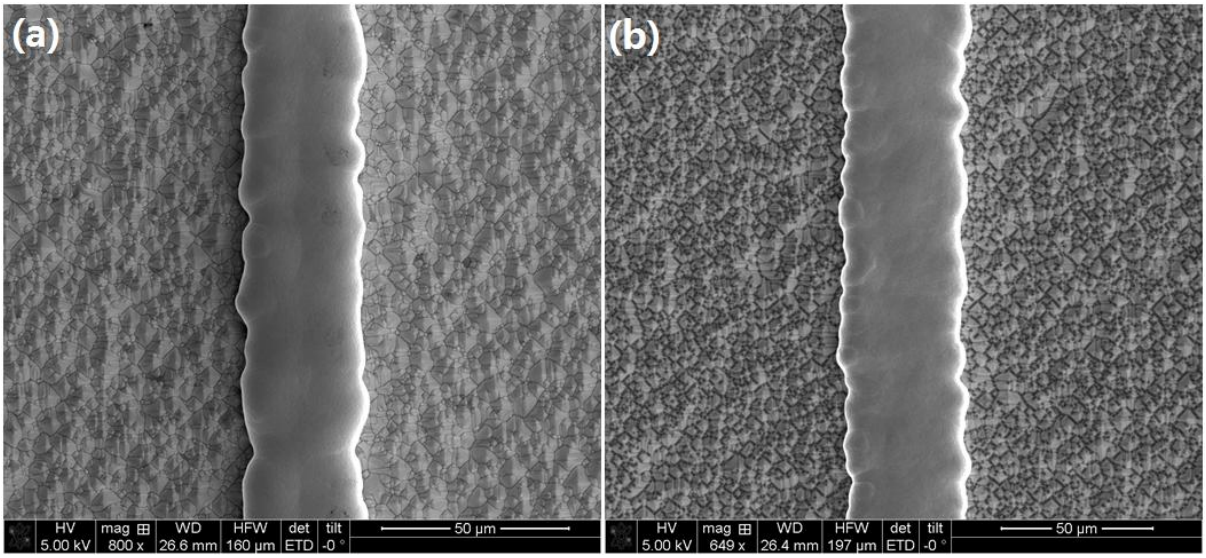

Figure 3-33. Uniform Cu plating arising from: (a) bias-assisted LIP Cu on n-type laser-doped grooves at 0.1 V bias voltage for 10 min; and (b) FIP Cu on the p-type laser-doped grooves at plating current density of 20 mA/cm^2 for 10 min.

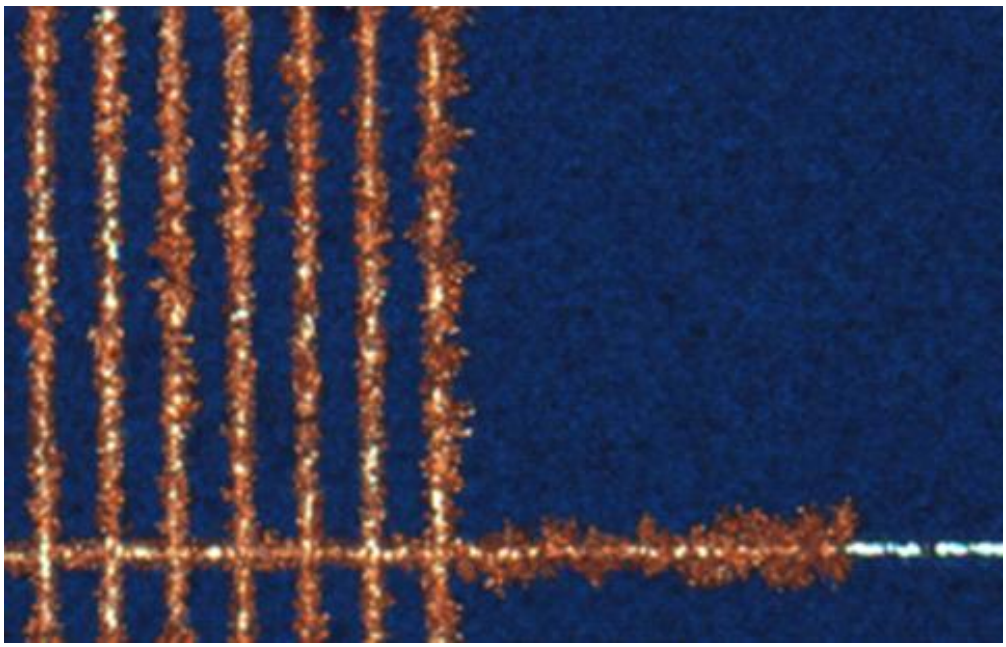

Figure 3-34. Optical microscope image showing dendritic crystallization of Cu arising from use of too high a plating current density. The Cu was plated at 120 mA/cm^2.

Unlike the light-induced current which is uniformly-generated in the emitter and flows laterally towards the n-type laser-doped grooves, the bias current in FIP flows through the n-type laser-doped grooves, and then through the wafer towards the exposed p-type laser-doped grooves. If the edges of the wafer are not well passivated with SiN_x, then the electrolyte can extend over them during single-side plating due to surface tension and plate to the non-passivated regions (see Figure 3-35). This plating at the wafer edges not only creates a path for shunting but also reduces the deposition rate of Cu at the p-type metal fingers. To address this issue it was necessary to adequately passivate the edges of the wafer during FIP.

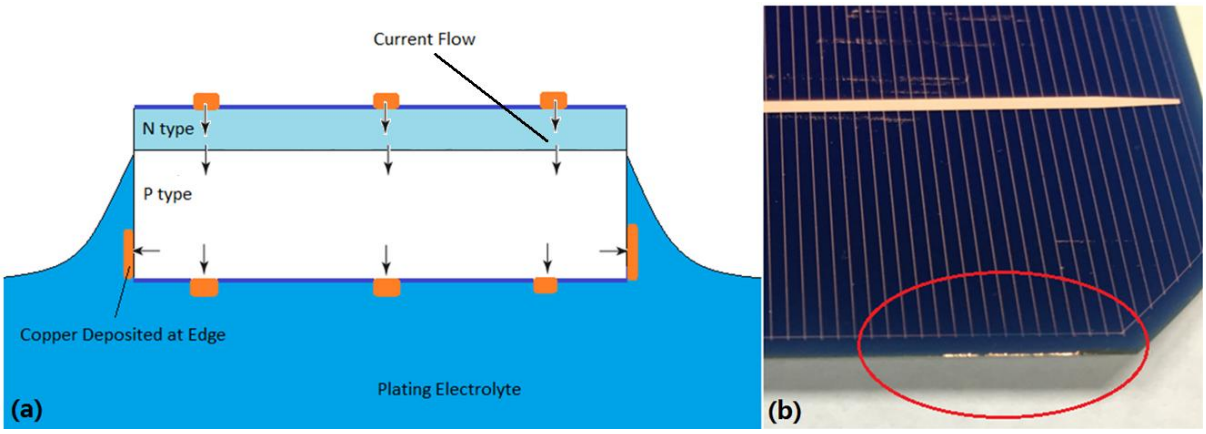

Figure 3-35. (a) Schematic diagram showing plating at the wafer edge during FIP due to lateral current flow; and (b) photo showing Cu plated at the edge of the wafer.

3.4.4 Conclusions

In this section, the requirements for effective plating of bifacial laser-doped Si solar cells were reported. It was concluded that there are two key factors that must be addressed in the plating process.

First, the laser-doped groove surfaces must be free of residue from doping and oxides before plating. Phosphorus laser doping will result in a residual PSG with lower laser-doping speeds resulting in heavier doping and more PSG residue at the surface which necessitates a longer HF deglazing time. On the p-type surface, if B spin-on sources are used for laser-doping, then a low laser-doping speed is required in order to avoid Schottky contacts. This low speed results in a residual BSG or BRL, which requires a longer deglazing time than required for the PSG residue. If plating is attempted without removing the residue, then the current applied to the rear of the cell is not uniformly distributed over the laser-doped grooves and dendritic ‘run away’ plating can occur. Consequently, it was concluded that an effective

strategy when some residue may remain was to plate with a low current density (e.g.,15 mA/cm^2) for a longer duration. Although the Ni nucleation may be non-uniform, the deposits eventually grow together to fully cover grooves. However, it should be noted that this strategy may have implications for contact adhesion which is discussed further in Chapter 5.

The second key factor is the correct selection of the plating current density and maintenance of the plating electrolytes. The plating current density for both Ni and Cu plating needs to be calculated based on the laser-doped opening area and should lie within the recommended plating rate range for the provided chemistry formulation. If it is possible that some residue remains on the laser-doped grooves, then it is best to plate Ni at a lower rate in the allowed range to reduce the possibility of 'run away plating' in the regions that are clear of residue. Similarly the plating rate of Cu needs to be well controlled so dendritic crystallization of Cu can be avoided. Plating rate control during FIP can be made more difficult if the edges of wafers are not well passivated. If the wafer edges are wet during plating then the current can flow through the edges and result in edge plating. This is most evident for Cu where the edge deposits are visually evident. Wafer edge plating can result in insufficient Cu deposition on the p-type laser-doped grooves and, if excessive, shunting. This edge plating should be avoided by insulating the exposed edges of the wafers from plating electrolyte. Finally, correct plating rate control also requires that the electrolyte should be carefully monitored due to the consumption of ions and evaporation of organic additives.

3.5 Bifacial Cell Fabrication

3.5.1 Introduction

Section 3.2.2 reported that Schottky contacts could result at p-type contact regions due to insufficient B doping. It has been shown that by reducing the laser doping speed and optimising the Ni/Cu plating process as explained in Section 3.4, Ohmic metal contacts can be achieved. However, in order to avoid the inversion layer shunting, which was concluded to contribute to the low *FF* reported in Section 3.2, a cell structure which employs a dielectric layer containing negative charges (e.g., AlO_x) was used in the further optimization of p-type bifacial solar cells since this negatively-charged layer induces an accumulation layer at the p-type surface [257-259]. This section reports on the fabrication of p-type bifacial laser-doped cells utilising the optimisations that have been discussed in the previous sections of this chapter.

3.5.2 Experimental

The process flow for the contact structuring and metallization was as shown in Figure 3-18 and Figure 3-29. In one group of cells (Group A), the p-type surface was passivated with 10 nm AlO_x/200 nm SiN_x and in the second group (Group B) of cells a 10 nm AlO_x/100 nm SiN_x layer was used. Both groups were passivated with 10 nm SiO_2 and 70 nm SiN_x on the n-type surface. The cell precursors were obtained from a screen-printed PERC production process, therefore, the rear SiN_x layer thickness was optimized for PERC cell contacting rather than for bifaciality. All cell precursors were obtained from a pilot line of an industry partner. The different rear passivation layers arose due to changing pilot line processing parameters and were not an intended variation in the experimental design (see Table 3-1).

Table 3-1. Cell precursor details and laser doping conditions used on the p-type surface for Groups A and B. Group 2012 represents the comparative details of the cell structure discussed in Section 3.2.3 and used in this section as a reference.

Groups	Front (n-type) Passivation	Rear (p-type) passivation	Laser doping conditions on p-type surface
Group A	10 nm SiO_2/70 nm SiN_x	10 nm AlO_x/200 nm SiN_x	Laser doping (0.5 m s^{-1}) **with B spin on source**
Group B	10 nm SiO_2/70 nm SiN_x	10 nm AlO_x/100 nm SiN_x	Laser doping (2 m s^{-1}) **without B spin on source**
Group 2012	10 nm SiO_2/70 nm SiN_x	10 nm SiO_2/ 200 nm SiN_x	Laser doping (0.5 m s^{-1}) **with B spin on source**

The p-type plating process was as described in Section 3.4 (i.e., Ni was plated with FIP for 5 min at a current density of 15 mA/cm^2 to achieve full coverage and then 10 μm Cu was plated (20 mA/cm^2) after 2 min Ni sintering.

Initial experiments involving the Group B cells resulted in large amounts of overplating. This problem was addressed by annealing the cells in a belt furnace (700 °C and 4600 mm s^{-1}) after both laser-doping steps had been performed. This step acted to densify the SiN_x and

recover some of the recombination loss due to laser-doping. Figure 3-36 shows PL images of a representative Group B cell after each of the steps. After laser doping, the damage due to the laser was obvious as the PL intensity was significantly reduced at the finger and busbar regions. The belt furnace annealing recovered some of the laser damage presumably due to hydrogen from SiN_x layer being released in the cell. After Ni and Cu plating, the PL intensity reduced slightly due to the metal contact recombination and shading from the plated grid, however it was still higher than immediately after laser doping.

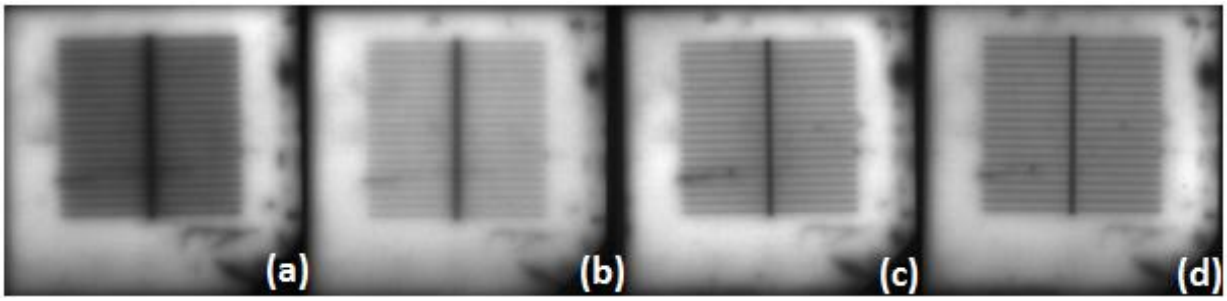

Figure 3-36. Photoluminescence images of a representation Group B cell: (a) immediately after laser doping; (b) after belt furnace anneal (700 ºC and 4600 mm s^{-1}); (c) after Ni plating; and (d) after Cu plating. All PL images were recorded with an exposure of 0.5 s at 5 V and are shown with the same intensity scale.

Sintering after Ni plating (for 2 or 5 min in a N_2 environment at 350 ^{0}C) was also attempted for the Group B cells in an attempt to increase the *FF* of the cells.

The fabricated cells were analysed using an in-house *I-V* tester in which the light intensity was calibrated to be 1-sun using a reference screen-printed cell. The measurement was performed with the n-type surface illuminated and the rear p-type metal grid in contact with the temperature controlled Cu block. The fabricated cells were also characterised using a Sinton Suns-Voc tester and spectral response measurements using QE/IOCE Measurement System from PV measurements Inc.

3.5.3 Results and Discussion

3.5.3.1 Group A

The *J-V* data recorded for Group A cells is presented in Table 3-2. The average cell efficiency and *FF* were 19.0% ± 0.2 and 0.75 ± 0.3, respectively. The high J_{sc} (40.3 ± 0.4 mA/cm^2) of the fabricated cells was due to the low metal shading fraction (estimated to be 4.1%) and the effectiveness of the rear AlO_x/SiN_x layer in trapping light in the device.

Although it is possible that the measured J_{sc} incorporated some albedo factor due to light passing out the rear of the cell and being reflected back into the cell by the Cu block, it was considered that this contribution was not significant as the Cu block was not highly reflective and most light transmitted through the cell was most likely either scattered or absorbed in the block.

The average implied V_{oc} of the cells before laser-doping and plating was 670 mV, 35 mV greater than the average actual V_{oc} values of 635 ± 3 mV. 57% of the V_{oc} reduction was attributed to the laser-doping processes, since after laser doping the iV_{oc} after laser doping anneal was 650 mV. The greatest V_{oc} loss occurred due to B laser-doping process. The V_{oc} of devices was also limited by some overplating on the n-type surface due to scratches in the SiN_x anti-reflection coating (ARC). Although the use of a thin SiO_2 layer under the SiN_x ARC is effective in minimising overplating [251], if the SiN_x becomes scratched in any way during the wafer handling, overplating can still occur. When metal plates to these scratched regions it contacts the lightly-doped emitter and, because there is limited shielding of the minority carriers at these sites, recombination can be enhanced at the surface and the V_{oc} is reduced. However, no overplating was observed for the p-type surface even though that surface was also protected by a SiN_x layer. It is proposed that over plating does not occur on the p-type surface because the current flows directly from the n-type to the p-type laser-doped regions during FIP and does not flow laterally along the p-type surface. In LIP, electrons are collected uniformly by the emitter and then travel laterally in the emitter towards the n+ regions. This means that high electron concentrations occur in the n-type Si emitter exposed by any defects in the ARC.

The cell efficiency was limited by the low *FF* of 74.7 ± 0.3. The average *pFF*, obtained from Suns-Voc measurements, was 80.0 ± 1.0 which is 2-3% lower than the ideal (n = 1) value estimated from the V_{oc} [260] which was 83.4%. It is also significantly lower than values of ~ 83.6% [74] that have been measured for n-type laser-doped plated cells with a full area Al BSF. This suggests that laser-damage, largely from the B laser-doping, is contributing to the low *pFF*.

The R_s values in Table 3-2 were estimated from the *J-V* curves measured at different light intensities [261]. The average R_s value of 0.89 ± 0.25 is higher than values of 0.28 Ω cm^2 measured for single-sided laser-doped cells in [214]. The contribution of spreading resistance

to R_s due to current crowding through the p-type bulk to the rear fingers was estimated to be 0.21 Ω cm^2 using the analysis described by Dullweber, et al. [262].

Table 3-2. Light *J-V* measurements for a batch of three laser-doped plated bifacial solar cells (Group A). The error bars represent the maximum and minimum values.

	V_{oc} (mV)	J_{sc} (mA/cm^2)	*FF* (%)	*pFF* (%)	*Efficiency* (%)	R_s (Ω.cm^2)
Average	635 ± 3	40.3 ± 0.4	74.7 ± 0.3	80.0 ± 1.0	19.0 ± 0.2	0.89 ± 0.25
Best cell	632	40.7	75.0	81.0	19.2	0.96

Figure 3-37 compares the *J-V* curves of the most efficient Group A and Group 2012 cells. Improved performance is evident on two aspects. First, the Group A cell has a higher J_{SC} due to the more optimized rear passivation dielectric stack containing AlO_x. Secondly, the *FF* of the Group A cell was increased from the value of 0.68 measured for the Group 2012 cell (see Section 3.2.3) to 0.75. The local ideality factor was significantly reduced over all injection levels (see Figure 3-38) and was ~ 1.5 for the Group A cell at *MPP*, compared to ~ 2.2 for the Group 2012 cell. The reduced local ideality factor was attributed to the interfacial AlO_x used for the Group A cell acting to eliminate inversion layer shunting due to non-uniform B laser doping. The ability of the AlO_x layer to eliminate the inversion layer contributions was also evident in the *QE* measurements. For the Group A cells, there was no significant difference in the EQE with and without bias light comparison (see Figure 3-39 and the discussion in Section 3.2). The improved rear surface performance of the cells passivated with AlO_x/SiN_x also contributed to the J_{sc} increase of 1.24 mA/cm^2 due to the higher *QE* response between 650 and 1100 nm over the cells in Group 2012 passivated with SiO_2/SiN_x.

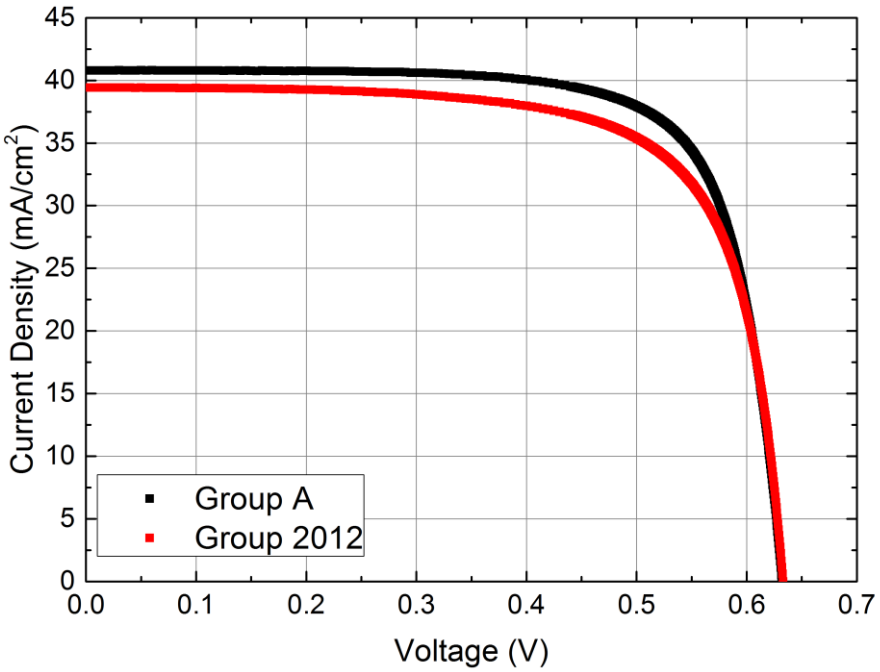

Figure 3-37. Comparison of *J-V* curves between the most efficient Group A (black) and Group 2012 (red) cells.

Figure 3-38 shows that significant higher order (n > 1) recombination still occurred in the Group A cells which limited the *FF* of the final cell. This problem was further investigated

using QSSPC and QSSPL and the results of these investigations are reported in Chapter 4 and also in Refs [263, 264].

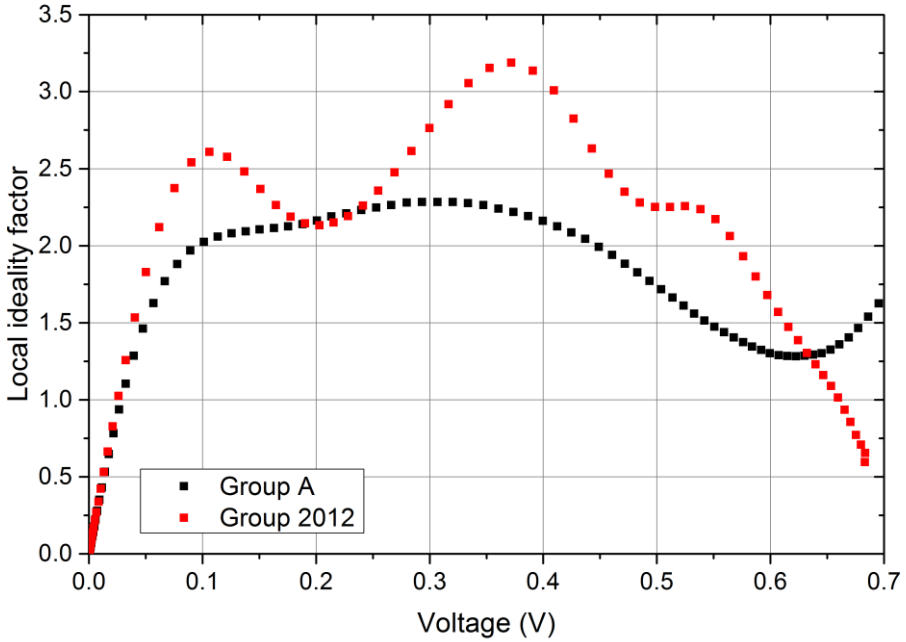

Figure 3-38. Local ideality factor curve of Group A (black) and Group 2012 (red) cells, Group 2012 cells shows more bumps and lumps in the curves suggested more recombination occurred in cells.

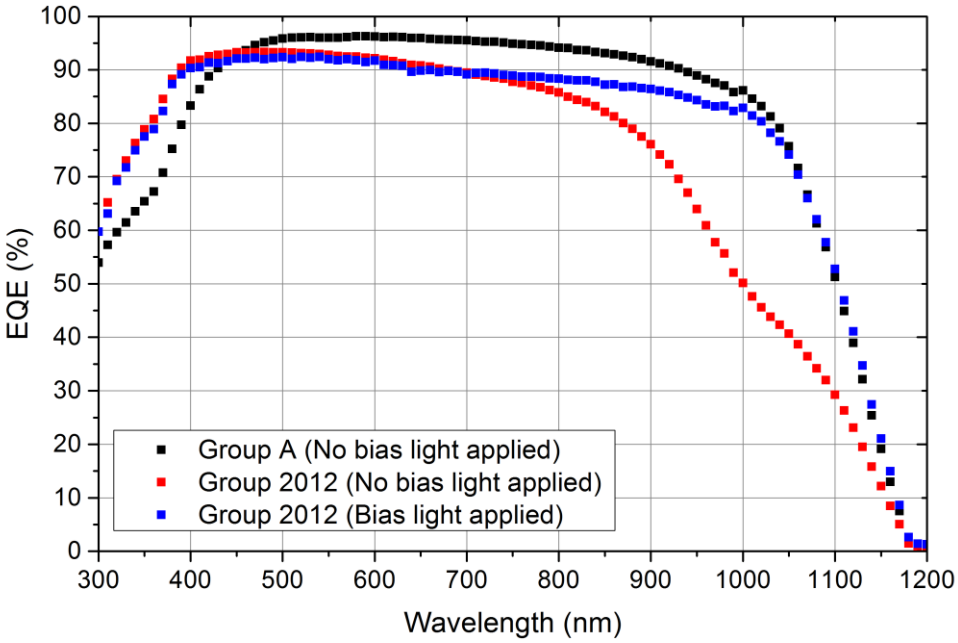

Figure 3-39. External quantum efficiency of representative Group A and 2012 cells showing the effect of bias light. The Group 2012 cell, which was passivated with SiO_2/SiN_x on the rear (p-type surface) experienced a reduced EQE in the 900-1200 nm wavelength range when no bias light was used.

The three major sources of loss incurred in solar cells are optical, resistive and recombination. The external quantum efficiency (*EQE)* and 1-reflection data for the most efficient Group A cell (19.2%) are shown in Figure 3-40. The loss analysis, which is based on the analysis reported in [265], visualises the optical and parasitic absorption losses at different wavelengths during the operation of a solar cell under one-sun AM1.5G illumination. The red region in Figure 3-40 represents the loss due to metal shading and front surface reflection, and the light blue region represents the losses due to the escape of long wavelength light from the front surface. The dark blue region represents the light, which is absorbed by the cell, but does not result in the generation of current (i.e., losses due to absorption of light by the metal or the SiN_x ARC). These losses are referred to as non-perfect internal quantum efficiency (*IQE)* losses.

By using the loss analysis method described in [266], the power loss of each mechanism was quantified and the distribution of power loss at one-sun maximum power point (*MPP)* is illustrated in Figure 3-41 and presented in detail in Table 3-3. The dominant loss in the cell is the forward-bias current at *MPP* which contributes 35% to the total loss, followed by series resistance at 20% and metal shading at 18% of the total power loss. The total power loss for the analysed cell was 6.8 mW /cm^2 which was slightly less than the 7.3 mW/cm^2 estimated for the 18.1% efficient screen-printed cell analysed by Aberle et al. [266]. However, although the plated cell demonstrated reduced optical losses compared to the screen-printed cell, its diode saturation current losses and resistive losses were increased.

The optical losses of the plated laser-doped cells can be further reduced by minimising damage to the SiN_x during processing and, with shorter HF deglazing durations, overplating can be eliminated. Additionally, the use of lasers which do not create so much lateral damage will allow narrower plated lines which will further reduce optical losses.

Reduction of recombination losses requires that the laser-damage incurred with the B laser doping process is reduced. This is perhaps the most challenging improvement as the experiments reported in Section 3.2.3 demonstrated the need to form a heavily-doped surface layer for ohmic contact to the plated metal. This necessitated a slower laser speed which is responsible for generating the lateral laser damage due to the deep melting and re-crystallization of Si during B laser doping. There are also recombination losses that can be eliminated by the reduction of overplating. Although these losses are not significant for cells which have only n-type laser-doped plated contact grids [74] , as evidenced by *pFF* values

exceeding 82%, the longer HF immersion duration required for these bifacial cells in order to etch the BRL/BSG caused additional thinning of the front surface SiN_x and hence more overplating. This problem could be addressed by using a more dense layer of SiN_x (e.g., by using direct PECVD to deposit the SiN_x [251, 267].

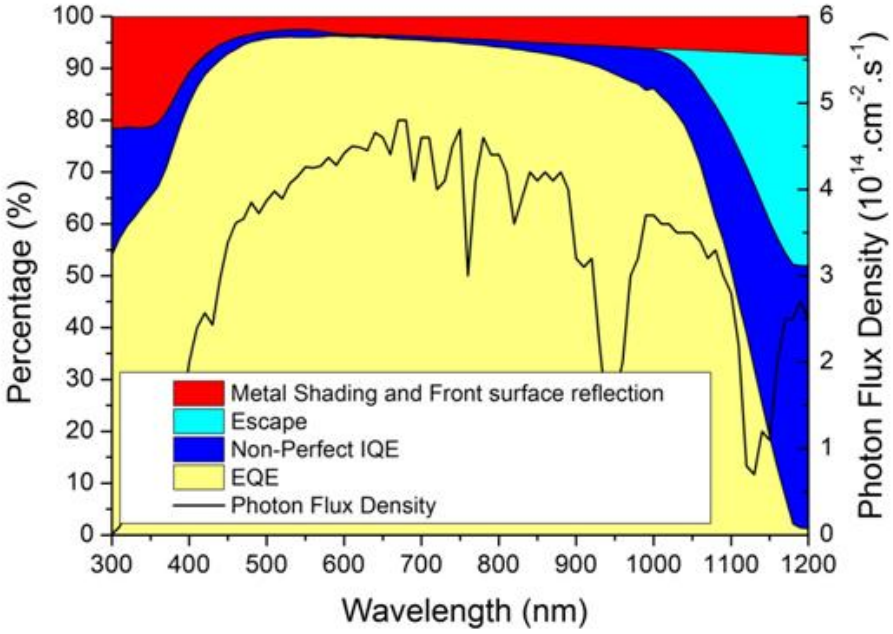

Figure 3-40. *EQE* and 1- Reflection of the most efficient bifacial solar cell in Group A. The dark blue region indicates parasitic absorption and the red region indicates the optical loss due to front-surface reflection and metal shading. The loss analysis assumed an AM 1.5G illumination spectrum, the photon flux of which is shown superimposed on the *EQE* data.

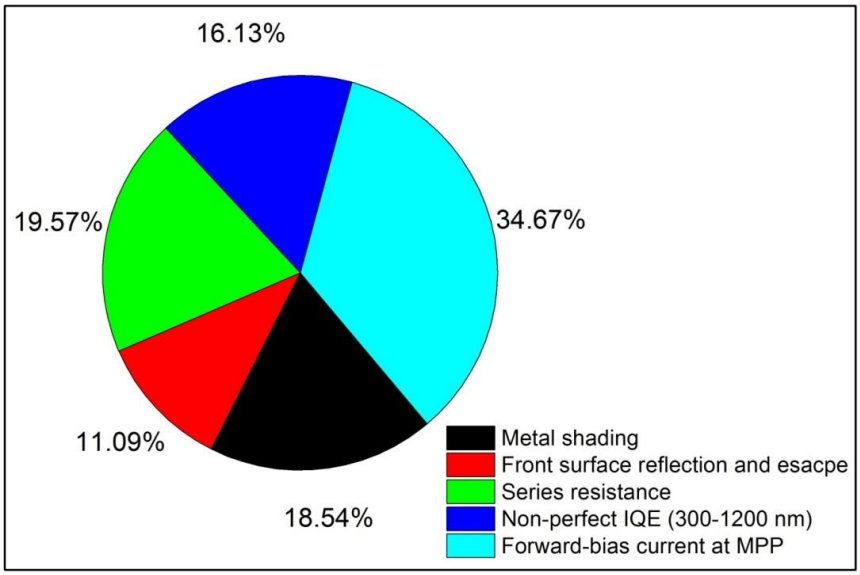

Figure 3-41. Percentage distribution of power losses at *MPP* under one-sun AM1.5G illumination.

Table 3-3. Summary of the loss mechanisms of the most efficient bifacial cell in Group A at *MPP* under one-sun AM1.5G illumination.

Loss Mechanism	Current density loss (mA/cm²)	Power loss (mW/cm²)	Screen print cell power loss (mW/cm²)
Optical loss [1] (300-1200nm)		**1.9**	**2.7**
Metal Shading	2.3	1.2	1.8
Front surface reflection and escape	1.4	0.70	0.90
Resistance losses [2]		**1.3**	**0.80**
Series Resistance		1.3	0.70
Shunt Resistance		0	0.10
Recombination losses		**3.4**	**3.8**
Non-perfect IQE [3](300-1200nm)	2.0	1.1	2.7
Forward-bias current at MPP [4]	n.a.	2.3	1.1
Total losses		**6.6**	**7.3**

[1] The optical loss is extracted from the reflectance measurement by PerkinElmer. The metal shading is calculated by: $J_{Shading\ loss} = \sum(\frac{(A_{finger}+A_{busbar})}{A_{total}} \times 100\% \times J_{wavelength})$

[2] The series resistance is estimated from *J-V* curves measured at different light intensities, the power losses due to resistance are calculated by: $P_{series} = R_s J_{mpp}^2$ **and** $P_{shunt} = \frac{V_{shunt}^2}{R_{shunt}}$, $Where\ V_{shunt} = V_{mpp} + R_s J_{mpp}$

[3] The non-perfect *IQE* loss includes the other optical losses inside the solar cell (parasitic absorption in the SiN_x and metal).

[4] The power loss in the diode due to forward-bias current is calculated by: $P = V_{shunt}(J_{sc} - J_{mpp})$.

3.5.3.2 Group B

Initial experiments were performed to determine whether laser doping through the AlO_x/SiN_x dielectric stack without using additional B source could dope the contact region sufficiently to avoid the formation of Schottky contacts. Figure 3-42 shows the Suns-Voc curve for a representative Group B cell (compared to that measured for a Group A cell and a cell that was laser-doped without either AlO_x or B source). The laser speed used for the Group B cell and the positive control which used neither AlO_x or B source was 2 m s^{-1}. This result

indicated that sufficient p-type doping was possible if the AlO_x was used as the dopant source in the absence of applied B source, confirming the findings reported in by [226, 227].

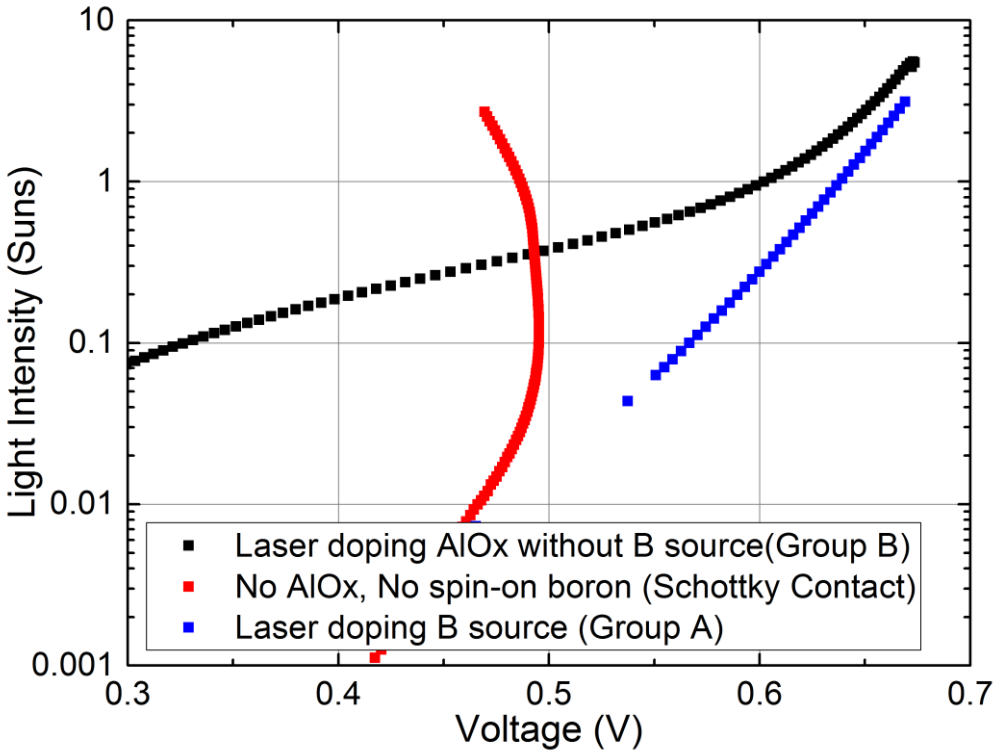

Figure 3-42. Comparison of Suns-Voc measurements for cells laser-doped through AlO_x/SiN_x without B source (black; Group B), without either AlO_x or B source (red) and laser-doped through AlO_x/SiN_x with a B source (blue; Group A).

Table 3-4 lists the *J-V* measurements for the Group B cells. Although a V_{oc} > 630 mV was achieved by including the belt furnace anneal, the *FF* was limited to 0.75. Sintering did not significantly improve the *FF* and, when the sintering duration was increased to 5 min, both the V_{oc} and *pFF* were reduced.

Figure 3-43 graphs the local ideality factor curves for Group B cells with different thermal treatments and a comparative Group A cell. The belt furnace annealing step after laser doping acts to reduce non-ideal recombination at low injection, however sintering appears to introduce new sources of recombination presumably due to excessive Ni penetration into the cell. However, all treatments (belt furnace annealing and sintering) appear to result in a similar ideality factor of 1.7-1.9 at 0.5 V (i.e., near MPP), thereby limiting the *pFF* of cells.

Table 3-4. Light *J-V* measurements of cells with laser-doping AlOx bifacial solar cells (Group B) with different thermal treatments

Thermal treatments after belt furnace anneal	V_{oc} **(mV)**	J_{sc} **(mA/cm^2)**	***FF*** **(%)**	***Efficiency*** **(%)**	***pFF*** **(%)**
No Sintering	638	39.3	0.74	18.4	78.1
2 minutes FIP Ni Sintering	637	39.1	0.75	18.7	79.4
5 minutes FIP Ni Sintering	631	39.1	0.73	17.9	78.1

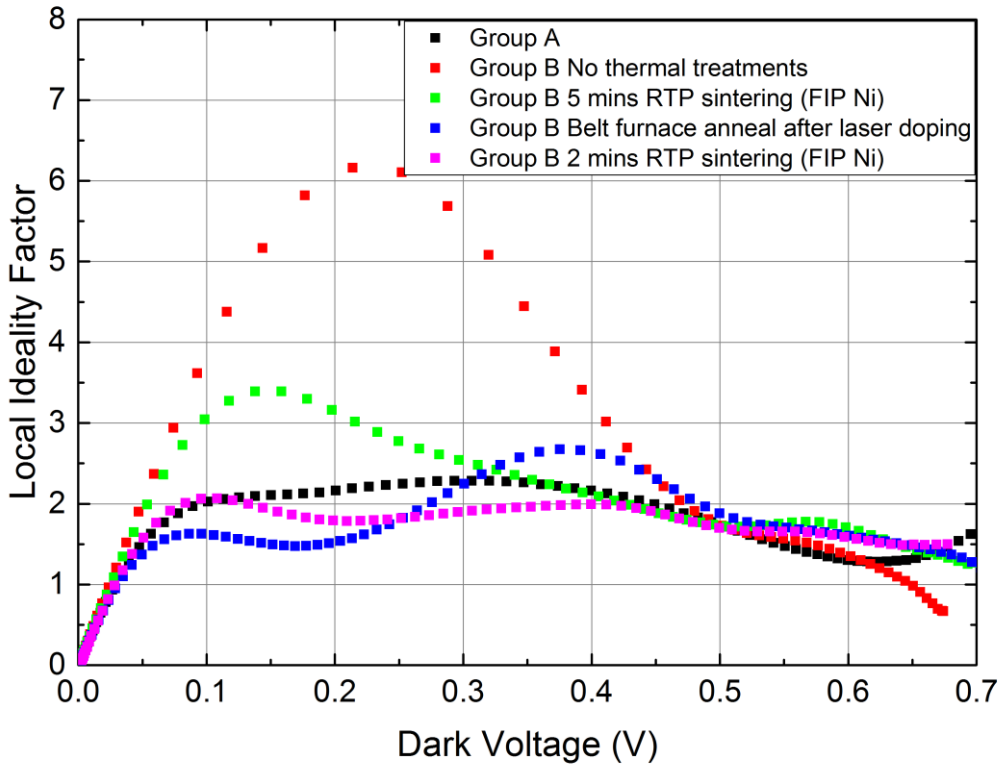

Figure 3-43 Injection dependent local ideality factor for a representative Group A cell and Group B cells with different thermal treatments.

Figure 3-44 compares more closely the injection-dependent local ideality factor of different cell structures and processing sequences. The increase in *FF* from 0.68 to 0.75 (for Group A and B cells) can be attributed to a reduction of the local ideality factor from 2.25 (2012) to 1.75 (Group A and B) at MPP (0.5 V). Shown for comparison in Figure 3-44 is the injection-dependent local ideality factor of an n-type bifacial cell with a B-diffused emitter (passivated with AlO_x/SiN_x) and phosphorous-doped BSF (passivated with SiN_x), where the p-type laser doping was achieved by laser scribing without B source through the AlO_x/SiN_x [268]. The n-type cell was bifacially-plated using the same process as was used for the p-type cells. The local ideality factor of the n-type cell was significantly reduced from that of the p-type cells at the MPP (1.25), enabling that cell to achieved a *pFF* of 81.66. The reduced non-ideal recombination was attributed to reduced laser damage when the laser-doping is performed through uniformly doped (diffused) surfaces.

Clearly the laser-doping process contributes a source of non-ideal recombination with the extent of damage being less if laser-doping is being performed through a diffused layer. However, it is more complex and costly to fabricated cells with both a diffused emitter and

BSF. Consequently, it would be useful to understand how to mitigate the laser damage. In Chapter 4, injection dependent QSSPL and QSSPC studies are reported which aimed to investigate how different processing steps introduce non-ideal recombination in bifacially laser-doped cells. It is shown that the changes in local ideality factor can arise both from laser-induced defects and from bulk Si effects where the thermal and illumination effects from the processing places defects/impurities in the Si into different recombination states.

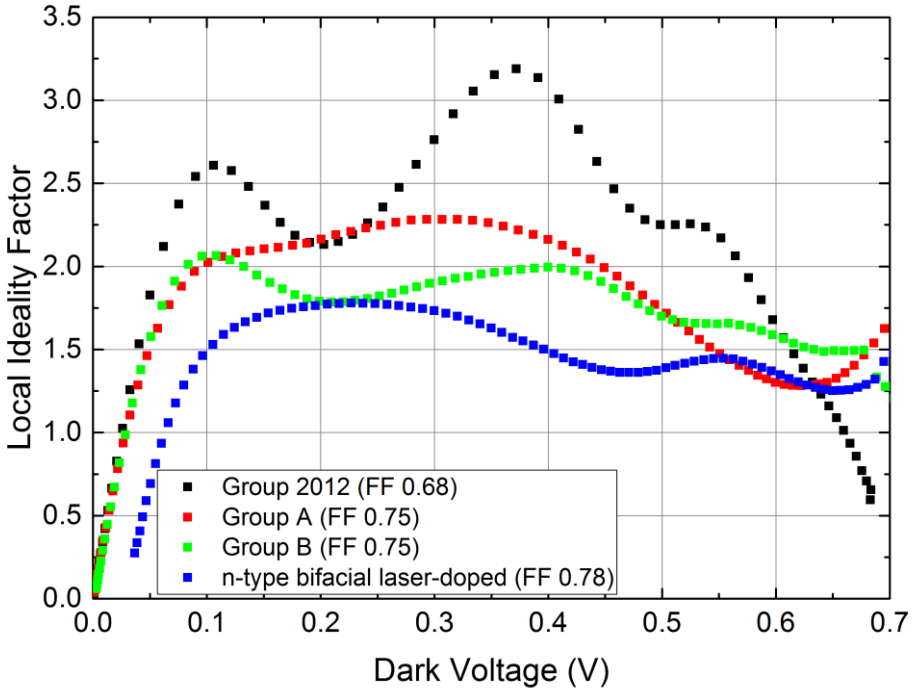

Figure 3-44 Injection dependent local ideality factors for representative 2012, Group A, Group B cells and a bifacially laser-doped n-type cell. The n-type cell data are from [268].

3.5.3.3 Group B Laser Doping Improvements

In an attempt to reduce the laser damage when laser-doping using AlO_x without added B source, use of a faster laser speed was attempted as Hallam et al. have reported that less defects form with faster laser speeds [226]. P-type laser-doping at a speed of 7 m s^{-1} can result in very smooth laser-doped surfaces (see Figure 3-24). However, the adhesion of the plated fingers was extremely poor (see Figure 3-45), and the plated Ni layer peeled off during the 2 min Ni plating process. This limited further improvement of the cell efficiency. It also served to highlight a further limitation of the bifacial laser-doping and plating process. Although the finger adhesion was exceptionally poor when fast laser scribing through the AlO_x/SiN*x* was trialled, adhesion was also not strong for the other cells. Although fingers

typically remained adherent to the cell surface for the other cells that were fabricated thereby permitting cell characterisation, the resulting cell busbars were not solderable. This means that alternative methods of interconnection would be required. Consequently, a more detailed study of contact adhesion was performed and the results of this study are reported in Chapter 5.

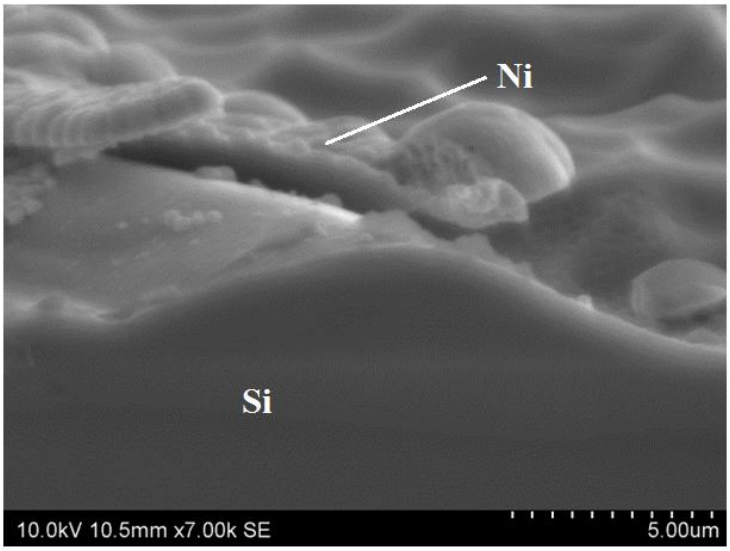

Figure 3-45 Scanning electron microscope image showing the poor adherence of the plated Ni to laser-doped grooves through a AlO_x/100 nm SiN_x dielectric stack where a laser speed of 7 m s^{-1} was used.

3.6 Conclusions

This chapter reports on the refinement of FIP, a method that enables metal to be plated on p-type Si regions of a p-n junction solar cell by forward biasing the junction. Like bias-assisted LIP, the cell surface to be plated is immersed in plating electrolyte and a bias current is applied through an electrode in contact with the dry surface of the wafer. It is demonstrated that similar plating rates can be achieved with FIP as can be achieved using bias-assisted LIP suggesting the potential feasibility of large scale production. Through the use of FIP and bias-assisted LIP, p-type laser-doped bifacial Si solar cells were fabricated with an energy conversion efficiency of 19.2%. This achievement required the solution of three key problems.

First, the need to use a low laser speed for p-type laser doping (with a B spin-on source) to form sufficiently heavily-doped *p*+ regions for ohmic contact resulted in the formation of a BRL or residual BSG in the laser-doped grooves. This residue was difficult to remove with

short HF immersion durations. Use of longer HF immersion times was undesirable as the SiN_x layers were etched increasing the likelihood of over-plating. To address this issue, it was found that longer Ni plating durations followed by sintering were required to achieve full coverage and form ohmic contacts.

The second problem, which was incurred with experiments pre-dating this thesis project, was the inversion layer shunting. This arose due to the positive stored charge in the SiN_x dielectric attracting minority carrier electrons to the surface which could leak through shunting paths present as a result of non-uniform doping at the laser-doped grooves. By use of an interfacial AlO_x layer under the SiN_x, the *FF* was increased from 0.68 to 0.75, this increase being largely achieved through a decreased local ideality factor at *MPP*.

The use of the low laser speed for B laser doping required for ohmic contact resulted in significant laser damage. To address this problem, laser-doping using AlOx as the dopant source was trialled. It was demonstrated that ohmic contacts could be achieved using this process, however although the visible laser damage was reduced, the *pFF* was not significantly increased suggesting that laser damage was still occurring. Although reduced laser damage was possible by increasing the laser speed, the resulting plated grids was insufficiently adherent to complete and characterise cells.

However, the experiments reported in this chapter highlighted two key problems for this new bifacial laser doping and plating process. First, the high local ideality factor at MPP limits the *FF* of cells. Even though visible laser damage was reduced through the use of AlO_x as the dopant source, the *FF* remained limited by non-ideal recombination occurring in the cell. Although some of this recombination was clearly introduced by the laser doping, it was not clear whether some of introduced recombination may have been arising from changes in the recombination states of defects in the bulk of the wafer. As surface recombination is minimised then the effects of recombination in the bulk can become more evident in the injection-dependent effective minority carrier lifetime [269]. This possibility is investigated further in Chapter 4, where it is shown that some cell processing steps (e.g., belt furnace annealing and illumination during LIP) can change the recombination state of B-O complexes.

A second problem that needs to be addressed is improved contact adhesion. Although laser damage can be reduced by increasing the laser-doping speed (through AlO_x/SiN_x) to achieve

shallower melting of the Si, the resulting laser-processed grooves are very smooth and the plated metal adheres very weakly to the surface. Surface roughness is known to play an important role in plated metal adhesion [256, 270]. Consequently, Chapter 5 of this thesis reports on a study which aims to understand better what is required for strong plated metal adhesion. In that chapter a new method for testing the adhesion of fingers is reported, and correlations between finger and busbar adhesion are examined in order to increase the understanding of the role of the Si surface and the plating process and chemistry on plated metal adhesion to Si solar cells.

CHAPTER 4
USE OF QSSPL AND QSSPC TO MONITOR PROCESS-INDUCED DEGRADATION

4.1 Introduction

4.1.1 Motivation

The injection level dependence of bulk Shockley-Read-Hall (SRH) recombination centres can lead to a reduced *FF* for cells, providing the recombination losses associated with the emitter and surfaces are sufficiently small to allow the bulk lifetime to dominate [269]. Due to the increased adoption of emitters with low recombination current densities and improved surface passivation, *FF*s observed for rear locally-passivated B-doped Cz cells may now be impacted by SRH recombination centres in the bulk of the wafer with asymmetric capture cross-sections, such as B-O complexes [271-274], and the state in which various processing steps leaves them. In this chapter, the injection-dependent local ideality factor, *m*, estimated from QSSPC and QSSPL measurements using the analysis presented in [275, 276], is used to investigate the effects of various processes on the recombination state of B-doped Cz wafers with a ~ 100 Ω/□ P-doped emitter and bifacially passivated with SiN_x deposited by PECVD. Of particular interest are changes due to light-soaking and regeneration [65], laser doping, and high-temperature (belt furnace) annealing. Boron-oxygen complexes are reported to have a strong asymmetry with respect to capture of electrons and holes [271-273], so it is reasonable to assume that these complexes may result in elevated *m* values at injection levels between the *mpp* and V_{oc} and hence may contribute to reduced *FFs* as much as suggested for interstitial Fe in [269]. Initial studies aimed to establish whether B-O defects could be activated in cells during cell processing (e.g., during LIP) and to determine their contribution to the values of *m*, and *FF*. Subsequent investigations applied a similar analysis to cells fabricated on the same wafers after P and B laser doping and high-temperature belt furnace annealing.

It has been shown in [263], which reports results of early experiments from this study, that analysis of injection-dependent effective minority carrier lifetimes, τ_{eff}, measured by a combination of QSSPL and QSSPC, can be used to identify different recombination states of

B-O complexes, provided that recombination at the wafer surfaces is minimised. The introduced recombination due to light soaking was modelled as a single SRH recombination centre corresponding to the deep-level B-O complex at E_c - E_t = 0.41 eV [271, 272], with the analysis resulting in an estimate for the electron:hole capture cross-section ratio (σ_n/σ_p) of ~14 for the introduced defect (compared to a value of 9.3 reported in [272]). However, in the study reported in [263], the wafers were not symmetrically-passivated, so it was difficult to definitively separate surface effects from bulk effects.

In later experiments, injection-dependent measurements of τ_{eff}, obtained using both QSSPL and QSSPC, were used to estimate the σ_n/σ_p ratio of the B-O complex following the steps of light soaking and regeneration [62, 65] in symmetrically-diffused p-type Cz wafers. These studies considered differences that may occur with different passivation dielectrics, especially SiN_x layers deposited by PECVD and thermally-grown SiO_2 layers. Nampalli et al. [70] have shown that a hydrogen source and illuminated thermal annealing are both required for stable regeneration of the deep-level B-O defect. Consequently, it was hypothesised that a SRH recombination analysis of injection-dependent τ_{eff} may be able to provide further evidence for the requirements of a hydrogen-containing dielectric to achieve stable regeneration. In initial experiments, where wafers passivated with thermal oxide underwent a rapid thermal anneal (RTA), the oxide surface passivation was degraded, making it difficult to discern changes occurring in the bulk due to light soaking and regeneration. Consequently, in later experiments a rapid thermal anneal (RTA) was performed before the thermal oxidation step. This resulted in low surface recombination velocities, thereby enabling changes in bulk recombination to be observed in the injection-dependent τ_{eff}. As reported in [263], the SRH defect was modelled using both the pre-light-soaked state and the regenerated state as the initial state, with the latter analysis providing insights as to whether the regeneration process changed the recombination properties of defects other than the B-O defect.

Although this work was motivated by the observation of lower than expected *FFs* in plated bifacial laser-doped cells on B-doped Cz wafers (see Chapter 3), it may be relevant to all cells where surface recombination losses are minimised to an extent that the effects of bulk recombination may begin to impact the *FF* of completed devices.

4.1.2 Objective

The primary objective of this work was therefore to develop a method by which the nature of recombination occurring within cells could be monitored during the fabrication process. Although each of QSSPL and QSSPC have been proposed for this function previously (e.g., see [271, 272, 275, 277]), in this study, data from both PL and PC measurements was used with a view to being able to possibly extend the analysis to metallised samples which would allow recombination changes in the bulk of the wafer to be monitored during a wider range of processing steps. Earlier studies have demonstrated that the recombination properties (e.g., σ_n/σ_p) of dominant SRH defects can be estimated from injection dependent τ_{eff} measurements by assuming that a processing step introduces a single SRH defect of a known energy level [271, 272].

Secondary objectives of the study were to: (i) compare the accuracy of the σ_n/σ_p values estimated using both QSSPL and QSSPC; and (ii) investigate the role of different dielectrics in the recombination properties of B-O complexes during the processes of light soaking and regeneration. The use of QSSPL in addition to QSSPC can enable measurements over the injection level range of ~ 2×10^{11} to ~10^{17} cm^{-3} which is larger than would be possible with the use of QSSPC alone.

4.2 Theory

4.2.1 QSS PL and PC Measurements

QSSPC and QSSPL are two commonly-used carrier lifetime measurement techniques used in the study of Si PV. This section will cover the basic theory for both measurement techniques. The Sinton lifetime tester from Sinton Instruments is currently used by almost every Si solar cell research institute and manufacturing company (see Figure 4-1).

Figure 4-1. The WCT-120 lifetime tester from Sinton Instruments [278]

Carrier lifetime measurement in semiconductors is well understood and can be achieved using various methods (e.g., microwave reflectance, capacitive coupling and the use of coils that inductive couple to a semiconductor wafer's conductivity) [279]. The Sinton lifetime tester, which was used for the QSSPC measurements performed in this thesis, determines the lifetime from inductively-measured photoconductance [223, 224]. It uses a flash lamp as the illumination source and monitors the lamp's intensity with a photodiode. The change in conductivity is measured using an induction coil to yield an estimate of the injection level (or excess carrier concentration), Δn, which is related to τ_{eff} by:

$$\tau_{eff} = \frac{n(t)}{G(t) - \frac{d(\Delta n)}{dt}} \qquad \text{Eq. } 4-1$$

where $G(t)$ is the generation rate and t is time. Eq. 4-1 represents the generalised form which can be simplified for the individual cases of transient, steady state and quasi-steady state measurements [222].

The simplest measurement involves exciting carriers with a single pulse of high intensity light, and then after the excitation is removed wafer conductivity is measured as a function of time. Although τ_{eff} can be estimated directly from the PC decay with no required knowledge of G in this so-called transient measurement, it requires that electrical carriers survive long

enough for sufficient measurement data to be collected. This is not always the case for samples where τ_{eff} is small (e.g., multi-crystalline materials or samples where the surfaces are not well passivated).

Fast decay of PC can be addressed by continued illumination. Under steady state conditions, *G* is constant during the measurement and all carriers that are generated must therefore recombine (i.e., $G = R$). In this mode, Δn is approximately uniform across the wafer, therefore resulting in the condition: [224]:

$$\tau_{eff} = \frac{\sigma_L}{J_{ph}(\mu_n + \mu_p)}, \qquad \text{Eq. } 4-2$$

where:

$$\sigma_L = \Delta n q(\mu_n + \mu_p) W \qquad \text{Eq. } 4-3$$

However, with steady state measurements it is difficult to achieve a sufficiently large range of illumination intensities without significantly increasing the sample temperature [280]. For this reason, the QSS approximation was introduced. With QSS measurements, the light pulse intensity is gradually reduced during the conductance measurement (i.e., *G* decays as a function of time), the assumption being that the sample approaches 'steady state' conditions as *G* is reduced from a maximum value to zero. With this method, the PC can be measured at different light intensities.

Quasi-steady state measurements can be performed with less complex equipment as there is no need for rapid switching of electronics (e.g., switching off the light before recording conductance) or temperature control (e.g., for sample cooling). The range of the τ_{eff} measurement is only limited by the signal strength of the sample, which extends the use of the QSS method to lower quality materials. The iV_{oc} can be calculated for p-type wafers from Δn using:

$$iV_{oc} = \left(\frac{kT}{q}\right) \ln\left(\frac{\Delta n(N_A + \Delta n)}{n_i^2}\right) \qquad \text{Eq. } 4-4$$

where k is Boltzmann's constant, T is the absolute temperature, N_A represents the acceptor dopant density of the wafers used, and n_i is the intrinsic carrier concentration of Si (9.65×10^9 cm^{-3} at 25 °C) [221].

Quasi-steady-state PL is a sensitive technique for measuring the injection level dependent effective lifetime for Si solar cells [281] , and has been used to measure lifetimes at low injection ($\Delta n < 10^9$ cm^{-3} [282]). At these injection levels, PC measurements are impacted by carrier trapping [283], depletion region modulation (DRM) [284, 285] and barriers to eddy currents [263, 286, 287]. Therefore, through the use of QSSPL, more accurate measurement at low injection levels can be achieved. The QSSPL system used for measurements in this chapter consisted of a modified Sinton stage, whereby a Si photodiode had been placed inside the coil area. This modification permitted the simultaneous measurement of PC and PL from the same area of the wafer. A 1.5 W 625 nm LED array was used for illumination, as the light pulse could be controlled temporally, enabling better signal-to-noise measurements to be acquired.

The PL intensity is related to the average excess carrier density through the Van Roosbroeck form [275, 288]:

$$I_{PL,rel} \propto np \qquad \text{Eq. } 4-5$$

$$I_{PL,rel} = A_i B(N_D + \Delta n)\Delta n \qquad \text{Eq. } 4-6$$

In Eq. 4-6, A_i is a scaling factor that accounts for re-absorption within the sample, B is the radiative recombination coefficient, and N_D is the doping concentration of the bulk Si. The value of Δn can then be calculated from the PL intensity using:

$$\Delta n = -\frac{N_D}{2} + \sqrt{\left(\frac{N_D}{2}\right)^2 + \frac{I_{PL,rel}}{A_i B(T)}} \qquad \text{Eq. } 4-7$$

where Ai is determined by minimisation of the determined lifetime between PL and PC in an injection range where the PC was not impacted by the previously mentioned artefacts.

4.2.2 Local Ideality Factor

The illuminated *I-V* curve is typically used to evaluate the performance of a Si solar cell after metallization (i.e., completed devices). However, this measurement requires completed devices and it is difficult to discern diode properties due to the light-generated current being orders of magnitude greater than the recombination current. Therefore, dark *I-V* curves are frequently used to monitor/probe diode properties of solar cells. Dark *I-V* curves are recorded in the dark (i.e., no light-generated current) with a bias voltage being used to sweep between 0 to 1.2 V to simulate the operating voltage range of the cell. Diode properties assessed through dark *I-V* measurements are therefore not affected by variations in the light intensity [281]. Furthermore, the voltage drop due to cell R_s is small due to the much smaller current magnitude. The measured *I* for a dark *I-V* measurement is given by:

$$I = I_{01}\left[exp\left(\frac{V - IR_s}{V_T}\right) - 1\right] + \frac{V - IR_S}{R_{sh}} \qquad \text{Eq. } 4-8$$

Since the slope of the dark *I-V* curve recorded for devices typically varies with *V*, the local ideality factor, *m*, can be defined as:

$$m = \frac{1}{V_T}\left[\frac{dV}{d(lnI)}\right] \qquad \text{Eq. } 4-9$$

Since there is an exponential relationship between *V* and *I*, after converting *I-V* data to an *m-V* curve, differences in the diode properties of cells become more evident. For example, local shunting arising from either mechanical scratches or recombination defects are emphasised by this transformation. Hameiri et al. demonstrated that *m* could also be determined from PC (carrier lifetime) measurements [276, 289].

$$m = \frac{1}{V_T}\left(\frac{d(ln(G))}{d(iV_{oc})}\right)^{-1} = \frac{q}{kt}G\left(\frac{d(iV_{OC})}{dG}\right) \qquad \text{Eq. } 4-10$$

where,

$$iV_{oc} = \frac{kt}{q} l\, n\left(\frac{np}{n_i^2}\right) \qquad \text{Eq. } 4-11$$

Figure 4-2 shows the measured effective lifetime curve and calculated local ideality factor curve of a p-type wafer. Hameiri et al. [276] demonstrated that a change in defect state can be observed as a shifting of the humps and bumps in the m-iV_{OC} curve. Taking this as a starting point for this chapter, calculations of m from effective lifetime measurements for sequential process steps were used to provide an understanding of changes in the recombination properties of defects.

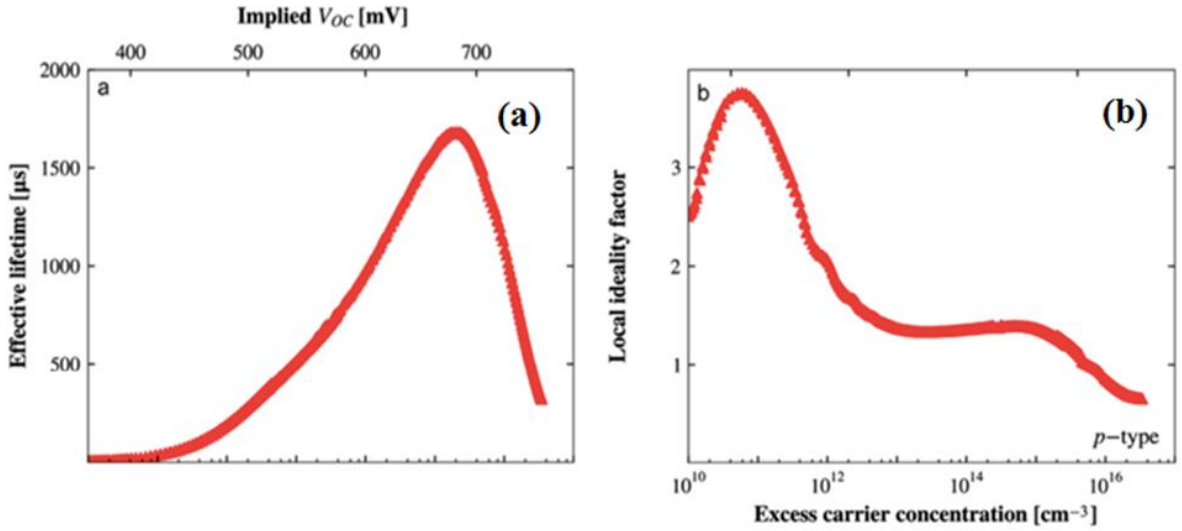

Figure 4-2. (a) Measured effective carrier lifetime; and (b)calculated local ideality factor curve (from [276]).

4.2.3 Light-induced Degradation and Regeneration

Photovoltaic modules are expected to be stable for at least 25 years, however exposure to light can impact the performance of p-type Si solar cells [290-292]. Figure 4-3 shows how τ_{eff} (graphed as a function of Δn) can be degraded with illumination for B-doped Cz wafers. Not only is the magnitude of τ_{eff} significantly reduced for all values of Δn, but the slope of the curve is also changed at different Δn. This leads to changes in the m-V curve. This result highlights the possibility that the recombination properties of other shallow and deep level defects might also be changed during different cell processing steps (e.g., thermal treatments or perhaps even during LIP or the applied bias currents of FIP). If surface recombination is carefully minimised by the application of appropriate dielectric coatings, then changes in the bulk recombination at defects may influence the τ_{eff} (Δn) and hence also the m-V curves which can be recorded through the use of QSSPC and QSSPL.

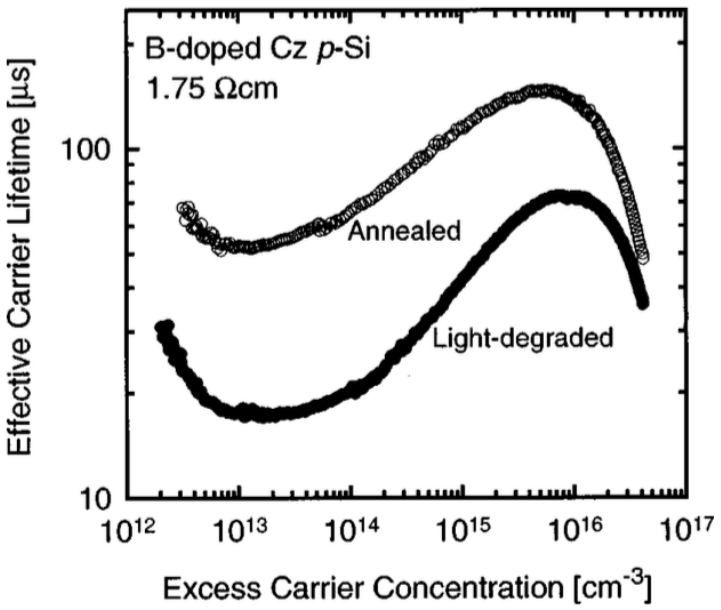

Figure 4-3. Measured τ_{eff} as a function of excess carrier concentration before and after light degradation for B-doped Cz Si wafers showing different slopes which would result in a change in a generated *m-V* curve (from [271]).

Boron-oxygen defects are an important impurity type for p-type Si solar cells, due to their ability to significantly reduce the performance of cells in the field. There are many theories proposing mechanisms for the formation of the recombination-active B-O complex (e.g., see Refs [61, 292-299]). Oxygen impurities, introduced during Cz ingot pulling, can become complexed with B dopant atoms during processing steps to form complexes which can become recombination active after different cell processing steps or in the field on exposure to light.

Recent research shows that these B-O defects are the recombination centres mainly responsible for lifetime degradation on exposure to light. The dominant recombination-causing B-O defect has been shown to have an energy level located close to the middle of the Si band gap, which is between E_V +0.35 and E_C -0.45 eV [61, 67, 69, 271, 299, 300].

In 2006, Herguth et al. reported that light-induced degradation due to B-O complexes could be regenerated by low temperature annealing under illumination (carrier injection) [62]. Since this initial report there have been numerous studies which attempt to explain this important ability to reverse a degradation effect that has a large impact on p-type Si modules. The possible implication of H, incorporated into the wafer from the firing of cells with H-rich dielectric layers, in this regeneration process was first proposed by Műnzer in 2009, and then

in 2010 Herguth et al. proposed a 3-state kinetic model to rationalise the role of the regeneration process in reducing recombination (see Figure 4-4). However, since this initial attempt to understand what occurs during the regeneration, two main theories have evolved.

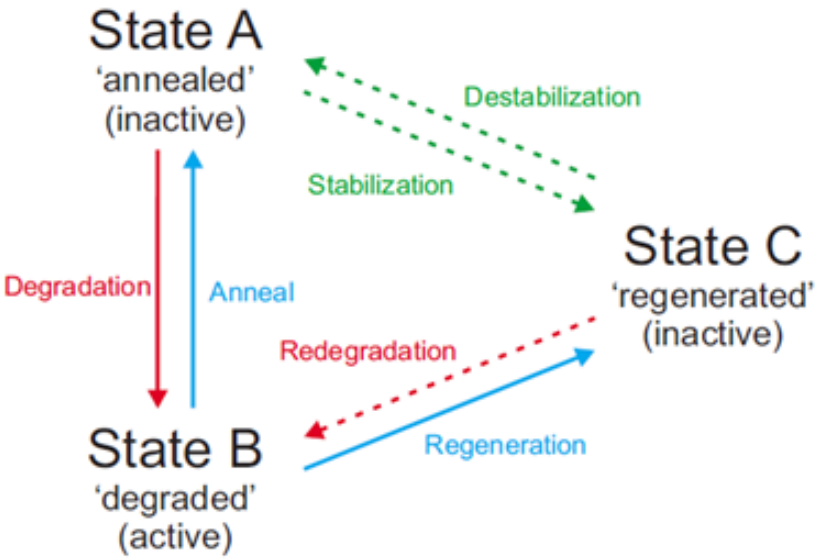

Figure 4-4. The 3-state model proposed by Herguth et al. to rationalise the formation and regeneration of recombination-active B-O complexes (from [64]).

Schmidt and Macdonald et al. [271, 274, 293, 301, 302] show that the concentration of the metastable B-O complex in p-type Si depends proportionally on the substitutional B concentration and quadratically on the interstitial O content. It is believed that the defect formation is based on fast-diffusing O dimers, which are captured by substitutional B. Walter et al. showed that that RTA in a belt furnace results in a dramatic change of the recombination properties of boron-doped Cz Si [303, 304]. They showed that the recombination-active defect concentration was reduced by fast cooling and postulated that this reduction in B-O degradation was due to the sinking of free Bi atoms into B nano-precipitates. These results demonstrated that the reduction in B-O degradation that can be achieved through the use of the regeneration process depends also on the prior thermal processing, and in particular the use of a RTA with a fast cooling rate. Walter et al. showed that regeneration of B-O defects could also be achieved in the absence of a H-rich dielectric layer. Figure 4-5 shows the recovery of lifetime of a p-type wafer passivated by unfired AlO_x after light-induced degradation.

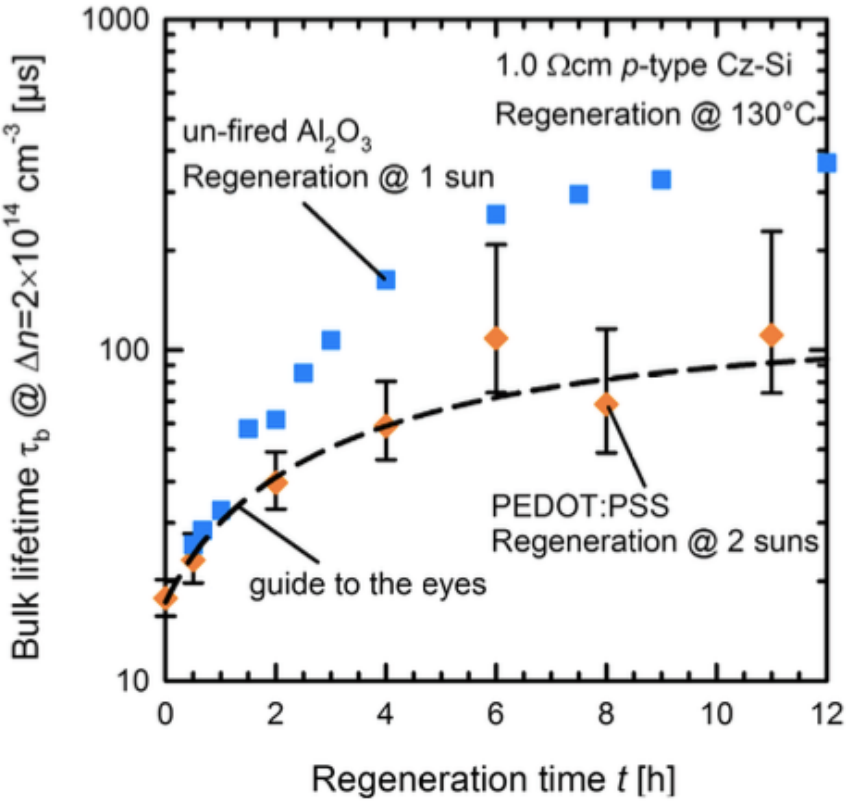

Figure 4-5. Bulk lifetime recovery from regeneration on a p-type Cz Si wafer with no SiN_x or H source, where blue squares show the wafer with un-fired Al_2O_3 experiencing a lifetime increase as function of regeneration time (from [303, 304]).

Another possible mechanism for the deactivation of B-O defects has been proposed by Wilking et al. and Hallam et al. [65, 67, 70, 299, 300, 305]. They propose that the light-induced degradation is caused by the formation of recombination active B-O related defects that can be passivated by H, the source of H being provided by SiN_x layers (deposited by PECVD) during firing. The provided H can eliminate recombination at B-O complexes in a subsequent 'regeneration' process which requires wafer heating and carrier injection [65]. This theory assumes that H in the SiN_x diffuses into the bulk of Si during the high-temperature annealing to regenerate the degraded cell, with larger amounts of H resulting in faster regeneration. Figure 4-6 shows that use of different SiN_x recipes can result in different regeneration rates, presumably due to the release of different amounts of H into the wafer, and that firing of the deposited layers is necessary for B-O regeneration.

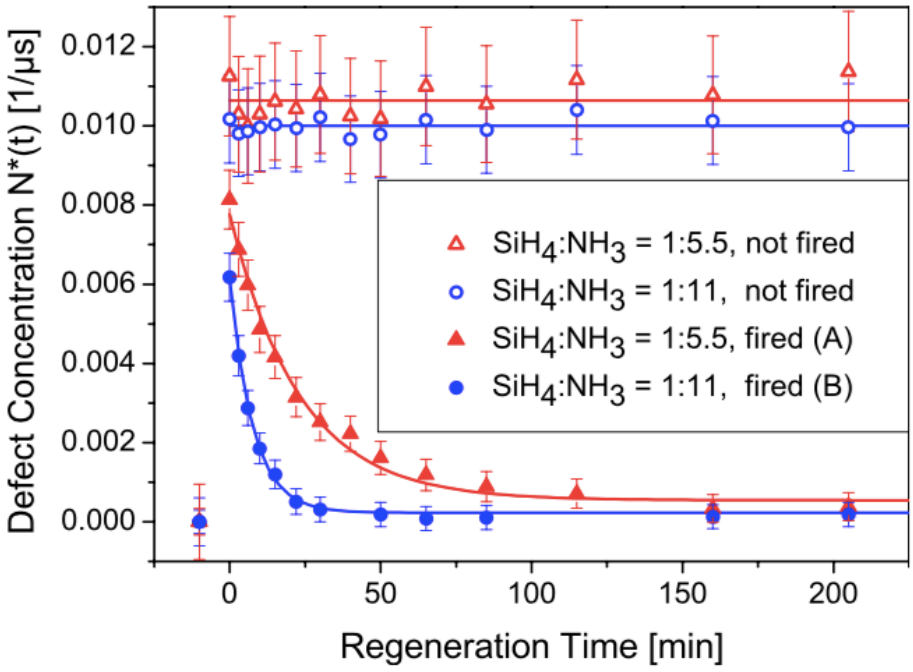

Figure 4-6. Comparison of defect concentration as the regeneration process is applied for wafers deposited using different SiN_x recipes. Open symbols denote measurements from cells that were not fired after SiN_x deposition (from [65]).

4.3 Experimental

This section reports on two key experimental studies. In the first study, the wafers were the same as the precursors used for bifacial p-type Si solar cells fabricated as described in Chapter 3. These wafers were passivated with SiO_2/SiN_x on the n-type surface and AlO_x/SiN_x on the p-type surface, and the aim of the experiments was to investigate the changes that occurred in the Si wafer during each of the processing steps and to investigate the impact of each process on the final cell performance. The iV_{OC} of the wafers was 680-700 mV after application of dielectric layers implying that recombination had been successfully minimised at both the n-type and p-type Si surfaces. This, therefore, made it possible to observe changes in recombination properties in the bulk of the Si wafer with cell processing steps. However, due to artefacts arising from the use of laser-cleaved edges and the non-symmetrical surface properties of the small cell, significant errors were incurred in the fitting of the injection dependent lifetime curves to the SRH models.

Consequently, in the second study, 125 mm symmetrically-diffused wafers were used (i.e., no laser-cleaved wafer edges). This reduced the contributions of edge recombination and errors

due to the asymmetric surface passivation on the SRH analysis. The use of symmetrical passivation enabled the effect of different dielectric layers (i.e., SiN_x, SiO_2) on the nature of recombination in the wafers following belt furnace annealing, light-induced degradation and regeneration to be investigated.

4.3.1 Substrate Preparation for the First Study

125 mm 1-3 Ω cm B-doped alkaline-textured Cz wafers were P-diffused to form emitters with a sheet resistance of ~ 100 Ω/□. After removal of the PSG, the rear surface was single-side etched to the remove the P-doped Si. The emitter and rear surfaces were then passivated with 10 nm thermal oxide + 70 nm SiN_x and 10 nm AlO_x (PECVD) + 70 nm SiN_x, respectively. Then, a set of wafers was cleaved into 9 equal-sized wafer fragments and B laser doping was performed along the perimeter of each of the fragments to ensure uniform emitter isolation across wafer fragments [306]. The injection-dependent τ_{eff} of each of the wafer fragments was monitored using QSSPL and QSSPC after the following processing steps shown in Figure 4-7.

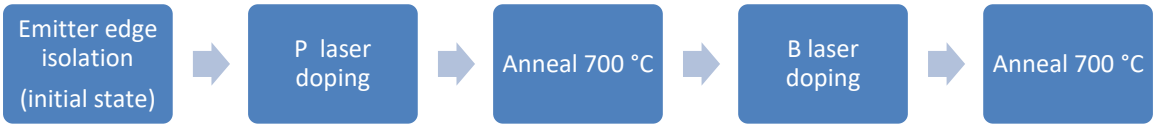

Figure 4-7. Flow diagram showing the processing steps (before light soaking) in the first study.

Phosphorus and B laser doping were performed using a 532 nm CW laser, with 85% phosphoric acid and a PBF1 B spin-on source (from Filmtronics) being used to form the n+ and p+ grids, respectively (see Section 3.3.2 for details). A representative wafer was selected to examine the impact of a belt furnace anneal, light soaking and the B-O regeneration process described in [65] on the m (iV_{oc}) curve. After each of these processes, the wafer was analysed as described in Section 4.4.1, resulting in an m (iV_{oc}) curve. The wafer was first annealed in an industrial belt furnace at a set peak temperature of 700 °C and a speed of 4600 mm/s, where it experienced the peak temperature for a period of 2-3 s. Light soaking was performed at 0.7 to 0.9 suns for 8 hours (natural outdoor sunlight) and the regeneration process was performed at 0.7-0.9 suns (natural outdoor sunlight) at 130 °C on a hot plate for 3 hours.

4.3.2 Substrate Preparation for the Second Study

The second study used alkaline-textured 156 mm 1-3 Ω cm B-doped 125 mm Cz wafers, where the wafers were P-diffused to form symmetrical emitters having a sheet resistance of ~ 120 Ω/□. A RTA at 700 ºC (as described for the first study in Section 4.3.1) was performed after diffusion (with the PSG in place) in a belt furnace to ensure that all the wafers were in an identical annealed state before the high-temperature oxidation, as the thermal history of the wafers was not known. After PSG removal, a 200 nm thermal oxide was grown on all wafers at a temperature of 950 ºC for 30 min, then wafers were divided into three groups. The oxide was removed from the surfaces of the Group A and B wafers and a 75 nm thick SiN_x layer having a refractive index of 2.09 was deposited on both wafer surfaces in a remote PECVD chamber (Roth & Rau MAiA) at 400 ºC. The Group A wafers then received a further RTA at 700 °C for a period of 2-3 s. All wafers were light-soaked for 2 days at 0.7 to 0.9 suns and then the regeneration process [65] was performed at 0.7 – 0.9 suns (using a halogen lamp) at 200 °C for 30 min. Finally, the light soaking step was repeated to establish the stability of the regeneration process. This process is summarised in Figure 4-8.

The reason for including Groups A and B was to identify the (recombination) impact of the RTA anneal at 700 ºC on the wafer after SiN_x deposition, and also to understand how this anneal impacts the following light-induced degradation and regeneration process. Group C was a reference group which was only passivated by thermal oxide (i.e., no source of hydrogen). These samples served to determine the importance of a H-containing dielectric on the subsequent light soaking and regeneration processes.

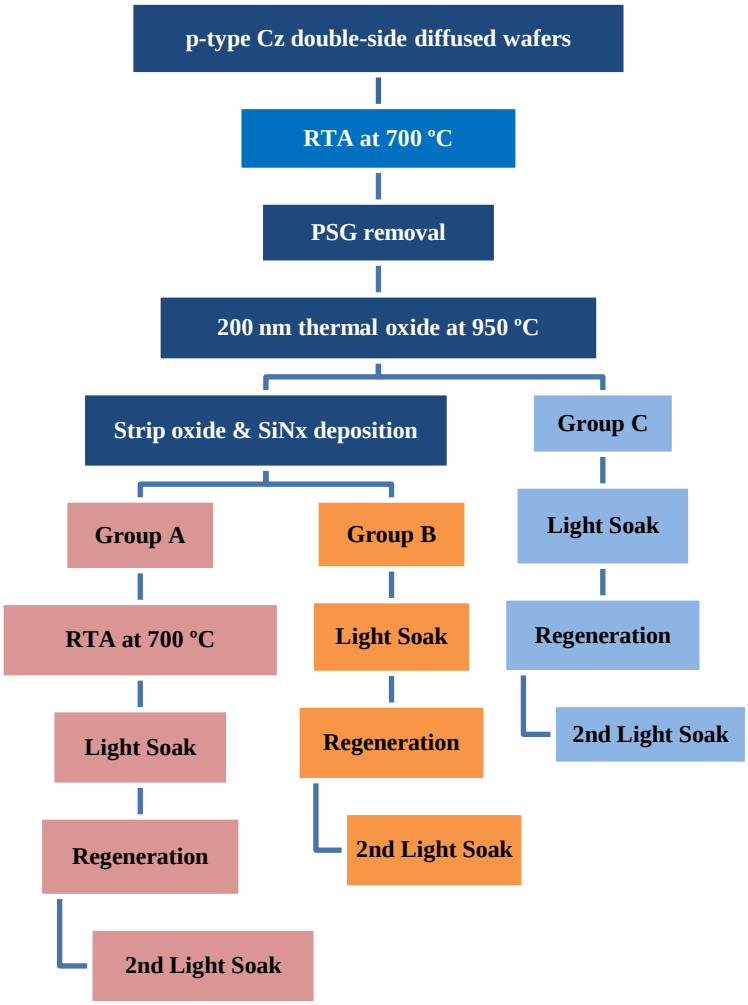

Figure 4-8. Flow diagram showing the processing steps (before light soaking) in the second study.

4.3.3 Light Soaking and Regeneration Arrangements

The light soaking was performed by placing the wafers between tempered glass used for module fabrication and a piece of white paper, as shown in Figure 4-9. This arrangement was used because it simulated the cell in a module in the field. The glass stack was then placed on the roof top for light soaking from 8 am to 5 pm. Light soaking was repeated for subsequent days until there was no further degradation (typically 2 days).

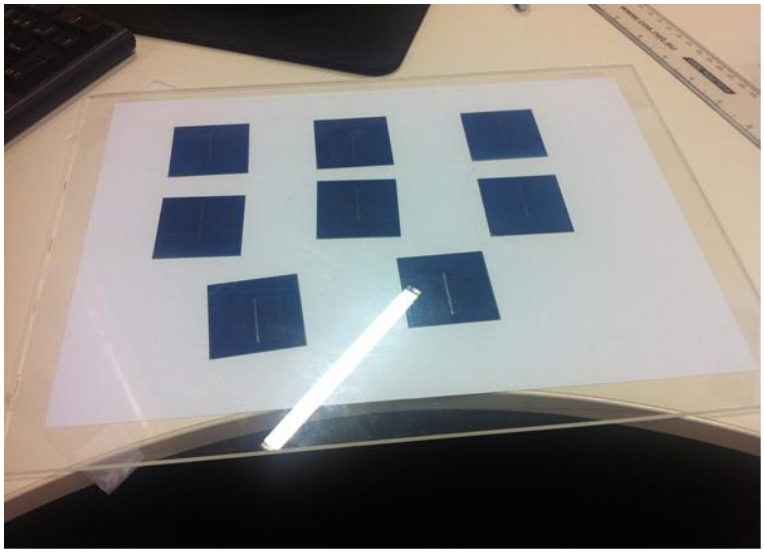

Figure 4-9. Light soaking arrangement showing cells (from the first study) sealed between a sheet of paper and a piece of tempered glass.

In the first study, the regeneration step was performed using a hot plate placed in direct sunlight. However, due to weather constraints, an artificial light with 6 halogen lamps was used in the second study to regenerate wafers/cells (see Figure 4-10). The light intensity of the lamps was calibrated to 0.7-0.9 suns, using a Si solar intensity meter.

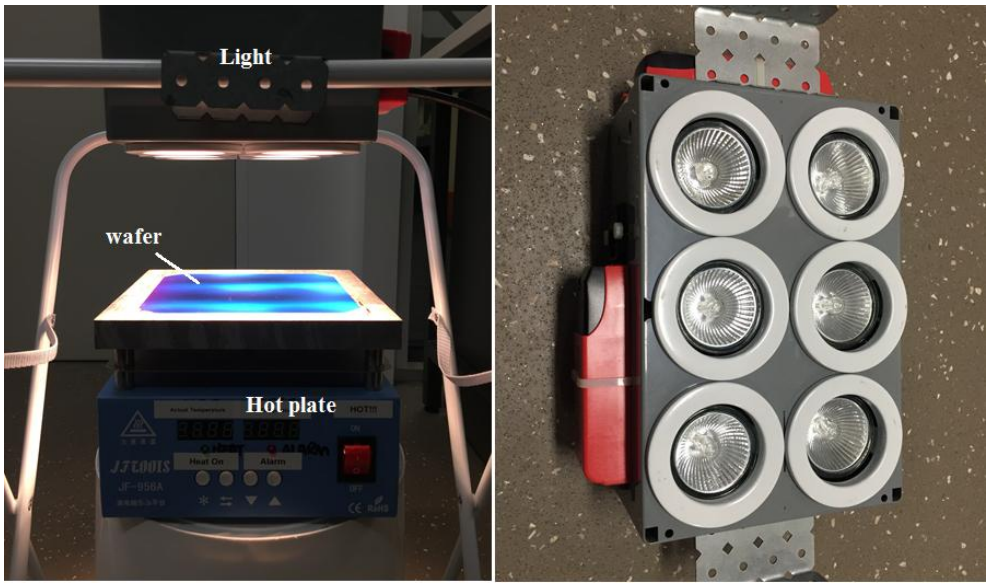

Figure 4-10. Regeneration arrangement with artificial halogen lights (used for the second study), showing the wafer placed on a hot plate with a controlled temperature of 200 °C.

4.3.4 QSS PL and PC Measurements

Quasi-steady-state PL and PC measurements were performed using a modified Sinton bridge WCT-120 (from Sinton Instruments) and a flash lamp, and then analysed using the generalised method [222, 307]. The system was modified to include a Si photodiode within the coil area to allow simultaneous measurement of PL and PC from the same area of the sample. The PL photodiode was connected to a trans-impedance amplifier before being read by a data acquisition card. The system also incorporated an LED with a computer controlled intensity, to allow controlled measurements at low illumination intensities. The experimental setup arrangement is shown in Figure 4-11.

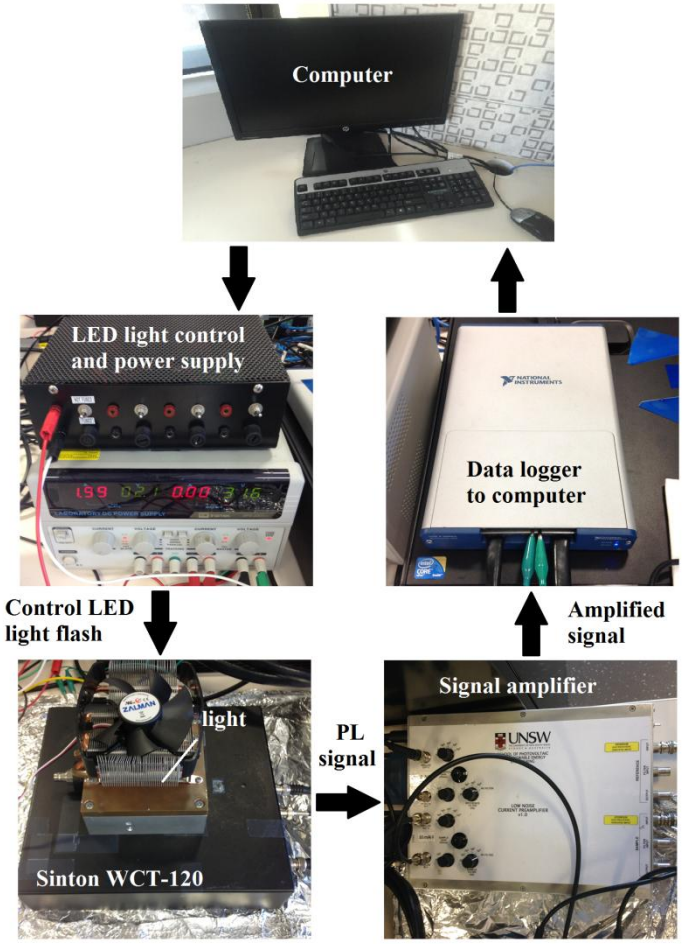

Figure 4-11. Measurement setup of QSSPL and PC for the experiment, where the flash was controlled by a desktop computer. After an LED flash, both the PL and PC data were amplified and recorded by a data logger, then stored and analysed by the computer.

In the first study, the QSSPL and QSSPC data were spliced together using the method described in [308, 309] resulting in τ_{eff} values over the injection range of 1×10^{9} to 4×10^{16}

cm^{-3}. In other words, the QSSPL and QSSPC data were combined, with QSSPL providing the low injection data (1×10^9 to ~ 10^{14} cm^{-3}) and QSSPC providing the high injection data (1×10^{14} to ~ 10^{16} cm^{-3}). In the second study, the injection range over which the QSSPL measurements were recorded was extended so that QSSPL data could generate τ_{eff} values over the entire injection range of 1×10^9 to 10^{17} cm^{-3}. For the QSSPL measurements, three different light sources were used to cover different illumination (injection) ranges (refer to Figure 4-12). Table 4-1 shows the details of the light sources.

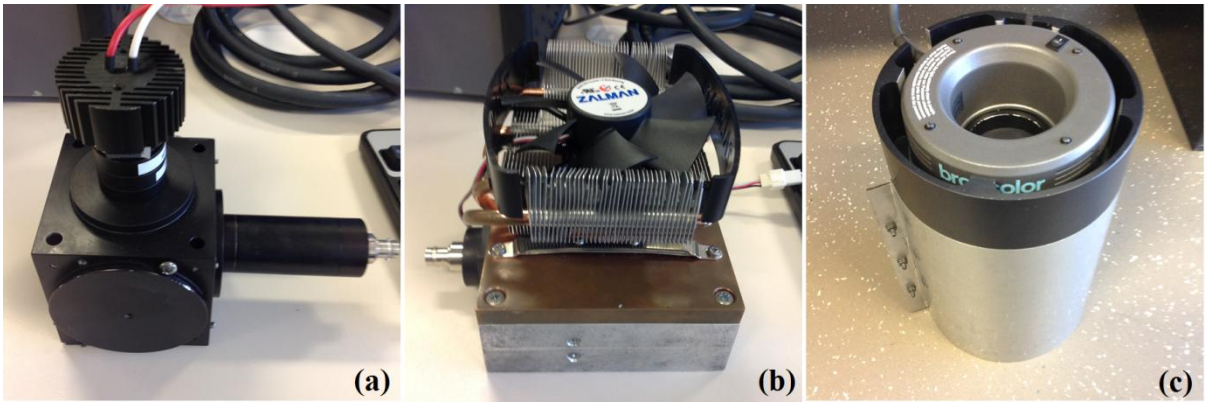

Figure 4-12. LED and flashlights used in this experiment (see Table 4-1 for details).

Table 4-1. Wavelength and light intensity of each light for QSSPL measurement

	LED (a)	LED (b)	Flash light (c)
Wavelength	810	625	flash lamp behind a short pass filter
Light intensity	0.1 Sun	1 Sun	100 Suns

4.3.5 Data Analysis and SRH Modelling

The iV_{oc} was calculated from the PC measurements at 1-sun using Eq. 4-4 which can be represented more generally as:

$$iV_{oc} = \frac{kT}{q}\left[\ln\left(\frac{np}{n_i^2}\right)\right] \qquad \text{Eq. } 4-12$$

where $p = N_A$ (B dopant concentration) and the minority carrier concentration of the p-type wafers, $n = \Delta n$ (obtained from the PC measurement). The value of n_i used was 9.65×10^9 cm^{-3} from Altermatt et al. at 25 °C [221]). The emitter recombination current density J_{0e} was calculated from the high injection data using:

$$\frac{1}{\tau_{eff}} - \frac{1}{\tau_{Auger}} = \frac{1}{\tau_{SRH}} + J_{0e}\frac{2\Delta n}{qWn_i^2} \qquad \text{Eq. } 4-13$$

The injection level dependent m curves were generated as described in [276]. This analysis assumes that, at a steady state, $G = U$. Therefore m can be calculated using [276]:

$$m = \frac{q}{kT}\left(\frac{\mathrm{d}\ln(G)^{-1}}{\mathrm{d}(iV_{oc})}\right) = \frac{q}{kT}U\frac{diV_{oc}}{\mathrm{d}U} \qquad \text{Eq. } 4-14$$

The value of m can be calculated from Δn using:

$$U = (np)^{\frac{1}{m}} = lnU = 1m\,ln[\Delta n(\Delta n + N)], \qquad \text{Eq. } 4-15$$

$$\frac{d\ln U}{d\Delta n} = \frac{1}{U}\frac{dU}{d\Delta n}, \qquad \text{Eq. } 4-16$$

$$\ln U = \frac{1}{m}\ln\Delta n + \frac{1}{m}\ln(\Delta n + N), \qquad \text{Eq. } 4-17$$

$$\frac{1}{U}\frac{dU}{d\Delta n} = \frac{1}{m}\frac{1}{\Delta n} + \frac{1}{m}\frac{1}{\Delta n + N}, \qquad \text{Eq. } 4-18$$

Therefore,

$$\frac{dU}{d\Delta n} = \frac{1}{m}\left(\frac{1}{\Delta n} + \frac{1}{\Delta n + N}\right)U \qquad \text{Eq. } 4-19$$

$$m = \frac{d\Delta n}{dU}U\left(\frac{1}{\Delta n} + \frac{1}{\Delta n + N}\right), \qquad \text{Eq. } 4-20$$

where $U = G$ at steady state.

The recombination state of a cell is influenced by the contributions of many individual SRH recombination centres. Therefore, it is difficult to extract the effect that processing may have

on a single SRH recombination centre, as the trap energies, E_t, and capture cross-sections of all contributing recombination sources are generally not known. However, if it is assumed that a process (e.g., "light soaking") activates a single dominant recombination centre in the wafer whilst leaving all other centres largely unchanged, then $\tau_{eff}(\Delta n)$ can be analysed using a difference method, whereby $\tau_{eff}(\Delta n)$ can be represented by the initial recombination state of the wafer [i.e., experimentally measured values of the initial state, $\tau_{eff,\text{init}}(\Delta n)$ and a single additional SRH centre, as represented in Eq. 4-21:

$$\frac{1}{\tau_{eff}(\Delta n)} = \frac{1}{\tau_{eff,init}(\Delta n)} + \frac{N_A + \Delta n}{\tau_{p0}(n_1 + \Delta n) + \tau_{n0}(N_A + p_1 + \Delta n)} \qquad \text{Eq. } 4-21$$

where n_1 and p_1 are the electron and hole density, respectively, when the Fermi level coincides with the energy of the recombination centre, E_t. If properties of the SRH recombination centre are known, then these can be used to fit Eq. 4-21 to the experimental data and estimate values for τ_{n0} and τ_{po} which represent the capture time constants or lifetimes of electrons and holes for the SRH recombination centre. The value of E_t, for the recombination-active B-O complex, has been reported to be 0.41 eV below the conduction band [272].

This SRH analysis, which is based on the assumption that a single defect is introduced by a process and therefore able to be modelled using the difference between two $\tau_{eff}(\Delta n)$ curves, has been previously reported, and in fact, was used by Rein et al. in their temperature- and injection-dependent lifetime QSS analysis of recombination arising from the B-O complex which determined the value of E_t used for this work [272]. Figure 4-13 illustrates how the light-soaked state was modelled using either the pre-light-soaked state or the regenerated state as the initial state.

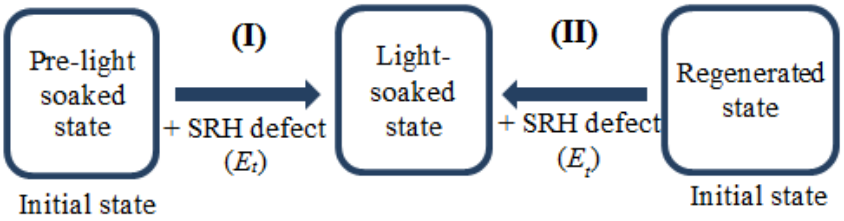

Figure 4-13. Schematic showing how the light-soaked injection-dependent τ_{eff} was modelled from a pre-light soaked state (Method I) and regenerated state (Method II). In all cases, E_t was assumed to be 0.41 eV below E_c.

4.4 Results and Discussion

4.4.1 First Study: Small Cell Analysis

The τ_{eff} (Δn) and m (iV_{OC}) curves for a representative cell recorded after different processing steps are shown in Figure 4-14 (a) and Figure 4-14 (b), respectively. Table 4-2 lists the values of iV_{oc} and m at 1-sun intensity and the values of J_{0s} estimated, as described in Section 4.3.4. The *pFF* was calculated based on the generation rate of electron-hole pairs, assuming a short circuit current density of 39 mA/cm^2; which is typical for the bifacial solar cells fabricated using these wafers (see Chapter 3).

The 700 °C anneal resulted in an increased τ_{eff} at all injection levels and a ~10 mV increase in the iV_{oc}. This increase is due to a decrease in J_{0s} by a factor of three, and most likely also an increased τ_{bulk}. However, the 1-sun m value increased from 1.1 to 1.3 after the 700 °C anneal. The reduction in J_{0s} is consistent with the theory that H, released from the SiN_x during annealing, reduces the density of interface states at the surface and therefore reduces the rate of surface recombination [310, 311]. Unfortunately, in this study, it was not possible to differentiate between recombination changes at the n-type and p-type surfaces due to the different dielectric layers that were employed to passivate the cell surfaces. The fact that m increased in the *mpp*-iV_{oc} range suggests that the recombination state of the Si wafer was significantly altered (from its initial state) by the annealing process.

Changes in the electron and hole capture cross-sections of a SRH recombination centre can result in a transition in the m (iV_{oc}) curve where the recombination changes from being limited by the capture of electrons to being limited by the capture of holes [281, 312-316]. However, this phenomenon has been primarily studied with respect to surfaces. For example, Aberle et al. [313] reported high ideality factors (and low *FFs*) due to changes in electron and hole capture cross-sections at the Si–SiO_2 interface. The m (iV_{oc}) curve that resulted after 700 °C annealing in this study could be explained by the introduction of a new SRH recombination centre or the change of an existing complex or state such that its columbic attraction of electrons/holes was significantly altered. Furthermore, it was not possible to distinguish whether this change occurred at the surface or in the bulk of the wafer.

After light soaking in the outdoor environment, τ_{eff} was reduced over the entire measured injection range and the iV_{oc} was reduced by 13 mV. Only a small increase in J_{0s} was

observed, which supports the conclusion that the reduced τ_{eff} was due to the formation of recombination active B-O complexes in the wafer (i.e., light-induced degradation (LID) [271, 317, 318]. The 1-sun *m* value was increased further to 1.5, which resulted in a significant reduction in the *pFF*. The regeneration anneal only partially recovered the τ_{eff} for $\Delta n > 10^{12}$ cm^{-3}. It is possible that the B-O complexes were not fully regenerated during the 3 hours and a longer regeneration time may have resulted in a greater recovery. However, when Δn was > 10^{13} cm^{-3} is considered, the regeneration anneal appears to return the wafer to the same "recombination state" as the 700 °C anneal, with the red and blue curves in Figure 4-14(b) being almost coincident and values of *m* at 1-sun being the same. The *pFF* was also recovered from 81.0% to 82.3% after the regeneration anneal, which is close the value of 82.5% estimated before the light soak. After the regeneration process, the J_{os} increased from that measured after the 700 °C anneal. However, this is consistent with some reactivation of defect states at the Si interface, which may be caused by release of H from passivating states. Corona-charging capacitance voltage measurements of the density of interface states, D_{it}, [319, 320] could be used to verify this hypothesis.

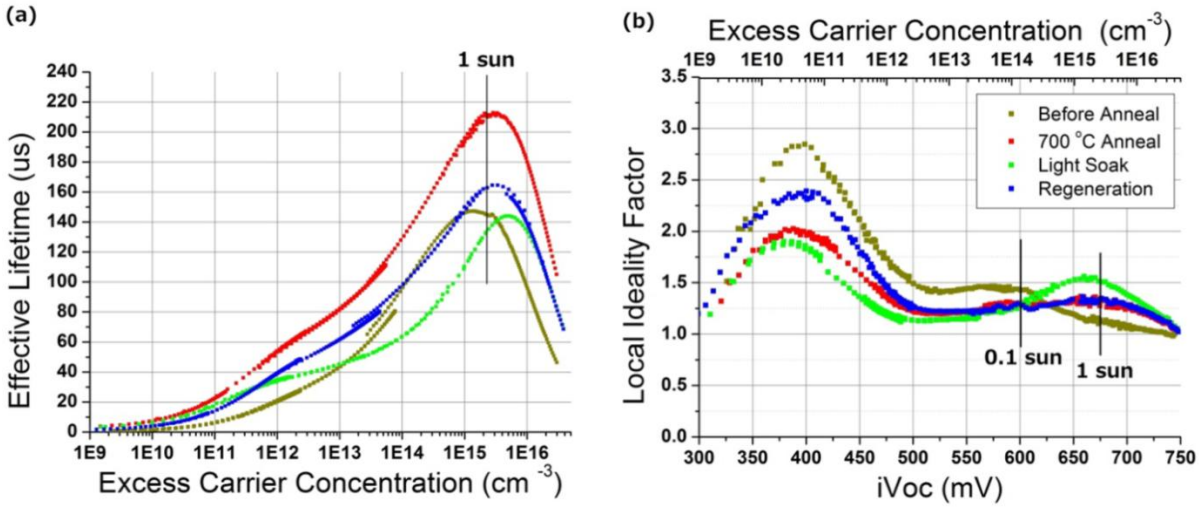

Figure 4-14. (a) Injection-dependent τ_{eff}; and (b) *m* (iV_{OC}) curves for a representative small cell after different annealing processes (first study).

Table 4-2. Summary of calculated cell parameters after each of the different annealing processes for the representative small cell from Figure 4-14.

Process	J_{os} (fA/cm^2)	*1-sun iVoc* (mV)	*1-sun m*	*pFF* (%)
Before anneal	77	675	1.1	82.2
700 °C Anneal	28	685	1.3	82.5
Light Soak	33	672	1.5	81.0
Regeneration	39	678	1.3	82.3

The results from Figure 4-14 suggest that the regeneration anneal leaves the wafer in an almost identical recombination state as the 700 ºC anneal process at higher injection levels. Consequently, τ_{n0} and τ_{po} were estimated for the simulated B-O defect using the 700 °C anneal state and then the regenerated state as the initial state, $\tau_{eff,init}(\Delta n)$. Figure 4-15 shows the initial, light-soaked and 'fitted' m (iV_{OC}) data when using the annealed state as the initial state [Figure 4-15 (a)] and the regenerated state as the initial state [Figure 4-15 (b)]. Figure 4-16 shows the same fits performed using the $\tau_{eff,}(\Delta n)$ data. Table **4-3** lists the estimated values of τ_{n0} and τ_{po} from the SRH modelling. Both fitting processes resulted in similar estimates for τ_{n0} and τ_{po}, which provided further evidence that the 700 °C anneal placed the wafer in a very similar recombination state as the regeneration anneal. The value of σ_n/σ_p was calculated to be 14.7 (when using the 700 °C annealed state as the initial state) and 14.0 (when using the regenerated state as the initial state) from τ_{n0} and τ_{po} using:

$$\frac{\sigma_n}{\sigma_p} = \frac{\tau_{p0}}{\tau_{n0}} \qquad Eq. 4-22$$

These values are higher than the values of 9.3 reported by Rein and Glunz [272] and 12 reported by Walter et al. [321] for the B-O defect. Expecting exact agreement to a ratio measured using temperature injection-dependent lifetime spectroscopy (used by Rein and

Glunz) is perhaps unreasonable, given that we cannot be sure that only a single SRH centre is activated by the light-soaking process. The estimate reported by Walter et al. was calculated at a single injection level ($\Delta n/p_0 = 0.1$) and assuming that τ_{eff} was calculated from the intrinsic lifetime with the addition of a single mid-gap B-O defect [321]. Simulations for a mid-bandgap defect (e.g., see [314]) predict that the transition peak in the *m* (iV_{oc}) curve can occur in the *mpp*-iV_{oc} range for σ_n/σ_p ratios of ~10. Although larger σ_n/σ_p ratios result in higher peaks in the *m* (iV_{oc}) data, the peak is shifted to lower injection levels where it does not significantly impact device performance.

As shown by Macdonald for recombination associated with Fe impurities [269], an increased concentration of B-O defects would be expected to result in a larger injection dependence of the SRH recombination, resulting in an even greater impact on *pFF*, up until the point where the cell's V_{oc} begins to be impacted. The analysis reported here may therefore be a useful way to investigate the properties of B-O complexes in cells. The ability to also extract *pFFs* from the QSSPL/PC data enables the effect of the recombination to be directly related to potential *FF* loss, with the *m* (iV_{oc}) curves providing a graphical link between physical recombination properties and the electrical diode model of a solar cell.

It is interesting to note that 700 °C annealing processes, which have been reported to achieve high implied V_{oc} values [299], may be placing B-O complexes in a state similar to the "regenerated" state and therefore providing further evidence for the role of H in the permanent deactivation of B-O defects [65]. Although the 1-sun *m* value associated with this state is less than that of the "light-soaked" state, it is still ~ 1.3, and therefore may indicate a difficulty in achieving both a high V_{oc} and high *FF* using the belt furnace annealing processes used in this work.

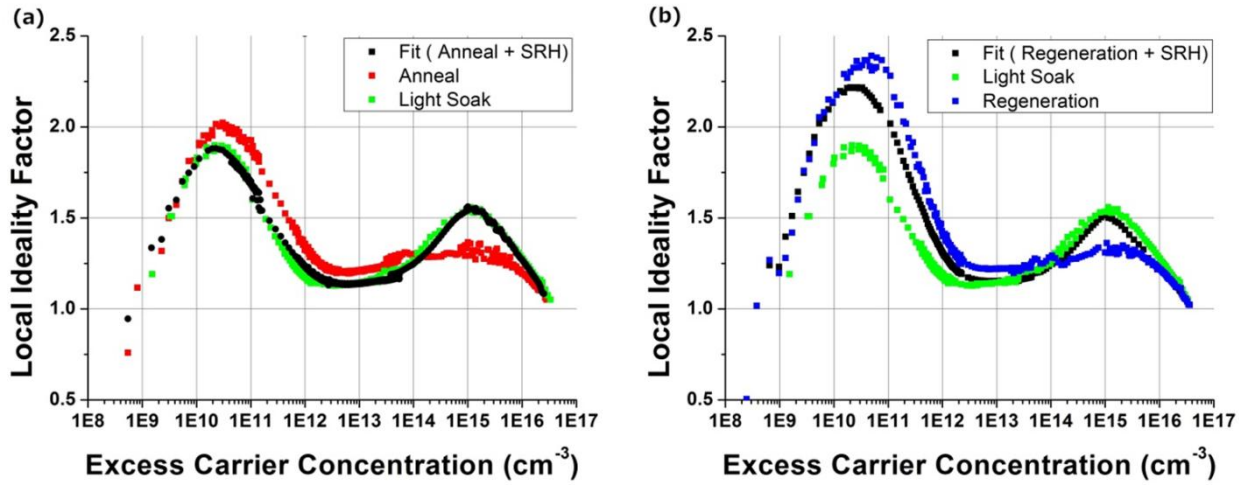

Figure 4-15. Injection-dependent *m* curves for an initial state, light-soaked state and the best fit of Eq.4-21 to the light soaked data, with the assumption of (a) an initial state after the wafer was annealed at 700 °C, and (b) an initial state after the wafer was regenerated. E_c -E_t = 0.41 eV was used for both fits [272].

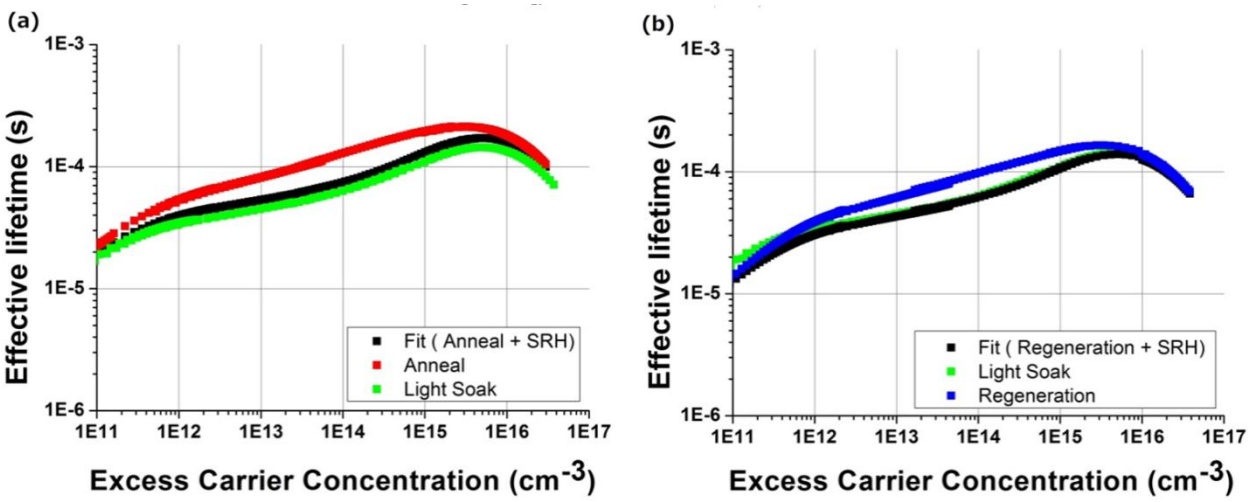

Figure 4-16. Injection-dependent τ_{eff} curves for an initial state, light-soaked state and the best fit of Eq. 4-21 to the light soaked data, with the assumption of (a) an initial state after wafer was annealed at 700 ºC, and (b) an initial state after the wafer was regenerated. E_c -E_t = 0.41 eV was used for both fits [272].

Table 4-3. Values of τ_{n0} and τ_{po} obtained by fitting Eq. 4-21 to the experimental light-soaked data. All fits assumed E_c -E_t = 0.41 eV

Initial Process	τ_{n0} (µs)	τ_{p0} (µs)	σ_n/σ_p
700 °C Anneal	150	2200	14.7
Regeneration	150	2100	14.0

To understand further how each step affected the value of *m*, a batch of cells was processed and monitored by QSSPL and PC after each step. Figure 4-17(b) graphs *m*, calculated from the QSSPL and QSSPC data recorded for a wafer fragment after laser doping and annealing processes, as a function of iV_{oc}. All of the wafer fragments were edge isolated (by B laser doping around the perimeter of the fragment) after cleaving from an initial 125 mm wafer to ensure that all fragments had the same edge recombination properties. Table 4-4 lists the effective J_{0s}, 1-sun *m* and iV_{oc} and *pFF* values of the same sample wafer fragment at each of the different processing stages. All wafer fragments showed a similar trend with processing, but the actual values differed slightly from fragment to fragment.

Although the P laser doping process reduced the iV_{oc}, it did not significantly affect the $m(iV_{oc})$ curve, implying that it did not introduce additional dominant SRH recombination centres in the wafer. The J_{0s} was slightly increased, which is to be expected, given some laser damage at the n-type surface. However, the first 700 °C anneal significantly changed the recombination state of the wafer. The value of *m* was reduced at low injection levels, but was increased to 1.3 - 1.4 in the $mpp\text{-}V_{oc}$ region, decreasing the *pFF*. As observed for the representative wafer reported previously, this anneal also decreased J_{0s}. However, there was no significant impact on the iV_{oc}.

The B laser doping resulted in a significantly decreased iV_{oc} and increased *m* in the $mpp\text{-}V_{oc}$ range to ~ 1.5, corresponding to a further reduction in the *pFF* to 81.1%. Boron laser doping, performed using a laser speed of 0.5 m s^{-1}, is known to create very deep locally-diffused p+ regions [160], thereby increasing the surface area of the recrystallised Si volume. The laser used for these experiments had a Gaussian beam shape. Consequently, less energy was absorbed at the edges of the laser grooves, resulting in non-uniformly doped Si and, in some cases, partially-opened regions which exposed lightly-doped Si at the surface. These non-uniform edge regions can significantly impact τ_{eff}.

The subsequent 700 °C anneal effectively returned the wafer to a similar recombination state as recorded for the first 700 °C anneal. There was some recovery of the iV_{oc} losses incurred by the B laser doping process, however the *m* value in the $mpp\text{-}V_{oc}$ range and the *pFF* were the same as recorded for the earlier 700 °C anneal. This suggested that the wafer was returned to the same recombination state even after the introduction of new SRH recombination centre(s) by the B laser doping process. The B laser-doped recombination state was simulated

using the method described in Section 4.4.1, assuming an initial state described by the τ_{eff} *(Δn)* data recorded after the first 700 °C anneal. Although it is possible that the B laser doping process may introduce further B-O defects, this analysis assumed a single mid-bandgap SRH recombination centre with E_t = 0.56 eV. The simulated data is shown with the experimental data in Figure 4-18 and the estimated values of τ_{n0} and τ_{po} are listed in Table 4-5. The value of σ_n/σ_p, calculated from τ_{n0} and τ_{po}, was 5.6. Although there is good agreement between the simulated and experimental data at high injection levels, differences exist at mid-injection levels, suggesting that the damage incurred by B laser doping may not be well described by the introduction of only one additional SRH recombination centre.

Cotter et al. [315] reported injection-dependent recombination, which was characterised by peaks in the *m* (iV_{oc}) curve in the *mpp*-V_{oc} range and reduced *FFs* for heavy B groove diffusions in double-sided buried contact p-type cells. They attributed this to diffusion-induced misfit dislocations. However, the peaks (and reduced *FFs*) were not observed for n-type cells. It is not known whether B laser doping results in similar dislocations, but it would be interesting to determine whether similar recombination is introduced by B laser doping of n-type cells. Although, clearly, there is still much to understand about what is occurring in cells once SRH recombination centres are introduced through processes like B laser doping, this study has demonstrated the injection dependent lifetime analysis can be used to investigate the nature of recombination changes after each processing step, with the use of QSSPL extending the injection level range over which the analysis can be performed.

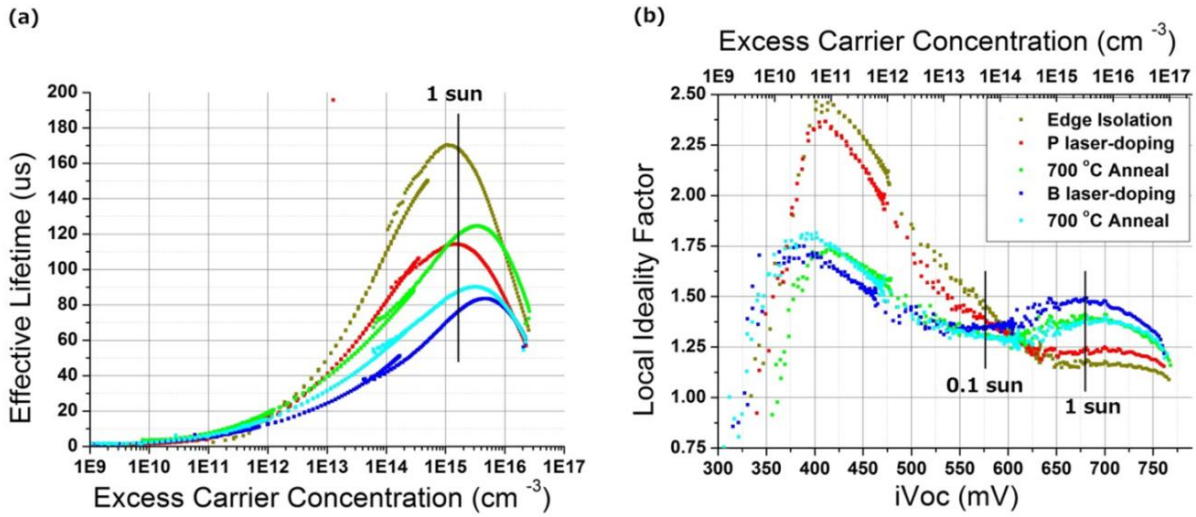

Figure 4-17. (a) Injection-dependent τ_{eff}; and (b) *m-iVoc* curves for a representative cell after different processes.

Table 4-4. Summary of calculated cell parameters after each of the different processes for the cell used for Figure 4-17.

Process	J_{os} (fA/cm^2)	*1-sun iVoc* (mV)	*1-sun m*	*pFF* (%)
Edge Isolation	106	665	1.1	82.0
P laser doping	116	654	1.2	81.7
Anneal 700 °C	53	654	1.4	81.4
B laser doping	57	636	1.5	81.1
Anneal 700 °C	60	645	1.4	81.4

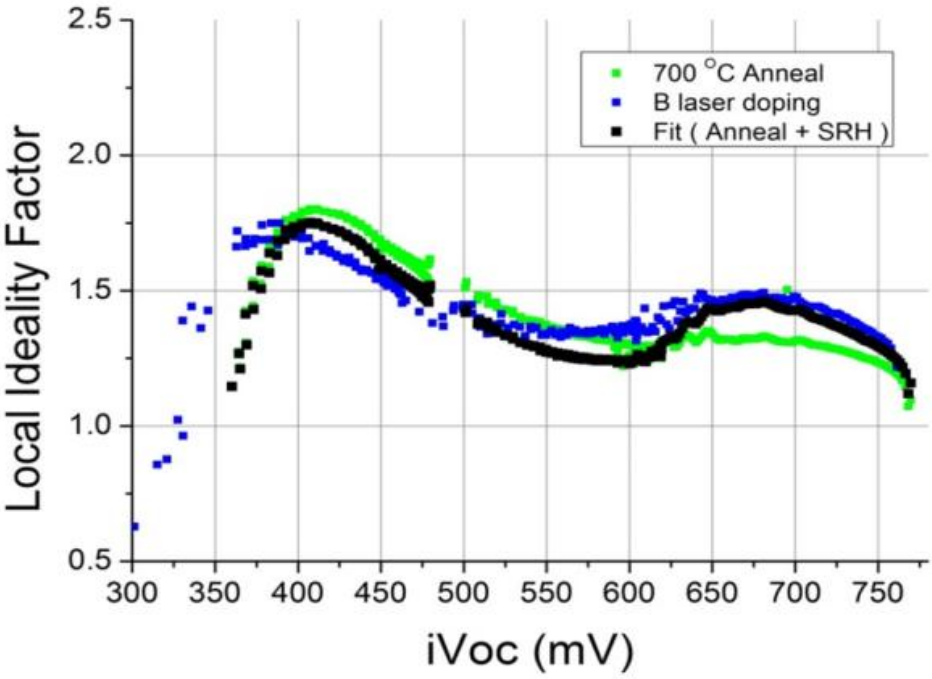

Figure 4-18. Injection-dependent *m* curves for an initial state (700 °C anneal), B laser-doped state and the best fit of Eq. 4-21 to the B laser-doped data. The fitted data assumed an E_t value of 0.56 eV (i.e., mid-gap).

Table 4-5. Values of τ_{n0} and τ_{po} obtained by fitting Eq. 4-21 to the experimental B laser-doped data. Data fitting assumed that $E_c - E_t$ = 0.56 eV.

Initial Process	τ_{n0} (μs)	τ_{p0} (μs)	σ_n/σ_p
700 °C Anneal	180	1000	5.6

In conclusion, this study investigated the possibility of cell processing steps changing the recombination properties of defects or complexes (such as B-O defects) in the Si bulk such that their asymmetric capture cross-sections can impact the *pFF* of the cell. Recombination at bulk defects having asymmetric capture cross-sections can be manifested in elevated *m* values in the *mpp*-V_{oc} region of cells in which recombination is minimised at the surfaces. Consequently, elevated *m* values detected during cell processing can provide an indicator for substantially reduced device *FF*, as predicted in [269]. Injection-dependent recombination has been described previously [281, 312-316], but the focus of these earlier studies was on surface recombination. The improved levels of surface passivation enabled by having hydrogenated SiN_x layers on both wafer surfaces raises the possibility that bulk recombination centres, such as B-O defects which are known to have σ_n/σ_p ratios of ~ 10, may begin impacting device *FF*.

This study demonstrated observed changes in the recombination state of cells fabricated using B-doped Cz wafers after introducing and eliminating recombination-active B-O defects, as described in [65], with QSSPL and QSSPC measurements. The generated *m* (iV_{oc}) curves represent recombination states of cells, and it was shown that the regeneration process described by Wilking et al. [65] places the cell in an almost identical recombination state as a 700 °C belt furnace anneal. Furthermore, B-O defects that were activated by light soaking were modelled as a single SRH recombination centre with an estimated σ_n/σ_p ratio of ~ 14 using a method which represented all the other sources of recombination in the wafer using τ_{eff} (Δn) data recorded before light soaking. This estimate is larger than the values of 9.3 and 12 that have been previously reported for B-O defects [69, 70, 272, 321]. However, there are a number of assumptions inherent in the analysis presented here, the first and foremost being the assumption that recombination introduced by light soaking was due to a single recombination centre and all other recombination in the wafer was unchanged by the process. The described method, however, does demonstrate how injection-dependent lifetime measurements using PL and PC can be combined and used to extract information about the nature of recombination in the device and indicates when *FFs* may be potentially impacted by various processing steps.

The use of QSSPL, in addition to QSSPC, allowed the injection range over which the injection-dependent lifetime analysis could be performed to be increased to 1×10^{11} cm^{-3} to 1×10^{17}. It was not clear from this initial study whether the increased injection range was an

advantage and consequently the value proposition of using QSSPL over just the injection-dependent τ_{eff} measurements from QSSPC was investigated further in the second study.

As mentioned in Chapter 3, this work was motivated by the observation of lower than expected *FFs* in the plated bifacial laser-doped p-type cells. The initial results demonstrated the effect of P and B laser doping on the $m(iV_{oc})$ curves generated from B-doped cells bifacially passivated with SiN_x. Although the B laser doping process introduced additional recombination to the cell, which was manifested in an elevated *m* value of 1.5 in the *mpp*-V_{oc} injection range, the additional recombination was not well modelled by a single SRH recombination centre in the mid-injection range. However, the results presented in this section clearly demonstrate how SRH recombination centres, with injection-dependent lifetimes due to an asymmetries in their σ_n/σ_p, can potentially decrease device *FF*. Also peaks in local ideality factor curves in the *mpp*-V_{oc} range can provide a useful graphical indicator of this injection-dependent recombination.

4.4.2 Second Study: Symmetrically-Passivated Wafers

As mentioned in the previous section, to improve the accuracy of the modelling, the second study used symmetrically-diffused (and passivated) full-area (125 mm) wafers instead of 4.5 cm cells (fabricated by cleaving cells from larger wafers). In this study, the use of using just QSSPL data (with PC being used only for calibration) for the injection-dependent SRH analysis was investigated as a possible way of increasing the accuracy of the SRH analysis by the inclusion of a wider injection range of data. In addition, this study investigated the role of the passivating dielectric on recombination in the wafers following the processes of belt furnace annealing, light soaking and regeneration. By comparing Group C wafers (passivated with thermal oxide), to Group A and B wafers (passivated by PECVD SiN_x), it was hypothesised that the contribution of a PECVD SiN_x layer to recombination changes should be observable, and by comparing the Group A and B wafers, the contribution of RTA annealing at 700 ^{o}C after SiN_x deposition to changes in recombination should be evident.

The experiment (see Figure 4-8) commenced with 18 wafers randomly picked from a set of 100 B-doped 1-3 Ω cm 125 mm Cz wafers. After the thermal oxidation step, concentric rings were observed to different extents in the PL images for a number of the wafers (see Figure 4-19). Such rings can form due to recombination at iron (Fe)-decorated O precipitates and surrounding crystal defects [322-325]. Most industrial Cz wafers contain Fe, which is

typically fortuitously gettered to the emitter by the P diffusion step [315, 326, 327]. However, in the processing sequence used in this study, gettered Fe (collected at the heavily-doped n-type surfaces of the wafers) may have been released back into the bulk of the wafer during the thermal oxidation, from where it was either gettered to or precipitated at O precipitates which form in rings corresponding to vacancy-rich regions which can occur in rapidly-grown ingots. Recombination in Fe-contaminated samples has been shown to depend on both the concentration of Fe and the density of O precipitates [328]. Murphy et al. proposed that if the Fe concentration is relatively low ($< 5 \times 10^{12}$ cm^{-3}), then it can be gettered (reversibly) at the precipitates, but higher contamination levels can result in irreversible precipitation [325]. In this study, the pre-oxidation RTA may have exacerbated this situation by initiating the nucleation of more O precipitates than would have otherwise have been present.

The extent of this problem varied between wafers, most likely as a result of differences in both the O and Fe concentrations between wafers. However, it was interesting to note that when SiN_x was deposited on 12 of the initial 18 wafers, the wafers having the most evident rings after thermal oxidation experienced a very large decrease in τ_{eff}, with the entire centre of the wafer being significantly degraded in PL intensity [see Figure 4-19 (c)]. Annealing after SiN_x deposition (for Group A wafers) improved these wafers' τ_{eff} values slightly, but the improvement was mostly in the peripheral regions rather than in the central regions of the wafer. This observation supports the theory that although H may be able to passivate dangling bonds associated with O precipitates [325, 329], it may be less effective at reducing recombination at Fe-decorated O precipitates. To minimise the effect of this problem on the remaining experiment, all of the wafers in which rings were evident in the PL images either immediately after thermal oxidation or after SiN_x deposition were eliminated from the subsequent analysis. This left only three wafer per group.

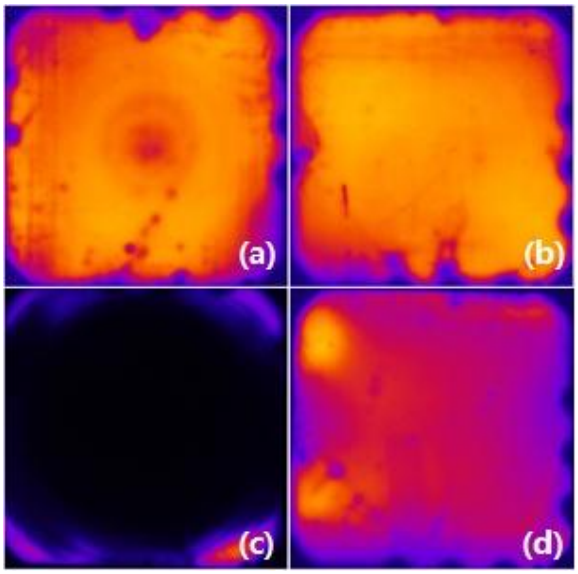

Figure 4-19. Images (a) and (b) show two wafers after the thermal oxidation step. The wafer in (a) shows evidence of annular regions of reduced τ_{eff}, whereas the wafer in (b) is reasonably uniform except for edge effects. The PL images in (c) and (d) were recorded after 75 nm SiN_x had been deposited (i.e., after SiO_2 removal). Whereas the τ_{eff} of the wafer imaged in (c) is seriously degraded, especially in the centre of the wafer, there is no evidence of "rings" in (d). All PL images were recorded using a BTi imaging tool with a 0.1 s exposure and are graphed using the same scale.

Figure 4-20 shows the injection-dependent τ_{eff} for representative wafers from each group of wafers and Table 4-6 lists the iV_{oc}, and J_{0s} for each group after each process. Low J_{0s} values of 4 fA/cm^2 were measured for both the SiN_x-coated and the thermal oxide-coated wafers, though for SiN_x it was necessary for the wafers to be annealed after deposition to achieve these low surface recombination currents. The first light soak did not change J_{0s} for Group A and C wafers, suggesting that the decrease in iV_{OC} that was measured was due to the introduction of recombination within the wafer, presumably largely due to the activation of B-O defects. However, for the Group B wafers, J_{0s} increased with light soaking, therefore making it difficult to determine where the introduced recombination was occurring.

The regeneration process increased the τ_{eff} and iV_{oc} of the SiN_x-coated wafers [see Figure 4-20 (a) and (b)] but further degraded the iV_{OC} of the thermal-oxide passivated wafers [see Figure 4-20 (c)]. Furthermore, the regenerated iV_{oc} was only stable during a second light soaking for Group A wafers (SiN_x with a post-deposition RTA), with the thermal-oxide passivated wafers degrading even further with the second light soaking. This result adds further evidence to the theory that a "fired" H-containing dielectric is required for stable B-O regeneration. Some recovery in iV_{oc} after regeneration was possible if the deposited SiN_x was not rapidly annealed (Group B) before light soaking, but this recovery was not stable. It was

also observed that during the process of light soaking/regeneration/light soaking, 'rings' started to appear in the SiO_2 passivated wafers (Group C), becoming progressively more evident with each step (see Figure 4-21). This raises the possibility that carrier injection with thermal annealing may also be enhancing impurity decoration of oxide precipitates, a possibility which requires further investigation. "Rings" did not become more evident in the PL images after light soaking and regeneration in the Group A and B wafers.

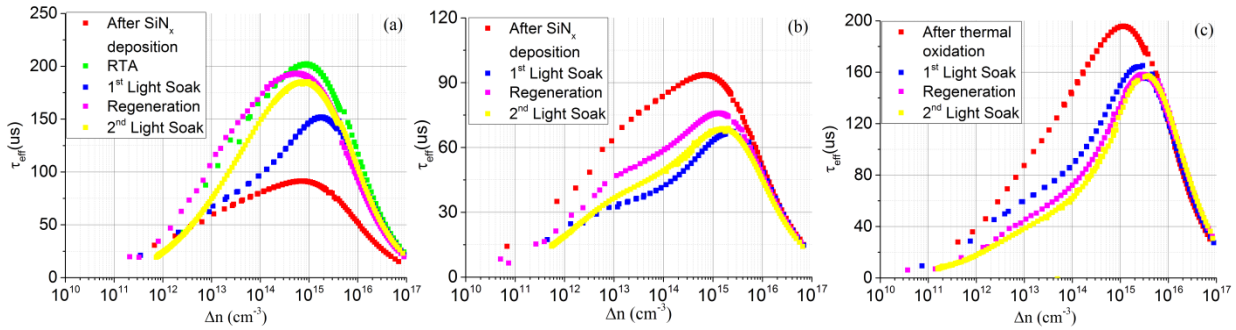

Figure 4-20. Injection-dependent τ_{eff} measured using QSSPL and PC for a representative wafer from (a) Group A (SiN_x with subsequent RTA); (b) Group B (SiN_x and no subsequent RTA); and (c) Group C (thermal oxide).

Table 4-6. Calculated iV_{OC} and J_{0s} values after each processing step for each group. NA = Not applicable to that group.

Process	Group A		Group B		Group C	
	iV_{oc} (mV)	J_{0s} (mA/cm^2)	iV_{oc} (mV)	J_{0s} (mA/cm^2)	iV_{oc} (mV)	J_{0s} (mA/cm^2)
After thermal oxidation	NA	NA	NA	NA	666 ± 2	4 ± 1
After SiNx deposition	657 ± 2	59 ± 6	654 ± 2	70 ± 7	NA	NA
After RTA	678 ± 2	4 ± 1	NA	NA	NA	NA
1st Light soak	671 ± 1	4 ± 1	643 ± 1	97 ± 10	657 ± 3	4 ± 1
Regeneration	676 ± 1	4 ± 1	650 ± 1	105 ± 10	654 ± 3	4 ± 1
2nd Light soak	675 ± 1	4 ± 1	644 ± 2	103 ± 10	649 ± 4	4 ± 1

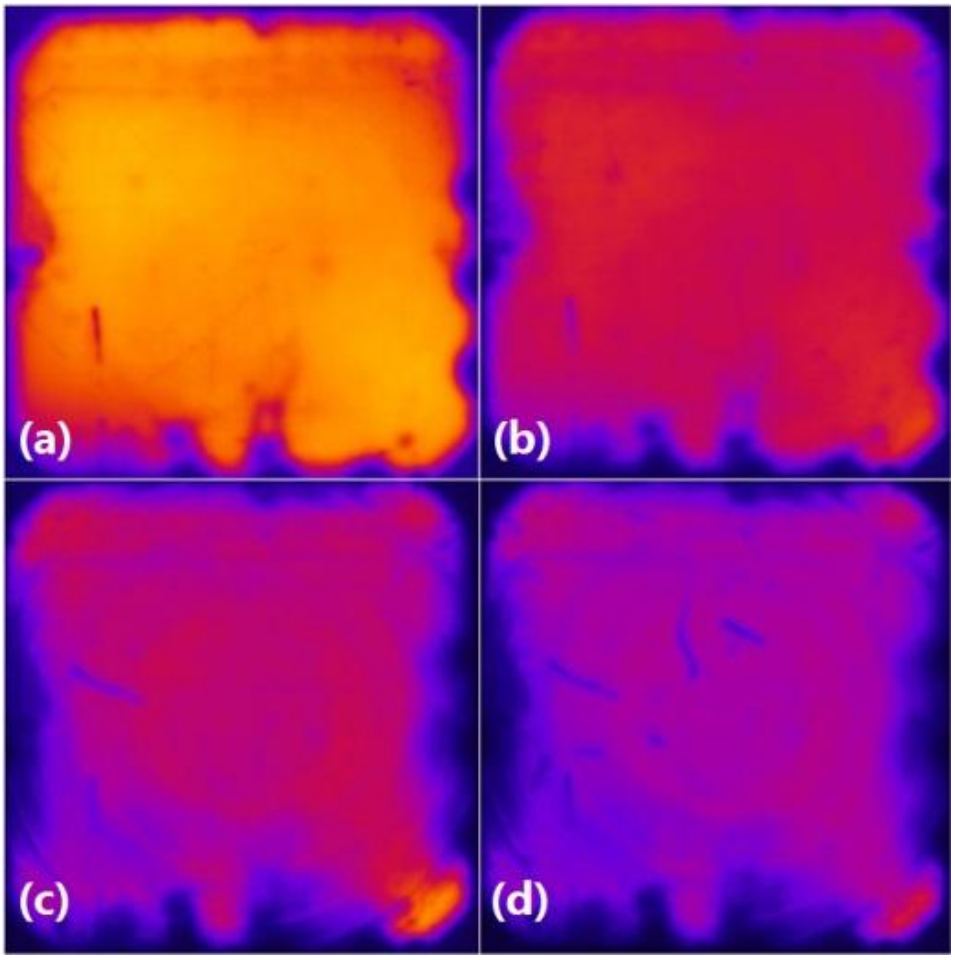

Figure 4-21. PL images of a Group C wafer which had been passivated with 200 nm SiO_2, recorded (a) after thermal oxide growth; (b) after a 1st light soak; (c) after regeneration; and (d) after the 2nd light soak.

The SRH modelling was performed separately for both the QSSPL and the QSSPC data in order to determine whether there were any advantages in using the wider injection range made possible in using QSSPL for the analysis. For all wafers, the light-soaked τ_{eff} (Δn) data were modelled assuming the introduction of a single SRH defect (E_c - E_t = 0.41 eV) and initial states of: (i) the RTA-annealed state; and (ii) the regenerated state (i.e., as was done in the first study). This resulted in estimates of σ_n/σ_p for each wafer, which were averaged for each Group (see Table 4-7).

Table 4-7. Estimated σ_n/σ_p values obtained from the QSSPL and QSSPC analyses, assuming the introduction of a single defect corresponding to the B-O defect (E_c - E_t = 0.41 eV) being introduced into the pre-light soaked state and regenerated state. The errors in the estimates for σ_n/σ_p represent the maximum deviation from the computed mean of the wafers in each group.

Group	Fitted σ_n/σ_p value with QSSPL		Fitted σ_n/σ_p value with QSSPC	
	From pre-light-soaked state	From regenerated state	From pre-light-soaked state	From regenerated state
Group A	9.7 ± 1.7	20.0 ± 11.3	9.7 ± 1.9	18.5 ± 4.5
Group B	16.6 ± 1.7	12.9 ± 10.8	13.8 ± 2.8	13.7 ± 1.3
Group C	23.3 ± 3.5	NA	15.7 ± 10.3	NA

Figure 4-22 compares the estimates of σ_n/σ_p obtained using the QSSPL and QSSPC analyses for all Groups of wafers with Figure 4-22 (a) showing the estimates obtained using the RTA state as the initial state and Figure 4-22 (b) showing the estimates obtained using the regenerated state as the initial state.

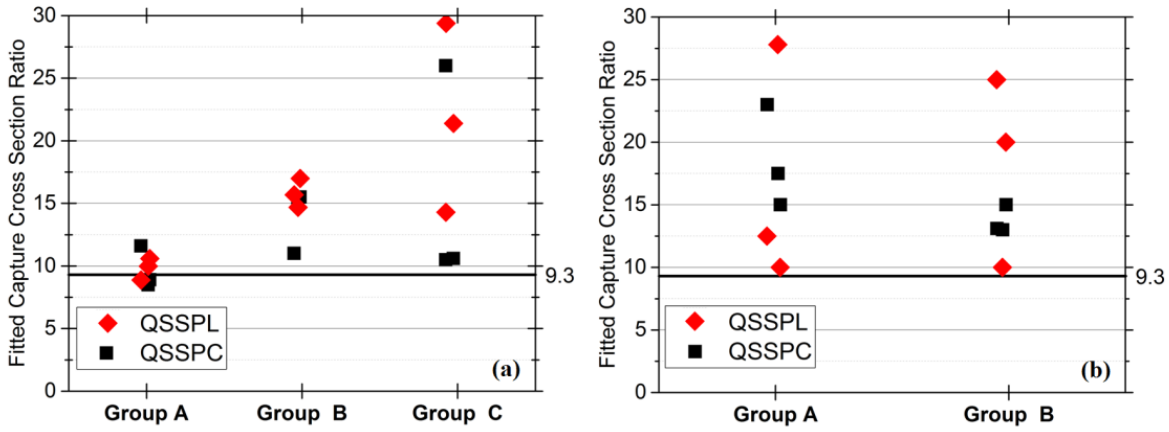

Figure 4-22. Estimates of σ_n/σ_p using the QSSPL (red) and QSSPC (black) measurements obtained using: (a) the RTA state as the initial state; and (b) the regenerated state as the initial state.

The average value of σ_n/σ_p estimated for the Group A wafers from their RTA initial state was 9.7 ± 1.7 and 9.7± 1.9 using the QSSPL and QSSPC data, respectively. This value is close to

the value of 9.3 reported by Rein et al.[272]; and closer to the previously-reported reference value than the estimates in the first study where contributions from asymmetric surface passivation and edges were expected to have added to the uncertainty of the SRH modelling.

The values of σ_n/σ_p estimated for the Group A wafers using the regenerated state as the initial state were 20.0 ± 11.3 and 18.5 ± 4.5 using the QSSPL and QSSPC data, respectively. These estimates are significantly larger and more variable than the values obtained from the RTA initial state, suggesting that either the light soaking and/or the regeneration process affected recombination at more than one defect. Such a large difference between the estimates for σ_n/σ_p arising from using the different initial states was not evident for the first study (seeTable 4-3), and so it is possible that the difference observed in the estimates for this study may have been due to the inclusion of the 700 ºC pre-anneal step (see Figure 4-8). This RTA step had been included to ensure that wafers from all Groups experienced a belt furnace anneal at 700 ºC, however the order of thermal processing is clearly critical as presumably O precipitates are placed in different states by high temperature treatments. This result also reinforces the importance of thermal history for the formation and regeneration of the B-O defect, and possibly other O-related defects, in p-type Cz wafers.

The average values of σ_n/σ_p estimated for both the Group B and C wafers from the RTA initial state were both larger using the QSSPL and QSSPC analyses. This highlights that both the annealing of the SiN_x after deposition and the application of a thermal oxide passivation layer can alter the σ_n/σ_p of a modelled single defect having an E_t corresponding to the B-O complex. Figure 4-22 (a) shows that the variance of the estimates is also significantly increased for wafers in Groups B and C. Although the values of σ_n/σ_p estimated using the regenerated states were not significantly larger than those estimated from the RTA state, the values were larger than the value of 9.3 reported by Rein et al.

Figure 4-23 shows the QSSPL and QSSPC analyses for a representative Group A wafer where the RTA-annealed state was used as the initial state for the SRH modelling. The value of σ_n/σ_p was estimated to be 10.1 ± 0.9 and 8.5 ± 0.5 for the QSSPL and QSSPC analysis, respectively, with the error in the estimates being calculated from the covariance matrix of the least squares fit [330]. Figure 4-24 shows the modelled light-soaked data for the same wafer using, in this case, the regenerated state as the initial state. There was a much larger difference in the σ_n/σ_p value estimated in this analysis, with values of 10.0 ± 0.7 and 15 ± 0.4,

being estimated for the QSSPL and QSSPC data, respectively. This larger difference may be due to the regeneration process also affecting recombination at other defects, and in particular, defects which influence the lower injection regions of the curves. This may have limited the accuracy and validity of the QSSPL modelling as the initial assumption of a single introduced defect was no longer valid.

Although the increased range of data obtained from the QSSPL might be expected to result in a more accurate estimate of σ_n/σ_p, the low injection data may also be impacted by recombination at the wafer edges or regions outside of the illuminated area [306]. This recombination can be more significant for diffused wafers (as used here), as carriers are more effectively conducted out of the PL detection region. Although the wafer area was larger in this study, the presence of diffused layers on both wafers surfaces may have permitted increased carrier conduction.

It can be seen that the σ_n/σ_p estimates obtained using QSSPL measurements using the regenerated state as the initial state were more variable than those using only QSSPC data. This variability was most likely introduced by the inclusion of the low injection data in the analysis as light soaking appears to also introduce recombination changes in the injection range of $\Delta n \sim 10^{13}$ cm^{-3} and so the assumption of the introduction of a single defect no longer holds. When the analysis is performed using just the QSSPC higher injection data, contributions from the low injection data that may affect the accuracy of the estimate are fortuitously avoided. However, it is still interesting to note that the variability incurred by including the low injection data in the analysis results in more variance when the regenerated data is used as the initial state. With the limited samples involved in the study it was difficult to explain why this occurred, with many possibilities existing (e.g., the RTA preceding light soaking may have introduced a defect affecting the low-injection data).

If the objective of the analysis was to accurately estimate the σ_n/σ_p for the deep-level B-O defect, and then a practical conclusion is to only measure the injection range where the expected asymmetric σ_n/σ_p is expected to be manifested in the τ_{eff} (Δn) data. If that can be achieved using QSSPC, then use of QSSPL may introduce unnecessary measurements and complications and reduce accuracy.

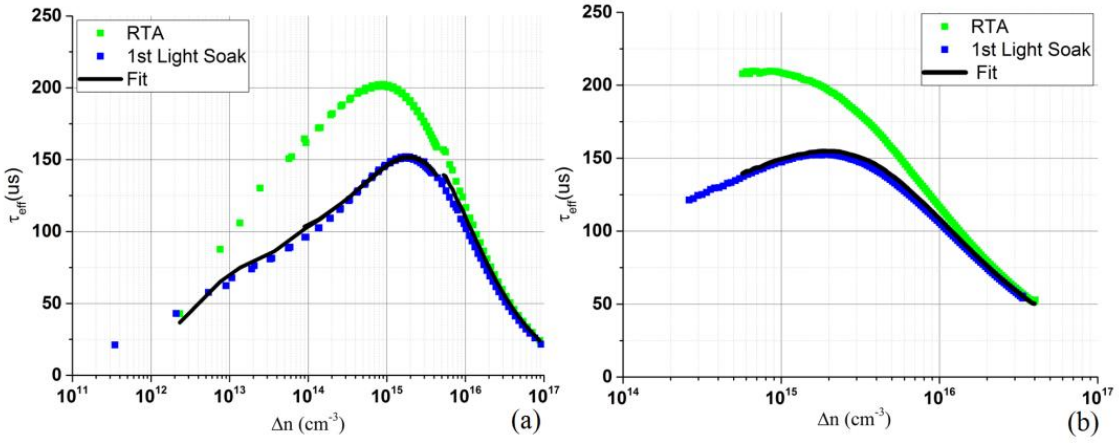

Figure 4-23. Injection-dependent τ_{eff} measured by (a) QSSPL and (b) QSSPC, representing the best fit of Eq.4-21 to the first light-soaked data using the RTA state as the initial state [i.e., Method I in Figure 4-13. The value of σ_n/σ_p was estimated to be 10.1 ± 0.9 and 8.5 ± 0.5 for (a) and (b) respectively. The error in the estimates was calculated from the covariance matrix of the least squares fit.

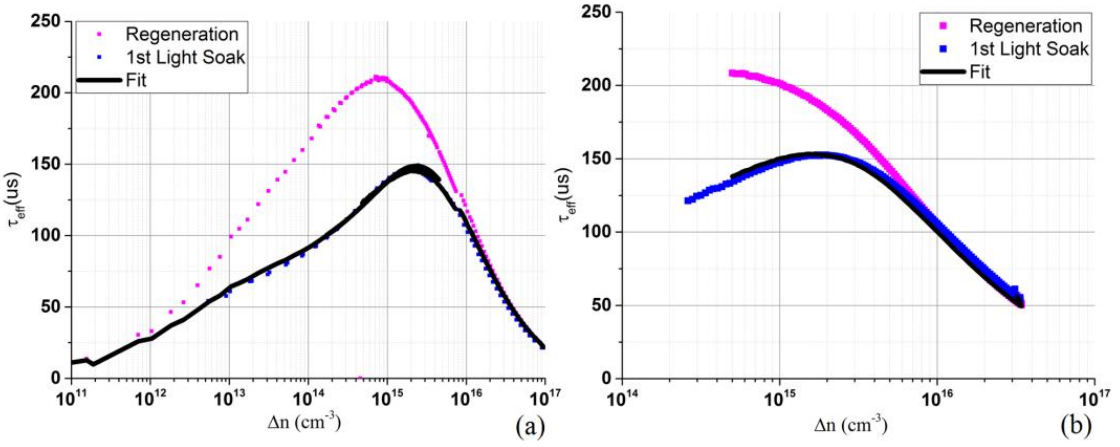

Figure 4-24. Injection-dependent τeff measured by (a) QSSPL and (b) QSSPC, representing the best fit of Eq. 4-21 to the first light soaked data from using the regenerated state as the initial state [i.e., Method II in Figure 4-13. The value of σ_n/σ_p was estimated to be 10.0 ± 0.7 and 15 ± 0.4 respectively. The error in the estimates was calculated from the covariance matrix of the least squares fit.

4.5 Conclusions

This study was motivated by the low *pFF* and multi-peaked *m-V* curves observed for the p-type bifacial solar cells, the fabrication of which was described in Chapter 3. Earlier experiments used a combination of QSSPL and QSSPC to investigate the effects of various cell processing steps on recombination in solar cells fabricated using the same cell structure as used for the bifacial p-type solar cells. It was shown that activation of B-O complexes in

the cells by light soaking can impact the *pFF* and be manifest in increased values of *m* in the injection range between the *mpp* and V_{OC}.

The recombination (introduced by light soaking) was modelled as a single SRH recombination centre at E_c - E_t = 0.41 eV and an σ_n/σ_p ratio of ~14. The effects of B and P laser doping on the injection-dependent *m* were also investigated. Boron laser doping was shown to introduce additional recombination in cells, as indicated by the increased value of *m* to ~ 1.5 in the injection range between the *mpp* and V_{OC}. However, in this initial experiment, the additional recombination was not well modelled by a single SRH recombination centre, especially in the mid-injection range, due to edge effects arising from the analysis of small cells and non-symmetric passivation. Finally, it was shown that high-temperature belt furnace anneals can place cells into a specific recombination state, and cells can be returned to this state by subsequent anneals even after additional recombination is introduced into cells by processes like laser doping.

A second study was then performed with the aim of increasing the accuracy of the modelling and further understanding the effect of the thermal annealing on p-type cells. Similar QSSPL and QSSPC measurements and modelling were performed but in this case 125 mm wafers with symmetric passivation were used to address the issues identified in the earlier study. With a higher intensity flash light, use of QSSPL measurements enabled τ_{eff} measurements over a larger range of injection levels than possible with QSSPC, potentially increasing the accuracy of estimates of the capture cross-section ratio of the deep-level B-O SRH defect. Although the value of σ_n/σ_p estimated using QSSPL (9.7 ± 1.7) and QSSPC (9.7 ± 1.9) for wafers symmetrically passivated with SiNx and subsequently rapidly fired were very similar and close to the value of 9.3 reported by Rein et al. for the B-O defect, significant differences in the ratio and larger variances in the within-group measurements resulted for wafers with SiN_x that were not annealed and wafers that were passivated with the thermal oxide. It was concluded that the inclusion of the low-injection QSSPL data may introduce inaccuracies arising from the conduction of excited carriers via the diffused emitter away from the measurement area. It is also possible that RTA, light soaking and/or regeneration processing steps may result in changes in the recombination properties of other defects which are manifest in the low-injection data. This may suggest that there is little advantage in using QSSPL over the more commonly used QSSPC measurements for these SRH analyses, and in

fact, such analyses may be best limited to the injection range at which the asymmetry of capture cross-sections becomes evident.

Additionally, the study confirmed that stable regeneration of τ_{eff} was only achieved when wafers were passivated with SiN_x and underwent a RTA after deposition. If wafers were not rapidly thermally annealed after SiN_x deposition, then the recovery of τ_{eff} observed with regeneration was not stable during a second light soak. Furthermore, the effective carrier lifetime of wafers passivated with a thermal oxide continued to decrease with light soaking, regeneration and a second light soaking, with the appearance of "rings" in the PL images of oxide-passivated wafers as they underwent light soaking and regeneration. This highlights the possible role of oxide precipitates in reactions occurring with light soaking and regeneration.

In summary, this work demonstrated that laser damage is not the only factor that results in a lower *FF* and high ideality factors in p-type bifacial solar cells, such as reported in Chapter 3. Use of a RTA could mitigate laser damage to some extent, but it has been shown in this chapter that RTA processes can also result in other side effects which could potentially lead to the degradation of fabricated cells in the long term, this degradation having origins which may extend back to the O defects which form during ingot growth.

CHAPTER 5
UNDERSTANDING PLATED METAL ADHESION

5.1 Introduction

5.1.1 Motivation

As discussed in previous chapters, Cu plating can reduce the consumption of Ag for Si PV manufacturing, whilst also offering the potential to increase cell efficiency by way of reduced shading due to very narrow fingers and contacting Si surfaces with low P concentrations. However, the previous chapters have shown that it can be challenging to plate busbars and fingers with sufficient adhesion to Si. For example, although in Chapter 3 it was demonstrated that bifacial laser-doped plated cells with an average efficiency of 19% could be fabricated, the finger and busbar adhesion of the plated grid was poor and hence soldered interconnection was not possible. Furthermore, although laser damage could be mitigated by using a fast laser speed to dope the contact regions through an AlO_x/SiN_x dielectric stack, the plated metal adhesion was too poor to fabricate any devices. Therefore, it was concluded that it is critical to understand why the plated metal adhesion is so poor if reliable plated PV module production is to be possible.

5.1.2 Objective

The primary objective of the experiments reported in this chapter was to investigate the critical factors that impact the adhesion of plated metal to Si solar cell surfaces and to explore whether the limited adhesion can be addressed sufficiently so that plated busbars can be soldered. To date, adhesion for cell metallisation has typically been assessed by busbar pull tests. However, when plating grids of fingers and busbars it is also important to ensure that fingers do not dislodge or peel during module fabrication. In this chapter, the contributions of the Si surface morphology and plated Cu properties to adhesion are evaluated using a combination of busbar pull tests and stylus-based adhesion measurements [37].

5.2 Cell Metallisation Adhesion Testing Methods

5.2.1 Busbar Pull Tests

Cell interconnection is a critical factor that affects the reliability and cost of Si PV modules. The industry standard method for cell interconnection is to solder alloy-coated Cu ribbons to the busbars and rear tabs of adjacent cells in a module. This interconnection method is widely accepted due to the advantages of low cost and high reliability, as it has been standardized in the semiconductor and microelectronic packing industries for many years. When the PV manufacturing industry adopted this interconnection technology, it also adopted the busbar pull test to evaluate bonding adhesion of the alloy-coated ribbons to the solar cell (e.g., see IEC 61189-3 [331, 332]).

Pull tests can be performed using different angles (see Figure 5-1) and pulling speeds, however comparison of pull forces requires the testing configuration to be fixed. The standards specifying the pull testing method do not define the angle and speed to be used for testing [331, 332] and consequently different testing conditions are frequently used, making it difficult to directly compare between published measurements.

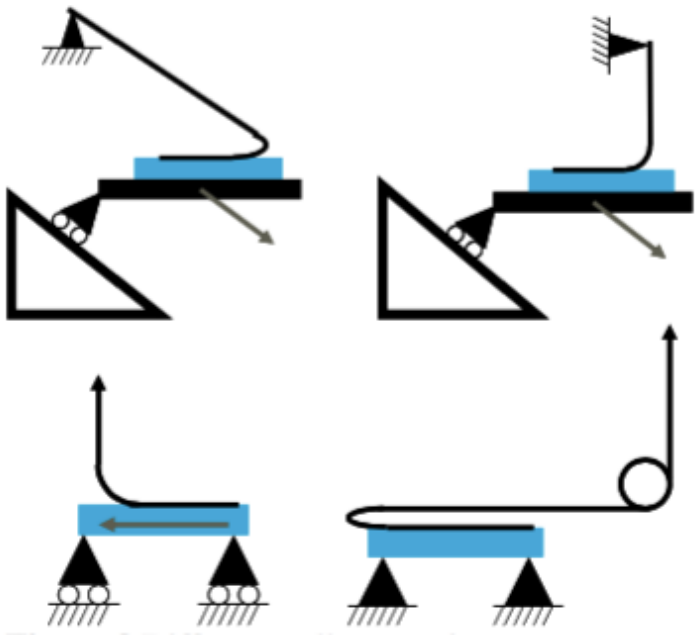

Figure 5-1. Schematic showing pull test configurations using different angles (from [332]).

With respect to the Si PV industry, the main argument for using a 180-degree angle pull test is that it can avoid wafer breakage during testing, as the force is applied parallel to the Si wafer. However, pulling at 180 degrees means that the measured force also includes contributions from ribbon bending. These contributions can be reduced by pulling the ribbon at an angle of 90 degrees and minimising wafer breakage by using two-block plates adjacent to the ribbon being tested (see Figure 5-2) [333]. However, even with this configuration, some cracking of the Si can be observed after measurement when the pulling force is large [333-335].

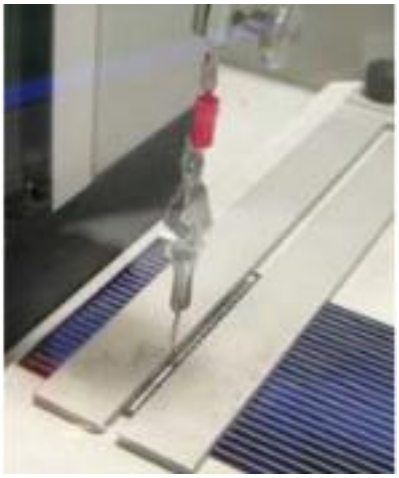

Figure 5-2. 90-degree pull test employed to reduce the chance of the solar cell breaking during measurement (from [333]).

Klengel further improved the 90-degree pull test by adding an additional opposing force to hold the solar cell in place a short distance before the peel point (see Figure 5-3) [332]. During the pull strength test, different failure modes can occur. When the adhesion force of the busbar is larger than the strength of the Si wafer, cracking of the Si is often observed during the measurement. However, this force recorded during the measurements is not the adhesion force of the busbar but the strength of the Si wafer. Therefore, it is important to avoid cracking of the Si wafer. By using the 90-degree pull test method with an additional opposing force, crack propagation in the Si during the pull test can be prevented and the recorded pull force can be shown to correlate with the fracture energy of the interface [332, 335].

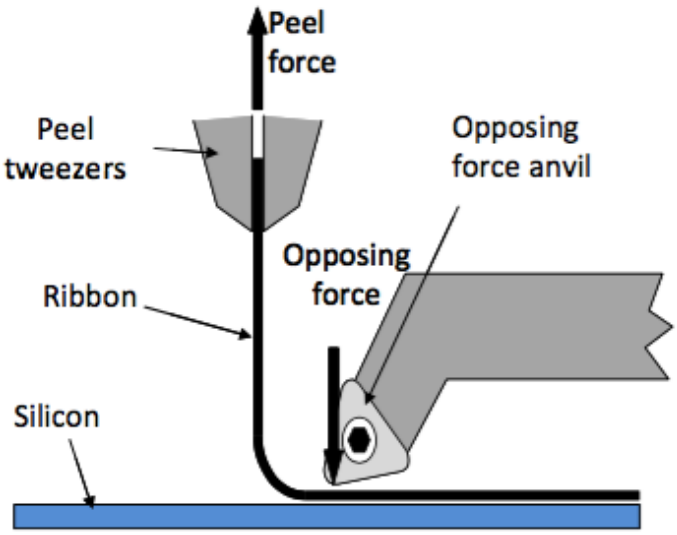

Figure 5-3. Improved testing of solder busbar proposed by Klengel [332], where an extra opposing holding force controls the peel (pull) angle.

However, as mentioned above, the standard for busbar pull test (IEC 61189-3) [335] does not specify which angle should be used and both the 180- and 90-degree pull test force measurements contain contributions from other factors in addition to the adhesive force of the cell busbar on the Si wafers. In reality, what typically occurs is that research centres and companies use different methods due to the limitation of their testing equipment and their personal preference.

5.2.2 Other Adhesion Testing Methods

Other testing methods for cell metallisation adhesion also exist. However, the basic theory is similar to that of busbar pull forces and evaluations typically involve measurements of the force required to detach one material from another. Many earlier methods (e.g., the tape test) were much simpler due to the lack of electronic force sensors [336-338]. Figure 5-4 below shows one of the basic versions of the tape test. In order to measure the adhesion force between the film and substrate, the tape is applied on the film and then pulled upward at an angle of 180 degrees. As the stickiness of the tape is a defined value which provides a constant force during the upward pulling, it can provide a measure of whether the film passes a certain adhesion criterion. However, it is difficult to extract more information about the process of peeling and to obtain a quantitative measure of the interfacial adhesion. This method, which is similar to the modern busbar pull test, has also been used to assess solar cell

finger adhesion [157, 339, 340]. In these qualitative assessments, the type of tape used must meet a certain specification otherwise relative comparisons are not possible.

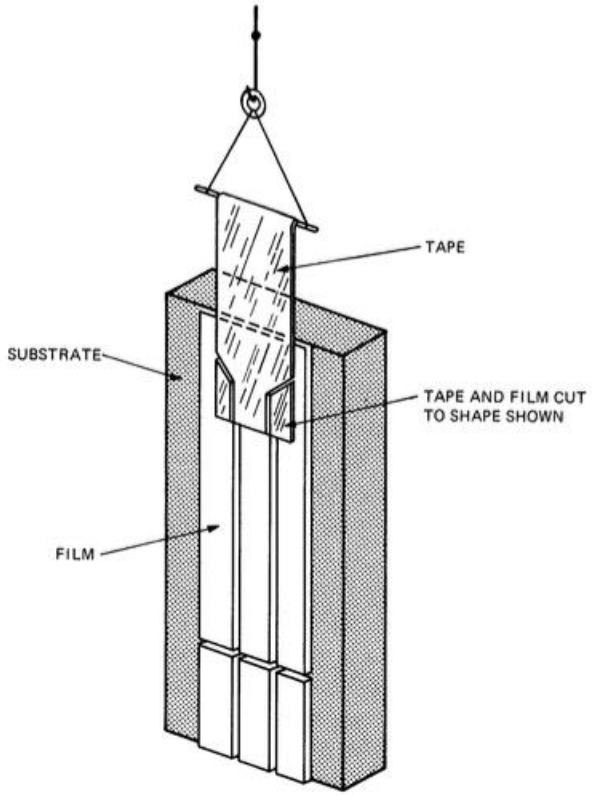

Figure 5-4. Tape pull test used to assess adhesion in the film industry[338].

Scratch or stylus testing methods have also been used to assess thin film adhesion [341-344]. In these methods, a sharp and hard stylus is used to scratch the top surface of the film with a downward loaded force. The stylus is typically mounted on force sensors, which can measure the force changes during the scratching motion. After the stylus has scratched the film surface, the film surface morphology changes (see Figure 5-5) and the failure mode can be identified by microscope. Heavens and Collins [345, 346] first used this method to quantitatively investigate the adhesion of metal films on glasses. After many years of development, scratch testing is now widely used in film adhesion measurement, especially in regard to evaluating ageing effects [337, 341, 347]. However, this method is not feasible for solar cell finger and busbar adhesion since it requires a large flat area of film.

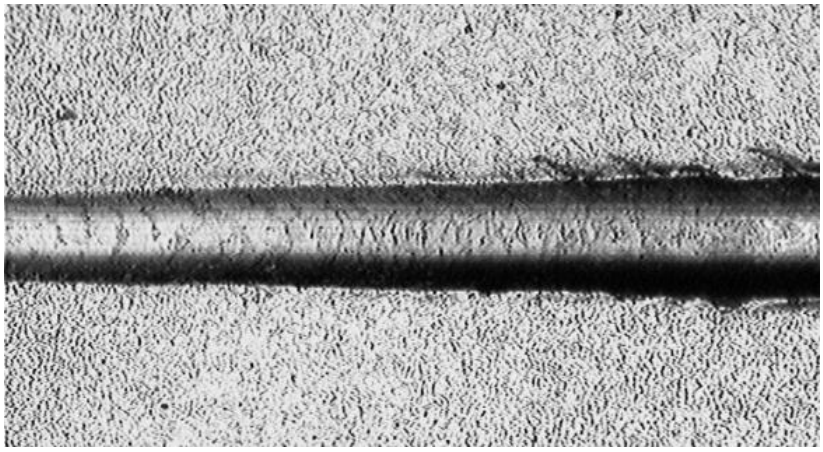

Figure 5-5. A sample film scratch test showing the scratch marks left behind on the film with increasing applied force, resulting in the formation of deeper grooves in the film (from [337]).

In another adhesion testing method, known as the four-point bending test (see Figure 5-6), a film sample is loaded on a steel substrate and an external load is applied with a compressive downward force. The film bends with the steel substrate and an acoustic emission transducer, mounted on the steel substrate, detects micro-fractures of the test film during bending. The acoustic signals can be correlated to the adhesion quality of the film [337, 348]. This method could potentially be used to assess interfacial adhesion of plated fingers and busbars on Si solar cells since the Si is thin and flexible and would also bend on application of the downward force. However, there have been no reports of the use of this method in the measurement or assessment of cell metallisation adhesion.

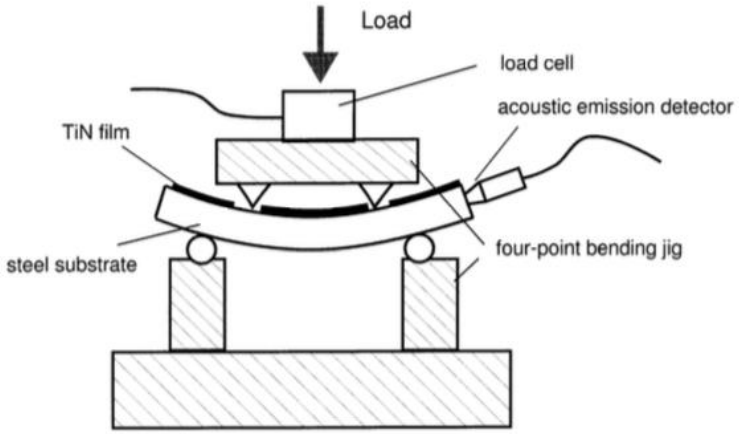

Figure 5-6. Schematic showing the operation of a four-point bending test (from [337]).

5.2.3 Stylus-based Adhesion Testing

Strong finger adhesion is critical for reliable plated metallisation; however, the scratch testing method used extensively in the film coating industry discussed previously is not suitable for finger adhesion tests since the measurement assumes a continuous film. In 2014, Young et al. adapted the scratch testing method to solar cell metallisation in their report of a stylus-based adhesion tester which could measure the lateral force required to dislodge metal fingers from the surface of a solar cell [349]. Figure 5-7 shows a photo of the weighted stylus used by Young et al. The stylus was mounted on a load cell, allowing the measurement of a lateral horizontal force as the stylus impacted fingers on a solar cell placed on an X-Y moving stage with vacuum chuck. During the measurement, the stylus (with a 0.7 mm tip) was in contact vertically with the solar cell surface and was freely able to move up and down due to its own weight or with an additional weight. As the stage with the solar cell moved laterally with respect to the stylus, the stylus impacted fingers and the load cell recorded the force required to dislodge them, F_D. The stage speed was able to be changed, but Young et al. typically used 0.5 mm/s to ensure sufficient force sampling during a finger impact to allow detection of the peak force. An additional weight on the stylus was used to ensure that the stylus did not 'slip' over fingers when the height of the fingers was insufficient to allow lateral dislodgement by the stylus. When the additional weight was used, the stage speed was increased to 1 mm/s to reduce the frictional losses associated with the relative motion across the solar cell surface [350].

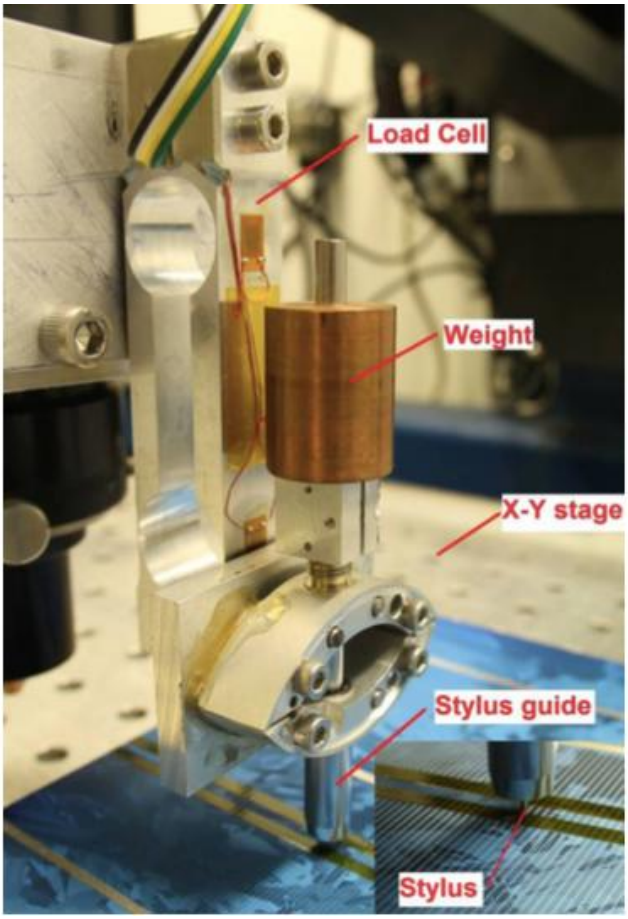

Figure 5-7. The finger adhesion tester reported by Young et al., which comprised of a weighted stylus on a force sensor. The solar cell being tested was moved laterally on a stage allowing individual fingers to be dislodged by the stylus (from [349]).

This finger adhesion test permitted the measurement of three useful metrics. The first metric is the peak dislodgement force, or F_D. After a stylus scan across a wafer (cell), the value of F_D can be extracted from the recorded time-sequential force measurements using a peak picking signal analysis algorithm. Histograms of F_D can then be generated to quantitatively compare between different metallisation processes (see, for example, Figure 5-8).

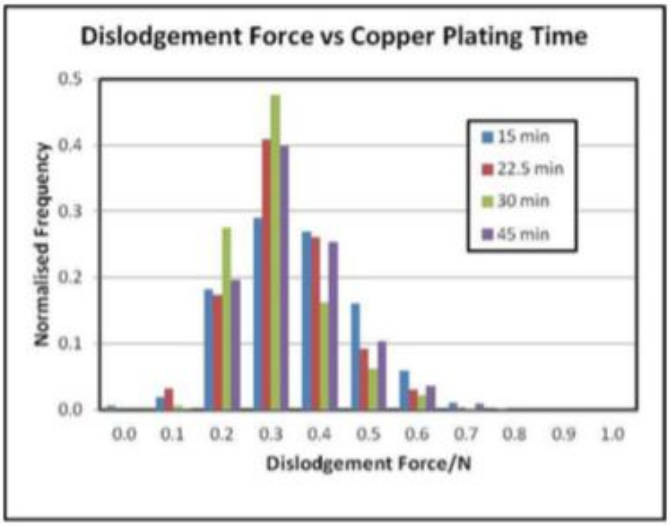

Figure 5-8. Histogram of F_D values recorded for cells, in which the Cu plating time was varied (from [349]).

The second metric that can be obtained using this testing method is the 'peel width' of the fingers. As the stylus dislodges fingers, the dissipated force results in fingers dislodging from the cell at both sides of the impact point and peeling laterally. The distance that the fingers peel can be measured and represented as a 'peel width'. Figure 5-9 shows how the 'peel width' can vary with different plating conditions (e.g., Cu plating duration). Finger peeling, which is discussed in more detail in this chapter, depends on both tensile stress in the metal finger (which can be affected by the plating process) and interfacial adhesion of the finger metal to the underlying Si. In the measurements reported by Young et al., tape was used to limit the extent of finger peeling so that multiple stylus scans could be performed across the wafer. However, within the non-taped regions of the cell, large visual differences in finger peeling were observable as a result of different metallisation conditions.

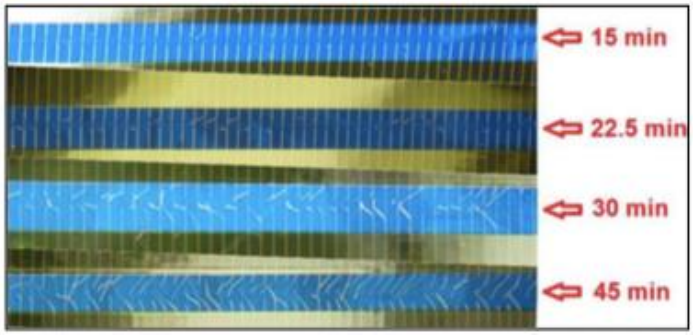

Figure 5-9. Photo of stylus scans for four different solar cells showing differences in peel width for different Cu plating durations (from [349]).

The third metric that can be obtained from this testing method is a mapping of F_D values across a cell. This is acquired by performing multiple scans across a metallised solar cell. This map of F_D values can show how the metallisation varies across an industrial 156 mm solar cell (see Figure 5-10). It can also be applied to screen-printed cells (see Appendix A). Cell F_D maps can be used to compare different plating conditions (e.g., anode position or chemical flows) and thereby assist in the identification of problems that may occur during the plating process.

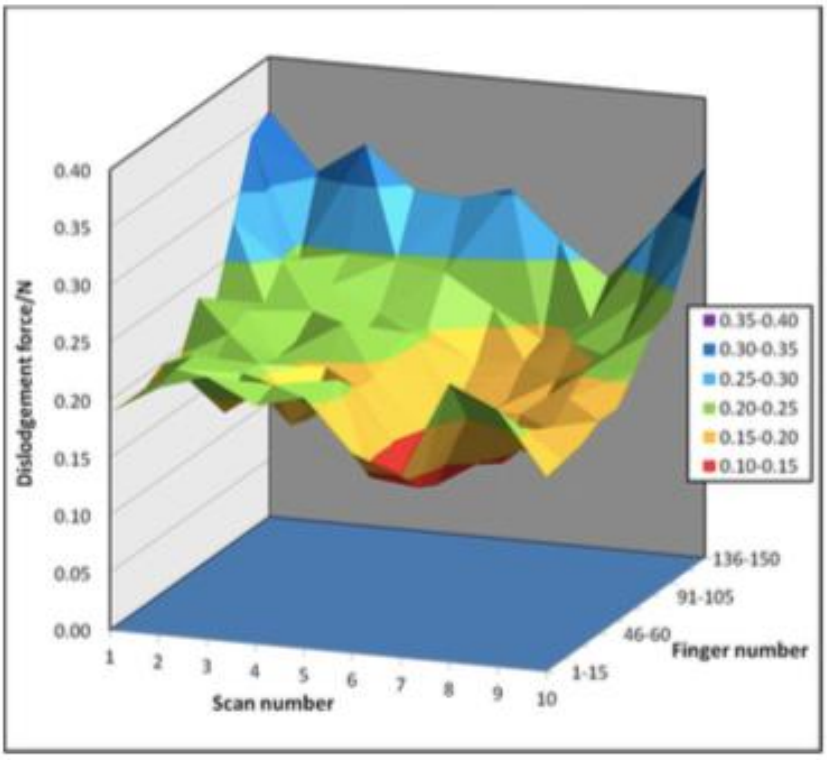

Figure 5-10. A map of F_D across a Cu-plated 156 mm laser-doped selective emitter cell showing a clear trend of lower F_D in one corner of the cell (from [349]).

These three metrics collectively suggest that the stylus-based testing method developed by Young et al. can represent a practical and useful metallisation metrology method. When cell fabrication is complete, *I-V* measurements can be used to assess electrical performance, PL imaging can be used to assess uniformity of minority carrier lifetime across a cell, and electroluminescence (EL) imaging can be used to identify non-uniformity in electrical contacting. However, none of these measurements can identify possible dislodgement or peeling of plated metal during module fabrication or during the lifetime of the module. For this reason, the stylus testing method reported by Young et al. was further developed at UNSW and was used in this thesis study to evaluate plated metal adhesion to Si solar cells.

In order to understand how the fingers respond to the lateral force applied by the stylus, an in-situ camera was installed to visually monitor the finger dislodgement process (see Figure 5-11) [351]. Chen et al. observed the existence of two distinct failure modes when the stylus impacted fingers. With softer and more fragile metal fingers (e.g., screen-printed Ag fingers), the stylus was observed to cut-through the finger with limited or no finger peeling [see Figure 5-11(a)]. This mode was classified as 'cut-off' mode. However, with the more rigid Cu-plated fingers, the stylus dislodged fingers, initially appearing to 'stretch' the fingers before they broke and peeled laterally from the point of impact [see Figure 5-11(b)]. This mode was referred to as 'dislodgement' mode. In some cases, when plated fingers were very short or very soft, cut-off mode was also observed. This observation suggests that fingers with a lower mechanical strength and strong interfacial adhesion are desirable for a reduction of finger peeling.

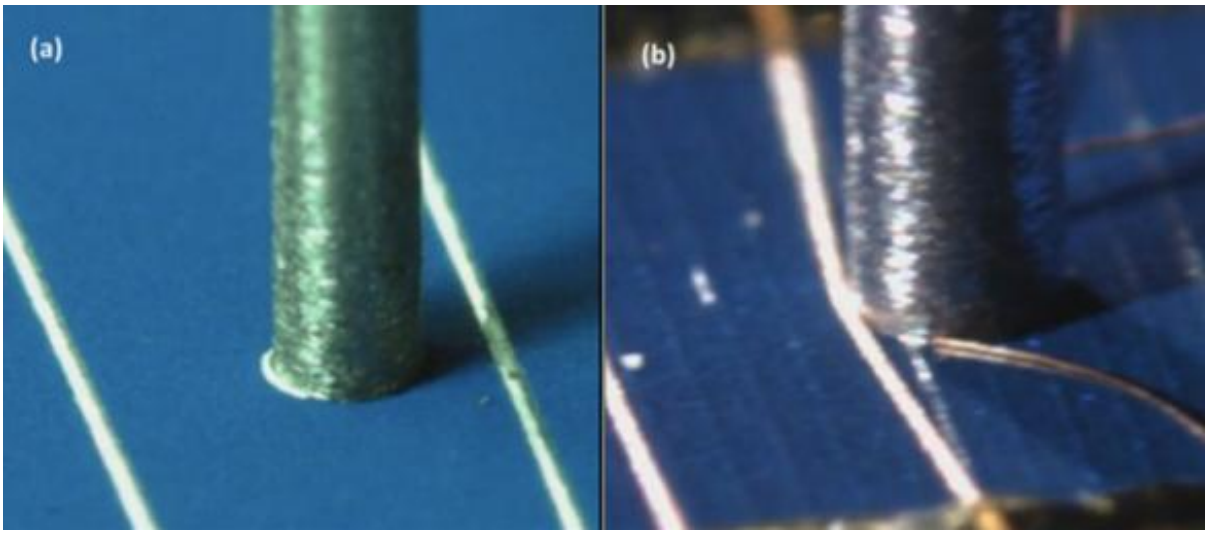

Figure 5-11. Recorded video frames showing the different failure modes that can occur on stylus impact: (a) cut-off failure shown for a screen-printed Ag finger; and (b) dislodgement failure shown for a plated Cu finger (from [351]).

The adhesion testing process, realised by the contributions of Young et al. and Chen et al., demonstrated the potential of stylus-based finger adhesion testing to be used to identify and monitor cell metallisation. The experiments reported in this chapter show how this testing method, used in conjunction with busbar pull testing, can be used to unravel the relationships between laser patterning, plating conditions and metallisation adhesion and cohesion.

5.3 Role of the Contact Opening Method

5.3.1 Introduction

In this section, the role of surface morphology, or surface roughness, in the adhesion of plated metal to Si solar cells will be discussed. Surface roughness is considered one of the most critical factors in metal adhesion. The cell fabrication experiments reported in Chapter 3 involved the use of a CW 532 nm laser to form the contact openings in the dielectric coating of both the n-type and p-type surfaces of the bifacial cells. The adhesion of Ni/Cu fingers plated to both the n-type and p-type laser-doped openings was observed to be poor.

This section reports on experiments in which the adhesion of Ni/Cu fingers, plated to openings formed by different laser processes (CW laser doping, ns and ps laser ablation), was measured and compared. Two different plating sequences were used for the laser-doped cells to assess their ability to improve the interfacial adhesion. The laser-ablated cells were all annealed after plating as this process has been demonstrated successfully before [38, 76, 78]. The adhesion was assessed using a combination of busbar pull forces and stylus-based finger adhesion measurements.

5.3.2 Experimental

In this experiment, two groups of wafers were prepared. Group A consisted of wafers that were laser-doped using a CW 532 nm laser (as described in Chapter 3), with subgroups, where the Ni was plated using a one-step Ni-plating process (Group A1) and a two-step Ni-plating process (Group A2). In Group B, the SiN_x ARC of the cells was ablated using either a ns or ps UV laser.

The Group A cells were fabricated from 156 mm alkaline-textured B-doped 1-3 Ω cm Cz Si wafers. Their emitters were P-diffused to a sheet resistance of 100 Ω/□ in a $POCl_3$ furnace. After PSG removal, a ~ 10 nm SiO_2 layer was thermally-grown on both wafer surfaces using dry oxidation and 75 nm of SiN_x (refractive index ~ 2.0) was deposited on the n-type surface by PECVD using a Roth & Rau MAiA tool. 200 nm SiN_x (Roth & Rau MAiA) was then deposited over the rear (p-type) thin SiO_2 layer (SiO_2/SiN_x rear passivation). Laser doping was performed using a 15 W 532 nm laser using 85% phosphoric acid and a PBF1 B spin-on source (from Filmtronics) to form the n+ and p+ grids, respectively. The laser speed for the

n-type side was 3 m s^{-1} and 0.5 m s^{-1} for the p-type side. The size of the finger-busbar grid was 23 mm × 23 mm.

The Group A1 cells were metallised using a one-step Ni plating process, (see Figure 5-12) in which, after the Ni annealing step, Cu was directly plated on the annealed NiSi surface. For the Group A2 cells, after Ni annealing, the surface was etched by immersion in HNO_3 for 15 min in order to remove any residual Ni and oxide, and a second Ni plating step was performed before Cu plating (see Figure 5-13). The cells were plated using bias-assisted LIP on the n-type surface and using FIP on the p-type surface. On both surfaces, the applied bias used with Ni (MacDermid Ni sulphamate) was 20 mA/cm^2) and with Cu (Technic $CuSO_4$) was 40 mA/cm^2. The final plated finger thickness was 10 µm for both surfaces. Annealing was performed for all Group A cells for 1 min by rapid thermal annealing (RTA) at 350 ºC in a N_2 ambient. For these cells, adhesion tests comprised of just stylus-based finger adhesion tests (see Section 5.2.3), as soldered busbars were insufficiently adherent to record a pull force.

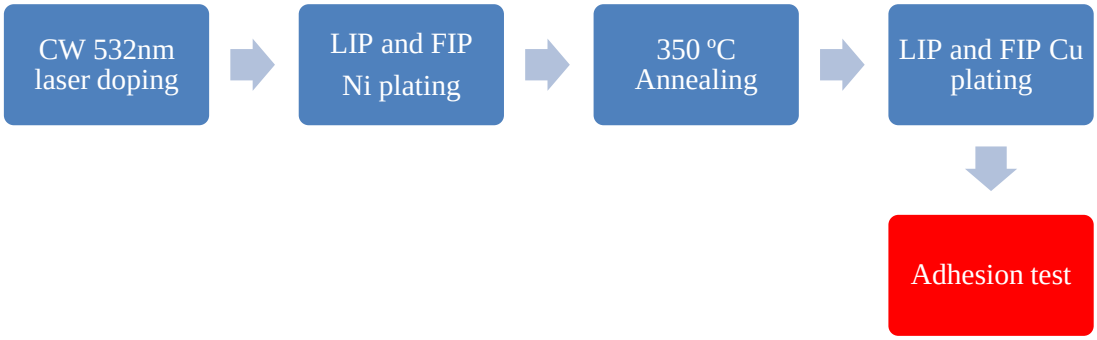

Figure 5-12. Metallisation process flow diagram for the laser-doped cells with a one-step Ni plating process (Group A1).

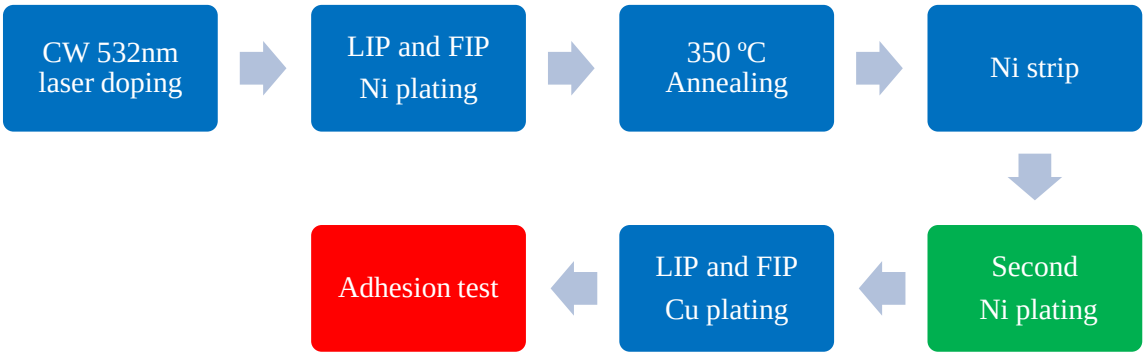

Figure 5-13. Metallisation process flow diagram for the laser-doped cells with a two-step Ni plating process (Group A2; green square shows the second Ni plating).

For the laser ablation group (i.e., Group B), P-diffused p-type alkaline-textured monocrystalline Cz wafers with 75 nm direct PECVD SiN_x and full-area Al back surface fields were laser-ablated using either a 248 nm ns Coherent Compex Pro laser (Group B1) or a 266 nm ps Lumera Super Rapid Nd:YAG laser with a BBO crystal for the 4th harmonic (Group B2). The ablated finger widths for the two lasers were 20 and 13 μm, respectively, and busbars were all ablated to a width of 1.5 mm. The cells were plated using bias-assisted LIP with Ni (MacDermid Ni sulphamate; 20 mA/cm^2) and Cu (MacDermid Helios EP2; 40 mA/cm^2) and then capped with immersion Ag (MacDermid Helios silver IM 452. All Group B cells were annealed after Ag capping for 1 min at 350 ºC in an RTP in N_2 ambient and then manually soldered with 1.5 mm interconnect ribbon (see Figure 5-14).

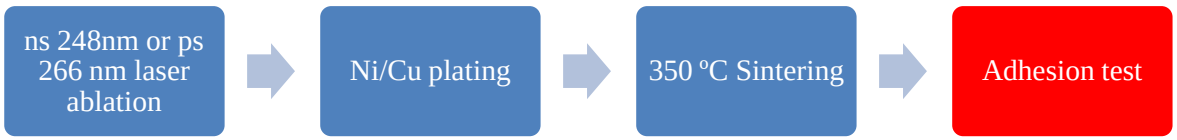

Figure 5-14. Metallisation process flow diagram for the UV laser-ablated cells (Group B).

Busbar pull tests were performed using an in-house built 180-degree pull tester, and the finger adhesion was evaluated using an in-house developed stylus-based adhesion tester functioning as described in Section 5.2.3.

5.3.3 Results

5.3.3.1 Laser-Doped Cells (Group A)

For all laser-doped cells, fingers were dislodged by the stylus, enabling direct comparison of finger F_D values between different cells and cell groups. Table 5-1 shows the measured F_D values for both surfaces of the plated laser-doped bifacial cells from Groups A1 and A2. The measured values were normalised to finger width to enable comparison between the fingers on the n-type surface (LIP) and p-type surface (FIP), because the finger widths arising from the different laser-doping processes differed (LIP 30 μm; FIP 45 μm). The average normalised F_D values for cells from Group A2 were a factor of two larger than the Group A1 cells for both the n-type and p-type surfaces. This confirms the findings of others that the two-step Ni plating process can enhance the adhesion of plated metal [27, 253, 256]. This increased adhesion is reported to be due to the formation of $NiSi_x$ during the annealing step [256]. It was also evident that the normalised F_D values of the fingers on the p-type surface were significantly greater than those for the n-type surface.

Table 5-1. Measured F_D values for p-type (FIP) and n-type (LIP) fingers of the laser-doped cells in Groups A1 and A2.The stated errors represent the standard deviation of the measurements.

Cell	LIP Group A1	FIP Group A1	LIP Group A2	FIP Group A2
F_D (N)	0.21 ± 0.05	0.42 ± 0.12	0.44 ± 0.13	0.85 ± 0.19
Normalised F_D (N/mm)	9.5 ± 2.3	19.1 ± 5.5	12.6 ± 3.7	24.3 ± 5.4

The visual images of the cell surface after adhesion testing showed significant differences in finger peeling between each process (see Figure 5-15). The p-type fingers (from FIP) of cells from both Group A1 and A2 experienced much less finger peeling than the n-type fingers. Similarly, peeling was significantly reduced for the n-type fingers of cells in Group A2 compared to those from Group A1.

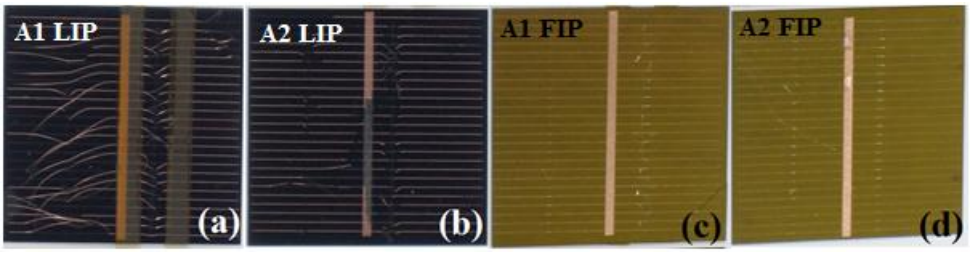

Figure 5-15. Peel width test for the different plated grids with: (a) n-type fingers (LIP) for Group A1; (b) n-type fingers (LIP) for Group A2; (c) p-type fingers (FIP) for Group A1; and (d) p-type fingers (FIP) for Group A2.

To further investigate the reasons for this difference in adhesion between the n-type and p-type fingers, after the finger adhesion test, the residue in the laser-doped grooves was examined. It was found that for the n-type fingers of cells in Group A1, adhesion always failed between the Si and Ni interface [see Figure 5-16(a)], which indicates a weak bonding between Si and plated Ni. For the p-type fingers, some Ni remained in the laser-doped grooves and, in some cases, only the Cu of the fingers was dislodged by the stylus [see Figure 5-16(b)]. This observation suggested that the adhesion between laser-doped Si and Ni was stronger for the p-type laser-doped fingers compared with n-type fingers. It was likely that the greater adhesion was due to the p-type grooves being much rougher, deeper and wider than the n-type laser grooves. The adhesion failure between Cu and Ni layers on the p-type fingers indicated that the Ni/Cu interface may have been impacted by the formation of a Ni oxide during the process (e.g., during rinsing after Ni plating), however it was difficult to confirm this because an oxide may also form during a measurement process.

Figure 5-16. One-step Ni plating (i.e., Group A1) showing: (a) complete removal of the Ni layer for n-type laser-doped grooves; and (b) retention of the Ni layer after adhesion testing of a p-type laser-doped groove.

For the cells from Group A2 (see Figure 5-17), adhesion failure mainly occurred at the Ni/Si interface for n-type surfaces, while dislodgement failure for the p-type fingers being more likely to occur at the Ni/Cu interface. This indicates that the adhesion of the Ni to Si was improved by the two-step Ni-plating method. It was also noted that in the n-type laser-doped grooves, the Si surface was changed from smooth and uniform to a rough surface with visible residues [see Figure 5-17(a)]. This may be due to Ni-Si alloy formation at the Si interface, however no traces of NiSi formation were able to be detected using either TEM/EDS imaging or Raman spectroscopy.

Figure 5-17. Optical microscope images of fingers after stylus testing for cells plated using two-step Ni plating for: (a) LIP fingers; and (b) FIP fingers. For (b) Ni remains adherent in the exposed grooves, indicating that the failure occurred at the Ni/Cu interface.

It can be concluded from this experiment that the two-step Ni plating process results in significantly higher finger adhesion than the single-step Ni plating process for laser-doped fingers. Furthermore, the adhesive properties of the p-type laser-doped fingers are distinctly different from those of the n-type fingers, with normalised F_D values being twice those measured for the n-type fingers and different interfaces failing on stylus impact (i.e., the Ni/Cu interface failing in some places before the Si/Ni interface). The reason for the increased F_D with the two-step process may be the removal of unreacted Ni and the roughening of the surface during the etching and replating process. Mondon et al. attributed the increased adhesion to $NiSi_x$ formation and void elimination during this two-step plating process [256]. They reported cross-sectional SEM images showing that both $NiSi_x$ and voids are formed at the Si interface and suggested that the void formation was due to the unbalanced inter-diffusion of Ni and Si during annealing and defects in the Ni. They showed that no voids existed before the annealing process, which suggests that the void formation occurred during annealing. In the presence of these voids, the adhesion between Ni and Si was poor, however etching the unreacted Ni and replating the Ni on the formed $NiSi_x$ was shown to remove the voids and increase the Ni adhesion to the Si such that busbar pull forces of up to 1 N/mm were possible. However, in this study, although the two-step Ni plating process resulted in increased F_D values, the plated metal adhesion for the Group A2 cells was not increased sufficiently to enable busbar pull testing of interconnected ribbon soldered to the busbars.

The larger F_D measured for the p-type fingers may be due to a number of factors, which include: (i) increased surface roughness due to the slower laser-doping speed used for the p-type grooves; (ii) wider fingers (though this is expected to be accounted for by normalising F_D with the width of the laser-doped opening); and (iii) slower regrowth of the native oxide after deglazing [256, 352].

This study also raises questions about the validity of directly comparing F_D values when different interfaces in a plated metal stack fail. Strictly, just as cut-off forces cannot be directly compared to dislodgement forces, the force required to dislodge Ni from Si is not directly comparable to that required to separate the Ni/Cu phases of the stack. Consequently it is necessary to always check which interface is failing in both busbar pull force tests and stylus-based adhesion tests.

5.3.3.2 Laser-Ablated Cells (Group B)

Figure 5-18(a) and Figure 5-18(b) show busbar regions where the SiN_x was ablated using the UV ns laser (Group B1) and UV ps laser (Group B2). Nanosecond laser pulses result in radiation, convection, vaporisation and melting in the Si, [173, 353, 354] and when they are used to ablate SiN_x from alkaline-textured surfaces, it is very common to observe a "ball" of Si exposed at the pyramid tips (see also Figure 5-19). This ball is believed to form as a result of the ns pulsed energy absorption being intensified at the pyramid tips and the resulting molten Si inflating due to the pressure of the evaporating Si [355]. The sides of the textured pyramids, however, remain relatively smooth in terms of nanoscale surface features.

Picosecond and femtosecond laser pulses can lead to a process called "cold ablation", where multiple photon absorption causes electrons to be stripped and pushed from the surface at high speed into a plasma cloud. The resulting coulombic attraction between the negatively-charged plasma and the positively-charged ions at the surface causes the surface material (e.g., SiN_x) to be removed or ablated from the surface [356]. This is an adiabatic process and does not significantly heat the substrate and hence little or no Si melting occurs. Ablation of SiN_x from a Si surface using a UV ps laser may not be a purely cold ablation process. The dielectric layer can also be removed by a process called "spallation", which involves the absorption of energy in a thin surface layer, creating a shock wave that can lift off material on the surface (e.g., a dielectric layer) [357, 358]. The relative contributions of cold ablation and

spallation depend on the wavelength of the laser, with cold ablation becoming the more dominant process with shorter wavelength lasers.

After ps UV ablation of SiN_x, the Si surface is considerably rougher in terms of nanoscale features than after ns laser ablation, with an interference pattern being evident on the surface [see Figure 5-18 (b)]. These patterns may arise due to hydrodynamic instabilities in the surface melt layer [189]. There is also an absence of the ball-like protrusions at the pyramid tips, suggesting that Si melting has been minimised.

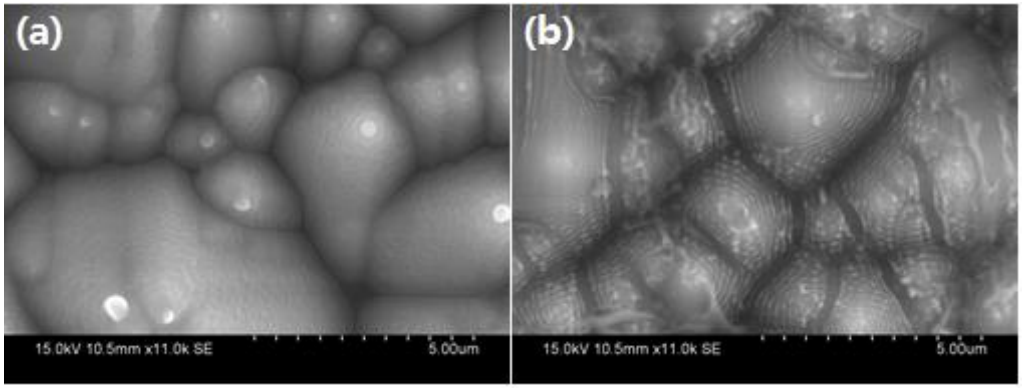

Figure 5-18 Alkaline-textured Si surface after SiN_x ablation using: (a) a 248 nm ns laser with a fluence of ~1.2 J cm^{-2}; and (b) a 266 nm ps laser with a fluence of 0.265 J cm^{-2}.

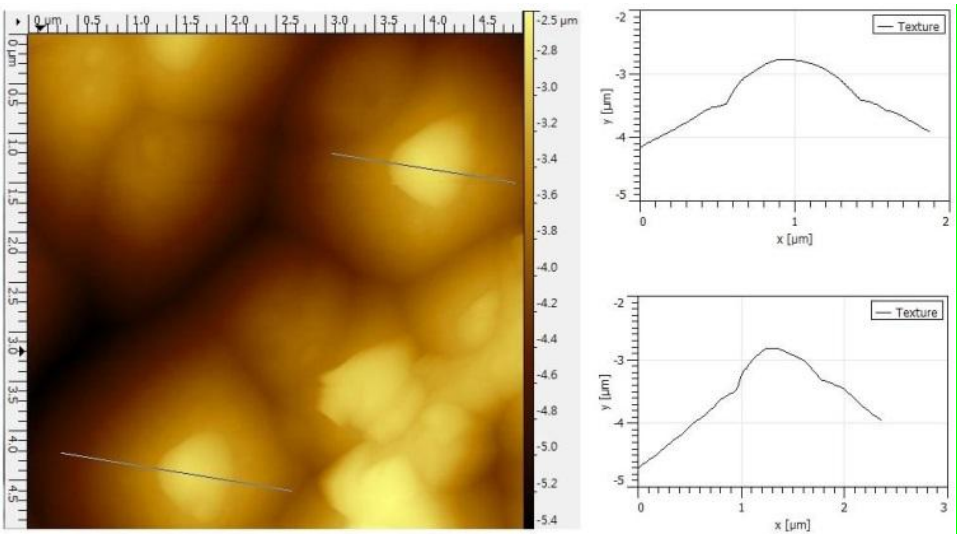

Figure 5-19 An atomic force microscope profile of an alkaline-textured surface where the SiN_x has been ablated using a 248 nm ns laser. Two cross-sections through pyramids are shown on the right illustrating "ball-like" protrusions from the pyramid tips due to molten Si flow during ablation.

The normalised F_D was 25 ± 22 N/mm and 148 ± 61 and for cells ablated using the 248 ns nm (Group B1) and 266 nm ps laser (Group B2), respectively (see Figure 5-20). Figure 5-21

shows sample cell surface regions after plated fingers had been dislodged. A two-sample t-test was used to determine whether the difference in F_D between Group B1 and Group B2 was significant. The results show that at the 0.05 significance level, the mean F_D of Groups B1 and B2 were significantly different for the cases of assumed equal variance and non-equal variance. Although the distributions of F_D in Figure 5-20 are not strictly Gaussian, the t-test is robust to non-normality especially in the limit of large samples numbers [359]. Therefore, it can be concluded that the 266 nm ps laser-ablated cell (Group B2) has a higher F_D than the ns laser-ablated cells (Group B1).

When the 248 nm ns laser was used for SiN_x ablation, the adhesion failure occurred between Si and Ni in 100% of the cases, indicating poor interfacial adhesion. However, when the SiN_x was ablated using the ps laser, fragments of Si were removed with the fingers in places, indicating regions of very strong adhesion of Ni to Si, especially considering that the ablated regions were only 13 μm wide. The greater interfacial adhesion resulting from ps laser ablation was also evident in the busbar pull test forces [see Figure 5-20 (b)], with an average pull force of 2.1 N/mm being recorded for cells where the SiN_x had been ablated using the 266 nm ps laser.

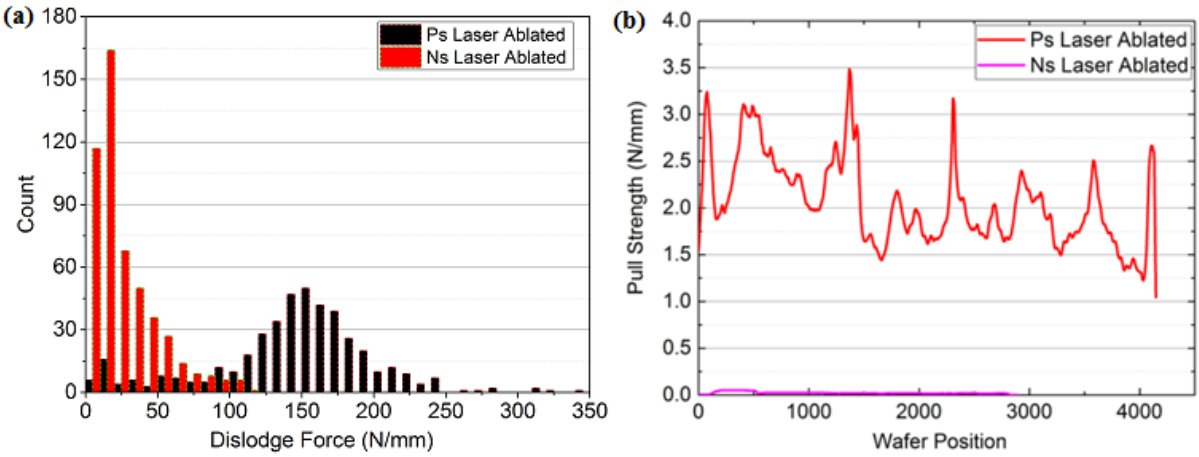

Figure 5-20. (a) Measured finger F_D values; and (b) 180° busbar pull test force for cells where the SiN_x ARC was ablated using the 248 nm ns laser or the 266 nm ps laser and Cu-plated at the recommended rate (the laser fluence was as reported for Figure 5-18).

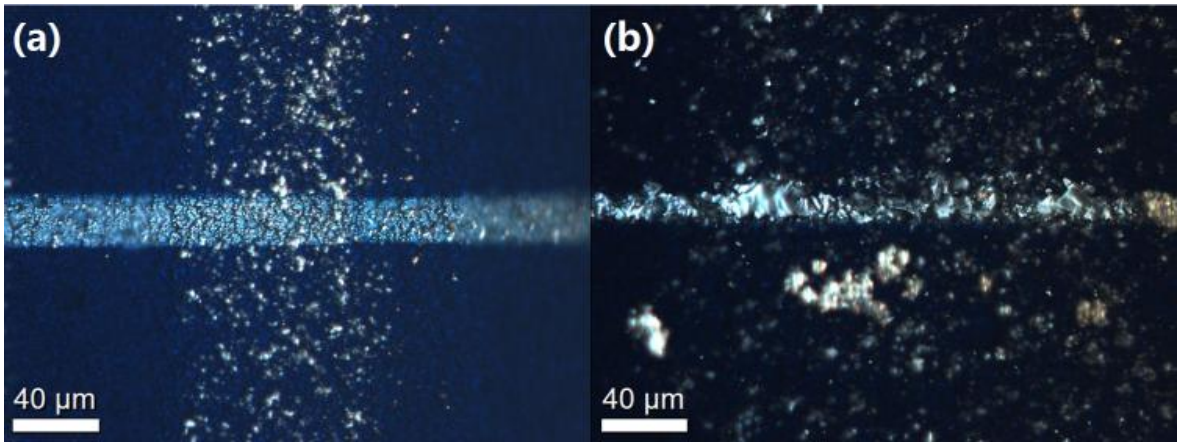

Figure 5-21. Cell surfaces after finger dislodgement: (a) a non-damaged Si surface after using the 248 nm ns laser to ablate the SiN_x (Group B1); and (b) showing fragments of Si removed when using the 266 nm ps laser for SiN_x ablation (Group B2).

5.3.4 Conclusions

In this section, stylus-based finger adhesion measurements were used to evaluate the adhesion of Cu-plated fingers to both the p-type and n-type laser doped grooves of the bifacial cells used for the experiments in Chapter 3. It was shown that a two-step plating process, in which unreacted Ni is etched after the Ni annealing step and the surface is re-plated with a thin layer of Ni before Cu plating, results in larger F_D values than the one-step Ni plating process. This result is consistent with the findings of Mondon et al. [256], who attributed the improved plated metal adhesion to the formation of a $NiSi_x$ and removal of voids, which is achieved by two-step plating. The function of the first Ni plating and annealing step is to form the $NiSi_x$. However, due to the non-uniform diffusion and defects in plated Ni crystal, voids occur after annealing. By etching back the plated Ni and re-plating, these voids can be eliminated, making possible significantly increased pull strength of up to 1 N/mm, at least for the study performed by Mondon et al. [256].

Larger F_D values were measured for the p-type laser-doped fingers compared to the n-type fingers. This increased adhesion may be due to annealing or surface roughness, but further experiments would be required to confirm this. Examination of the origins of the adhesion failure showed that the stylus impact caused failure of the Ni/Cu interface rather than the Ni/Si interface for many of the p-type fingers. This finding highlights the importance of checking where adhesion fails on stylus impact before direct measurements of stylus peak force are directly compared.

This study also demonstrated that larger F_D values can result by forming contact regions for metal plating using a UV laser to ablate the SiN_x from the Si surface with minimal melting or doping of the underlying Si. Use of a ns laser results in smooth pyramid surfaces with some extrusion of molten Si being evident at the pyramid tips. Less Si melting is evident with the use of ps laser ablation due to the shorter laser pulses, and after ablation of the SiN_x, the Si surface is covered with nanoscale ripples. This nanostructuring may contribute to the significantly greater normalised F_D values that were measured from the ps laser-ablated Si surfaces of 148 ± 61 N/mm, compared to the values of 25 ± 22 N/mm obtained for the UV ns laser-ablated surface. Both the ps- and ns- laser ablated cells were annealed after the plating of Ni/Cu and Ag, permitting all the wet processing steps to be completed before drying and annealing. The ps-laser ablated F_D values were significantly greater than those measured for the laser-doped bifacial cells (i.e., 24.3 ± 5.4 and 12.6 ± 3.7 for the p-type and n-type laser-doped grooves, respectively) when using the two-step Ni plating process.

The significantly increased interfacial adhesion enabled by the use of UV ps laser ablation for contact formation permitted the plated cells to be interconnected by soldering, an achievement not possible for any of the laser-doped cells. An average 180-degree busbar pull force of 2.1 N/mm was measured for Ni/Cu/Ag plated cells where the SiN_x ARC was ablated using a UV ps laser. This force is comparable to values routinely measured for three-busbar screen-printed cells [331, 332].

5.4 Effect of Plating Rate on Adhesion

5.4.1 Introduction

Although ps laser ablation has been demonstrated by several groups to enable sufficiently adherent Cu plated metallisation that allows cells to be interconnected by soldering [38, 40, 41, 76, 78, 360], the problem of finger peeling is not frequently discussed or reported. Finger peeling (see Figure 5-22), which can occur even though the pull strength of busbars is relatively high, is a critical issue that affects module reliability and yield [150]. Fingers may not peel immediately after plating, but may lift off the Si sometime after plating (e.g., while cells are stacked and waiting for interconnection) or perhaps also once the cells are encapsulated in a module. If the peeling occurs at the finger tips, the electrical impact of the

defect may be minimal, but modules will still fail for aesthetic reasons, thereby reducing module yield.

This section reports on experiments which were designed to investigate the contribution of plating rate to finger adhesion. Control of plating rate can be challenging with LIP. Although use of a bias current can address variability in plating rate due to a variable light-induced current, in cells with busbars and fingers, non-uniform plating can still occur due to the different opened areas in the grid. This issue is discussed in more detail in Section 5.5.

Plating rate can influence the material properties of plated metal. For example, stress can build up in plated metal depending on the rate at which metal is deposited, resulting in peeling or poor adhesion [338, 361-365]. If the fingers plate faster than the busbars, the extent of introduced stress will be different in each of the fingers and busbars. If the busbars plate slower, there may be very little stress evolved in the busbar regions and strong busbar adhesion may result. However, if the fingers plate faster, larger amounts of stress can be expected to be introduced into the plated metal, resulting in poorer finger adhesion and peeling. Consequently, it was proposed that for a reliable metallisation process, it is necessary to monitor both busbar and finger adhesion.

In the experiments reported in this section, finger adhesion was measured using the stylus-based tester for different plating rates. The study focused on Cu plating rates, as for typical plating conditions, the Ni thickness is typically < 1 μm, which is a small fraction of a total finger height of ~ 10 μm. Nano-indentation measurements were used to correlate plating rate with plated metal properties (e.g., hardness and Young's modulus), to further understand how the plating rate may affect the propensity of plated metal fingers to peel. The experiments all used short pulse laser ablation to form the contact regions, since this contact formation method was demonstrated in the previous section to result in adherent busbars as evidenced by strong busbar pull forces.

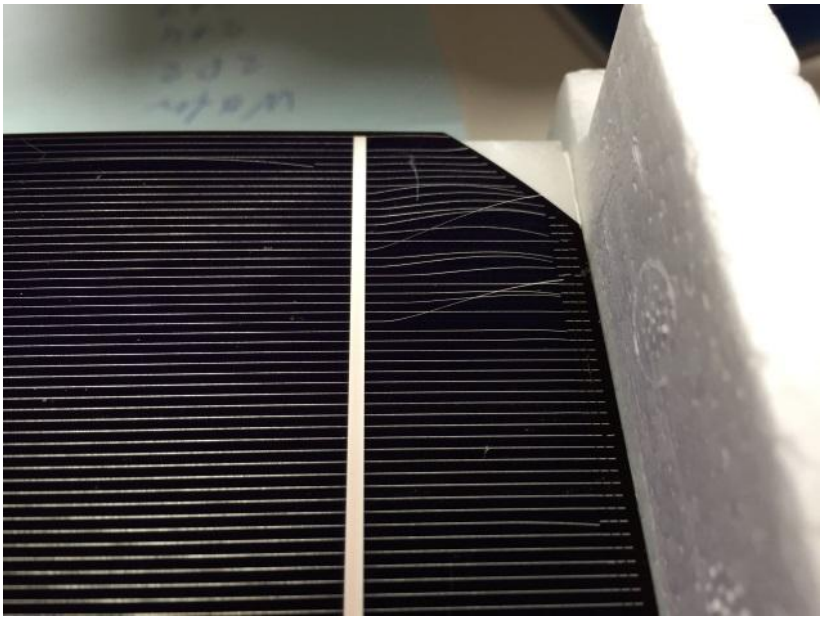

Figure 5-22. Example cell showing the case of fingers peeling and curving upward at the cell edges after plating and annealing.

5.4.2 Experimental

All experiments used P-diffused 1-3 Ω cm B-doped alkaline-textured monocrystalline Cz Si wafers to achieve an emitter having a sheet resistance of 120 Ω/□, a surface concentration of 4×10^{19} cm^{-3} and a junction depth of 0.4 μm. The illuminated surfaces of the wafers were coated with 75 nm of SiN_x deposited by direct PECVD, and the rear surfaces were screen-printed with Al and fired to form an Al-doped p+ layer and a rear electrode.

Laser ablation of the SiN_x to form openings for plated metal grids was performed using a Lumera SuperRapid 266 nm ps laser (Coherent) integrated into a galvo/stage micromachining system with a laser fluence of 0.265 J/cm^2. Three 1.5 mm wide busbars were ablated for all cells and fingers were spaced with a pitch of 1.4 mm. A pinning line [366] was ablated around the perimeter of the cell. The width of the ablated fingers was ~ 12 um. The laser-ablated cells were all plated using bias-assisted LIP with Ni (from a Barrett SN1 solution; MacDermid) at a current density of 20 mA/cm^2, then Cu was plated using Helios Cu EP2 [367] (from MacDermid) using the plating rates defined in Table 5-2.

Wafers were divided into 3 groups, as shown in Table 5-2, and plated at different current densities with the same illumination conditions (250 W/m^2 light intensity at the surface). The plating current densities used in this experiment for the slow, mid-range and fast plating rates were all within the recommended plating range for the Cu EP2 plating electrolyte.

Table 5-2. Cu plating rates used for the different experimental groups.

Chemistry	Recommended Plating Rate (mA/cm^2)	Plating Rate	
		Label	Current Density (mA/cm^2)
Helios Cu EP2	20 - 80	Slow	20
		Mid-range	40
		Fast	80

The nano-indentation measurements were performed using a NHT2 device nano-indenter with a diamond Berkovich tip from CSM Instruments. Nine independent measurements of Young's modulus (*E*) were recorded for each plating condition at each of the labelled positions on the test structures shown in Figure 5-23. The values of *E* reported were calculated from the measurement of hardness (*H*) using the method described by Oliver & Pharr [368, 369] and a Poisson's ratio (for Cu) of 0.3. The reason for using *E* rather than *H* for the analysis is that *E* is a measure of the stiffness of solid material while *H* is the relative resistance that a surface imposes to the penetration of a harder body. In the stylus finger adhesion test, the stylus typically deforms and dislodges the Cu fingers instead of penetrating the metal. Consequently, it was considered more relevant to use *E*.

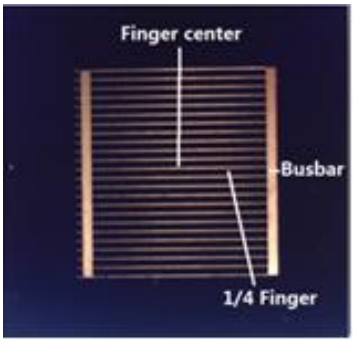

Figure 5-23. Grid pattern used for the nano-indentation measurements to determine the effect of plating rate on the finger metal properties.

5.4.3 Results

Figure 5-24 (a) shows the 180° busbar pull force of cells plated at different Cu plating rates. A pull force exceeding 2 N/mm was recorded along the entire busbar for cells plated with the different plating rates, with no significant difference in pull force being observable with the different plating rates. However, the finger adhesion measurements showed a very different

picture [see Figure 5-24 (b)], with very low normalized F_D forces being measured for the cell where Cu was plated at the fast rate. The cells plated at the slow and mid-range plating rates resulted in an F_D of 134-148 N/mm. However, the cells plated using the fast plating rate resulted in a low mean F_D of 65 N/mm. The variance of the measurements was large for all plating rates, suggesting unacceptable variation in finger adhesion across the 156 mm cells even for the slower plating rates. However, the distribution of F_D for the fast-plated cell was characterised by a large fraction of the finger impacts having an F_D < 20 N/mm and a long tail extending to higher F_D values.

Whilst these large changes were occurring with the measured F_D when fast plating was used, there was no significant difference in the 180° busbar pull force. Therefore, the increased propensity for fingers to peel with fast plating would not have been detected if only busbar pull forces had been used to monitor the metallisation process. It should be noted that even though UV ps laser ablation was used to ablate the finger regions, finger peeling with fast plating was still observed.

It is proposed that a low F_D results from either: (i) poor interfacial adhesion (e.g., as observed when a ns laser is used to ablate the SiN_x, as reported in [370]); or (ii) loss of elasticity of the metal (high E), which limits the ability of the metal conductor to dissipate the energy introduced by the stylus impact away from the impact area. In the second case, if the impact energy cannot be readily dissipated, fingers will dislodge at a lower force. Either cause for a low F_D is undesirable for reliable plated metallisation. If sharp wafer edges impact the plated fingers during packing of metallised cells, then non-elastic or stiff metal conductors will be more likely to dislodge and peel. Although low levels of finger peeling may not significantly affect the electrical performance of a module, they will have an aesthetic impact and therefore reduce yield.

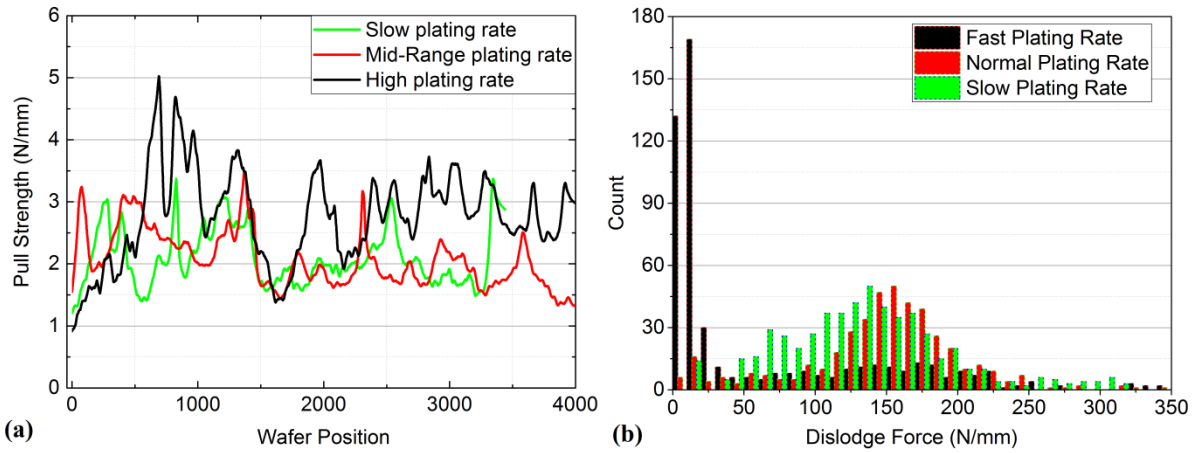

Figure 5-24. (a) 180º busbar pull force for cells Cu-plated using a fast, mid-range, and slow plating rate using the Helios EP2 Cu plating formulation; and (b) normalised finger F_D. All cells were ablated using the 266 nm ps laser and a fluence of 0.265 J/cm^2 and annealed after Cu plating for 1 min at 350 ºC in N_2.

Finger peeling after plating is commonly attributed to stress evolving in the plated Cu [371]. Figure 5-25 shows how the stress from fast plating of Ni can cause a plated cathode sheet from a Hull test [372] to bend when the plating current density is too high (i.e., when the sheet is too close to the anode). If the evolved stress is considerable, it can be directly determined using measurements of deformation [373]. However, this typically requires the use of test structures and significant quantities of metal, which may not accurately reflect the situation that exists in narrow plated Cu fingers used for metal grids of solar cells. Stress can also be directly measured using X-ray diffraction using a range of inclination angles [374, 375], but this approach requires long measurement times and averaging over many fingers to reduce the signal-to-noise ratio. Another method, which has been used by Song et al. [370] to monitor the evolution of stress during self-annealing, involves measuring the intensity of the (111) and (200) XRD peaks [376, 377].

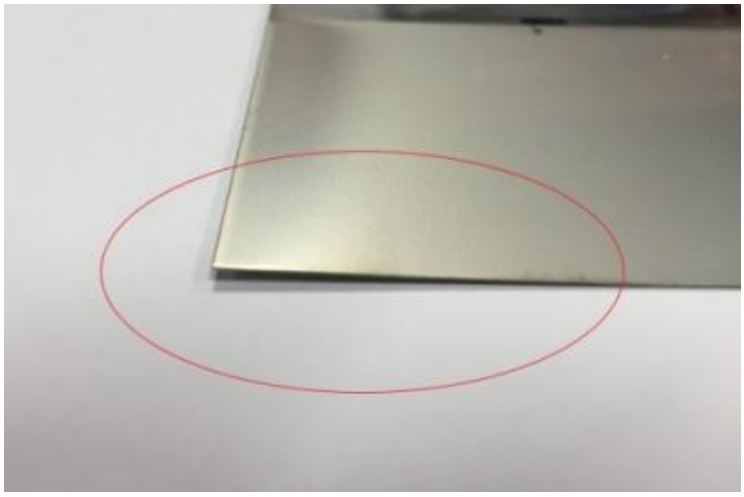

Figure 5-25. Plated Ni layer bending the flat cathode sheet in a Hull cell test due to use of a high plating current density.

Stress can evolve due to an increase in the stiffness or rigidity of the metal, so an alternative approach is to directly measure *E*. Changes in *E* may be evident before the results of excessive stress (i.e., finger peeling or deformation). Consequently, these measurements can be a more sensitive measure of potential metallisation problems. Figure 5-26 graphs *E*, obtained from nano-indentation measurements, at different grid locations of the test structures shown in Figure 5-23, where the Cu was plated at a slow, mid-range and fast plating rate. The measured value of *E* was 50-70 GPa and significantly less than expected for bulk Cu (dashed line in Figure 5-26) when slow and mid-range Cu plating rates were used. However, when a fast plating rate was used, the value of *E* and the variance of the measurements increased.

Increased rigidity or stiffness can arise due to a number of reasons. First, in addition to the metal salt, plating electrolytes contain C-based additives [245, 246, 378, 379]. Carbon can be incorporated into the plated metal, and being a covalently bonded material, tends to increase the rigidity of metals [380]. Second, H formed during the plating process, can interact with impurities, causing increased metal stiffness and resulting in H embrittlement of plated metal in extreme cases [381]. Both C and H can become located in the interstitial sites of the Cu face-centred-cubic lattice of grains making the Cu less elastic [380]. Fast plating can result in a higher H evolution rate and increased incorporation of impurities between grains due to non-uniform grain sizes [381-383]. These factors can contribute to increased rigidity which is reflected in the higher values of *E*.

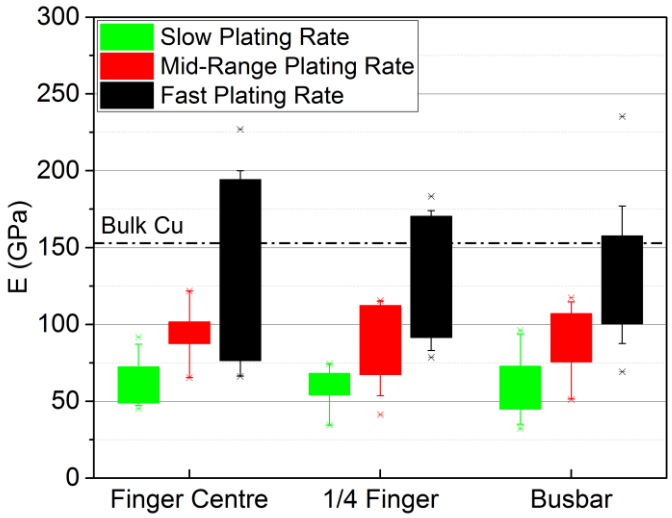

Figure 5-26. Young's modulus measurements at different locations on the test structures shown in Figure 5-23 (before annealing) which were ablated using a 266 nm ps laser and plated at a slow, mid-range and fast plating rate using Helios EP2 chemistry. The dashed line indicates the value of *E* expected for bulk Cu.

Figure 5-27 shows that for ps laser-ablated fingers, a fast Cu plating rate results in more extensive finger peeling than if a mid-range or slow plating rate is used. As discussed earlier, if the Cu is more rigid (has a higher *E*), it is more difficult for the energy from impacts to be dissipated along a finger, and consequently, the impact energy imparted by the stylus must be dissipated at the site of impact. Because rigid conductors are more difficult to break, the proceeding stylus imparts a lateral force which causes the fingers to peel. Figure 5-27 (a) and (d) show that the finger peeling that results from ps laser-ablated fingers when Cu is plated at a fast rate can be as extensive as observed for ns laser-ablated openings, which are known to result in weaker interfacial adhesion [370].

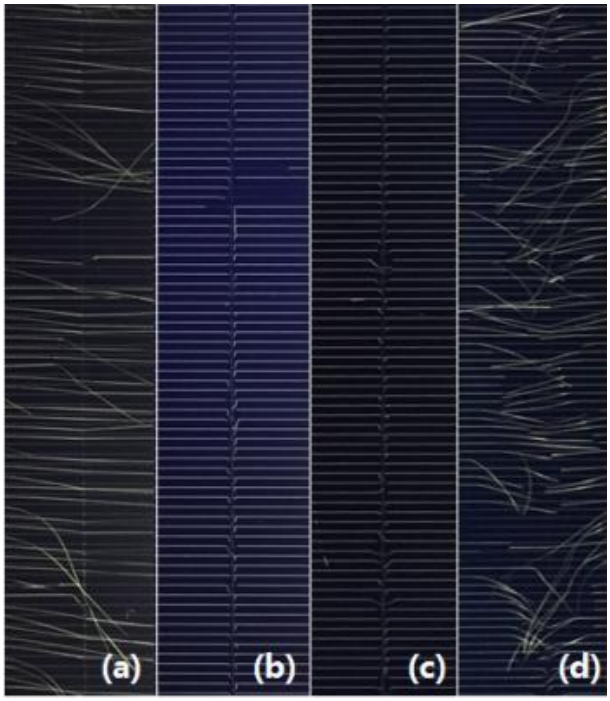

Figure 5-27. Peel widths of fingers ablated and plated using: (a) a ps UV laser and a fast Cu plating rate,; (b) a ps UV laser and the recommended Cu plating rate; (c) a ps UV laser and a slow plating rate; and (d) a ns UV laser and a recommended plating rate.

5.4.4 Conclusions

In conclusion, although acceptable busbar pull forces were measured when fast plating of ps laser-ablated fingers was used, low F_D values were measured for the fingers and they peeled more extensively than when a slow plating rate was used. Fast plating was shown to result in metal fingers with a higher rigidity or stiffness (characterised by high values of E). It was proposed that this increased rigidity makes it more difficult to dissipate energy from the stylus' impact, leading to lower F_D values and increased finger peeling. Also, the stress build-up in the fingers is larger for fast plating rates, which increases the chance of finger peeling, especially at the edge of the wafer where the deposition rate is faster. Although the stylus is an introduced artificial impact, it does simulate ways in which external forces may be applied to plated cells (e.g., contact with sharp wafer edges during cell stacking and sorting) which consequently may reflect some of the causes of finger peeling in a manufacturing environment.

5.5 Effects of Chemistry and Pattern Geometry

5.5.1 Introduction

Plated metal properties, and hence finger adhesion, can also be affected by the chemistry of plating electrolytes and the patterning structures. This section discusses experiments in which finger adhesion and nano-indentation measurements were used to investigate the impact of using different Cu plating electrolytes on finger adhesion. The experiments compared nitrate-based and sulphate-based Cu plating electrolytes. Although most Cu electroplating uses $CuSO_4$ chemistry, nitrate-based chemistry may result in less defects being introduced into the plated Cu crystal and thereby less induced stress [384].

Song et al. reported that that Cu-plated fingers can self-anneal after plating if not immediately annealed after plating [384, 385]. During this process, the Cu grains grow in size in order to minimise energy due to the incorporation of defects during the electrodeposition of the Cu. They showed that fingers plated using a $CuSO_4$ electrolyte self-annealed at a faster rate than fingers plated using a $Cu(NO_3)_2$ electrolyte and concluded that this was due to the increased number of defects introduced into the plated Cu [384]. Use of different counter-ions can result in different competing reactions (e.g., H evolution) and also the incorporation of different impurities in the plated metal. Both of these factors can result in the as-plated metal fingers having different properties. Also, because the effects of the different chemistries may also be influenced by plating rate, the effects of chemistry may affect the fingers and busbars differently.

As mentioned in Section 3.4, grid geometry can change the current density distribution at the opened areas of the grid. This factor was investigated further in order to understand the impact of changes in grid geometry on plated grid reliability. This is of particular interest with the current trend of having an increased number of busbars on cells.

5.5.2 Experimental

Experiments were performed using 23 × 23 mm test structures for improved accuracy and consistency of processing. All test structures were fabricated from 156 mm 1-3 Ω cm B-doped alkaline-textured monocrystalline Cz wafers diffused with P to achieve an emitter having a sheet resistance of 120 Ω/□, a surface concentration of 4×10^{19} cm^{-3} and a junction

depth of 0.4 μm. The illuminated surfaces of the wafers were coated with 75 nm of SiN_x deposited by direct PECVD and the rear surfaces were screen-printed with Al and fired to form an Al-doped p+ layer and a rear electrode. The wafers were then cleaved to form the smaller asymmetric test structures (see Figure 5-28). Laser ablation of the SiN_x was used to form openings for plated metal grids using a Lumera SuperRapid 266 nm ps laser (Coherent) integrated into a galvo/stage micromachining system with a laser fluence of 0.265 J/cm^2.

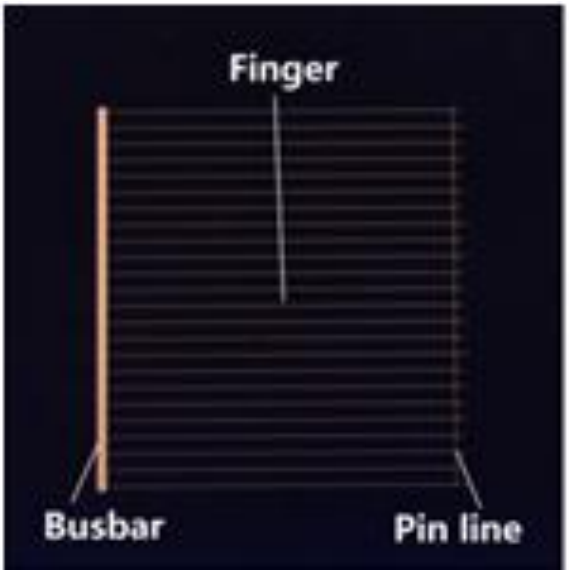

Figure 5-28. Grid pattern used for the Cu plating and nano-indentation measurements.

The laser-ablated cells were all plated using bias-assisted LIP of Ni (from a Barrett SN1 solution; MacDermid) using a current density of 20 mA/cm^2. Cu was then plated using either Helios Cu EP2 [367] (from MacDermid) or $CuSO_4/H_2SO_4$ (from Technic INC) as shown in Table 5-3. The cell structures were not annealed immediately after plating unless specified otherwise. The metal properties were determined by using nano-indentation measurements, as described in section 5.4.

Table 5-3. Cu plating electrolytes and plating rates used for the plating chemistry and grid geometry experiments.

Chemistry	Recommended Plating Rate (mA/cm^2)	Plating Rate	
		Label	Current Density (mA/cm^2)
Helios Cu EP2	20 - 80	Mid-range	40
		Fast	80
$CuSO_4/H_2SO_4$[1]	20 - 80	Mid-range	40
		Fast	80

5.5.3 Results

Figure 5-29 shows the value of *E* measured for test structures plated with the nitrate-based chemistry (i.e., EP2) and sulphate-based chemistry at two different plating rates. Two factors were observed in this comparison group showing the effect of plating rate and plating chemistry on the value of *E* of plated fingers. First, a higher plating rate resulted in a larger value of *E*. As explained by Song et al.[384], with a low plating rate (e.g., 20 mA/cm^2), the plated Cu forms a fine granular Cu microstructure after plating and then self-anneals over a period of up to 25 days resulting in gradually increased grain sizes. However, with a higher plating rate (e.g., 40 mA/cm^2), the self-annealing occurs much faster, taking only 2 days to complete. Song et al. concluded that tensile stress increases with grain growth and if the stress exceeds a critical value, degradation of the dominant as-plated (100) Cu texture can occur. Therefore, a higher plating rate will lead to increasingly fast self-annealing, resulting in increased tensile stress, which may also result in the likelihood of fingers dislodging from the Si surface. In this experiment, although measuring *E* was not a direct method for measuring tensile stress, the measurements showed a very similar trend to the self-annealing process. Secondly, significantly higher and more variable values of *E* were measured for the test structures plated using a $CuSO_4$ electrolyte compared to the $Cu(NO_3)_2$ electrolyte. Use of the Helios Cu EP2 chemistry has been reported to reduce H_2 evolution during Cu plating because the nitrate ion is reduced before H+ at high plating current densities [386] due to the larger standard electrode potential of the nitrate ion. Consequently, Yakobsen et al. proposed that H evolution can be effectively reduced at the cathode to a larger extent when using a Cu $(NO_3)_2$ electrolyte compared to using a $CuSO_4$ electrolyte. This may contribute to reduced H incorporation in the plated Cu and lower values of *E* with the $Cu(NO_3)_2$ chemistry.

Furthermore, the recrystallisation (i.e., grain growth) was considerably faster for fingers plated using the $CuSO_4$ electrolyte than observed for fingers plated at the same current density in the $Cu(NO_3)_2$ electrolyte. This suggests a higher defect density in the Cu immediately after plating using the $CuSO_4$ electrolyte, with the higher defect density providing a higher driving force for Cu self-annealing.

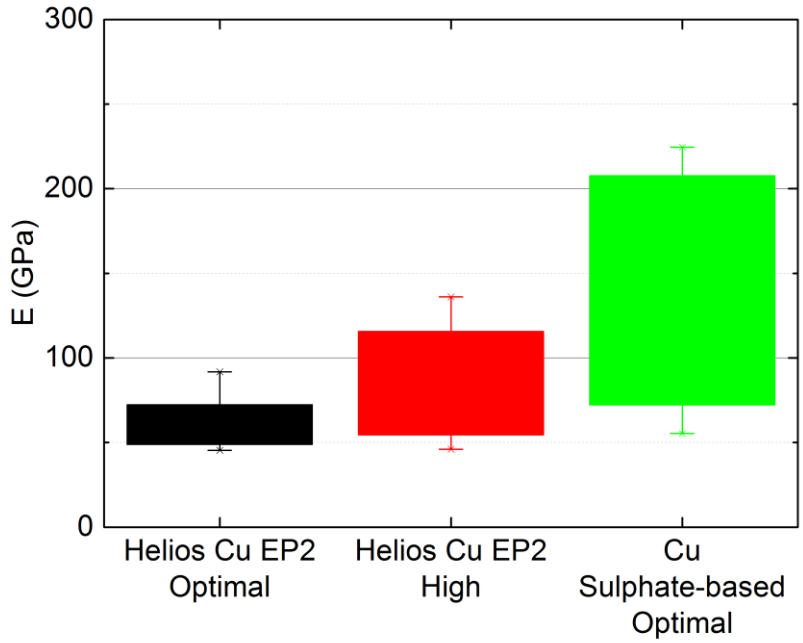

Figure 5-29. Young's modulus measurements for test structures plated with a $Cu(NO_3)_2$ electrolyte (EP2) and a $CuSO_4$ electrolyte. The nano-indentation measurements were performed midway between the busbar and the pinning line (see Figure 5-28).

Figure 5-30 shows the measured *E* for test structures plated at a mid-range and fast plating rate using a $CuSO_4$ electrolyte. Another factor that may contribute to the higher *E* with the $CuSO_4$ chemistry is the incorporation of S into the plated metal. Sulphur impurities can affect the nucleation of new grains during Cu deposition [380] and therefore may also result in further increased *E*. However, most studies only consider the S that is introduced through use of additives and not from the sulphate anion of the electrolyte.

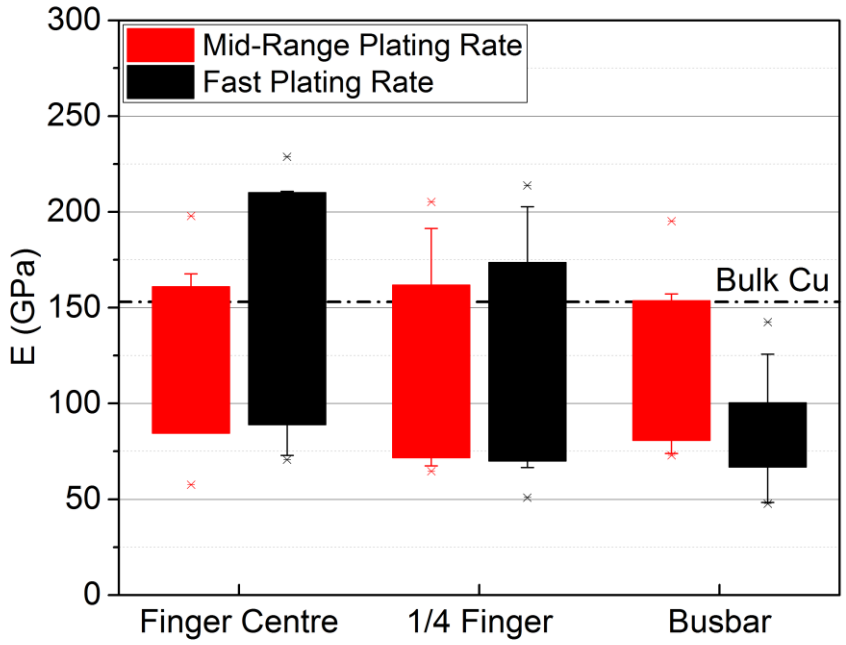

Figure 5-30. Young's modulus measurements at different locations on the test structures shown in Figure 5-28 (before annealing) which were ablated using a 266 nm ps laser and plated at a mid-range and fast plating rate using $CuSO_4$ chemistry.

The increased variance observed with fast plating for both chemistries may be a direct consequence of variations in the plating rate at different regions of the test structures. Alternatively, it may result if impurities are incorporated in the plated metal differently across the test structure. Figure 5-31 suggests that for the $Cu(NO_3)_2$ chemistry, grid geometry does not significantly affect the rigidity of the plated metal before annealing. However, a trend toward lower *E* closer to the busbar was observed when the Cu was plated from a $CuSO_4$ electrolyte. The lower *E* in the busbar regions can be attributed to a lower plating rate in these regions than experienced by the fingers. Busbars have a larger opening area fraction than fingers (see Figure 5-32), and consequently, use of a uniform bias current results in a lower plating rate in these regions. Adding to this non-uniformity is the fact that the presence of a plated Ni seed layer means that there is very little light-induced current driving the plating at the busbars due to shading. In the test structures plated at a fast rate with $CuSO_4$ chemistry, the different plating rate resulted in the height of the plated busbars and fingers being 7 and 15 um, respectively. Although thick plated busbars are not necessary for solder-interconnected cells, a plating process must ensure that the height of the fingers immediately adjacent to the busbars is not reduced such that current delivery to the busbars is impacted [36].

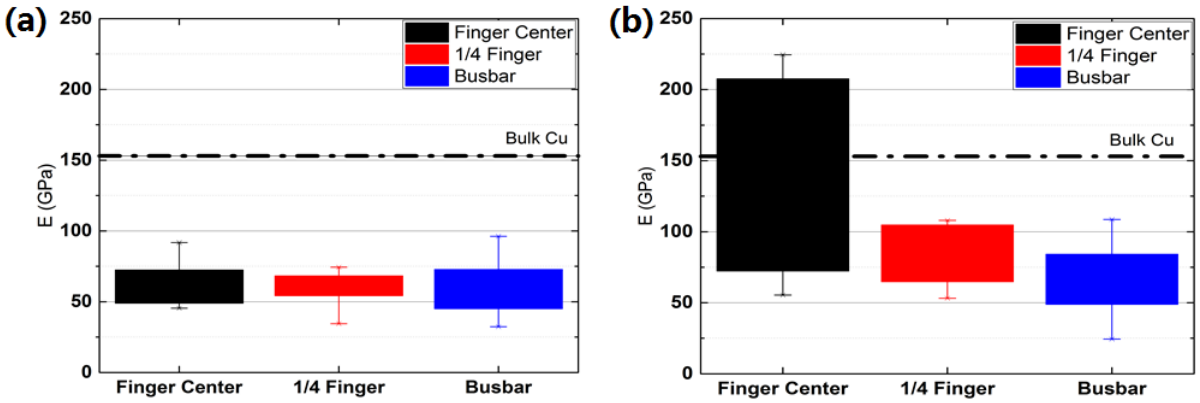

Figure 5-31. Young's modulus measured for fingers plated using: (a) $Cu(NO_3)_2$ (i.e., EP2); and (b) $CuSO_4$ chemistry, at different positions along a finger (see Figure 5-28).

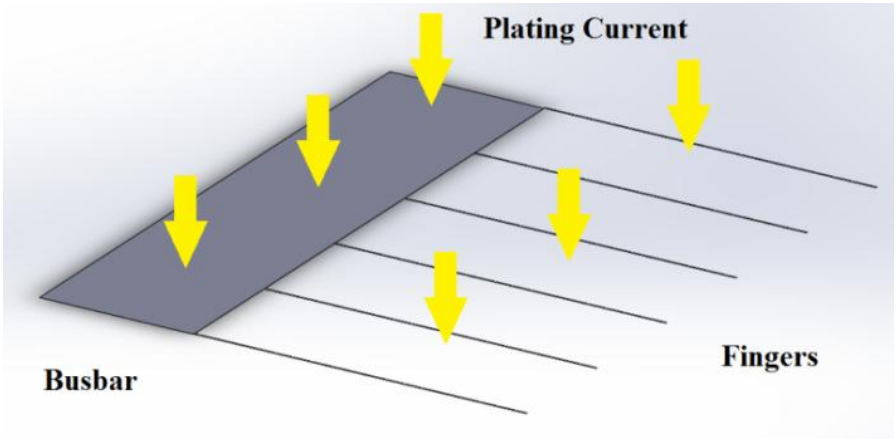

Figure 5-32. Schematic showing how different opening areas can affect the local plating rate when a uniform bias current is used during plating.

5.5.4 Conclusions

In this section, it was shown that Cu fingers plated using a $Cu(NO_3)_2$ electrolyte are less rigid (i.e., lower *E*) than fingers plated using the same plating rate using a $CuSO_4$ electrolyte. This difference in finger properties may arise due to reduced impurity incorporation when using the $Cu(NO_3)_2$ electrolyte. The nano-indentation measurements of *E* are consistent with the findings of Song et al. who showed that: (i) fingers plated with a $Cu(NO_3)_2$ electrolyte self-annealed slower than those plated with a $CuSO_4$ electrolyte due to fewer incorporated impurities; and (ii) faster self-annealing can introduce more stress in plated fingers as indicated by a degradation of the initial (100) grain texture in favour of more (111) texture [384]. This suggests that use of a plating electrolyte that can minimise impurity incorporation is important for metal finger elasticity and may directly impact the likelihood of finger peeling after plating.

It was also shown that grid geometry can affect the finger metal properties. The difference in opening area for busbars and fingers can result in a lower plating rate at busbars than at fingers due to the non-uniformly distributed plating current. Faster plating at fingers distant from busbars can result in higher values of *E* than closer to the busbar, making finger ends more likely to dislodge and peel. Use of thinner busbars and pinning lines at the edge of wafer may reduce the likelihood of very fast plating rates at fingers distant from the busbar and consequent finger peeling. The trend towards an increased number of busbars on the cell is expected to minimise non-uniformities of plating rate as the distance to an adjacent busbar is reduced for all fingers and busbars are thinner for achievement of similar shading fractions used for three-busbar cells.

5.6 Effect of Annealing

5.6.1 Introduction

It is often found that RTA after plating results in finger peeling, especially at the edge of the laser doped metal plated cells and laser ablated cells. However, annealing after Ni plating has been reported to improve adhesion (see Section 5.3.3). These observations appear contradictory, as it would be expected that RTA after plating should increase interfacial adhesion. However, if annealing is performed after Cu plating, the situation is more complex as differences in the thermal expansion coefficients of Si and Cu must also be considered in addition to changes at the Si-Ni interface. Therefore, in this section, experiments which investigated the role of annealing and plating rate on interfacial adhesion are reported.

5.6.2 Experimental

Experiments used 156 mm P-diffused 1-3 Ω cm boron-doped alkaline-textured monocrystalline Cz wafers to achieve an emitter having a sheet resistance of 120 Ω/□, a surface concentration of 4×10^{19} cm^{-3} and a junction depth of 0.4 um. The illuminated surfaces of the wafers were coated with 75 nm of SiN_x deposited by direct PECVD, and the rear surfaces were screen-printed with Al and fired to form an Al-doped p+ layer and a rear electrode. Some of the 156 mm wafers were cleaved to test structures for nano-indentation measurements (see Figure 5-33).

All laser ablation of the SiN_x to form openings for plated metal grids was performed using a Lumera SuperRapid 266 nm ps laser (Coherent) integrated into a galvo/stage micromachining system with a laser fluence of 0.265 J/cm^2. The laser ablation pattern for the 156 mm cells was the same as described in Section 5.4.

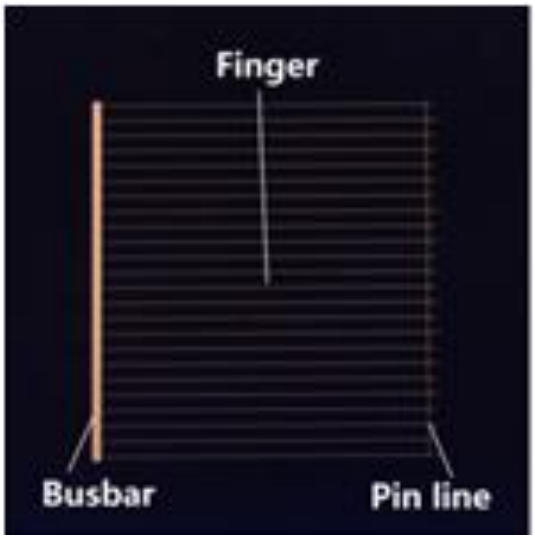

Figure 5-33. Grid patterns used for the nano-indentation measurements for the investigation into post-plating annealing.

The laser-ablated cells were all plated using bias-assisted LIP of Ni (from a Barrett SN1 solution; MacDermid) and Cu was then plated using Helios Cu EP2 [367]; MacDermid and $CuSO_4/H_2SO_4$ from Technic INC (see Table 5-4) in 3 groups. The metal properties (i.e., value of *E*) were determined by using a nano-indenter as described in Section 5.4.2.

Table 5-4. Cu plating electrolytes and plating rates used for experiments.

Chemistry	Recommended Plating Rate (mA/cm^2)	Plating Rate	
		Label	Current Density (mA/cm^2)
Helios Cu EP2	20 - 80	Mid-range	40
		Fast	80
$CuSO_4/H_2SO$	20 - 80	Mid-range	40

5.6.3 Results

Although analysis of metal properties before annealing can be used to understand how plating chemistry and grid geometry can affect the properties of the metal fingers, cells are typically

annealed before interconnection and stylus-based adhesion testing. Consequently, F_D and nano-indentation measurements were also performed after annealing in an RTP at 350 °C in N_2 for 1 min. Figure 5-34 shows frequency histograms of the measured F_D from 156 mm cells plated using the Helios EP2 electrolyte at a mid-range rate [see Figure 5-34(a)] and a fast rate [see Figure 5-34(b)]. The value of F_D increased from 100 ± 56 N/mm to 148 ± 61 N/mm after annealing for cells plated at the mid-range plating rate. However, when Cu was plated at the fast rate, the F_D remained low after annealing.

Rapid thermal annealing can introduce stress in thin metal fingers due to the mismatch in the thermal expansion coefficients of the plated metal and Si. Since the Ni layer is very thin, the introduced elastic strain, ε, can be considered to occur due to mismatches in the thermal expansion coefficients between Cu (α_{Cu} = 16.6 um/mK [387]) and Si (α_{Si} = 3.0 um/mK [388]) and is given by:

$$\varepsilon = -(\alpha_{Cu} - \alpha_{Si})(T_{RT} - T_{anneal}) \qquad \text{Eq. } 5-1$$

where T_{RT} and T_{anneal} represent room temperature and the peak annealing temperature (in K), respectively. For a cooling Cu finger on Si, the elastic accommodation strain will be positive and therefore tensile stress will be introduced [389]. Copper grain growth or densification also occurs on thermal annealing [370, 377] (see Figure 5-35). Therefore, different plating rates result in different as-plated grain sizes, while after annealing, Cu grains all become larger and similarly sized. The elimination of grain boundaries and merging of small grains, which largely occurs during the heating phase, also generates tensile stress [377]. Since the kinetics and extent of Cu self-annealing can depend on the nature of impurities incorporated at the grain boundaries [384], it is reasonable to assume that a similar dependence may exist for thermal annealing.

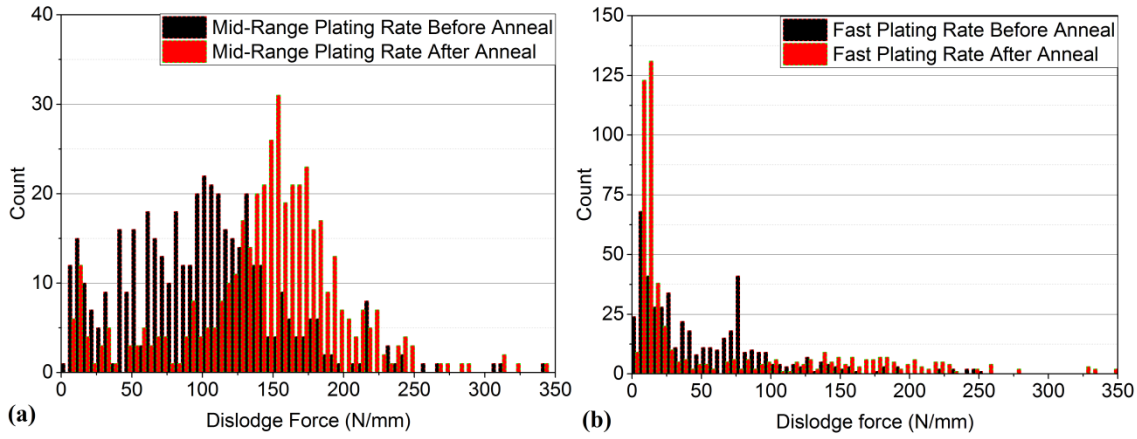

Figure 5-34. Frequency histograms of F_D measurements for cells where the SiN_x was ablated using a 266 nm ps laser and the Cu was plated using a Helios EP2 electrolyte at: (a) a mid-range plating rate; and (b) a fast rate, before and after annealing at 350 °C for 1 min in N_2.

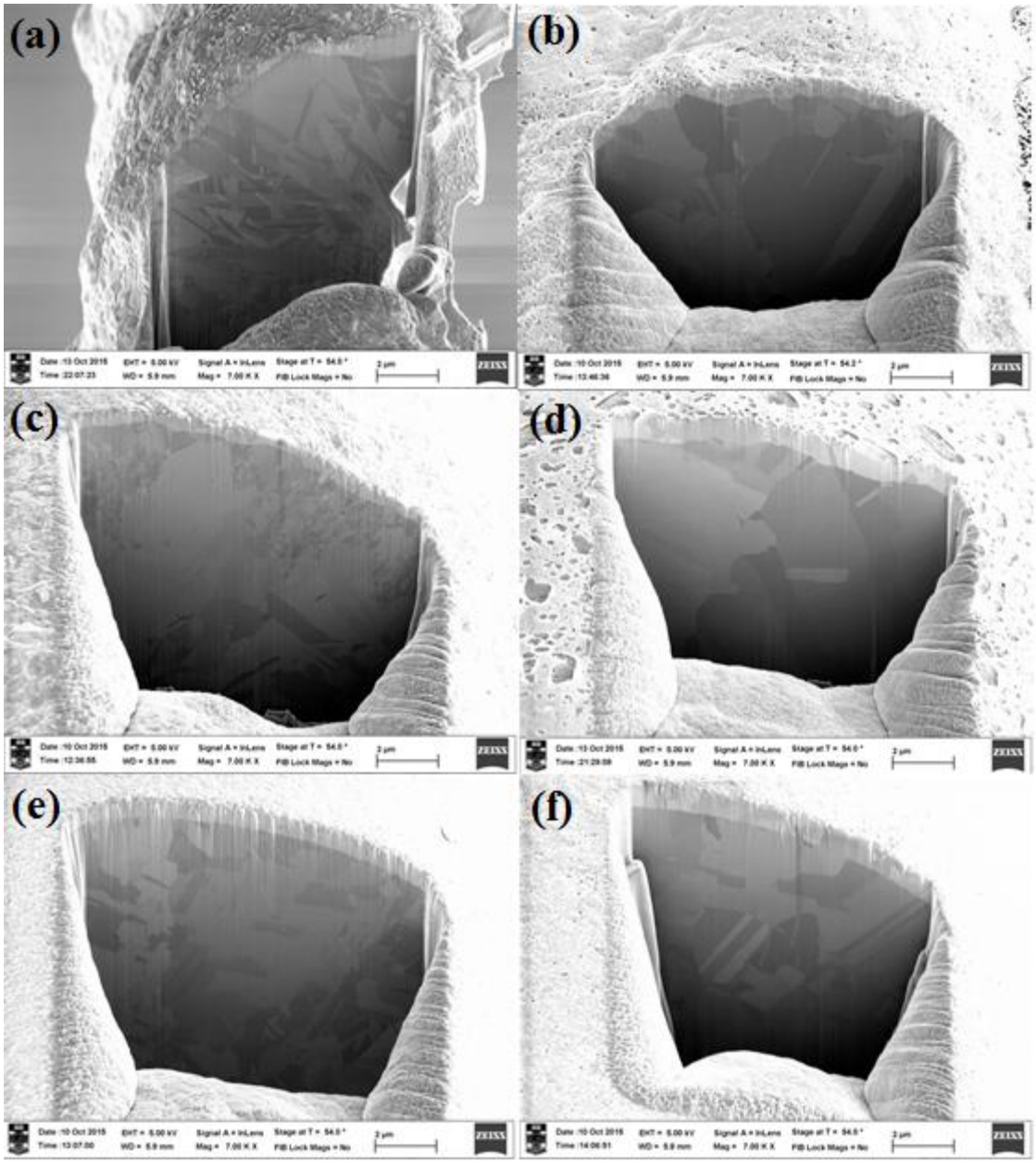

Figure 5-35. Cross-sectional images of Helios EP2 electrolyte plated Cu grain changes before annealing for (a) slow plating; (c) mid-range plating; and (e) fast plating; and after annealing for: (b) slow plating; (d) mid-range plating; and (f) fast plating.

Figure 5-36 shows the nano-indentation measurements of *E* before and after annealing for test structures plated using the Helios EP2 electrolyte [Figure 5-36(a)] and the $CuSO_4$ electrolyte [Figure 5-36(b)]. The value of *E* only increased for measurements in the middle of the finger when the Helios EP2 electrolyte was used; but was increased for all regions when the grid was plated using a $CuSO_4$ electrolyte. It should be noted that the nano-identation measurements were performed several weeks after plating and so some densification would have already occurred through self-annealing [370, 377]. It would be ideal to be able to

perform the nano-indentation measurement immediately after plating to monitor the evolution of *E* as densification proceeds, as reported by Song et al. [370], for grain growth monitoring. The significant difference in the measurements for the two chemistries highlights the role of impurities in the plated fingers' response to annealing. The low value of *E* obtained after annealing test structures are plated using the Helios EP2 electrolyte [see Figure 5-36 (a)] may be advantageous for soldered cell interconnection as the "softer" Cu may help dissipate the thermal stress that is incurred during the soldering process.

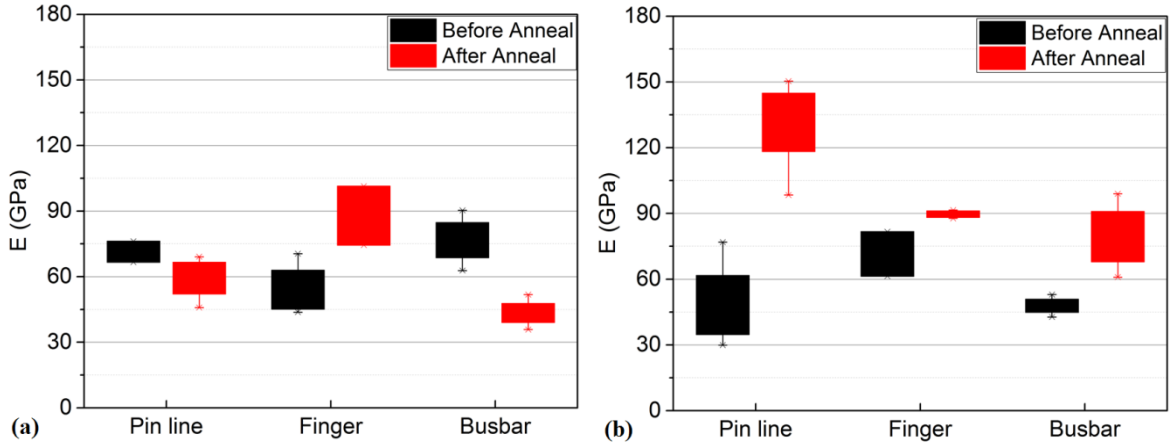

Figure 5-36. (a) Young's modulus measurements at fingers on test structures which were ablated using a 266 nm ps laser and plated at the mid-range rate using Helios EP2 chemistry; and (b) the $CuSO_4$ chemistry, before and after RTP Annealing at 350 °C for 1min in N_2.

5.6.4 Conclusions

Rapid thermal annealing after plating results in changes in the physical properties of the plated metal fingers. These changes, which can arise from stress introduced through the thermal mismatch between Cu and Si and impurity-driven densification, are dependent on the plating rate and electrolyte and can impact the value of F_D measured. It was shown that when a mid-range plating rate was used for the $Cu(NO_3)_2$ plating electrolyte, RTA after plating increased the average F_D from 100 ± 56 N/mm to 148 ± 61 N/mm. However, if a fast plating rate was used for the same chemistry, the value of F_D remained low (i.e., there was no significant improvement).

At the same time, with an RTA, the thermal mismatch in the plated Cu and the Si wafer can induce a force that can detach the plated metal. Fast-plated fingers are stiffer (i.e., higher value of *E*) and therefore less able to stretch and dissipate the force. This can lead to finger

peeling after annealing and low F_D values after annealing. Furthermore, it was also found in these experiments that the value of E always increased after annealing when a $CuSO_4$ electrolyte was used. However, when a $Cu(NO_3)_2$ electrolyte was used to plate the Cu, E only increased in the middle of the fingers, with decreased values of E being observed at the busbars and pinning lines. The resulting 'softer' fingers are more able to accommodate forces introduced by lateral impacts, which is consistent with larger F_D values and less peeling after impacts. Softer" Cu busbars may also help dissipate thermal stresses that are introduced during the soldering process.

5.7 Conclusions

In this chapter, it was demonstrated that finger adhesion can be quantitatively assessed using a stylus-based metallisation testing method that measures the force required to dislodge fingers. Provided that the failure mode that occurs on stylus impact is the same, measurements of F_D can be used as a measure of plated finger adhesion, to compare between different plating processes and complement the previously-used busbar pull forces to assess the reliability of plated metal grids.

It was shown that use of a two-step Ni plating process can significantly increase the average value of F_D for laser-doped contact openings, and that larger F_D values result from the fingers plated to the p-type openings of bifacial laser-doped cells than those plated to the n-type openings. However, in all cases the adhesion of the plated metal to the laser-doped contact openings was too poor to permit soldering of interconnection wire and measurement of pull forces. For this reason, attention was turned to the use of laser ablation to form the contact openings.

Use of a ps UV laser to ablate the SiN_x was shown to increase the value of F_D to values of 148 ± 61 N/mm, which was significantly greater than values of 25 ± 22 and 24.3 ± 5.4 for ns UV laser ablated contact openings and the best laser-doped contacts (i.e., p-type grooves plated using the two-step Ni process), respectively. The large improvement in plated contact adhesion was attributed to the nanoscale roughness of the Si surface after ablation of the SiN_x. Although the plated metal adhesion achieved using ps UV laser ablation was sufficient to allow soldered interconnection and busbar pull forces exceeding 1 N/mm, the large

variance of the F_D values remains a concern for the reliability of plated metallisation and will need to be investigated further in the future.

Currently most Si PV manufacturers rely solely on busbar pull forces for metallisation adhesion measurements. However it was shown that, with plated metal grids, busbar pull forces can exceed 1 N/mm but low F_D values and finger peeling can result. This situation can arise because the geometry of the metal grid can result in much faster plating rates occurring at fingers than at the busbars due to different opened areas. Fast plating was shown to result in metal fingers with a higher rigidity or stiffness (through nanoindentation measurements of E) and it was proposed that this increased rigidity makes it more difficult to dissipate energy from the stylus' impact, leading to lower F_D and increased finger peeling. Although the stylus is an introduced artificial impact, it does simulate ways in which external forces may be applied to plated cells (e.g., contact with sharp wafer edges during cell stacking and sorting). This finding of low F_D values whilst busbar pull forces remain above an acceptable lower limit has important ramifications for the introduction of metal plating for Si PV manufacturing and suggests that finger adhesion must also be monitored.

Finger adhesion is also sensitive the Cu plating chemistry used. The introduction of impurities during Cu plating can drive a densification process which can introduce stress into the fingers resulting in reduced F_D and finger peeling. It was shown that use of a $Cu(NO_3)_2$ electrolyte results in plated fingers with lower rigidity (i.e., value of E from nanoindentation measurements) than result from the use of a $CuSO_4$ chemistry. This was assumed to be due to different impurity incorporation during plating (e.g., fewer impurities or impurities that do not introduce stress on grain growth).

The nano-indentation measurements also confirmed that the plated metal properties varied depending on the geometry of the metal grid. For most measurements, the plated Cu was more rigid in finger regions distant from a busbar and it was proposed that this may occur as a result of the faster Cu plating rate that is expected to occur at the fingers during bias-assisted LIP compared to the busbar due to busbar's larger shaded area during Cu plating.

Annealing after plating can result in increased F_D values provided that the Cu plating rate is well controlled. If the Cu is plated at a fast rate, then the value of E can increase with annealing, the value of F_D remains low and finger peeling can occur, especially in regions that are distant from busbars and when $CuSO_4$ chemistries are used. The low value of E

obtained after annealing test structures plated using the $Cu(NO_3)_2$ electrolyte may also be advantageous for soldered cell interconnection with the “softer” Cu-plated busbars assisting in the dissipation of thermal stress during soldering.

Although busbar pull tests may be routinely used as the metric to assess metal grid adhesion for Si solar cells, this study highlights the risks in doing so, especially for plated metallisation. Reliable metallisation requires an understanding of the effects of grid geometry, plating chemistry and control of plating rate over a cell. Although it is generally known that plating rate and chemistry can affect the physical properties of electroplated metal, this study demonstrates that these changes in metal properties can be measured on completed cells and spatial variations over the surface of the cell can be identified thereby allowing process uniformity to be monitored.

Finally returning to the initial motivation for this study, it was concluded that in order to improve the adhesion of the laser-doped bifacial cells such that cells could be interconnected by soldering it would be necessary to increase the surface roughness of laser doped surface. Since the laser-doping process that resulted in the least laser damage (i.e., highest efficiency potential) also resulted in the smoothest grooves, this remains a challenging goal and it is difficult to see how ins situ doping and surface roughness can be achieved in a single laser process.

CHAPTER 6
CONCLUSIONS AND FUTURE WORK

6.1 Thesis Summary

The aim of this thesis was to investigate industrially-feasible processes for contact formation and metal plating for p-type Si solar cells, and in particular, to further the understanding of the role of contact formation in fabricating reliable and adhesive plated metal contacts. The thesis was motivated by the need to reduce the metallisation cost of Si PV cells by using Cu as the main conductor instead of Ag without compromises in cell efficiency

The thesis commenced in Chapter 3 with an investigation into the fabrication of bifacially-plated laser-doped p-type Si solar cells. Although the previously-reported LIP process can be used to plate a Ni/Cu grid to the n-type surface of p-n junction Si solar cells, the new process of FIP was required to plate the Ni/Cu grid to the p-type surface. In FIP, the p-type surface is made cathodic by forward-biasing the p-n junction through the application of an electric field across the cell. This application of FIP to the direct plating of p-type Si (described in this thesis) is disclosed in the granted US Patent 9,269,851 and applies not only to plating of bifacial Si cells but also to the plating of B-doped emitters of n-type cells [78, 195, 390, 391]. In parallel to the work reported in this thesis, Papet et al. demonstrated the use of forward-biasing of a heterojunction cell to achieve plating of a metal grid on the TCO surface adjacent to the p-type amorphous Si layers of heterojunction cells [192, 193].

Bifacial laser-doped p-type cells having a maximum efficiency of 19.2% were plated with Ni/Cu using a combination of LIP and FIP implemented with single side immersion and a soft electrical contact for biasing. The soft contact developed through this thesis significantly reduced wafer breakage over the earlier plating arrangements described by Zhao [200]. Although the ability to bifacially laser-dope and plate p-type cells with Ni and Cu presents a low-cost cell design with the potential for higher efficiency than screen-printed cells with an Al BSF due to being: (i) bifacially-passivated; and (ii) able to utilise an albedo factor through absorption of light from the rear surface, Chapter 3 identified two key problems. First, the creation of defects during the laser-doping process was shown to impact both the V_{OC} and *pFF* of final devices (though the introduction of non-ideal recombination). Second, the plated

grid adhered weakly to the laser-doped Si. Not only did the poor adhesion preclude soldered interconnection of cells, the plated finger adhesion was also poor, especially when fast laser doping through an AlO_x dielectric (in the absence of B source) was used to form the contact areas on the p-type surface of the cells. These two problems were investigated further in Chapter 4 and Chapter 5, respectively.

Chapter 4 described the use of injection-dependent minority carrier lifetime analysis of the SRH recombination occurring in cells' bulk after different processing steps using QSSPL and QSSPC measurements. The objective of this study was to understand the reason(s) underlying the low *pFF* of ~ 0.80 measured for the bifacial laser-doped cells fabricated and reported in Chapter 3. Analysis of bulk recombination was possible because the recombination at the cells' surface was maintained at a low rate due to being coated with dielectrics which resulted in low J_{0s} values. It was shown that B laser doping introduced additional recombination in cells, as indicated by the increased value of *m* (to as high as 1.5) in the injection range between the *mpp* and V_{OC}. However, it was difficult to model the additional recombination by a single mid-gap SRH recombination centre, due to edge effects arising from the analysis of small cells and the non-symmetric passivation of the bifacial cells. It was also possible that multiple defects were introduced by the B laser doping process increasing the difficulty of the analysis.

Since it was suspected that changes in the recombination state of the deep-level B-O defect occurred during annealing of the cells, additional experiments were performed on larger symmetrically-passivated wafers and used to estimate the σ_n/σ_p for the B-O defect using an E_t value of E_C - 0.41 eV and the $\tau_{eff}(\Delta n)$ data measured from wafers in a pre-light soaked, light-soaked and regenerated state. Values of 9.7 ± 1.7 and 9.7 ± 1.9 (similar to the value of 9.3 reported by Rein et al. [272]) were obtained using QSSPL and QSSPC measurements, respectively, for wafers that were symmetrically-passivated with SiN_x and rapidly annealed after deposition. This study confirmed that stable regeneration of τ_{eff} was only achieved when wafers were passivated with SiN_x and underwent a RTA after deposition. If wafers were not rapidly thermally annealed after SiN_x deposition or passivated with a thermal oxide then the recovery of τ_{eff} observed with regeneration was not stable during a second light soaking step.

Although injection-dependent minority carrier lifetime analyses have been reported previously using QSSPC [272] and local ideality factors from QSSPL [275], this was the first

study that directly compared estimated recombination parameters (such as the σ_n/σ_p for an introduced defect) calculated using both methods. However, it was concluded that the inclusion of the low-injection QSSPL data in these injection-dependent minority carrier lifetime analyses may introduce inaccuracies arising from: (i) the conduction of excited carriers via the diffused emitter away from the measurement area; and (ii) biasing the fitting by the inclusion of contributions from recombination of other defects which are manifest in the low-injection data. This suggests that there is little advantage in using QSSPL over the more commonly-used QSSPC measurements for these SRH analyses, and in fact, such analyses may be best limited to the injection range at which the asymmetry of capture cross-sections becomes evident.

Chapter 5 reported on investigations into the poor finger adhesion observed for the bifacially-plated laser-doped cells reported in Chapter 3. A key conclusion of this study was that surface roughness is one of the most important factors for plated metal adhesion to a Si surface. Use of UV ps laser ablation to form the contact regions can result in a nanoscale roughness that can enable average 180º busbar pull forces of > 2 N/mm and make possible soldered interconnection of cells. However, when contact openings were achieved using laser-doping (as used in Chapter 3 of this thesis) or using ns laser ablation, the busbar pull forces were too low to be measured.

The peeling of plated fingers observed for the plated laser-doped bifacial cells motivated the adoption of stylus-based adhesion testing of plated cells. For most plated cells, stylus impact resulted in 'dislodgement' failure, with 'cut-off' only being detected with either very wide or highly-adherent fingers. It was shown that plated Ni/Cu/Ag fingers adhere significantly more strongly to contact openings formed using ps UV laser ablation than formed using ns UV laser ablation or laser doping, with the average F_D for Ni/Cu/Ag plated fingers for ps- and ns-ablated surfaces being measured to be 148 and 25 N/mm, respectively.

Although busbar pull forces are routinely used in industry as a measure of contact adhesion, it was also shown that busbar adhesion is not always a good indicator of plated finger adhesion because, when plating a metal grid for a cell, different plating current densities can occur at the busbar and finger regions due to the different geometrical arrangements of fingers and busbars. For ps laser-ablated cells, use of fast plating did not impact the busbar pull forces but

the average F_D was reduced from148 N/mm to 65 N/mm due to stress evolution arising from the faster plating at regions of the cell distant from the busbars.

Experiments also employed nanoindentation measurements of E to analyse the effect of plating rate and electrolyte composition. When plating was performed at a rate corresponding to the middle of the recommended plating rate for the formulation, the values of E measured in fingers of test structures plated in a $Cu(NO_3)_2$ electrolyte were in the range of 50-90 GPa (Measured $E_{Bulk,Cu}$ = 152 GPa) when a $Cu(NO_3)_2$ electrolyte was used and 55-225 GPa when a $CuSO_4$ electrolyte was used. The greater rigidity of fingers plated using the $CuSO_4$ electrolyte, and variation in rigidity within and between different samples, presumably arises due to increased impurity incorporation. Increased finger rigidity increases the propensity of fingers to peel if impacted, reduces the F_D and increases the likelihood of reduced adhesion after post-plated RTA. This result highlights the need to understand the role of chemistry for reliable plated metallisation.

6.2 Original Contributions

The original contributions of this thesis are summarised below.

1. The use of FIP to plate Ni and Cu to p-type Si surfaces of bifacial laser-doped solar cells was demonstrated resulting in cells with efficiencies as high as 19.2%.

    - As mentioned above, the FIP plating process described in Chapter 3 of this thesis and in Ref [197] is disclosed in granted US Patent 9,269,851 and represents the culmination of three Undergraduate Thesis projects at UNSW [199-201].
    - Through-wafer FIP can be implemented using the same plating tool as used for LIP and 10 μm of Cu can be plated within 10 min.

2. This thesis identified that a key performance limiting issue for the bifacial laser-doped p-type cell structure was the p-type laser doping.

    - When laser doping using a B source, a low laser speed must be used to achieve ohmic contacts, however use of the low laser speed introduces damage in the bulk of the wafer.

- If the AlO_x is used as a dopant source, this laser-induced damage can be significantly reduced through the formation of very thin finger regions by using a fast laser doping speed but finger adhesion is reduced to the point devices cannot be fabricated.

3. A method was introduced for monitoring the changes in SRH recombination that occur in a cell's Si bulk after different processing steps using injection-dependent minority carrier lifetimes obtained using a combination of QSSPL and QSSPC measurements.
4. The first demonstration of combining (and comparing) QSSPL and QSSPC injection-dependent minority carrier lifetime measurements to estimate the capture cross section ratios of electron and holes for B-O defects after light soaking, belt furnace annealing and regeneration processes.
5. The first report of the use of injection-dependent minority carrier lifetime analysis to show that SiN_x layer and a following RTA are required for stable regeneration of the B-O defect in light-soaked wafers.
6. The injection-dependent minority carrier lifetime analyses identified key problems associated with using low-injection data in the estimation of recombination parameters from $\tau_{eff}(\Delta n)$ data measured using QSSPL.
7. This thesis represents the first report of the use stylus-based adhesion testing to evaluate the effects of different contact opening methods, plating rate, plating chemistry, grid geometry and annealing on plated finger adhesion.
8. This thesis represents the first report of the use of nanoindentation to measure the rigidity of plated fingers and to correlate these measurements with F_D measurements.
9. It was identified that it can be insufficient to evaluate plated metal adhesion using only busbar pull tests, because differences in effective plating current densities across a cell can result in strong busbar adhesion but fast plating at the fingers can result in poor finger adhesion and excessive finger peeling after stylus impact.

    - This finding has important implications for companies developing alternative (plated) metallisation capability and suggests the need to incorporate appropriate metallisation metrology if Ni/Cu plating is to be introduced into large scale manufacturing.

6.3 Future Work

The investigations in this thesis have also highlighted a number of areas of future research. There is scope to extend the work reported in each of the three experimental chapters as described below.

As mentioned in Chapter 3, p-type laser-doping damage can be significantly reduced by laser doping through AlO_x dielectric layers (i.e., without B source). Hallam et al. [226] have demonstrated that *FF*s > 78% and cell efficiencies > 20% cell can be achieved by laser doping through AlO_x and then contacting the doped regions using evaporated Al sintered at low temperature. However for plated bifacial cells, the problem that needs to be addressed is the adhesion of plated metal to these thinner and smooth surfaces that result from laser doping. In Chapter 5, it is shown how ps laser ablation can create a rough nanoscale surface that can significantly increase the adhesion of plated metal. It therefore may be possible, to more closely characterise this roughness (e.g., through imaging and contact angle measurements) to identify the key requirements for strong adhesion. Required roughness may be able to be achieved by chemical etching methods or physical structuring (discussed further below), however during any 'roughening' process, damage to the Si needs to be considered carefully.

The QSSPL and QSSPC recombination monitoring method introduced in Chapter 4 could be used to improve the bifacial cell fabrication process. Injection dependent QSSPL measurements can be recorded after bifacial cell metallisation, allowing information about additional recombination introduced by metallisation to be directly assessed. Although this was attempted in the current thesis project, the effective minority carrier lifetimes were low due to laser damage after the B laser doping process so a useful analysis was not possible. However, if this was attempted using laser-doping through AlO_x, the higher expected lifetimes may permit the analysis. It would also be useful to investigate the nature of recombination introduced during RTA after Ni plating.

Finally, there are many aspects regarding finger and busbar adhesion of plated metal to Si that can be investigated further. There are two studies that may be of particular value in terms of improved understanding. First, it would be useful to investigate the fundamental reason(s) for the increased adhesion that results from the nanoscale roughness exposed in the Si by ps laser ablation of coating dielectrics. For example, does the nanoscale roughness affect the

nucleation of the Ni or the wettability of the Si surface by the plating electrolyte? This understanding may allow for specific engineering of surfaces (e.g., chemical etching, physical or optical structuring) to achieve strong adhesion. Second, it would be attractive to manufacturers if a non-contact test could be developed for adhesion assessment. Not only is the stylus-based test described in this thesis a destructive test, it is also relatively slow which limits the number of cells that can be realistically tested. A non-contact test would allow rapid testing without using cells from production.

APPENDIX A. LIST OF PUBLICATIONS

Journal Papers

1. **X. Wang**, P.-C. Hsiao, W. Zhang, B. Johnston, A. Stokes, Q. Wei, A. Fell, S. Surve, Y. Shengzhao, P. Verlinden and A. Lennon (2016) Untangling the Mysteries of Plated Metal Finger Adhesion: Understanding the Contributions from Plating Rate, Chemistry, Grid Geometry and Sintering, *IEEE J. of Photovolt*., **6(5)**, 1167 – 1174.
2. R. Schmidt, D. Davidsen, H. Li, A. To, **X. Wang**, A. Han, X. An, J. Colwell, C. Chan, A. Wenham, M. Stenbæk Schmidt, A. Boisen, O. Hansen, S. Wenham, A. Barnett (2016) Black silicon laser-doped selective emitter solar cell with 18.1% efficiency, *Solar Energy Materials and Solar Cells*, **144**, 740-747.
3. N. Song, W. Zhang, P.-C. Hsiao, **X. Wang**, J. Colwell and A. Lennon (2016) Copper Microstructure Evolution in Light-induced Plated Metal Grids for Silicon Solar Cells: Implications for Reliable Metallization, *J. Electrochem. Soc*., **163 (4)**, H1136-H1143.
4. P.-H. Lu, D. Lin, **X. Wang**, A. Lennon, S. Wenham (2015) Laser doping through anodic aluminium oxide silicon solar cell, *Solar Energy Materials and Solar Cells*, **14**5, 349–357
5. J. Cui, Z. Ouyang, Z. Hameiri, **X. Wang**, A. Lennon (2015), Ultralow Interface State Density Achieved by Light-Induced Anodization of Aluminum on Silicon Solar Cell Surfaces, *IEEE J. of Photovolt*., **5(4)**, 1-7.
6. **X. Wang**, V. Allen, V. Vais, Y. Zhao, B. Tjahjono,Y. Yao, S. Wenham, A. Lennon (2014) Laser-doped metal-plated bifacial silicon solar cells, *Solar Energy Materials and Solar Cells* , **131**, 37-45.
7. J. Cui, **X. Wang**, R. Opila, A. Lennon (2013) Light-induced anodisation of silicon for solar cell passivation, *J. Appl. Phys*., **114**, 184101.

Peer-Reviewed Papers from Conferences

1. N. Song, P.-H. Hsiao, W. Zhang, **X. Wang**, J. Colwell, Z. Li and A. Lennon (2016) Post-plating annealing of light induced plated copper fingers: Implications for reliable metallization, 6th Workshop on Metallization and Interconnection for Crystalline

Silicon Solar Cells, 2-3 May, Konstanz, Germany, to be published in *Energy Procedia*.

2. **X. Wang**, P.-C. Hsiao, W. Zhang, X. Wang, B. Johnston, A. Stokes, A. Fell, S. Surve, Y. Shengzhao, P. Verlinden and A. Lennon (2016) Monitoring of adhesion for plated metallisation: Why busbar pull tests are not sufficient, 7-10 March, Silicon PV 2016, Chambery, France, *Energy Procedia*, **92**, 978–983.
3. **X. Wang**, M. Juhl and A. Lennon (2016) Injection-dependent carrier lifetime analysis of recombination due to boron-oxygen complexes in wafers passivated with different dielectrics, 7-10 March, Silicon PV 2016, Chambery, France, *Energy Procedia*, **92**, 265-273.
4. J. Tong, Z. Ouyang, **X. Wang** and A. Lennon (2015) Ultra-thin tunnel oxides formed by field-induced anodisation for carrier-selective contacts, Silicon PV 2015, 23-25 March, Konstanz, Germany, *Energy Procedia*, **77**, 840–847.
5. R. Chen, W. Zhang, **X. Wang**, X. Wang and A. Lennon (2014) Failure modes identified during adhesion testing of metal fingers on silicon solar cells, Metallisation Workshop, 20-21 October, Konstanz, Germany, *Energy Procedia*, **67**, 194-202.
6. A. Lennon, S. Flynn, T. Young, N. Nampalli, M. Edwards, R. Evans, Y. Yao, P-C. Hsiao, **X. Wang**, V. Allen, R. Chen, L. Mai, A. Sugianto, V. Vais, D. Jordan, R. Egan, S. Wenham (2014) Addressing perceived barriers to the adoption of plated metallisation for silicon photovoltaic manufacturing, Solar 2014 Conference, Melbourne, May (Oral). Published in the *Proceedings of the 52nd Annual Conference*, 72-82.
7. A. Lennon, J. Tong and **X. Wa**ng (2014) Requirements to achieve field-induced anodisation for silicon surface passivation, Silicon PV 2014, 25-27 March,'s-Hertogenbosch, The Netherlands. *Energy Procedia*, **55**, 855-864.
8. **X. Wang**, M. Juhl, M. Abbot, Y. Yao, Z. Hameiri and A. Lennon (2014) Use of QSSPC and QSSPL to monitor recombination processes in p-type silicon solar cells, Silicon PV 2014, 25-27 March, 's-Hertogenbosch, The Netherlands, *Energy Procedia*, 55, 169-178.
9. J. Cui, **X. Wang**, R. Opila, A. Lennon (2014) Characterization of Silicon Oxides Formed by Light-Induced Anodisation for Silicon Solar Cell Surface Passivation, *MRS Online Proceedings*, **1647**, doi:10.1557/opl.2014.350.

Conference Papers (Papers not Peer Reviewed)

1. N. Song, W. Zhang, P.-C. Hsiao, **X. Wang,** and A. Lennon (2016) Self-annealing behavior and rapid thermal processing of light-induced plated copper fingers on silicon solar cells, 43rd IEEE Photovoltaic Specialist Conference, 5-10 June, Portland, Oregon, 1980-1983.
2. P-C. Hisao, Z. Ouyang. **X. Wang** and A. Lennon (2015) Investigating light-induced plating of silicon solar cells using in-situ current-voltage analysis, 42nd IEEE Photovoltaics Specialist Conference, 15-19 June, New Orleans, LA, USA, 1-4.
3. Z. Li, R. Chen, Y. Yao, W. Zhang, **X. Wang**, I. Perez-Wurfl, A. Lennon (2014) Patterning and Metallization of Silicon Solar Cells by Inkjet-Printed Functional Ink on a Photoresist Layer, 40th IEEE Photovoltaics Specialists Conference, 2499-2501.
4. J. Cui, **X. Wang** and A. Lennon (2014) Anodic aluminium oxide rear passivated laser-doped selective-emitter solar cells, 40th IEEE Photovoltaics Specialist Conference, 8-13 June, Denver, CO, USA, 0586-0589.
5. J. Cui, **X. Wang** and A. Lennon (2013) Light-induced anodisation of aluminium for rear surface passivation, 28th European Photovoltaic Solar Energy Conference, 30 Sep – 4 Oct, Paris, France, 2079-2082.
6. A. Lennon, J. Yeo, P. H. Lu, Y. Sun, **X. Wang**, Z. Lu, Y. Li and V. Vais (2013) Field-induced anodization for silicon solar cell passivation, 39th IEEE Photovoltaics Specialist Conference, 16-21 June Tampa, Florida, 1257-1259.
7. J. Cui**, X. Wang** and A. Lennon (2013) Light-induced anodisation of aluminium for rear surface passivation, *28th European Photovoltaic Solar Energy Conference*, 30 Sep – 4 Oct, Paris, France, 2079-2082.

Patents

1. J. Cui and **X. Wang**, A method of anodising a surface of a semiconductor device, WO2014153597, Filed 24 March 2014.
2. V. Vais, A. Lennon, S. Wenham, J. Ji, A. Wenham, J. Tong and **X. Wang**, Passivation scheme for solar cells, US9385247, Granted 5 July 2016.

APPENDIX B. LIST OF ABBREVIATIONS

$H_2N-(CH_2)_n-NH-R$	Alkylated polyalkylenemine
AlO_x	Aluminium oxide
Al	Aluminum
AL BSF	Aluminum back surface field
ARC	Anti-reflection coating
B	Boron
BRL	Boron rich layer
BSG	Boron silicate glass
B-O	Boron-oxygen
CLEP	Contactless electroplating
CW	Continues wave
Cu	Copper
$CuSO_4$	Copper (II) sulfate
$CuCl_2$	Copper(II) chloride
$Cu(NO_3)_2$	Copper(II) nitrate
Cz	Czochralski
DI	Deionized
DRM	Depletion region modulation
EL	Electroluminescence
EQE	External quantum efficiency
FIP	Field-induced plating
FBP	Forward bias plating
HIT	Hetero-junction technology
HF	Hydrofluoric acid
H_2SiF_6	Hydrofluosilicic Acid
H	Hydrogen
HCl	Hydrogen chloride
IC	Integrated circuit
IBC	Interdigitated back contact
IQE	Internal quantum efficiency
Fe	Iron

LBD	Laser Buried Grid
LDSE	Laser doped selective emitter
LED	Light emitting diode
LID	Light-induced degradation
LIP	Light-induced plating
LIPSS	Laser induced periodic surface structure
MPP	Maximum power point
ns	Nanosecond
Ni	Nickel
$NiSi_x$	Nickel silicide
PERC	Passivated emitter and rear cell
PERL	passivated emitter, rear locally-diffused
PERT	Passivated emitter, rear totally diffused
P	Phosphorus
PSG	Phosphosilicate glass
PC	Photoconductance
PL	Photoluminescence
PV	Photovoltaic
ps	Picosecond
PECVD	plasma-enhanced chemical vapour deposition
Pt	Platinum
$C_{2n}H_{4n+2}O_{n+1}$	Polyethylene glycol
QE	Quantum efficiency
QSS	Quasi-steady state
QSSPC	Quasi-steady state photoconductance
QSSPL	Quasi-steady state photoluminescence
RTA	Rapid thermal anneal
SEM	Scan electron microscope
SRH	Shockley-Read-Hall
Si	Silicon
SiO_2	Silicon dioxide
SiN_x	Silicon nitride
Ag	Silver

R_1-$(S)_n$-RSO_3M	Sulfo sulfonate compounds
TDS	Technical data sheets
TEM	Transmission electron microscopy
TCO	Transparent conducting oxide
UV	Ultraviolet
H_2O	Water

APPENDIX C. LIST OF SYMBOLS

I	Current
T	Absolute temperature
$A_{Busbars}$	Area of busbars
$A_{fingers}$	Area of fingers
$A_{Intersections}$	Area of intersection regions
k	Boltzmann's constant
t_{bulk}	Bulk lifetime
E_c	Conduction band
J_0	Dark saturation current density
D_{it}	Density of interface states
F_D	Dislodge force
N_D	Doping concentration of the bulk silicon
N_A	Doping density
τ_{eff}	Effectvie lifetime
ε	Elastic strain
n	Electron density
Te	Electron temperature
ke	Electron thermal conductivity
σ_n/σ_p	Electron/hole capture cross-section ratio
q	Elementary charge of electron
J_{0e}	Emitter saturation current density
E_t	Energy of the recombination centre
D_n	Excess carrier density
α_{Cu}	Expansion coefficients of copper
α_{Si}	Expansion coefficients of silicon
FF	Fill factor
G	Generation
$G(t)$	Generation rate
H	Hardness
Ce	Heat capacities of electron
Ci	Heat capacities of lattice subsystems
$Q(z)$	Heat flux
p	Hole density

iV_{oc}	Implied open circuit voltage
n_i	Intrinsic carrier concentration of Si
S	Laser heating source term
$I(t)$	Laser intensity
Ti	Lattice subsystem temperature
m	Local ideality factor
mpp	Maximum power point
$J_{DS\text{-}middlerange}$	Mid in the optimal range specified for the chemistry
Δn	Minority carrier concentration
V_{oc}	Open circuit voltage
Υ	Parameter characterizing the electron-lattice coupling
T_{anneal}	Peak annealing temperature
z	Perpendicular direction to the substrate surface
$I_{plating}$	Plating current
P	Power
P_s	Power loss due to series resistance
P_{sh}	Power loss due to shunt
pFF	pseudo fill factor
B	Radiative recombination coefficient
R	Recombination
R	Reflectance
T_{RT}	Room temperature
A_i	Scaling factor for re-absorption within the sample
R_s	Series resistance
Isc	Short circuit current
Jsc	Short circuit current density
R_{sh}	Shunt resistance
i	Surface transmissivity
t	Time
E_v	Valence band
V	Voltage
E	Young's modulus

BIBLIOGRAPHY

[1] ITRPV. "International Technology Roadmap for Photovoltaic Results 2015," 30 Oct, 2016.

[2] Hanky. "Automatic Screen Printing Line for Silicon Wafer Solar Cell," Nov 12, 2016.

[3] cngcoins.com. "Classical Numismatic Group, INC," Dec 10, 2016.

[4] J. L. Clement, “Antibacterial Silver,” vol. 1, no. 5-6, pp. 467-82, 1994.

[5] S. l. metals. "The Antibacterial Effects of Silver and it's compounds," Nov 23, 2016.

[6] S. Pal, Y. K. Tak, and J. M. Song, “Does the Antibacterial Activity of Silver Nanoparticles Depend on the Shape of the Nanoparticle? A Study of the Gram-Negative Bacterium Escherichia coli,” *Applied and environmental microbiology,* vol. 73, no. 6, pp. 1712-1720, March, 2007.

[7] C. Marambio-Jones, and E. M. V. Hoek, “A review of the antibacterial effects of silver nanomaterials and potential implications for human health and the environment,” *Journal of Nanoparticle Research,* vol. 12, no. 5, pp. 1531-1551, 2010.

[8] S. Silver, “Bacterial silver resistance: molecular biology and uses and misuses of silver compounds,” *FEMS Microbiology Reviews,* vol. 27, no. 2-3, pp. 341-353, 2003.

[9] M. Rai, A. Yadav, and A. Gade, “Silver nanoparticles as a new generation of antimicrobials,” *Biotechnology Advances,* vol. 27, no. 1, pp. 76-83, 2009.

[10] C. Research. "A (Photovoltaic) silver bull in China," Nov 21, 2016.

[11] M. P. Saefong. "Forget gold, silver is on fire and could hit $25 an ounce by the end of 2016 " Nov, 2016.

[12] J. Desjardins. "The Silver Series: World’s Growing Demand For Silver " Nov 11, 2016.

[13] Silverinstitute.org. "2016 Silver Market Trends," Nov 22, 2016.

[14] A. Critchlow. "Silver no longer the poor man’s gold as solar demand surges," Nov 3, 2016.

[15] Inversting.com. "Silver historical data," Nov 16, 2016.

[16] ITRPV.net. "International Technology Roadmap for Photovoltaic 2013," Nov 11, 2016.

[17] D. Collins. "Chinese Silver Investment Going Parabolic," Nov 23, 2016.

[18] J. Gray. "Silver Fern confirms Chinese investor," Nov 12, 2016.

[19] T. Durden. "The Chinese Start Buying Silver: BofA Says "Momentum Breaks Out To Highest In Years"," Nov 11, 2016.

[20] A. Stevenson. "Cramer: Yes, silver is poor man's gold," Nov 11, 2016.

[21] L. R. Brown, *Plan B 2.0: Rescuing a Planet Under Stress and a Civilization in Trouble*, p.^pp. 109, New York: W.W. Norton, 2006.

[22] F. Gómez, J. I. Guzmán, and J. E. Tilton, "Copper recycling and scrap availability," *Resources Policy,* vol. 32, no. 4, pp. 183-190, 2007.

[23] A. Agrawal, and K. K. Sahu, "Problems, prospects and current trends of copper recycling in India: An overview," *Resources, Conservation and Recycling,* vol. 54, no. 7, pp. 401-416, 2010.

[24] Inversting.com. "Copper historical data," Nov 16, 2016.

[25] J. H. Wohlgemuth, S. Narayanan, and R. Brenneman, "Cost effectiveness of high efficiency cell processes as applied to cast polycrystalline silicon." pp. 221-226 vol.1.

[26] A. Lennon, Y. Yao, and P. S. Wenham, "Evolution of metal plating for silicon solar cell metallisation," *Progress in Photovoltaics: Research and Applications,* pp. 1454-1468, 2012.

[27] S. Wenham, "Buried-contact silicon solar cells," *Progress in Photovoltaics: Research and Applications,* vol. 1, no. 1, pp. 3-10, 1993.

[28] S. R. Wenham, C. B. Honsberg, and M. A. Green, "Buried contact silicon solar cells," *Solar Energy Materials and Solar Cells* vol. 34, no. 1-4, pp. 101-110, 1994.

[29] S. R. Wenham, C. B. Honsberg, and M. A. Green, "Buried contact silicon solar cells," *Solar Energy Materials and Solar Cells,* vol. 34, no. 1, pp. 101-110, 1994/09/01, 1994.

[30] M. A. Green, S. R. Wenham, J. Zhao, S. Bowden, A. M. Milne, M. Taouk, and F. Zhang, "Present status of buried contact solar cells." pp. 46-53 vol.1.

[31] M. Alonso-Abella, F. Chenlo, A. Alonso, and D. González, "Toledo PV Plant 1 MWp – 20 Years of Operation." pp. 2728 - 2733.

[32] Z. Shi, S. R. Wenham, and J. Ji, "Mass production of the innovative PLUTO solar cell technology," in IEEE Photovoltaics Specialists Conference, Philadelphia, 2009.

[33] Z. Wang, P. Han, H. Lu, H. Qian, L. Chen, Q. Meng, N. Tang, F. Gao, Y. Jiang, J. Wu, W. Wu, H. Zhu, J. Ji, Z. Shi, A. Sugianto, L. Mai, B. Hallam, and S. Wenham, "Advanced PERC and PERL production cells with 20.3% record efficiency for standard commercial p-type silicon wafers," *Progress in Photovoltaics: Research and Applications,* vol. 20, no. 3, pp. 260-268, 2012.

[34] B. S. Tjahjono, M. J. Yang, C.-Y. Lan, J. Ting, A. Sugianto, H. Ho, N. Kuepper, B. Beilby, T. Szpitalak, and S. R. Wenham, "18.9% Efficient Laser Doped Selective Emitter Solar Cell on Industrial Grade p-Type Czochralski Wafer." pp. 1396-1400.

[35] J. Bartsch, M. Kamp, D. Hartleb, C. Wittich, A. Mondon, B. Steinhauser, F. Feldmann, A. Richter, J. Benick, M. Glatthaar, M. Hermle, and S. W. Glunz, “21.8% Efficient n-type Solar Cells with Industrially Feasible Plated Metallization,” *Energy Procedia*, vol. 55, pp. 400-409, 2014/01/01, 2014.

[36] A. Mondon;, J. Bartsch;, M. Kamp;, A. Brand;, B. Steinhauser;, N. Bay;, J. Horzel;, M. Glatthaar;, and S. W. Glunz;, “Plated nickel-copper contacts on C-Si: from microelectronic processing to cost effective silicon solar cell production,” in 29th European PV Solar Energy Conference and Exhibition, Amsterdam, The Netherlands 2014.

[37] T. Young, K. Khee, A. Lennon, R. Egan, O. Wilkie, and Y. Yao, "Design and characterization of an adhesion strength tester for evaluating metal contacts on solar cells." pp. 2550-2553.

[38] L. Tous, R. Russell, J. Das, R. Labie, M. Ngamo, J. Horzel, H. Philipsen, J. Sniekers, K. Vandermissen, L. van den Brekel, T. Janssens, M. Aleman, D. H. van Dorp, J. Poortmans, and R. Mertens, “Large Area Copper Plated Silicon Solar Cell Exceeding 19.5% Efficiency,” *Energy Procedia*, vol. 21, no. 0, pp. 58-65, 2012.

[39] R. Russell, L. Tous, A. Uruena de castro, I. Kuzma Filipek, D. Hendrickx, F. Duerinckx, J. Szlufcik, Y. Yao, and T. Soederstroem, "The potential for Cu-free Ni plated contacts enabled by smart wire connection technology." pp. 20-21 October.

[40] J. Horzel, N. Bay, M. Passig, M. Sieber, J. Burschik, H. Kühnlein, A. Brand, A. Letize, B. Lee, D. Weber, and R. Böhme, "Low cost metallisation based on Ni/Cu plating enabling high efficiency industrial solar cells." pp. 507-512.

[41] S. Kluska, J. Bartsch, A. Büchler, G. Cimiotti, A. A. Brand, S. Hopman, and M. Glatthaar, “Electrical and Mechanical Properties of Plated Ni/Cu Contacts for Si Solar Cells,” *Energy Procedia*, vol. 77, pp. 733-743, 2015.

[42] P. Verlinden, "Advanced Module Concepts," *Photovoltaic Solar Energy*, pp. 502-510: John Wiley & Sons, Ltd, 2016.

[43] T. Söderström, P. Papet, and J. Ufheil, "Smart wire connection technology." pp. 495-499.

[44] P. Papet, L. Andreetta, D. Lachenal, G. Wahli, J. Meixenberger, B. Legradic, W. Frammelsberger, D. Bätzner, B. Strahm, Y. Yao, and T. Söderström, “New Cell

Metallization Patterns for Heterojunction Solar Cells Interconnected by the Smart Wire Connection Technology," *Energy Procedia,* vol. 67, pp. 203-209, 2015.

[45] Y. Yao, P. Papet, J. Hermans, T. Söderström, H. Mehlich, M. König, A. Waltinger, D. Habermann, and A. Richter, "Module integration of solar cells with diverse metallization schemes enabled by SmartWire Connection Technology." pp. 1-5.

[46] D. M. Chapin, C. S. Fuller, and G. L. Pearson, "A New Silicon p-n Junction Photocell for Converting Solar Radiation into Electrical Power," *Journal of Applied Physics,* vol. 25, no. 5, pp. 676-677, 1954.

[47] G. Raisbeck, "The Solar Battery," *Scientific American,* vol. 193, no. 6, pp. 102-110, 1955.

[48] J. Perlin, *From Space to Earth: The Story of Solar Electricity,* p.^pp. 26-30, Ann Arbor, MI 48107, United States: Aatec Publications, 1999.

[49] J. Perlin, *The Silicon Solar Cell Turns 50,* vol. BR-520-33947, 2004.

[50] JPL, *Electricity from Photovoltaic Solar Cells. Flat-Plate Solar Array Report: Volume V: Process Development,* Jet Propulsion Laboratory for the U.S. Department of Energy, 1986.

[51] E. L. Ralph, "Recent advances in low-cost solar cell processing." pp. 315-316.

[52] M. B. Field, and L. R. Scudder, "Application of thick-film technology to solar cell fabrication." pp. 303-308.

[53] D.-H. Neuhaus, and A. Munzer, "Industrial Silicon Wafer Solar Cells," *Advances in OptoElectronics,* vol. 2007, pp. 24521, 2007.

[54] maths.ox.ac.uk. "Screen printing for silicon PV devices," Nov 22, 2016.

[55] K. D. Shetty, M. B. Boreland, V. Shanmugam, J. Cunnusamy, C.-K. Wu, S. Iggo, and H. Antoniadis, "Lightly Doped Emitters for High Efficiency Silicon Wafer Solar Cells," *Energy Procedia,* vol. 33, no. 0, pp. 70-75, 2013.

[56] H. Wagner, A. Dastgheib-Shirazi, B. Min, A. E. Morishige, M. Steyer, G. Hahn, C. d. Cañizo, T. Buonassisi, and P. P. Altermatt, "Optimizing phosphorus diffusion for photovoltaic applications: Peak doping, inactive phosphorus, gettering, and contact formation," *Journal of Applied Physics,* vol. 119, no. 18, pp. 185704, 2016.

[57] H. Huang, J. Lv, Y. Bao, R. Xuan, S. Sun, S. Sneck, S. Li, C. Modanese, H. Savin, and A. Wang, "20.8% industrial PERC solar cell: ALD Al 2 O 3 rear surface passivation, efficiency loss mechanisms analysis and roadmap to 24%," *Solar Energy Materials and Solar Cells,* vol. 161, pp. 14-30, 2017.

[58] A. W. Blakers, A. Wang, A. M. Milne, J. Zhao, and M. A. Green, “22.8% efficient silicon solar cell,” *Applied Physics Letters,* vol. 55, no. 13, pp. 1363-1365, 1989.

[59] P. P. Altermatt, and K. R. McIntosh, “A Roadmap for PERC Cell Efficiency towards 22%, Focused on Technology-related Constraints,” *Energy Procedia,* vol. 55, pp. 17-21, //, 2014.

[60] M. A. Green, “The Passivated Emitter and Rear Cell (PERC): From conception to mass production,” *Solar Energy Materials and Solar Cells,* vol. 143, pp. 190-197, 2015.

[61] A. Herguth, G. Schubert, M. Kaes, and G. Hahn, "A New Approach to Prevent the Negative Impact of the Metastable Defect in Boron Doped CZ Silicon Solar Cells." pp. 940-943.

[62] A. Herguth, G. Schubert, M. Kaes, and G. Hahn, "Avoiding boron-oxygen related degradation in highly boron doped Cz silicon." pp. 530-534.

[63] A. Münzer, "Hydrogenated silicon nitride for regeneration of light induced degradation." pp. 1558-1561.

[64] A. Herguth, and G. Hahn, “Kinetics of the boron-oxygen related defect in theory and experiment,” *Journal of Applied Physics,* vol. 108, no. 11, pp. 114509, 2010.

[65] S. Wilking, A. Herguth, and G. Hahn, “Influence of hydrogen on the regeneration of boron-oxygen related defects in crystalline silicon,” *Journal of Applied Physics,* vol. 113, no. 19, pp. 194503, 2013.

[66] S. Wilking, C. Beckh, S. Ebert, A. Herguth, and G. Hahn, “Influence of bound hydrogen states on BO-regeneration kinetics and consequences for high-speed regeneration processes,” *Solar Energy Materials and Solar Cells,* vol. 131, no. 0, pp. 2-8, 2014.

[67] B. J. Hallam, P. G. Hamer, S. R. Wenham, M. D. Abbott, A. Sugianto, A. M. Wenham, C. E. Chan, G. Xu, J. Kraiem, and J. Degoulange, “Advanced bulk defect passivation for silicon solar cells,” *IEEE Journal of Photovoltaics,* vol. 4, no. 1, pp. 88-95, 2014.

[68] N. Nampalli, B. J. Hallam, C. E. Chan, M. D. Abbott, and S. R. Wenham, “Influence of Hydrogen on the Mechanism of Permanent Passivation of Boron-Oxygen Defects in p-Type Czochralski Silicon,” *Photovoltaics, IEEE Journal of,* vol. 5, no. 6, pp. 1580-1585, 2015.

[69] N. Nampalli, B. Hallam, C. Chan, M. Abbott, and S. Wenham, “Evidence for the role of hydrogen in the stabilization of minority carrier lifetime in boron-doped Czochralski silicon,” *Applied Physics Letters,* vol. 106, no. 17, pp. 173501, 2015.

[70] B. J. Hallam, P. G. Hamer, S. Wang, L. Song, N. Nampalli, M. D. Abbott, C. E. Chan, D. Lu, A. M. Wenham, L. Mai, N. Borojevic, A. Li, D. Chen, M. Y. Kim, A. Azmi, and S. Wenham, “Advanced Hydrogenation of Dislocation Clusters and Boron-oxygen Defects in Silicon Solar Cells,” *Energy Procedia,* vol. 77, pp. 799-809, 2015/08/01, 2015.

[71] D. Kray, A. Fell, S. Hopman, K. Mayer, G. Willeke, and S. Glunz, “Laser Chemical Processing (LCP): A versatile tool for microstructuring applications,” *Appl. Phys. A,* vol. 93, pp. 99-103, 2008.

[72] S. J. Eisele, T. C. Röder, J. R. Köhler, and J. H. Werner, “18.9% efficient full area laser doped silicon solar cell,” *Applied Physics Letters,* vol. 95, no. 13, pp. 133501, 2009.

[73] D. Kray, and K. R. McIntosh, “Analysis of selective phosphorus laser doping in high efficiency solar cells,” *IEEE Trans. Electron Devices,* vol. 56, no. 8, pp. 1645-1650, 2009.

[74] B. Hallam, S. Wenham, A. Sugianto, L. Mai, C. Chong, M. Edwards, D. Jordan, and P. Fath, “Record Large-Area p-Type CZ Production Cell Efficiency of 19.3% Based on LDSE Technology,” *IEEE Journal of Photovoltaics,* vol. 1, no. 1, pp. 43-48, 2011.

[75] C. E. Dubé, B. Tsefrekas, D. Buzby, R. Tavares, W. Zhang, A. Gupta, R. J. Low, W. Skinner, and J. Mullin, “High efficiency selective emitter cells using patterned ion implantation,” *Energy Procedia,* vol. 8, no. 0, pp. 706-711, 2011.

[76] R. Russell, L. Tous, H. Philipsen, J. Horzel, E. Cornagliotti, M. Ngamo, P. Choulat, R. Labie, J. Beckers, J. Bertens, M. Fujii, J. John, J. Poortmans, and R. Mertens, "A simple copper metallisation process for high cell efficiencies and reliable modules." pp. 538-543.

[77] C. Geisler, W. Hördt, S. Kluska, A. Mondon, S. Hopman, and M. Glatthaar, "Continuous wave laser processing for electrical and mechanical stable Ni-Cu solar cells."

[78] J. T. Horzel, Y. Shengzhao, N. Bay, M. Passig, D. Pysch, H. Kuhnlein, H. Nussbaumer, and P. Verlinden, “Industrial Si Solar Cells With Cu-Based Plated Contacts,” *IEEE Journal of Photovoltaics,* vol. 5, no. 6, pp. 1595-1600, 2015.

[79] A. Lennon, “Dielectric Patterning for Commercial High Efficiency Silicon Solar Cells,” PhD Thesis, The University of New South Wales, 2010.

[80] M. M. Hilali, A. Rohatgi, and B. To, "Review and Understanding of Screen-Printed Contacts and Selective-Emitter Formation." p. Medium: ED; Size: 11 pp. pages.

[81] M. M. Hilali, “Understanding and development of manufacturable screen-printed contacts on high sheet-resistance emitters for low-cost silicon solar cells,” Electrical and Computer Engineering Georgia Institute of Technology, 2005.

[82] S. Riegel, F. Mutter, G. Hahn, and B. Terheiden, "Contact formation in the silver/aluminum thick film firing process – a phenomenological approach." pp. 2353-2356.

[83] S. Riegel, F. Mutter, T. Lauermann, B. Terheiden, and G. Hahn, “Review on screen printed metallization on p-type silicon,” *Energy Procedia,* vol. 21, pp. 14-23, 2012/01/01, 2012.

[84] R. Hoenig, M. Duerrschnabel, W. van Mierlo, Z. Aabdin, J. Bernhard, J. Biskupek, O. Eibl, U. Kaiser, J. Wilde, F. Clement, and D. Biro, “The Nature of Screen Printed Front Side Silver Contacts - Results of the Project MikroSol,” *Energy Procedia,* vol. 43, pp. 27-36, 2013/01/01, 2013.

[85] J. D. Fields, M. I. Ahmad, V. L. Pool, J. Yu, D. G. Van Campen, P. A. Parilla, M. F. Toney, and M. F. A. M. van Hest, “The formation mechanism for printed silver-contacts for silicon solar cells,” *Nat. Commun.,* vol. 7, Jan, 2016.

[86] M. M. Hilali, A. Rohatgi, and S. Asher, “Development of screen-printed silicon solar cells with high fill factors on 100 Ω/sq emitters,” *IEEE Transactions on Electron Devices,* vol. 51, no. 6, pp. 948-955, 2004.

[87] A. Mette, C. Schetter, D. Wissen, S. Lust, S. W. Glunz, and G. Willeke, "Increasing the Efficiency of Screen-Printed Silicon Solar Cells by Light-Induced Silver Plating." pp. 1056-1059.

[88] R. Woehl, M. Hörteis, and S. W. Glunz, “Analysis of the Optical Properties of Screen-Printed and Aerosol-Printed and Plated Fingers of Silicon Solar Cells,” *Advances in OptoElectronics,* vol. 2008, 2008.

[89] M. Ju, Y.-J. Lee, J. Lee, B. Kim, K. Ryu, K. Choi, K. Song, K. Lee, C. Han, Y. Jo, and J. Yi, “Double screen printed metallization of crystalline silicon solar cells as low as 30 μm metal line width for mass production,” *Solar Energy Materials and Solar Cells,* vol. 100, pp. 204-208, 2012.

[90] S. W. Glunz, “High-Efficiency Crystalline Silicon Solar Cells,” *Advances in OptoElectronics,* vol. 2007, pp. 15, 2007.

[91] H. de Moor, A. Weeber, J. Hoornstra, and W. Sinke, "Fine-line screen printing for silicon solar cells." pp. 154-170.

[92] J. Hoornstra, S. Roberts, H. De Moor, and T. Bruton, “First experiences with double layer stencil printing for low cost production solar cells,” *2nd World PVSEC,* 1998.

[93] J. Hoornstra, and B. Heurtault, "Stencil print applications and progress for crystalline silicon solar cells." pp. 989 - 992.

[94] J. Hoornstra, H. De Moor, A. Weeber, and P. Wyers, "Improved front side metallization on silicon solar cells with stencil printing." p. 5.

[95] H. Hannebauer, T. Falcon, J. Cunnusamy, and T. Dullweber, “Single Print Metal Stencils for High-efficiency PERC Solar Cells,” *Energy Procedia,* vol. 98, pp. 40-45, 2016.

[96] H. Hannebauer, T. Dullweber, T. Falcon, X. Chen, and R. Brendel, “Record Low Ag Paste Consumption of 67.7 mg with Dual Print,” *Energy Procedia,* vol. 43, no. 0, pp. 66-71, 2013.

[97] H. Hannebauer, T. Dullweber, T. Falcon, and R. Brendel, “Fineline Printing Options for High Efficiencies and Low Ag Paste Consumption,” *Energy Procedia,* vol. 38, no. 0, pp. 725-731, 2013.

[98] H. Hannebauer, T. Dullweber, T. Falcon, and R. Brendel, “Fineline Printing Options for High Efficiencies and Low Ag Paste Consumption,” *Energy Procedia,* vol. 38, pp. 725-731, 2013/01/01, 2013.

[99] ITRPV, *International Technology Roadmap for Photovoltaic: 2015 Results,* 2016.

[100] A. Mette, D. Pysch, G. Emanuel, D. Erath, R. Preu, and S. W. Glunz, “Series resistance characterization of industrial silicon solar cells with screen-printed contacts using hotmelt paste,” *Progress in Photovoltaics: Research and Applications,* vol. 15, no. 6, pp. 493-505, 2007.

[101] D. Erath, A. Filipović, M. Retzlaff, A. K. Goetz, F. Clement, D. Biro, and R. Preu, “Advanced screen printing technique for high definition front side metallization of crystalline silicon solar cells,” *Solar Energy Materials and Solar Cells,* vol. 94, no. 1, pp. 57-61, 2010.

[102] K. F. Teng, and R. W. Vest, "Ink jet assisted metallization for low cost flat plate solar cells." pp. 1430-1434.

[103] D. A. Roberson, R. B. Wicker, L. E. Murr, K. Church, and E. MacDonald, "Microstructural and Process Characterization of Conductive Traces Printed from Ag Particulate Inks," *Materials,* vol. 4, no. 6, pp. 963, 2011.

[104] A. Mette, P. L. Richter, M. Hörteis, and S. W. Glunz, "Metal aerosol jet printing for solar cell metallization," *Progress in Photovoltaics: Research and Applications,* vol. 15, no. 7, pp. 621-627, 2007.

[105] X. Chen, K. Church, and H. Yang, "High speed non-contact printing for solar cell front side metallization." pp. 001343-001347.

[106] M. Hörteis, and S. Glunz, "Fine line printed silicon solar cells exceeding 20% efficiency," *Prog. Photovolt: Res. & Appl.,* vol. 16, pp. 555-560, 2008.

[107] M. Hörteis, J. Bartsch, V. Radtke, A. Filipovic, and S. Glunz, "Different aspects of seed layer-printed and light-induced plated front side contacts." pp. 985-988.

[108] J. M. Hoey, A. Lutfurakhmanov, D. L. Schulz, and I. S. Akhatov, "A Review on Aerosol-Based Direct-Write and Its Applications for Microelectronics," *Journal of Nanotechnology,* vol. 2012, pp. 22, 2012.

[109] K. K. B. Hon, L. Li, and I. M. Hutchings, "Direct writing technology—Advances and developments," *CIRP Annals - Manufacturing Technology,* vol. 57, no. 2, pp. 601-620, 2008.

[110] A. Ebong, B. Rounsaville, I. Cooper, K. Tate, A. Rohatgi, S. Glunz, M. Horteis, A. Mette, and M. Gundermann, "High efficiency silicon solar cells with ink jetted seed and plated grid on high sheet resistance emitter." pp. 001363-001367.

[111] A. Ebong, I. Cooper, K. Tate, B. Rounsaville, F. Zimbardi, V. Upadhyaya, A. Rohatgi, M. Dovrat, E. Kritchman, and D. Brusilovsky, "Implementing narrow front silver gridlines through ink jet machine for high quality contacts to silicon solar cells." pp. 001050-001053.

[112] A. Ebong, and N. Chen, "Metallization of crystalline silicon solar cells: a review." pp. 102-109.

[113] G. O. Mallory, and J. B. Hajdu, "Electroless Plating - Fundamentals and Applications," William Andrew Publishing/Noyes.

[114] G. Oskam, J. G. Long, A. Natarajan, and P. C. Searson, "Electrochemical deposition of metals onto silicon," *Journal of Physics D: Applied Physics,* vol. 31, no. 16, pp. 1927, 1998.

[115] M. Schlesinger, and M. Paunovic, *Modern Electroplating,* p.^pp. 249: Wiley, 2011.

[116] S. R. Wenham, and M. A. Green, *Buried contact solar cell*, US US Patent 4,726,850,to Unisearch Limited (Kensington, AU) 1988.

[117] S. R. Wenham, and M. A. Green, *Method of making buried contact cells*, US US Patent 4,748,130,to Unisearch Limited (Kensington, AU) 1988.

[118] N. Mason, R. Russell, A. Artigao, J. Fernandez, O. Nast-Hartley, J. Sherborne, P. Banda, R. Bueno, G. Martinez, and T. Bruton, "New Generation BP Solar Saturn cell in production: The BBP7180 module."

[119] N. Mason, T. Bruton, and M. A. Balbuena, "Laser grooved buried grid silicon solar cells: From pilot line to 50 Mwp manufacture in ten years." pp. 227-229

[120] S. Eager, N. Mason, T. Bruton, J. Sherborne, and R. Russell, "Buried contact cell technology – New manufacturing processes with safety and environmental benefits." pp. 69-72.

[121] L. Tous, D. H. van Dorp, R. Russell, J. Das, M. Aleman, H. Bender, J. Meersschaut, K. Opsomer, J. Poortmans, and R. Mertens, "Electroless nickel deposition and silicide formation for advanced front side metallization of industrial silicon solar cells," *Energy Procedia,* vol. 21, pp. 39-46, 2012.

[122] A. Rehman, and S. Lee, "Review of the Potential of the Ni/Cu Plating Technique for Crystalline Silicon Solar Cells," *Materials,* vol. 7, no. 2, pp. 1318, 2014.

[123] M. Paunovic, "Electroless Deposition of Copper," *Modern Electroplating*, pp. 433-446: John Wiley & Sons, Inc., 2010.

[124] S. Eager, N. Mason, T. Bruton, J. Sherborne, and R. Russell, "Environmentally Friendly Processes in the Manufacture of Saturn Solar Cells." pp. 62-65.

[125] M. Green, J. Zhao, A. Wang, and S. Wenham, "Progress and outlook for high-efficiency crystalline silicon solar cells," *Solar Energy Materials and Solar Cells*, vol. 65, no. 1, pp. 9-16, 2001.

[126] L. Tous, "22% Bifacial n-PERT Cells with Ni/Ag Co-plated Contacts and Voc ~690 mV."

[127] A. Cuevas, A. Luque, J. Eguren, and J. del Alamo, "50 Per cent more output power from an albedo-collecting flat panel using bifacial solar cells," *Solar Energy,* vol. 29, no. 5, pp. 419-420, 1982/01/01, 1982.

[128] U. A. Yusufoglu, T. M. Pletzer, L. J. Koduvelikulathu, C. Comparotto, R. Kopecek, and H. Kurz, "Analysis of the Annual Performance of Bifacial Modules and Optimization Methods," *IEEE Journal of Photovoltaics,* vol. 5, no. 1, pp. 320-328, 2015.

[129] A. P. Abbott, S. Nandhra, S. Postlethwaite, E. L. Smith, and K. S. Ryder, “Electroless deposition of metallic silver from a choline chloride-based ionic liquid: a study using acoustic impedance spectroscopy, SEM and atomic force microscopy,” *Physical Chemistry Chemical Physics*, vol. 9, no. 28, pp. 3735-3743, 2007.

[130] X. Xu, X. Luo, H. Zhuang, W. Li, and B. Zhang, “Electroless silver coating on fine copper powder and its effects on oxidation resistance,” *Materials Letters,* vol. 57, no. 24, pp. 3987-3991, 2003.

[131] S. Shukla, S. Seal, Z. Rahaman, and K. Scammon, “Electroless copper coating of cenospheres using silver nitrate activator,” *Materials Letters,* vol. 57, no. 1, pp. 151-156, 2002.

[132] M. Schlesinger, "Electroless and Electrodeposition of Silver," *Modern Electroplating*, pp. 131-138: John Wiley & Sons, Inc., 2010.

[133] A. Lennon, Y. Yao, and S. Wenham, “Evolution of metal plating for silicon solar cell metallisation,” *Progress in Photovoltaics: Research and Applications,* vol. 21, no. 7, pp. 1454-1468, 2013.

[134] X. Zhang, Z. Chen, and K. N. Tu, “Immersion nickel deposition on blank silicon in aqueous solution containing ammonium fluoride,” *Thin Solid Films,* vol. 515, no. 11, pp. 4696-4701, 2007.

[135] J. Rodriguez, W. Zhang, S. Lim, and A. Lennon, “Improved Metal Adhesion with Galvanic Nickel Plating to Silicon Solar Cells,” *Solar Energy Materials & Solar Cells* 2016.

[136] X. Wang, P. C. Hsiao, W. Zhang, B. Johnston, A. Stokes, Q. Wei, A. Fell, S. Surve, Y. Shengzhao, P. Verlinden, and A. Lennon, “Untangling the mysteries of plated metal finger adhesion: Understanding the contributions from plating rate, chemistry, grid geometry, and sintering,” *IEEE Journal of Photovoltaics,* vol. 6, no. 5, pp. 1167-1174, 2016.

[137] L. Tous, D. Van Dorp, R. Russell, J. Das, M. Aleman, H. Bender, J. Meersschaut, K. Opsomer, J. Poortmans, and R. Mertens, “Electroless nickel deposition and silicide formation for advanced front side metallization of industrial silicon solar cells,” *Energy Procedia,* vol. 21, pp. 39-46, 2012.

[138] B. J. Sinkule, and L. Ortolano, *Implementing Environmental Policy in China*: Praeger, 1995.

[139] W. Späth, *Verfahren zur galvanischen Abscheidung einer Metallschicht auf der Oberfläche eines Halbleiterkörpers*, D. Patentschrift, 1975.

[140] D. LF, Methods of plating by means of light, US. Patent, 1979.

[141] R. T. Lowson, “Aluminium corrosion studies. IV* Pitting Corrosion ” *Australian Journal of Chemistry*, 1978.

[142] V. C, *Corrosion of aluminium*, Elsevier, 2004.

[143] S. W. Glunz, M. Aleman, J. Bartsch, N. Bay, K. Bayer, R. Bergander, A. Filipovic, S. Greil, A. Grohe, M. Horteis, A. Knorz, M. Menko, A. Mette, D. Pysch, V. Radtke, P. Richter, D. Rudolph, T. Rublack, C. Schetter, D. Schmidt, O. Schultz, and R. Woehl, "Progress in advanced metallization technology at Fraunhofer ISE." pp. 1-4.

[144] G. Jiun-Hua, B. S. Tjahjono, and J. E. Cotter, "19.2% efficiency n-type laser-grooved silicon solar cells." pp. 983-986.

[145] J. Bartsch, V. Radtke, C. Schetter, and S. W. Glunz, “Electrochemical methods to analyse the light-induced plating process,” *Journal of Applied Electrochemistry,* vol. 40, no. 4, pp. 757-765, 2010.

[146] Y. Yao, “Electrochemical Metal Deposition for Silicon Solar Cells,” University of New South Wales, 2012.

[147] P.-C. Hsiao, Z. Ouyang, X. Wang, and A. Lennon, "Investigating light-induced plating of silicon solar cells using in-situ current-voltage analysis." pp. 1-4.

[148] nb-technologies. "suncup® - smart plating," Nov 22, 2016.

[149] RENA. "InCellPlate®," Nov 22, 2016.

[150] A. Lennon, S. Flynn, T. Young, N. Nampalli, M. Edwards, R. Evans, Y. Yao, P.-H. Hsiao, X. Wang, V. Allen, R. Chen, L. Mai, A. Sugianto, V. Vais, D. Jordan, R. Egan, and S. Wenham, "Addressing perceived barriers to the adoption of plated metallisation for silicon photovoltaic manufacturing." pp. 73-82.

[151] Besi. "Meco DPL," Nov 12, 2016.

[152] A. Sugianto, B. S. Tjahjono, J. H. Guo, and S. R. Wenham, "Impact of laser induced defects on the performance of solar cells using localised laser doped regions beneath the metal contact." pp. 1759-1762.

[153] A. Sugianto, J. Bovatsek, S. Wenham, B. Tjahjono, G. Xu, Y. Yao, B. Hallam, X. Bai, N. Kuepper, C. M. Chong, and R. Patel, "18.5% laser-doped solar cell on CZ p-type silicon." pp. 000689-000694.

[154] B. Tjahjono, “Laser doped selective emitter solar cells,” University of New South Wales, 2010.

[155] B. Tjahjono, J.-H. Guo, Z. Hameiri, L. Mai, A. Sugianto, S. Wang, and S. R. Wenham, "High efficiency solar cell structure through the use of laser doping." pp. 966-969.

[156] D. Kray, M. Aleman, A. Fell, S. Hopman, K. Mayer, M. Mesec, R. Muller, G. P. Willeke, S. W. Glunz, B. Bitnar, D. H. Neuhaus, R. Ludemann, T. Schlenker, D. Manz, A. Bentzen, E. Sauar, A. Pauchard, and B. Richerzhagen, "Laser-doped silicon solar cells by Laser Chemical Processing (LCP) exceeding 20% efficiency." pp. 1-3.

[157] D. Kray, N. Bay, G. Cimiotti, S. Kleinschmidt, N. Kösterke, A. Lösel, M. Sailer, A. Träger, H. Köhnlein, H. Nussbaumer, C. Fleischmann, and F. Granek, "Industrial LCP selective emitter solar cells with plated contacts." pp. 000667-000671.

[158] C. Carlsson, A. Esturo-Breton, M. Ametowobla, J. R. Kohler, and J. H. Werner, "Laser doping for selective silicon solar cell emitter." pp. 938-941.

[159] A. Wang, “High Efficiency PERC and PERL Silicon Solar Cells,” Ph. D. Thesis, The University of New South Wales, Australia, 1992.

[160] B. Hallam, C. Chan, A. Sugianto, and S. Wenham, “Deep junction laser doping for contacting buried layers in silicon solar cells,” *Solar Energy Materials and Solar Cells,* vol. 113, pp. 124-134, 2013.

[161] J. Fu, J. B. Heng, and C. J. X. Beitel, Z., *Photovoltaic Devices with Electroplated Metal Grids*, US US 2014/096823,to Silevo, Inc., USPTO, 2014.

[162] C. E. Dube, and R. Gonsiorawski, "Improved contact metallization for high efficiency EFG polycrystalline silicon solar cells." pp. 624-628.

[163] A. Grohe, C. Harmel, A. Knorz, S. Glunz, R. Preu, and G. Willeke, "Selective laser ablation of anti-reflection coatings for novel metallization techniques." pp. 1399-1402.

[164] S. Correia, J. Lossen, M. Wald, K. Neckermann, and M. Bähr, "Selective laser ablation of dielectric layers."

[165] P. Engelhart, "Laser processing for high-efficiency silicon solar cells." pp. 72020S-72020S-11.

[166] P. Engelhart, S. Hermann, T. Neubert, H. Plagwitz, R. Grischke, R. Meyer, U. Klug, A. Schoonderbeek, U. Stute, and R. Brendel, “Laser ablation of SiO2 for locally contacted Si solar cells with ultra-short pulses,” *Progress in Photovoltaics: Research and Applications,* vol. 15, no. 6, pp. 521-527, 2007.

[167] A. Knorz, M. Aleman, A. Grohe, R. Preu, and S.W. Glunz, “Laser Ablation of Antireflection Coatings for Plated Contacts Yielding Solar Cell Efficiencies Above 20 %,” in 24th European Photovoltaic Solar Energy Conference, Hamburg, Germany, 2009.

[168] A. Metz, D. Adler, S. Bagus, H. Blanke, M. Bothar, E. Brouwer, S. Dauwe, K. Dressler, R. Droessler, T. Droste, M. Fiedler, Y. Gassenbauer, T. Grahl, N. Hermert,

W. Kuzminski, A. Lachowicz, T. Lauinger, N. Lenck, M. Manole, M. Martini, R. Messmer, C. Meyer, J. Moschner, K. Ramspeck, P. Roth, R. Schönfelder, B. Schum, J. Sticksel, K. Vaas, M. Volk, and K. Wangemann, "Industrial high performance crystalline silicon solar cells and modules based on rear surface passivation technology," *Solar Energy Materials and Solar Cells*, vol. 120, Part A, pp. 417-425, 2014.

[169] M. V. Shugaev, C. Wu, O. Armbruster, A. Naghilou, N. Brouwer, D. S. Ivanov, T. J. Y. Derrien, N. M. Bulgakova, W. Kautek, B. Rethfeld, and L. V. Zhigilei, "Fundamentals of ultrafast laser–material interaction," *MRS Bulletin*, vol. 41, no. 12, pp. 960-968, 2016/12/001, 2016.

[170] M. D. Perry, B. C. Stuart, P. S. Banks, M. D. Feit, V. Yanovsky, and A. M. Rubenchik, "Ultrashort-pulse laser machining of dielectric materials," *Journal of Applied Physics*, vol. 85, no. 9, pp. 6803-6810, 1999.

[171] J. Meijer, K. Du, A. Gillner, D. Hoffmann, V. S. Kovalenko, T. Masuzawa, A. Ostendorf, R. Poprawe, and W. Schulz, "Laser Machining by short and ultrashort pulses, state of the art and new opportunities in the age of the photons," *CIRP Annals - Manufacturing Technology*, vol. 51, no. 2, pp. 531-550, 2002/01/01, 2002.

[172] X. Liu, D. Du, and G. Mourou, "Laser ablation and micromachining with ultrashort laser pulses," *IEEE Journal of Quantum Electronics*, vol. 33, no. 10, pp. 1706-1716, 1997.

[173] M. D. Shirk, and P. A. Molian, "A review of ultrashort pulsed laser ablation of materials," *Journal of Laser Applications*, vol. 10, no. 1, pp. 18-28, 1998.

[174] M. D. Shirk, P. A. Molian, and A. P. Malshe, "Ultrashort pulsed laser ablation of diamond," *Journal of Laser Applications*, vol. 10, no. 2, pp. 64-70, 1998.

[175] B. C. Stuart, M. D. Feit, S. Herman, A. M. Rubenchik, B. W. Shore, and M. D. Perry, "Nanosecond-to-femtosecond laser-induced breakdown in dielectrics," *Physical Review B*, vol. 53, no. 4, pp. 1749-1761, 1996.

[176] J. Zhu, G. Yin, M. Zhao, D. Chen, and L. Zhao, "Evolution of silicon surface microstructures by picosecond and femtosecond laser irradiations," *Applied surface science*, vol. 245, no. 1, pp. 102-108, 2005.

[177] F. Costache, S. Kouteva-Arguirova, and J. Reif, "Sub–damage–threshold femtosecond laser ablation from crystalline Si: surface nanostructures and phase transformation," *Applied Physics A*, vol. 79, no. 4-6, pp. 1429-1432, 2004.

[178] Q. Wu, Y. Ma, R. Fang, Y. Liao, Q. Yu, X. Chen, and K. Wang, “Femtosecond laser-induced periodic surface structure on diamond film,” *Applied Physics Letters,* vol. 82, no. 11, pp. 1703-1705, 2003.

[179] J. Bonse, S. V. Kirner, S. Höhm, N. Epperlein, D. Spaltmann, A. Rosenfeld, and J. Krüger, "Applications of laser-induced periodic surface structures (LIPSS)." pp. 100920N-1.

[180] I. Gnilitskyi, and A. P. Serro, “Laser Nanopatterning for Wetability Applications,” 2017.

[181] A. Borowiec, and H. Haugen, “Subwavelength ripple formation on the surfaces of compound semiconductors irradiated with femtosecond laser pulses,” *Applied Physics Letters,* vol. 82, no. 25, pp. 4462-4464, 2003.

[182] J. Sipe, J. F. Young, J. Preston, and H. Van Driel, “Laser-induced periodic surface structure. I. Theory,” *Physical Review B,* vol. 27, no. 2, pp. 1141, 1983.

[183] P. Fauchet, and A. Siegman, “Observations of higher-order laser-induced surface ripples on⟨ 111⟩ germanium,” *Applied Physics A: Materials Science & Processing,* vol. 32, no. 3, pp. 135-140, 1983.

[184] P. Fauchet, and A. Siegman, “Surface ripples on silicon and gallium arsenide under picosecond laser illumination,” *Applied Physics Letters,* vol. 40, no. 9, pp. 824-826, 1982.

[185] G. Gorodetsky, J. Kanicki, T. Kazyaka, and R. Melcher, “Far UV pulsed laser melting of silicon,” *Applied Physics Letters,* vol. 46, no. 6, pp. 547-549, 1985.

[186] T. Anthony, and H. Cline, “Surface rippling induced by surface-tension gradients during laser surface melting and alloying,” *Journal of Applied Physics,* vol. 48, no. 9, pp. 3888-3894, 1977.

[187] Y. Lu, J. Yu, and W. Choi, “Theoretical analysis of laser-induced periodic structures at silicon-dioxide/silicon and silicon-dioxide/aluminum interfaces,” *Applied physics letters,* vol. 71, no. 23, pp. 3439-3440, 1997.

[188] J. Yu, and Y. Lu, “Effects of rapid thermal annealing on ripple growth in excimer laser-irradiated silicon-dioxide/silicon substrates,” *Applied surface science,* vol. 154, pp. 670-674, 2000.

[189] E. Gurevich, and S. Gurevich, “Laser Induced Periodic Surface Structures induced by surface plasmons coupled via roughness,” *Applied Surface Science,* vol. 302, pp. 118-123, 2014.

[190] Y. Yao, P. Papet, J. Hermans, T. Söderström, H. Mehlich, M. König, A. Waltinger, D. Habermann, and A. Richter, "Module integration of solar cells with diverse metallization schemes enabled by SmartWire Connection Technology." pp. 1-5.

[191] A. Lorenz, A. Senne, J. Rohde, S. Kroh, M. Wittenberg, K. Krüger, F. Clement, and D. Biro, “Evaluation of Flexographic Printing Technology for Multi-busbar Solar Cells,” *Energy Procedia*, vol. 67, pp. 126-137, 2015/04/01, 2015.

[192] R. Boehme, Y. Andrault, A. Buechel, and P. Papet, "Method of manufacturing electrical contacts of a silicon solar cell structure," Google Patents, 2011.

[193] P. Papet, J. Hermans, T. Söderström, M. Cucinelli, L. Andreetta, D. Bätzner, W. Frammelsberger, D. Lachenal, J. Meixenberger, B. Legradic, B. Strahm, G. Wahli, W. Brok, J. Geissbühler, A. Tomasi, C. Ballif, E. Vetter, and S. Leu, "Heterojunction solar cells with electroplated Ni/Cu front electrode." pp. 1976-1979.

[194] Z. Li, P.-C. Hsiao, W. Zhang, R. Chen, Y. Yao, P. Papet, and A. Lennon, “Patterning for Plated Heterojunction Cells,” *Energy Procedia*, vol. 67, pp. 76-83, 2015.

[195] W. Cai, S. Yuan, Y. Sheng, W. Duan, Z. Wang, Y. Chen, Y. Yang, P. P. Altermatt, P. J. Verlinden, and Z. Feng, “22.2% Efficiency n-type PERT Solar Cell,” *Energy Procedia*, vol. 92, pp. 399-403, 2016.

[196] V. Vais, A. J. Lennon, S. R. Wenham, J. J. Ji, and A. M. Wenham, "Metal contact scheme for solar cells," Google Patents, 2016.

[197] X. Wang, V. Allen, V. Vais, Y. Zhao, B. Tjahjono, Y. Yao, S. Wenham, and A. Lennon, “Laser-doped metal-plated bifacial silicon solar cells,” *Solar Energy Materials and Solar Cells*, vol. 131, no. 0, pp. 37-45, 2014.

[198] V. Vais, “Contactless Electroplating for Silicon Solar Cells ”, School of Photovoltaic and Renewable Energy Engineering, The University of New South Wales 2010.

[199] V. Vais, “Contactless Electroplating for Silicon Solar Cells,” University of New South Wales, 2010.

[200] Y. Zhao, “Field Induced Plating for Bifacial Silicon Solar Cell ”, School of Photovoltaic and Renewable Energy Engineering, University of New South Wales 2011.

[201] X. WANG, “Field-Induced Plating for Bifacial Laser-Doped Silicon Solar Cells ”, School of Photovoltaic and Renewable Energy Engineering, The University of New South Wales 20112.

[202] R. T, der, P. Grabitz, S. Eisele, C. Wagner, K. J. R, hler, and J. H. Werner, "0.4% absolute efficiency gain of industrial solar cells by laser doped selective emitter." pp. 000871-000873.

[203] Z. Hameiri, L. Mai, A. Sproul, and S. R. Wenham, “18.7% efficient laser-doped solar cell on p-type Czochralski silicon,” *Applied Physics Letters,* vol. 97, no. 22, pp. 222111, 2010.

[204] S. W. Glunz, J. Nekarda, H. Mäckel, and A. Cuevas, “Analyzing back contacts of silicon solar cells by Suns-VOC-measurement at high illumination densities,” in 22nd European Photovoltaic Solar Energy Conference, Milan, Italy, 2007.

[205] A. B. Sproul, and M. A. Green, “Improved value for the silicon intrinsic carrier concentration from 275 to 375 K,” *Journal of Applied Physics,* vol. 70, no. 2, pp. 846-854, 1991.

[206] G. H. Yordanov, O. M. Midtg, and T. O. Saetre, "Ideality factor behavior between the maximum power point and open circuit." pp. 0729-0733.

[207] O. Breitenstein, P. Altermatt, K. Ramspeck, M. A. Green, J. Zhao, and A. Schenk, "Interpretation of the Commonly Observed I-V Characteristics of C-SI Cells Having Ideality Factor Larger Than Two." pp. 879-884.

[208] J. Schmidt, A. Merkle, R. Brendel, B. Hoex, M. C. M. v. de Sanden, and W. M. M. Kessels, “Surface passivation of high-efficiency silicon solar cells by atomic-layer-deposited Al2O3,” *Progress in Photovoltaics: Research and Applications,* vol. 16, no. 6, pp. 461-466, 2008.

[209] B. Kuhlmann, A. G. Aberle, R. Hezel, and G. Heiser, “Simulation and optimization of metal-insulator-semiconductor inversion-layer silicon solar cells,” *IEEE Transactions on Electron Devices,* vol. 47, no. 11, pp. 2167-2178, 2000.

[210] R. E. Thomas, R. B. North, and C. E. Norman, “Low cost - high efficiency MIS/inversion layer solar cells,” *IEEE Electron Device Letters,* vol. 1, no. 5, pp. 79-80, 1980.

[211] M. Grauvogl, A. G. Aberle, and R. Hezel, "17.1% efficient truncated-pyramid inversion-layer silicon solar cells." pp. 433-436.

[212] S. Dauwe, L. Mittelstadt, A. Metz, J. Schmidt, and R. Hezel, "Low-temperature rear surface passivation schemes for >20% efficient silicon solar cells." pp. 1395-1398 Vol.2.

[213] O. Breitenstein, J. P. Rakotoniaina, S. Neve, M. H. A. Rifai, and M. Werner, "Shunt types in multicrystalline solar cells." pp. 987-990 Vol.1.

[214] Y. Yao, J. Rodriguez, J. Cui, A. Lennon, and S. Wenham, “Uniform plating of thin nickel layers for silicon solar cells,” 2013.

[215] J. Bartsch, M. Kamp, D. Hartleb, C. Wittich, A. Mondon, B. Steinhauser, F. Feldmann, A. Richter, J. Benick, M. Glatthaar, M. Hermle, and S. W. Glunz, “Proceedings of the 4th International Conference on Crystalline Silicon Photovoltaics (SiliconPV 2014)21.8% Efficient n-type Solar Cells with Industrially Feasible Plated Metallization,” *Energy Procedia,* vol. 55, pp. 400-409, 2014/01/01, 2014.

[216] P. Wendt, E. Coyle, and N. Gallagher, “Stack filters,” *IEEE Transactions on Acoustics, Speech, and Signal Processing,* vol. 34, no. 4, pp. 898-911, 1986.

[217] R. J. McIntyre, “The distribution of gains in uniformly multiplying avalanche photodiodes: Theory,” *IEEE Transactions on Electron Devices,* vol. 19, no. 6, pp. 703-713, 1972.

[218] P. Biber, and W. Strasser, "The normal distributions transform: a new approach to laser scan matching." pp. 2743-2748 vol.3.

[219] B. Hallam, S. Wenham, H. Lee, E. Lee, H. Lee, J. Kim, and J. Shin, “Effect of edge junction isolation on the performance of laser doped selective emitter solar cells,” *Solar Energy Materials and Solar Cells,* vol. 95, no. 12, pp. 3557-3563, 2011.

[220] S. R. Wenham, and M. A. Green, *Self aligning method for forming a selective emitter and metallization in a solar cell*, United States,to Unisearch Limited, 2002.

[221] P. P. Altermatt, A. Schenk, F. Geelhaar, and G. Heiser, “Reassessment of the intrinsic carrier density in crystalline silicon in view of band-gap narrowing,” *Journal of Applied Physics,* vol. 93, no. 3, pp. 1598-1604, 2003.

[222] H. Nagel, C. Berge, and A. G. Aberle, “Generalized analysis of quasi-steady-state and quasi-transient measurements of carrier lifetimes in semiconductors,” *Journal of Applied Physics,* vol. 86, no. 11, pp. 6218-6221, 1999.

[223] R. A. Sinton, and A. Cuevas, “Contactless determination of current–voltage characteristics and minority-carrier lifetimes in semiconductors from quasi-steady-state photoconductance data,” *Applied Physics Letters,* vol. 69, no. 17, pp. 2510-2512, 1996.

[224] R. A. Sinton, A. Cuevas, and M. Stuckings, "Quasi-steady-state photoconductance, a new method for solar cell material and device characterization." pp. 457-460.

[225] Z. Hameiri, L. Mai, T. Puzzer, and S. R. Wenham, “Influence of laser power on the properties of laser doped solar cells,” *Solar Energy Materials and Solar Cells,* vol. 95, no. 4, pp. 1085-1094, 2011.

[226] B. Hallam, A. Urueña, R. Russell, M. Aleman, M. Abbott, C. Dang, S. Wenham, L. Tous, and J. Poortmans, “Efficiency enhancement of i-PERC solar cells by implementation of a laser doped selective emitter,” *Solar Energy Materials and Solar Cells*, vol. 134, pp. 89-98, 3//, 2015.

[227] B. Xiao, L. Mai, D. Lin, B. Hallam, C. M. Chong, A. Lennon, and S. Wenham, "Study of p-type laser doping using ALD AlOx as a dopant source." pp. 3032-3035.

[228] S. C. Hung, S. C. Shiu, J. J. Chao, and C. F. Lin, "Formation of cylindrical profile of Si by KrF excimer laser system for optical interconnect." pp. 5-8.

[229] Y. He, D. Du, B. Sui, L. Xiong, and H. Zhang, "Surface modification of roll by pulsed ND:YAG laser: bump formation caused by martensitic transformation." pp. 157-160 vol.1.

[230] P. Zahariev, N. Mechkarov, G. Danev, and J. Ihlemann, "Micro bump formation on preheated BK7-glass by excimer laser irradiation." pp. 1-1.

[231] J. Brannon, R. White, A. C. Tam, and P. Baumgart, “A study of pulsed-laser bump formation on smooth glass substrates,” *IEEE Transactions on Magnetics,* vol. 34, no. 4, pp. 1789-1791, 1998.

[232] A. C. Tam, J. K. Pour, T. Nguyen, D. Krajnovich, P. Baumgart, T. Bennett, and C. Grioropoulos, “Experimental and theoretical studies of bump formation during laser texturing of Ni-P disk substrates,” *IEEE Transactions on Magnetics,* vol. 32, no. 5, pp. 3771-3773, 1996.

[233] O. Homburg, F. Toennissen, H. Ganser, T. Mitra, and V. Lissotschenko, "Refractive Gauss-to-Tophat Beam Shapers Improve Structure Quality and Speed in Micro-machining." pp. 1-1.

[234] D. J. McCulloch, and S. D. Brotherton, “Surface roughness effects in laser crystallized polycrystalline silicon,” *Applied Physics Letters,* vol. 66, no. 16, pp. 2060-2062, 1995.

[235] A. Marmorstein, A. T. Voutsas, and R. Solanki, “A systematic study and optimization of parameters affecting grain size and surface roughness in excimer laser annealed polysilicon thin films,” *Journal of Applied Physics,* vol. 82, no. 9, pp. 4303-4309, 1997.

[236] C. J. Evans, and J. B. Bryan, ““Structured”, “Textured” or “Engineered” Surfaces,” *CIRP Annals - Manufacturing Technology,* vol. 48, no. 2, pp. 541-556, 1999/01/01, 1999.

[237] L. Benea, P. L. Bonora, A. Borello, and S. Martelli, “Wear corrosion properties of nano-structured SiC–nickel composite coatings obtained by electroplating,” *Wear,* vol. 249, no. 10–11, pp. 995-1003, 2001.

[238] M. R. Vaezi, S. K. Sadrnezhaad, and L. Nikzad, “Electrodeposition of Ni–SiC nano-composite coatings and evaluation of wear and corrosion resistance and electroplating characteristics,” *Colloids and Surfaces A: Physicochemical and Engineering Aspects,* vol. 315, no. 1–3, pp. 176-182, 2/15/, 2008.

[239] Y. Tsukada, S. Tsuchida, and Y. Mashimoto, "Surface laminar circuit packaging." pp. 22-27.

[240] S. Caporali, A. Fossati, A. Lavacchi, I. Perissi, A. Tolstogouzov, and U. Bardi, “Aluminium electroplated from ionic liquids as protective coating against steel corrosion,” *Corrosion Science,* vol. 50, no. 2, pp. 534-539, 2008.

[241] W. Tian, F. Q. Xie, X. Q. Wu, and Z. Z. Yang, “Study on corrosion resistance of electroplating zinc–nickel alloy coatings,” *Surface and Interface Analysis,* vol. 41, no. 3, pp. 251-254, 2009.

[242] A. Sugianto, O. Breitenstein, B. Tjahjono, A. Lennon, L. Mai, and S. R. Wenham, “Impact of Localized Regions with Very High Series Resistances on Cell Performance,” *Prog. Photovolt: Res. & Appl.,* pp. (in press), 2011.

[243] V. A. Vas'ko, I. Tabakovic, S. C. Riemer, and M. T. Kief, “Effect of organic additives on structure, resistivity, and room-temperature recrystallization of electrodeposited copper,” *Microelectronic Engineering,* vol. 75, no. 1, pp. 71-77, 7//, 2004.

[244] M. Stangl, J. Acker, V. Dittel, W. Gruner, V. Hoffmann, and K. Wetzig, “Characterization of electroplated copper self-annealing with investigations focused on incorporated impurities,” *Microelectronic Engineering,* vol. 82, no. 2, pp. 189-195, 2005.

[245] P. M. Vereecken, R. A. Binstead, H. Deligianni, and P. C. Andricacos, “The chemistry of additives in damascene copper plating,” *IBM Journal of Research and Development,* vol. 49, no. 1, pp. 3-18, 2005.

[246] Y.-M. Lin, and S.-C. Yen, “Effects of additives and chelating agents on electroless copper plating,” *Applied Surface Science,* vol. 178, no. 1–4, pp. 116-126, 2001.

[247] John P. Healy, D. Pletcher, and M. Goodenough, “The chemistry of the additives in an acid copper electroplating bath: Part I. Polyethylene glycol and chloride ion,” *Journal of Electroanalytical Chemistry* vol. 338, no. 1-2, pp. 155-165, Oct, 1992.

[248] W. Shao, and G. Zangari, “Dendritic Growth and Morphology Selection in Copper Electrodeposition from Acidic Sulfate Solutions Containing Chlorides,” *The Journal of Physical Chemistry C*, vol. 113, no. 23, pp. 10097-10102, 2009/06/11, 2009.

[249] A. Watson, *Acid copper electroplating baths containing brightening and leveling additives* to M&T Chemicals Inc., U. Patent, 1983.

[250] T. I. f. I. a. P. E. Circuits. "IPC-TM-650 Test Methods Manual," Dec 11, 2016.

[251] S. Wang, A. Lennon, B. Tjahjono, L. Mai, B. Vogl, and S. Wenham, “Overcoming over-plating problems for PECVD SiNx passivated laser doped p-type multi-crystalline silicon solar cells,” *Solar Energy Materials and Solar Cells,* vol. 99, pp. 226-234, 2012.

[252] M. A. Green, C. M. Chong, F. Zhang, A. Sproul, J. Zolper, and S. R. Wenham, "20% efficient laser grooved, buried contact silicon solar cells." pp. 411-414 vol.1.

[253] E. J. Lee, D. S. Kim, and S. H. Lee, “Ni/Cu metallization for low-cost high-efficiency PERC cells,” *Solar Energy Materials and Solar Cells,* vol. 74, no. 1–4, pp. 65-70, 2002.

[254] D. L. Meier, and D. K. Schroder, “Contact resistance: Its measurement and relative importance to power loss in a solar cell,” *IEEE Transactions on Electron Devices,* vol. 31, no. 5, pp. 647-653, 1984.

[255] D. K. Schroder, and D. L. Meier, “Solar cell contact resistance: A review,” *IEEE Transactions on Electron Devices,* vol. 31, no. 5, pp. 637-647, 1984.

[256] A. Mondon, M. N. Jawaid, J. Bartsch, M. Glatthaar, and S. W. Glunz, “Microstructure analysis of the interface situation and adhesion of thermally formed nickel silicide for plated nickel–copper contacts on silicon solar cells,” *Solar Energy Materials and Solar Cells,* vol. 117, pp. 209-213, 2013.

[257] F. Werner, Y. Larionova, D. Zielke, T. Ohrdes, and J. Schmidt, “Aluminum-oxide-based inversion layer solar cells on n-type crystalline silicon: Fundamental properties and efficiency potential,” *Journal of Applied Physics,* vol. 115, no. 7, pp. 073702, 2014.

[258] C. J. Edwardson, P. G. Coleman, T.-T. A. Li, A. Cuevas, and S. Ruffell, “Positron annihilation studies of the AlOx/SiO2/Si interface in solar cell structures,” *Journal of Applied Physics,* vol. 111, no. 5, pp. 053515, 2012.

[259] S. Duttagupta, F. Lin, K. D. Shetty, A. G. Aberle, and B. Hoex, “Excellent boron emitter passivation for high-efficiency Si wafer solar cells using AlOx/SiNx dielectric

stacks deposited in an industrial inline plasma reactor," *Progress in Photovoltaics: Research and Applications,* vol. 21, no. 4, pp. 760-764, 2013.

[260] M. A. Green, "Solar cell fill factors: General graph and empirical expressions," *Solid-State Electronics,* vol. 24, no. 8, pp. 788-789, 1981.

[261] D. Pysch, A. Mette, and S. W. Glunz, "A review and comparison of different methods to determine the series resistance of solar cells," *Solar Energy Materials and Solar Cells,* vol. 91, no. 18, pp. 1698-1706, 2007.

[262] T. Dullweber, S. Gatz, H. Hannebauer, T. Falcon, R. Hesse, J. Schmidt, and R. Brendel, "19.4% -Efficient Large Area Rear-Passivated Screen-Printed Silicon Solar Cells," WIP, 2011.

[263] X. Wang, M. Juhl, M. Abbott, Z. Hameiri, Y. Yao, and A. Lennon, "Use of QSSPC and QSSPL to Monitor Recombination Processes in P-Type Silicon Solar Cells," in 4th SiliconPV 2014, 's-Hertogenbosch, The Netherlands, 2014.

[264] X. Wang, M. Juhl, and A. Lennon, "Injection-dependent carrier lifetime analysis of recombination due to boron-oxygen complexes in wafers passivated with different dielectrics by QSSPL and QSSPC," in 6th International Conference on Silicon Photovoltaics, Chambery, France, 2016.

[265] Z. C. Holman, A. Descoeudres, L. Barraud, F. Z. Fernandez, J. P. Seif, S. De Wolf, and C. Ballif, "Current Losses at the Front of Silicon Heterojunction Solar Cells," *Photovoltaics, IEEE Journal of,* vol. 2, no. 1, pp. 7-15, 2012.

[266] A. G. Aberle, W. Zhang, and B. Hoex, "Advanced loss analysis method for silicon wafer solar cells," *Energy Procedia,* vol. 8, no. 0, pp. 244-249, 2011.

[267] E. Lee, H. Lee, J. Choi, D. Oh, J. Shim, K. Cho, J. Kim, S. Lee, B. Hallam, S. R. Wenham, and H. Lee, "Improved LDSE processing for the avoidance of overplating yielding 19.2% efficiency on commercial grade crystalline Si solar cell," *Solar Energy Materials and Solar Cells,* vol. 95, no. 12, pp. 3592-3595, 12//, 2011.

[268] V. Allen, "Field Plating to N-type Bifacial Silicon Solar Cells ", School of Photovoltaic and Renewable Energy Engineering, The University of New South Wales 2012.

[269] D. Macdonald, and A. Cuevas, "Reduced fill factors in multicrystalline silicon solar cells due to injection-level dependent bulk recombination lifetimes," *Progress in Photovoltaics: Research and Applications,* vol. 8, no. 4, pp. 363-375, 2000.

[270] A. Karpour, and S. R. Wenham, "The importance of surface roughness in the adhesion of electroless-plated metal in inkjet printed grooves." pp. 001410-001413.

[271] J. Schmidt, and A. Cuevas, “Electronic properties of light-induced recombination centers in boron-doped Czochralski silicon,” *Journal of Applied Physics,* vol. 86, no. 6, pp. 3175-3180, 1999.

[272] S. Rein, and S. W. Glunz, “Electronic properties of the metastable defect in boron-doped Czochralski silicon: Unambiguous determination by advanced lifetime spectroscopy,” *Applied Physics Letters,* vol. 82, no. 7, pp. 1054-1056, 2003.

[273] K. Bothe, and J. Schmidt, “Electronically activated boron-oxygen-related recombination centers in crystalline silicon,” *Journal of Applied Physics,* vol. 99, no. 1, pp. 013701, 2006.

[274] J. Schmidt, and K. Bothe, “Structure and transformation of the metastable boron- and oxygen-related defect center in crystalline silicon,” *Physical Review B,* vol. 69, no. 2, pp. 024107, 2004.

[275] T. Trupke, R. A. Bardos, M. D. Abbott, and J. E. Cotter, “Suns-photoluminescence: Contactless determination of current-voltage characteristics of silicon wafers,” *Applied Physics Letters,* vol. 87, no. 9, pp. -, 2005.

[276] Z. Hameiri, K. McIntosh, and G. Xu, “Evaluation of recombination processes using the local ideality factor of carrier lifetime measurements,” *Solar Energy Materials and Solar Cells,* vol. 117, pp. 251-258, 2013.

[277] B. Mitchell, T. Trupke, J. W. Weber, and J. Nyhus, “Bulk minority carrier lifetimes and doping of silicon bricks from photoluminescence intensity ratios,” *Journal of Applied Physics,* vol. 109, no. 8, pp. 083111, 2011.

[278] S. Instruments. "WCT-120," Nov 14, 2016.

[279] D. K. Schroder, *Semiconductor Material and Device Characterization*: Wiley-IEEE Press, 2006.

[280] A. Cuevas, and D. Macdonald, “Measuring and interpreting the lifetime of silicon wafers,” *Solar Energy,* vol. 76, no. 1–3, pp. 255-262, 2004.

[281] K. R. McIntosh, “Lumps, Humps and Bumps: Three Detrimental Effects in the Current-Voltage Curve of Silicon Solar Cells,” Ph. D. Thesis, Centre for Photovoltaic Engineering, The University of New South Wales, Australia, 2001.

[282] J. Giesecke, T. Niewelt, M. Rüdiger, M. Rauer, M. Schubert, and W. Warta, “Broad range injection-dependent minority carrier lifetime from photoluminescence,” *Solar Energy Materials and Solar Cells,* vol. 102, pp. 220-224, 2012.

[283] R. Bardos, T. Trupke, M. Schubert, and T. Roth, “Trapping artifacts in quasi-steady-state photoluminescence and photoconductance lifetime measurements on silicon wafers,” *Applied Physics Letters,* vol. 88, no. 5, pp. 053504, 2006.

[284] M. Bail, M. Schulz, and R. Brendel, “Space-charge region-dominated steady-state photoconductance in low-lifetime Si wafers,” *Applied Physics Letters,* vol. 82, no. 5, pp. 757-759, 2003.

[285] P. J. Cousins, D. H. Neuhaus, and J. E. Cotter, “Experimental verification of the effect of depletion-region modulation on photoconductance lifetime measurements,” *Journal of Applied Physics,* vol. 95, no. 4, pp. 1854-1858, 2004.

[286] C. Chan, M. Abbott, B. Hallam, M. Juhl, D. Lin, Z. Li, Y. Li, J. Rodriguez, and S. Wenham, “Edge isolation of solar cells using laser doping,” *Solar Energy Materials and Solar Cells,* vol. 132, pp. 535-543, 2015.

[287] M. Juhl, C. Chan, M. D. Abbott, and T. Trupke, “Anomalously high lifetimes measured by quasi-steady-state photoconductance in advanced solar cell structures,” *Applied Physics Letters,* vol. 103, no. 24, pp. 243902, 2013.

[288] W. Van Roosbroeck, and W. Shockley, “Photon-radiative recombination of electrons and holes in germanium,” *Physical Review,* vol. 94, no. 6, pp. 1558, 1954.

[289] M. Abbott, J. Cotter, T. Trupke, and R. Bardos, “Investigation of edge recombination effects in silicon solar cell structures using photoluminescence,” *Applied physics letters,* vol. 88, no. 11, pp. 114105, 2006.

[290] H. Fischer, and W. Pschunder, "Investigation of photon and thermal induced change in silicon solar cells." pp. 404 – 411.

[291] V. G. Weizer, H. W. Brandhorst, J. D. Broder, R. E. Hart, and J. H. Lamneck, “Photon-degradation effects in terrestrial silicon solar cells,” *Journal of Applied Physics,* vol. 50, no. 6, pp. 4443-4449, 1979.

[292] J. Schmidt, "Light-induced degradation in crystalline silicon solar cells." pp. 187-196.

[293] D. Macdonald, F. Rougieux, A. Cuevas, B. Lim, J. Schmidt, M. Di Sabatino, and L. Geerligs, “Light-induced boron-oxygen defect generation in compensated p-type Czochralski silicon,” *Journal of Applied Physics,* vol. 105, no. 9, pp. 093704, 2009.

[294] J. Benick, A. Richter, M. Hermle, and S. W. Glunz, “Thermal stability of the Al2O3 passivation on p-type silicon surfaces for solar cell applications,” *physica status solidi (RRL)-Rapid Research Letters,* vol. 3, no. 7-8, pp. 233-235, 2009.

[295] K. Bothe, R. Sinton, and J. Schmidt, “Fundamental boron–oxygen-related carrier lifetime limit in mono-and multicrystalline silicon,” *Progress in Photovoltaics: Research and Applications,* vol. 13, no. 4, pp. 287-296, 2005.

[296] M. A. Green, “Crystalline and thin-film silicon solar cells: state of the art and future potential,” *Solar Energy,* vol. 74, no. 3, pp. 181-192, 2003.

[297] J. Adey, R. Jones, D. Palmer, P. Briddon, and S. Öberg, “Degradation of boron-doped Czochralski-grown silicon solar cells,” *Physical review letters,* vol. 93, no. 5, pp. 055504, 2004.

[298] J. Schmidt, A. G. Aberle, and R. Hezel, "Investigation of carrier lifetime instabilities in Cz-grown silicon." pp. 13-18.

[299] B. J. Hallam, S. R. Wenham, P. G. Hamer, M. D. Abbott, A. Sugianto, C. E. Chan, A. M. Wenham, M. G. Eadie, and G. Xu, “Hydrogen passivation of BO defects in Czochralski silicon,” *Energy Procedia,* vol. 38, pp. 561-570, 2013, 2013.

[300] P. Hamer, B. Hallam, M. Abbott, and S. Wenham, “Accelerated formation of the boron–oxygen complex in p-type Czochralski silicon,” *physica status solidi (RRL) – Rapid Research Letters,* vol. 9, no. 5, pp. 297-300, 2015.

[301] J. Schmidt, K. Bothe, and R. Hezel, "Formation and annihilation of the metastable defect in boron-doped Czochralski silicon." pp. 178-181.

[302] J. Schmidt, “Light-Induced Degradation in Crystalline Silicon Solar Cells ” *Solid State Phenomena,* vol. 95-96, pp. 187-196, 2003.

[303] D. C. Walter, B. Lim, K. Bothe, R. Falster, V. V. Voronkov, and J. Schmidt, “Lifetimes exceeding 1 ms in 1-Ω cm boron-doped Cz-silicon,” *Solar Energy Materials and Solar Cells,* vol. 131, pp. 51-57, 2014.

[304] D. C. Walter, B. Lim, K. Bothe, V. V. Voronkov, R. Falster, and J. Schmidt, “Effect of rapid thermal annealing on recombination centres in boron-doped Czochralski-grown silicon,” *Applied Physics Letters,* vol. 104, no. 4, pp. 042111, 2014.

[305] S. Wilking, C. Beckh, S. Ebert, A. Herguth, and G. Hahn, “Influence of bound hydrogen states on BO-regeneration kinetics and consequences for high-speed regeneration processes,” *Solar Energy Materials and Solar Cells,* vol. 131, pp. 2-8, 12//, 2014.

[306] C. E. Chan, M. D. Abbott, M. K. Juhl, B. J. Hallam, X. Bo, and S. R. Wenham, “Assessing the Performance of Surface Passivation Using Low-Intensity Photoluminescence Characterization Techniques,” *IEEE Journal of Photovoltaics,* vol. 4, no. 1, pp. 100-106, 2014.

[307] M. Kerr, and A. Cuevas, “Generalized analysis of the illumination intensity vs. open-circuit voltage of solar cells,” *Solar Energy,* vol. 76, no. 1, pp. 263-267, 2004.

[308] T. Trupke, R. A. Bardos, and M. D. Abbott, “Self-consistent calibration of photoluminescence and photoconductance lifetime measurements,” *Applied Physics Letters,* vol. 87, no. 18, pp. -, 2005.

[309] Z. Hameiri, T. Trupke, N. Gao, R. A. Sinton, and J. W. Weber, “Effective bulk doping concentration of diffused and undiffused silicon wafers obtained from combined photoconductance and photoluminescence measurements,” *Progress in Photovoltaics: Research and Applications,* vol. 21, no. 5, pp. 942-949, 2013.

[310] B. Hoex, S. Heil, E. Langereis, M. Van de Sanden, and W. Kessels, “Ultralow surface recombination of c-Si substrates passivated by plasma-assisted atomic layer deposited Al 2 O 3,” *Applied Physics Letters,* vol. 89, no. 4, pp. 042112, 2006.

[311] H. Mäckel, and R. Lüdemann, “Detailed study of the composition of hydrogenated SiN x layers for high-quality silicon surface passivation,” *Journal of Applied Physics,* vol. 92, no. 5, pp. 2602-2609, 2002.

[312] S. J. Robinson, A. G. Aberle, and M. A. Green, “Recombination saturation effects in silicon solar cells,” *Electron Devices, IEEE Transactions on,* vol. 41, no. 9, pp. 1556-1569, 1994.

[313] A. G. Aberle, S. W. Glunz, A. W. Stephens, and M. A. Green, “High-eficiency silicon solar cells: Si/SiO2, interface parameters and their impact on device performance,” *Progress in Photovoltaics: Research and Applications,* vol. 2, no. 4, pp. 265-273, 1994.

[314] P. Cousins, C. Honsberg, A. Sproul, and F. Cotter, "The effect of SRH on the fill factor of double sided buried contact solar cells,."

[315] J. E. Cotter, G. H. Guo, P. J. Cousins, M. D. Abbott, F. W. Chen, and K. C. Fisher, "P-type vs. n-type silicon wafers: Prospects for high-efficiency, commercial silicon solar cells ".

[316] Z. Hameiri, and K. R. McIntosh, "On the use of local ideality factor obtained from effective carrier lifetime measurements."

[317] J. Schmidt, C. Berge, and A. G. Aberle, “Injection level dependence of the defect-related carrier lifetime in light-degraded boron-doped Czochralski silicon,” *Applied Physics Letters,* vol. 73, no. 15, pp. 2167-2169, 1998.

[318] K. Bothe, J. Schmidt, and R. Hezel, "Effective reduction of the metastable defect concentration in boron-doped Czochralski silicon for solar cells." pp. 194-197.

[319] M. Wilson, J. Lagowski, L. Jastrzebski, A. Savtchouk, and V. Faifer, "COCOS (corona oxide characterization of semiconductor) non-contact metrology for gate dielectrics," *AIP Conference Proceedings,* vol. 550, no. 1, pp. 220-225, 2001.

[320] M. Wilson, D. Marinskiy, A. Byelyayev, J. D'Amico, A. Findlay, L. Jastrzebski, and J. Lagowski, "The present status and recent advancements in corona-Kelvin non-contact electrical metrology of dielectrics for IC-manufacturing," in 21th ECS Meeting 2006.

[321] D. C. Walter, B. Lim, and J. Schmidt, "Realistic efficiency potential of next-generation industrial Czochralski-grown silicon solar cells after deactivation of the boron–oxygen-related defect center," *Progress in Photovoltaics: Research and Applications,* vol. 24, no. 7, pp. 920-928, 2016.

[322] J. Haunschild, I. E. Reis, J. Geilker, and S. Rein, "Detecting efficiency-limiting defects in Czochralski-grown silicon wafers in solar cell production using photoluminescence imaging," *physica status solidi (RRL) – Rapid Research Letters,* vol. 5, no. 5-6, pp. 199-201, 2011.

[323] P. K. Kulshreshtha, Y. Yoon, K. M. Youssef, E. A. Good, and G. Rozgonyi, "Oxygen Precipitation Related Stress-Modified Crack Propagation in High Growth Rate Czochralski Silicon Wafers," *Journal of The Electrochemical Society,* vol. 159, no. 2, pp. H125-H129, January 1, 2011, 2011.

[324] J. D. Murphy, R. E. McGuire, K. Bothe, V. V. Voronkov, and R. J. Falster, "Minority carrier lifetime in silicon photovoltaics: The effect of oxygen precipitation," *Solar Energy Materials and Solar Cells,* vol. 120, Part A, pp. 402-411, 2014.

[325] J. D. Murphy, R. E. McGuire, K. Bothe, V. V. Voronkov, and R. J. Falster, "Competitive gettering of iron in silicon photovoltaics: Oxide precipitates versus phosphorus diffusion," *Journal of Applied Physics,* vol. 116, no. 5, pp. -, 2014.

[326] D. Macdonald, and L. Geerligs, "Recombination activity of interstitial iron and other transition metal point defects in p-and n-type crystalline silicon," *Applied Physics Letters,* vol. 85, no. 18, pp. 4061-4063, 2004.

[327] G. Coletti, R. Kvande, V. Mihailetchi, L. Geerligs, L. Arnberg, and E. Øvrelid, "Effect of iron in silicon feedstock on p-and n-type multicrystalline silicon solar cells," *Journal of applied physics,* vol. 104, no. 10, pp. 104913, 2008.

[328] J. D. Murphy, M. Al-Amin, K. Bothe, M. Olmo, V. V. Voronkov, and R. J. Falster, "The effect of oxide precipitates on minority carrier lifetime in n-type silicon," *Journal of Applied Physics,* vol. 118, no. 21, pp. 215706, 2015.

[329] M. Koizuka, and H. Yamada-Kaneta, “Gap states caused by oxygen precipitation in Czochralski silicon crystals,” *Journal of Applied Physics,* vol. 84, no. 8, pp. 4255-4258, 1998.

[330] P. R. Bevington, *Data Reduction and Error Analysis for the Physical Sciences*, p.^pp. 58-64, New York: McGraw-Hill, 1969.

[331] J. H. Wohlgemuth, D. W. Cunningham, P. Monus, J. Miller, and A. Nguyen, "Long Term Reliability of Photovoltaic Modules." pp. 2050-2053.

[332] R. Klengel, M. Petzold, D. Schade, and B. Sykes, "Improved testing of soldered Busbar interconnects on silicon solar cells." pp. 1-5.

[333] Andrew M. Gabor, S. M. Mike Ralli, Luis Alegria, Chris Bordonaro, Joe Woods, and L. Felton, "Soldering induced damage to thin Si solar cells and detection of cracked cells in modules."

[334] S. Kajari-Schröder, I. Kunze, U. Eitner, and M. Köntges, “Spatial and orientational distribution of cracks in crystalline photovoltaic modules generated by mechanical load tests,” *Solar Energy Materials and Solar Cells,* vol. 95, no. 11, pp. 3054-3059, 2011.

[335] J. Wendt, M. Träger, R. Klengel, M. Petzold, D. Schade, and R. Sykes, "Improved quality test method for solder ribbon interconnects on silicon solar cells." pp. 1-4.

[336] J. Kim, K. S. Kim, and Y. H. Kim, “Mechanical effects in peel adhesion test,” *Journal of Adhesion Science and Technology,* vol. 3, no. 1, pp. 175-187, 1989/01/01, 1989.

[337] H. Ollendorf, and D. Schneider, “A comparative study of adhesion test methods for hard coatings,” *Surface and Coatings Technology,* vol. 113, no. 1–2, pp. 86-102, 3/12/, 1999.

[338] K. L. Mittal, “Adhesion Measurement of Thin Films,” *ElectroComponent Science and Technology,* vol. 3, no. 1, pp. 21-42, 1976.

[339] Joseph Karas, Lynne Michaelson, Mariela Lizet Castillo, Krystal Munoz, Mark Bailly, Harsh Jain, Austin Akey, Jim Rand, Tom Tyson, Tonio Buonassisi, and S. Bowden, “Addressing adhesion and reliability concerns of copper-plated c-Si solar cells and modules ” in 2016 IEEE Photovoltaic Specialists Conference, Portland, 2016.

[340] N. Bay, J. Horzel, M. Passig, M. Sieber, J. Burschik, H. Kühnlein, J. Bartsch, A. Brand, A. Mondon, and D. Eberlein, “Reliable contact formation for industrial solar cells by laser ablation and Ni/Cu plating,” *Proc. 29th EU-PVSEC,* pp. 1272-6, 2014.

[341] S. J. Bull, “Failure mode maps in the thin film scratch adhesion test,” *Tribology International,* vol. 30, no. 7, pp. 491-498, 1997/07/01, 1997.

[342] P. A. Steinmann, Y. Tardy, and H. E. Hintermann, “Adhesion testing by the scratch test method: The influence of intrinsic and extrinsic parameters on the critical load,” *Thin Solid Films,* vol. 154, no. 1, pp. 333-349, 1987/11/12, 1987.

[343] A. J. Perry, “Scratch adhesion testing of hard coatings,” *Thin Solid Films,* vol. 107, no. 2, pp. 167-180, 1983/09/16, 1983.

[344] P. A. Steinmann, and H. E. Hintermann, “A review of the mechanical tests for assessment of thin-film adhesion,” *Journal of Vacuum Science & Technology A: Vacuum, Surfaces, and Films,* vol. 7, no. 3, pp. 2267-2272, 1989.

[345] L. Collins, J. Perkins, and P. Stroud, “Effect of ion bombardment on the adhesion of aluminium films on glass,” *Thin Solid Films,* vol. 4, no. 1, pp. 41-45, 1969.

[346] O. Heavens, “Some factors influencing the adhesion of films produced by vacuum evaporation,” *J. Phys. Radium,* vol. 11, no. 7, pp. 355-360, 1950.

[347] J. Valli, “A review of adhesion test methods for thin hard coatings,” *Journal of Vacuum Science & Technology,* vol. 4, 3 July, 1986.

[348] S.J. Bull, D. S. Rickerby, A. Matthews, A. Leyland, A.R. Pace, and J. Valli, “The use of scratch adhesion testing for the determination of interfacial adhesion: The importance of frictional drag ” *Surface and Coatings Technology* vol. 36, no. 1-2, pp. 503-517, 1 December, 1988.

[349] T. L. Young, K. Hee, A. J. Lennon, R. J. Egan, O. Wilkie, and Y. Yao, "Design and characterization of an adhesion strength tester for evaluating metal contacts on silicon solar cells." pp. 2550-2553.

[350] T. L. Young, "Use of adheison tester," 2013.

[351] Ran Chen, Wei Zhang, Xi Wang, Xi Wang, and A. Lennon, “Failure Modes Identified during Adhesion Testing of Metal Fingers on Silicon Solar Cells ” in the Fifth Workshop on Metallization for Crystalline Silicon Solar Cells, 2015, pp. 194-202.

[352] M. W. Lane, C. E. Murray, F. R. McFeely, P. M. Vereecken, and R. Rosenberg, “Liner materials for direct electrodeposition of Cu,” *Applied Physics Letters,* vol. 83, no. 12, pp. 2330-2332, 2003.

[353] N. M. Bulgakova, and A. V. Bulgakov, “Pulsed laser ablation of solids: transition from normal vaporization to phase explosion,” *Applied Physics A,* vol. 73, no. 2, pp. 199-208, 2001/08/01, 2001.

[354] C. Momma, B. N. Chichkov, S. Nolte, F. von Alvensleben, A. Tünnermann, H. Welling, and B. Wellegehausen, “Short-pulse laser ablation of solid targets,” *Optics Communications,* vol. 129, no. 1–2, pp. 134-142, 1996.

[355] T. O. a. M. M. Yoshiki Nakata, “Nano-Sized Hollow Bump Array Generated by Single Femtosecond Laser Pulse,” *Japanese Journal of Applied Physics*, vol. 42, 18 November 2003.

[356] S. S. Harilal, J. R. Freeman, P. K. Diwaker, and A. Hassanein, "Femtosecond Laser Ablation: Fundamentals and Applications," *Laser-Induced Breakdown Spectroscopy, Springer Series in Optical Sciences*, pp. 143-164, Berlin Heidelberg: Springer-Verlag, 2014.

[357] G. Paltauf, and P. E. Dyer, “Photomechanical Processes and Effects in Ablation,” *Chemical Reviews*, vol. 103, no. 2, pp. 487-518, 2003/02/01, 2003.

[358] D. E. Grady, “The spall strength of condensed matter,” *Journal of the Mechanics and Physics of Solids*, vol. 36, no. 3, pp. 353-384, 1988/01/01, 1988.

[359] T. W. Anderson, and D. A. Darling, “A Test of Goodness of Fit,” *Journal of the American Statistical Association*, vol. 49, no. 268, pp. 765-769, 1954/12/01, 1954.

[360] J. Horzel, “Shifting the limits with cu based metallisation and advanced plating technology,” in Metallisation Workshop, Konstanz, Germany, 2014.

[361] D. Davies, and J. A. Whittaker, “Methods of testing the adhesion of metal coatings to metals,” *Metallurgical Reviews*, vol. 12, no. 1, pp. 15-26, 1967/01/01, 1967.

[362] MALLORY, and G. O., *The relationship between stress and adhesion of electroless nickel-phosphorus deposits on zincated aluminium*, Orlando, FL, ETATS-UNIS: American Electroplaters and Surface Finishers Society, 1985.

[363] W. Zhang, Y. L. Yao, and I. C. Noyan, “Microscale Laser Shock Peening of Thin Films, Part 1: Experiment, Modeling and Simulation,” *Journal of Manufacturing Science and Engineering*, vol. 126, no. 1, pp. 10-17, 2004.

[364] Y. Shacham-Diamand, and Y. Sverdlov, “Electrochemically deposited thin film alloys for ULSI and MEMS applications,” *Microelectronic Engineering*, vol. 50, no. 1–4, pp. 525-531, 2000.

[365] J. K. Luo, A. J. Flewitt, S. M. Spearing, N. A. Fleck, and W. I. Milne, “Young's modulus of electroplated Ni thin film for MEMS applications,” *Materials Letters*, vol. 58, no. 17–18, pp. 2306-2309, 2004.

[366] M. H. Wu, Y. W. Tai, W. M. Chen, and Y. F. Chen, "Solar cell and its electrode structure," US Patents, 2012.

[367] I. W. Boyd, V. Craciun, and A. Kazor, “Vacuum-Ultra-Violet and Ozone Induced Oxidation of Silicon and Silicon-Germanium,” *Japanese Journal of Applied Physics*, vol. 32, no. 12S, pp. 6141, 1993.

[368] W. C. Oliver, and G. M. Pharr, “Measurement of hardness and elastic modulus by instrumented indentation: Advances in understanding and refinements to methodology,” *Journal of Materials Research,* vol. 19, no. 01, pp. 3-20, 2004.

[369] W. C. Oliver, and G. M. Pharr, “An improved technique for determining hardness and elastic modulus using load and displacement sensing indentation experiments,” *Journal of Materials Research,* vol. 7, no. 06, pp. 1564-1583, 1992.

[370] N. Song, P.-C. Hsiao, W. Zhang, X. Wang, and A. Lennon, "Self-annealing behaviors of light induced plated copper fingers and rapid thermal processing effect ".

[371] S. Lopatin, C. Gay, D. Eaglesham, J. O. Dukovic, and N. Y. Kovarsky, "Pulse plating of a low stress film on a solar cell substrate," Google Patents, 2008.

[372] R. O. Hull, “Current density range characteristics, their determination and application,” *Proc. Amer. Electroplaters' Soc,* vol. 27, pp. 52-60, 1939.

[373] W. Yamamoto, "Internal stress testing device for high speed electroplating," Google Patents, 2000.

[374] T. Ito, H. Azuma, and S. Noda, “Internal Stress of C o S i 2 Films Formed by Rapid Thermal Annealing,” *Japanese Journal of Applied Physics,* vol. 33, no. 10R, pp. 5681, 1994.

[375] M. Yu, J. Zhang, D. Li, Q. Meng, and W. Li, “Internal stress and adhesion of Cu film/Si prepared by both MEVVA and IBAD,” *Surface and Coatings Technology,* vol. 201, no. 3–4, pp. 1243-1249, 2006.

[376] Y. Tsuru, M. Nomura, and F. R. Foulkes, “Effects of boric acid on hydrogen evolution and internal stress in films deposited from a nickel sulfamate bath,” *Journal of Applied Electrochemistry,* vol. 32, no. 6, pp. 629-634, 2002.

[377] H. Lee, S. S. Wong, and S. D. Lopatin, “Correlation of stress and texture evolution during self- and thermal annealing of electroplated Cu films,” *Journal of Applied Physics,* vol. 93, no. 7, pp. 3796-3804, 2003.

[378] A. Frank, and A. J. Bard, “The Decomposition of the Sulfonate Additive Sulfopropyl Sulfonate in Acid Copper Electroplating Chemistries,” *Journal of The Electrochemical Society,* vol. 150, no. 4, pp. C244-C250, April 1, 2003, 2003.

[379] A. Gangulee, “The Structure of Electroplated and Vapor-Deposited Copper Films,” *Journal of Applied Physics,* vol. 43, no. 3, pp. 867-873, 1972.

[380] S. H. Brongersma, E. Kerr, I. Vervoort, A. Saerens, and K. Maex, “Grain Growth, Stress, and Impurities in Electroplated Copper,” *Journal of Materials Research,* vol. 17, no. 03, pp. 582-589, 2002.

[381] Y. Okinaka, and S. Nakahara, “Hydrogen Embrittlement of Electroless Copper Deposits,” *Journal of The Electrochemical Society,* vol. 123, no. 4, pp. 475-478, April 1, 1976, 1976.

[382] S. P. Hau-Riege, and C. V. Thompson, “In situ transmission electron microscope studies of the kinetics of abnormal grain growth in electroplated copper films,” *Applied Physics Letters,* vol. 76, no. 3, pp. 309-311, 2000.

[383] C. H, "Electrodeposition of copper from acid baths," US Patents, 1973.

[384] N. Song, W. Zhang, P.-C. Hsiao, X. Wang, J. Colwell, and A. Lennon, “Copper Microstructure Evolution in Light-Induced Plated Metal Grids for Silicon Solar Cells: Implications for Reliable Metallization,” *Journal of The Electrochemical Society,* vol. 163, no. 14, pp. H1136-H1143, January 1, 2016, 2016.

[385] N. Song, W. Zhang, P. C. Hsiao, X. Wang, and A. Lennon, "Self-annealing behavior and rapid thermal processing of light induced plated copper fingers on silicon solar cells."

[386] E. Yakobson, A. Letize, and K. Crouse, *High speed copper plating process,* US WO 2014137638, 2014.

[387] F. C. Nix, and D. MacNair, “The Thermal Expansion of Pure Metals: Copper, Gold, Aluminum, Nickel, and Iron,” *Physical Review,* vol. 60, no. 8, pp. 597-605, 10/15/, 1941.

[388] Y. Okada, and Y. Tokumaru, “Precise determination of lattice parameter and thermal expansion coefficient of silicon between 300 and 1500 K,” *Journal of applied physics,* vol. 56, no. 2, pp. 314-320, 1984.

[389] W. D. Nix, “Mechanical properties of thin films,” *Metallurgical Transactions A,* vol. 20, no. 11, pp. 2217-2245, 1989.

[390] J. Bartsch, M. Kamp, D. Hartleb, C. Wittich, A. Mondon, B. Steinhauser, F. Feldmann, A. Richter, J. Benick, M. Glatthaar, M. Hermle, and S. W. Glunz, "21.8 % Efficient n-type solar cells with industrially feasible plated metallization."

[391] S. Liu, M. Lin, C. Wei, K. Lai, C. Chuang, and C. Li, "Electrical Properties of Forward Bias Plated Ni-Cu Contacts on N-type PERT Solar Cells."